MULTI-WAVELENGTH STUDY OF WOLF RAYET STARS

Thesis submitted
for the degree of
Doctor of Philosophy (Science)
in
Physics (Experimental)

by

Subhajit Kar

Department of Physics

University of Calcutta

2025

Dedicated to my Maa and Papa.

Declaration

I, Subhajit Kar, hereby declare that I am the sole author of this thesis and the works presented in it are my own and have been generated by me as a result of my original research. To the best of my knowledge, this thesis contains no material previously published by any other person except where due acknowledgment has been made. This thesis contains no material that has been accepted as part of the requirements of any other academic degree or non-degree program, in English or any other language.

Acknowledgements

This thesis would not have been possible without the support, guidance, and encouragement of many remarkable people. First and foremost, I would like to express my deepest gratitude to my **supervisor**, Dr. *Ramkrishna Das*, for his invaluable mentorship, patience, and continuous support. His expertise, encouragement, and timely motivation have profoundly shaped my research and academic growth, and I am incredibly grateful for the opportunities he provided me along this journey.

I would also like to thank my annual evaluation committee members, Prof. *Soumen Mondal* and Prof. *Sunandan Gangopadhayay*, for their time, feedback, and invaluable suggestions. Their critical insights and constructive suggestions have greatly enriched my research works.

I am grateful to my collaborators, whose knowledge and enthusiasm made our projects challenging and rewarding. Special thanks to Dr. *Tapas Baug* (SNBNCBS), Dr. *Blesson Mathew* (Christ University), my friend Mr. *Rajorshi Bhattacharya* (UNM), Prof. *Ylva Philstorm* (NRAO), and Dr. *Megan O. Lewis* (Leiden Observatory) for their collaboration, support, and shared commitment to excellence in research. I would like to extend my gratitude to Dr. *Sayantan Bhattacharya* (my senior from undergraduate University) who helped me initially with the installation of CMFGEN modeling code. I am also deeply appreciative of the faculty and staff at S.N. Bose Centre for providing a nurturing environment conducive to academic inquiry.

My heartfelt thanks go to my group members: Dr. *Rahul Bandopadhayay*, Dr. *Ruchi Pandey*, Mr. *Gesesew Reta Habtie*, Mr. *Avijit Mandal*, and Ms. *Sakshi Chaudhary*. Their camaraderie, encouragement, and moral support have been a source of strength throughout my Ph.D., making even the most challenging moments enjoyable and enriching.

To my seniors, colleagues, and friends: *Dhrimadri da*, *Samrat da*, *Alik da*, *Siddhartha da*, *Anuvab da*, *Rajib*, *Shashank*, *Ariful*, *Usman*, *Dorothy*, *Diya*, *Tunir*, *Subhadip*, *Aman*, *Ajay*, and *Soumita*. Your friendship has been a constant source of joy throughout this journey. Thank you for being there when I had some medical problems. Your camaraderie towards me is something I will miss anywhere else. You have been there whenever I felt lonely and depressed. Whether it was conversations, impromptu tea breaks, or words of encouragement when I doubted myself, your support has made all the difference, and I am deeply grateful to have you by my side. Also, I appreciate the support of the friends and the Observational Astronomy post-doctoral researchers at the SN Bose Centre for being a part of my Ph.D. journey.

I am deeply grateful to all my school *teachers*; and undergraduate and postgraduate university/institute *professors* for their unwavering support and guidance during my early academic journey. Their teachings and encouragement laid the foundation for my growth, and I truly wouldn't have come this far without their influence and belief in me.

Lastly, I want to express my heartfelt gratitude to my **family**, whose unwavering love, belief, and encouragement have been my greatest source of strength throughout this journey. To my parents, Papa (Mr. *Alok Kumar Kar*) and Maa (late Mrs. *Pritikona Kar*), thank you for instilling in me a passion for learning and for always supporting my ambitions. Papa, your struggle has always been my source of inspiration, and Maa, your memory will always be the backbone of my life. I often wish you were here with us today to witness this achievement of mine. Maa, your soul knows how deeply I love you. You were not just my loving mother but also my greatest cheerleader and dearest friend. It's still hard for me to write about you without tears, but I've grown emotionally stronger now—just as you would have wanted—so you can be even prouder of me. To my elder brother (Mr. *Chiranjit Kar*), you have been my shoulder during the toughest times. Your boundless love and support have carried me through the heart-wrenching pain of losing Maa. I am forever grateful for the care and comfort you've given me when I needed it the most. To my sister-in-law (Mrs. *Nishna Razdan*), your understanding, encouragement, and love as an elder sister have been truly special. Words cannot fully express how much your kindness and care have meant to me. Your presence has been a constant source of warmth and reassurance.

"namah purastad atha prishthatas te
namo 'stu te sarvata eva sarva
ananta-viryamita-vikramas tvam
sarvam samapnoshi tato 'si sarvah"

Publications

1. "Investigation of [KSF2015] 1381-19L, a WC9-type star in the high extinction Galactic region" - **S. Kar**, R. Das and T. Baug, 2024, ApJ, 968, 60.

2. "Detection of high-frequency pulsation in WR 135: investigation of stellar wind dynamics"- **S. Kar**, R. Das, B. Mathew, T. Baug, and A. Mandal, 2024, AJ, 168, 199.

3. "Classification of Wolf Rayet stars using Ensemble-based Machine Learning algorithms" - **S. Kar**, R. Bhattacharyya, R. Das, Y. Pihlström and M. Lewis, ApJ, 977, 170.

4. "Morpho-kinematic and photoionization models of the multipolar structures in planetary nebula NGC 6572"- R. Bandyopadhyay, R. Das, P. Mudumba and **S. Kar**, MNRAS, 524, 1547-1559.

Abstract

WR stars are hot, luminous Population I massive stars that evolve from O-type MS stars via intrinsic mass loss or binary mass transfer. Their spectra feature broad emission lines of highly ionized helium, nitrogen, carbon, and sometimes oxygen, arising from their UV radiation-driven supersonic stellar winds. These winds cause extreme mass loss, enriching the ISM and promoting young star formation. WR stars are classified into WN, WC, and WO types based on chemical composition and into early or late types based on wind ionization levels.

This thesis explores some less understood phenomena in WR stellar winds. To achieve our goals, we obtained multi-wavelength spectroscopic and photometric data of WR stars across optical to IR, and developed radiative transfer-based models for stellar characterization.

WCL stars, found predominantly in metal-rich galaxies like the MW, exhibit high mass-loss rates and are progenitors of Type Ic SN. They often display excess IR emission from circumstellar dust formed via wind-wind interactions in binaries. Our analysis of a highly extinguished WC9 star reveals it as the brightest WC9 star in the MW, evolving from an isolated O-type MS star with or without rotation. Notably, no excess IR emission indicative of circumstellar dust is observed.

Late-type WR stars show higher intrinsic variability than early types. We investigate variability in WCL stars, focusing on a WC8 star with multi-order pulsation harmonics. Our analysis reveals that subsonic winds are driven by Fe vii-ix opacity, while C iv and He ii opacities drive supersonic winds. Fe-opacity triggers SMI, producing pulsations and clumps. The smaller clumps oscillate under higher-order harmonics, while larger ones affect outer wind variability.

A significant number of WR stars remain hidden due to interstellar dust extinction but are detectable in IR. Based on IR colors and positions, we develop robust ML models with XGB algorithm to identify WR stars in the MW with better accuracy and predict their chemical subtypes (WC or WN). These models outperform existing methods and have uncovered new WR stars in the local arm of the MW.

Contents

List of Figures

Chapter 1

Introduction

1.1 Wolf Rayet Stars: An historical overview

Around 158 years ago, two French astronomers, Charles J.E. Wolf and Georges Rayet, at the Paris Observatory were observing the Cygnus constellation when they identified 3 optically bright stellar objects (Wolf & Rayet, 1867). Using a spectrograph, they noticed something unusual in the spectra of those stars. Instead of the typical absorption lines seen in most stellar spectra, these stars exhibited strong and broad emission lines, which were rarely observed at the time. These emission lines indicated that the stars were surrounded by hot, dense, and fast-moving stellar winds, a characteristic feature of these stars. Wolf and Rayet's observations were groundbreaking because they challenged the understanding of stellar spectra, leading to further investigations into massive stars with extreme mass loss and their evolution. Such stars were later named after them as Wolf Rayet (WR) stars. Later advancements in spectroscopy allowed astronomers to classify WR stars more accurately and understand that the emission lines come from highly ionized helium, nitrogen, carbon, and oxygen in the outer layers of these stars.

Over time, WR stars became a distinct class of massive stars in advanced stages of evolution, specifically characterized by the loss of their outer hydrogen layers, which exposed their hot, dense cores. This early discovery laid the foundation for a century of research exploring the processes of stellar wind acceleration, mass loss, and the evolutionary connection between WR stars and other high-mass stars.

1.2 WR stars: General perspective

Stars with mass greater than 8 $M_\odot$ are regarded as massive stars. These stars occupy the top right corner of the Hertzsprung-Russel (HR) diagram (see Fig. 1.1 (a)) as they exhibit high luminosity (10^4-10^6 $L_\odot$) and temperature (2×10^4-6×10^4 K) compared to other stellar objects. During their Main Sequence (MS) phase, massive stars undergo core H-burning to generate sufficient radiation pressure to sustain against the inwards contraction due to gravity. Such stars at a later stage of their evolution tend to expand to maintain a temperature gradient between the core and the surface. During this process, the highly ionized outer layers detach from the surface. The expanding layers undergo recombination transitions and give rise to broad and strong emission lines. Such phases of massive stars are identified as WR stars. However, not all massive stars (with MS mass $<25M_\odot$) tend to achieve this phase in their life cycle as they lack sufficient mass and wind momentum (in the case of single stars) or mass transfer efficiency (for binary systems). In Sec. 1.3.2, I examine various evolutionary scenarios for the formation of WR stars.

Massive stars are known for their shorter lifetimes (some million years) as they lose matter due to intrinsic mass loss and matter exchange (in the binary system) from their atmosphere to the surroundings and contribute significantly to the chemical evolution of the host galaxies. The WR-phase of the Population I massive stars exists for hardly 1/10th of their entire lifetime. WR stars exhibit comparable physical properties to their MS O-type predecessors (see Fig. 1.1 (b)). The WR stars are extremely hot ($3\text{x}10^4 - 2\text{x}10^5$ K) and luminous ($10^4 - 10^6 L_\odot$). However, during this phase, they exhibit stronger mass outflows ($\dot{M}_{WR} \sim 10^{-5} M_\odot/yr$ which is almost 10 times of $\dot{M}_O$) due to powerful stellar winds ($\geq$1000 km s^{-1}) and ionizing UltraViolet (UV) radiation from the stellar interiors. Supersonic winds expel nuclear-burning products from the star's inner layers, feeding mechanical energy into the Inter Stellar Medium (ISM) and simultaneously enriching the chemical content.

1.3 Characteristics of WR stars

Massive stars during their WR phase provide scope for studying the physical and chemical processes that are said to occur at a later stage in the life cycle of massive MS stars, such as stellar shell dynamics; interaction of radiation with circumstellar material ejected during the earlier evolutionary phases; formation, evolution, and destruction of grains and large molecules, etc. To explore any of these aspects, it is crucial to understand the key characteristics of WR stars, which I discuss in the following subsections.

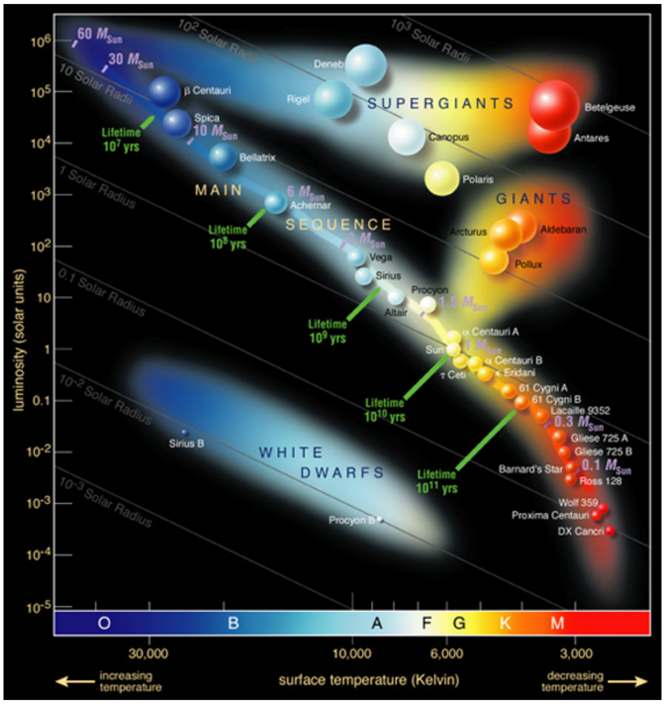

(a) Positions of different stellar classes based on their temperature and luminosity. The range of stellar lifetimes and sizes of the classes are also marked. Image credits: European Space Agency

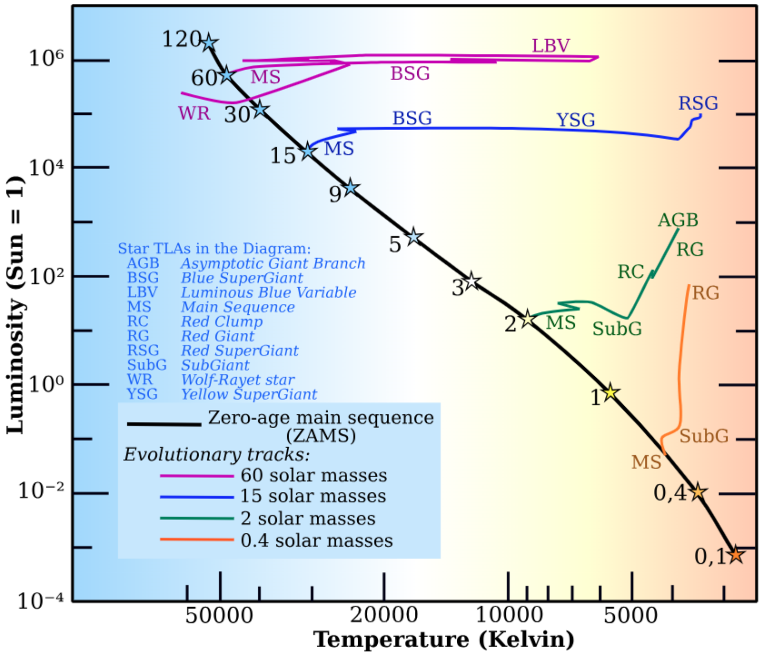

(b) Evolutionary tracks of non-rotating stars illustrating their successive phases from the MS onward, based on mass. The WR phase is located close to its O-type predecessor (60 $M_\odot$). Image credits: Rursus (creator) and B. Jankuloski (modified), Licensed under CC by 3.0

Figure 1.1: HR diagrams

1.3.1 Classes of WR stars

Spectroscopic analysis reveals that WR stars either lack hydrogen or contain only trace amounts in their envelopes. This could have occurred due to the loss of the outer H-rich layers during the earlier stages of their evolution, either by mass loss from stellar winds or mass stripping by a binary companion. However, as the WR star evolves, the inner nuclear-processed layers of the star are revealed by the stellar winds, starting with nitrogen-rich layers (from the CNO-cyle), followed by helium-rich and later carbon-rich (from He-burning) layers. These expanding layers participate in the recombination transitions, giving rise to distinct emission-line spectra, that form the base of WR classification.

Based on the chemical composition of the envelopes, WR stars are divided into three primary subtypes (discussed below): WN, WC, and WO, each corresponding to different dominant chemical elements in their atmospheres, reflecting different evolutionary stages. Further, the ionization state of the atmosphere and the mass-loss rate help refine the sub-classes among the primary ones.

- **WN Stars**: These stars exhibit spectra dominated by helium and nitrogen lines and are mainly classified based on the line ratios (Smith et al., 1996): He II λ5412/ He I λ5876 and N V λ4603/N III λ4640. Based on the emission line ratio (see Fig. 1.2 (a) and 1.2(b)), the WN class is further divided into 8 sub-categories (i.e. WN 2-9): WN 2-6 are designated as Early WN-type (WNE), with high ionization and WN 6-9 as Late WN-type (WNL), with low ionization. Some WN-type stars show weak emission lines of hydrogen (Balmer/Pickering decrement) present in their outer envelopes. Such objects are called non-classical WR stars and are suffixed with 'h'. WNh-stars that also depict H-absorption lines are further designated as WNha. Furthermore, according to (Hiltner & Schild, 1966), WN subclasses are distinguished (as WN-b and WN-not b) based on the values of Full Width Half Maxima (FWHM) of He II λ4686 and the Equivalent Width (EW) of He II λ5411. These parameters indicate the nature of stellar winds in the atmosphere.

- **WC Stars**: Characterized by the carbon emission lines, WC stars signify a more evolved phase where He-burning products dominate the surface. WC stars are classified (Crowther et al., 1998) based on the line strength ratio of C IV $\lambda\lambda$5801-12 and C III λ5696 along with weak emission lines of oxygen (O III-V). These stars are similarly classified (see Fig. 1.2 (c) and 1.2(d)) into Early WC-type (WCE): WC 4-6 and Late WC-type (WCL): WC 7-9 subtypes based on the line strengths of C III and C IV, indicating variations in surface temperature and wind properties. WCE tend to show stronger, higher ionization lines compared to their WCL counterparts.

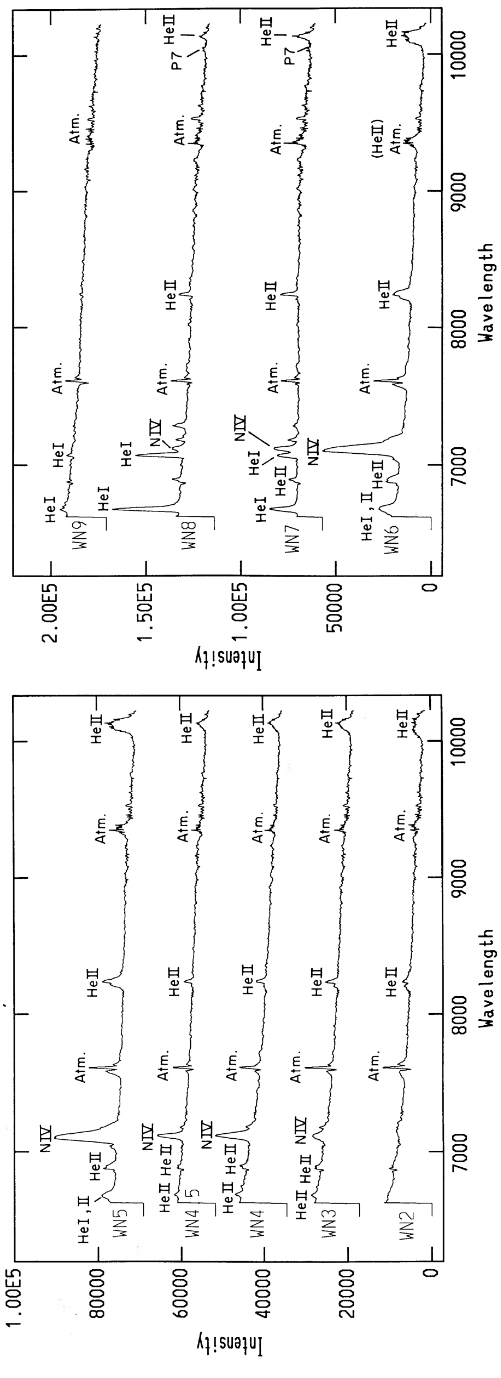

(a) WNE-type stars

(b) WNL-type stars

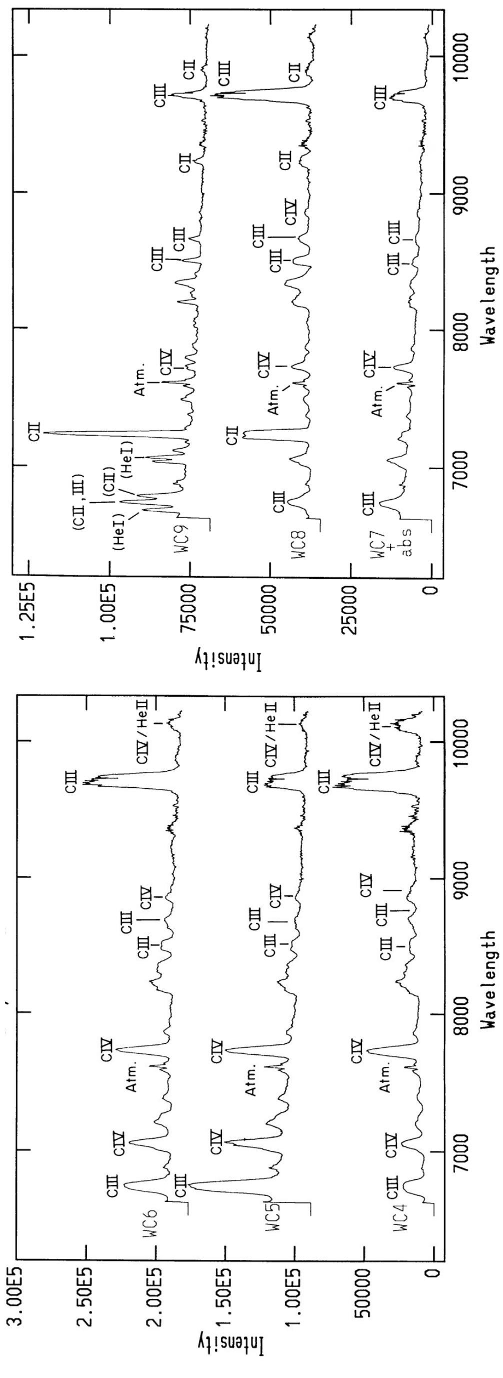

(c) WCE-type stars

(d) WCL-type stars

Figure 1.2: Spectral montage of different WR-subtypes that are identified from the relative line strengths of different ionized species. Taken from Conti et al. (1990)

- **WO Stars**: The WO class, comprising the rarest WR stars, mainly exhibit lines of higher oxygen ions (O VI-VII), particularly O VI $\lambda\lambda$3811-34 and O V $\lambda\lambda$5572-98 (van der Hucht, 2001) and C IV. Based on the presence of ionized states of oxygen, WO stars are classified into WO 1-4 subtypes, with WO 1 stars typically exhibiting the highest ionization levels.

1.3.2 Evolutionary channels

WR stars are said to have descended from the O-type MS stars which undergo H-burning at the stellar core to produce Helium through the CNO cycle ($T_{core} > 10^7$).

$$\begin{gathered}
{}^{12}\mathrm{C} + {}^{1}\mathrm{H} \rightarrow {}^{13}\mathrm{N} + \gamma \\
{}^{13}\mathrm{C} + {}^{1}\mathrm{H} \rightarrow {}^{14}\mathrm{N} + \gamma \\
{}^{14}\mathrm{N} + {}^{1}\mathrm{H} \rightarrow {}^{15}\mathrm{O} + \gamma \\
{}^{15}\mathrm{O} \rightarrow {}^{15}\mathrm{N} + e^{+} + \nu_e \\
{}^{15}\mathrm{N} + {}^{1}\mathrm{H} \rightarrow {}^{12}\mathrm{C} + {}^{4}\mathrm{He}
\end{gathered}$$

While the WR stars are said to be burning helium (via triple-alpha process) at the core ($T_{core} > 10^8$) to produce carbon.

$$\begin{gathered}
{}^{4}\mathrm{He} + {}^{4}\mathrm{He} \rightarrow {}^{8}\mathrm{Be} \\
{}^{8}\mathrm{Be} + {}^{4}\mathrm{He} \rightarrow^{12} \mathrm{C} + \gamma
\end{gathered}$$

To understand the characteristics of WR stars, it is at first important to explore the physical mechanisms that contribute to their formation. In the following subsections, I discuss the evolutionary channels that can lead to the formation of WR stars from the massive O-type stars.

Single star system

Just like the intermediate mass (0.8-8$M_\odot$) stars, the massive stars follow a lifecycle mainly governed by nuclear fusion processes in their cores. Also, convection plays a significant role in the evolution of the stars during the MS. Taking into account the mass loss due to fast stellar winds (Conti, 1976) (also known as the "Conti Scenario"), the Galactic O-type MS stars, depending on their mass, go through different evolutionary stages as identified by Crowther et al. (1995) and Crowther (2007).

As stated earlier, in the MS phase, the enormous energy output from the core H-burning leads to high radiation pressure that counterbalances gravitational collapse. Due to their high luminosities, massive stars lose substantial mass through stellar winds, even on the MS, which intensifies with increasing stellar mass and luminosity. Stars remain in the MS-phase for most of their lifetime depending upon their mass, with the heavier ones with shorter MS-phase (about $3 - 5 \times 10^6$ yrs).

In the post-MS phase, as the core hydrogen exhausts, the star contracts, and outer layers begin to expand, progressing to the Blue SuperGiant (BSG) phase. Depending on the initial mass (M<60 $M_\odot$), the outer layers of the BSG expand further, leading to the Red SuperGiant (RSG) phase. At a certain stage of evolution, as the core contracts to a critical density and temperature, helium fusion initiates, forming carbon and oxygen. However, for stars heavier than 60 $M_\odot$, the mass-loss mechanism does not allow the stars to enter the RSG phase; rather, they erupt and become luminous objects known as Luminous Blue Variable (LBV). With the decreasing hydrogen abundance, sufficient energy is not produced to expand the outer layers; therefore, the temperature of the star starts increasing. The powerful stellar winds from the RSG/LBV phase remove the hydrogen from the outer layers as the star evolves towards the bluer side of the HR diagram. This leads to the formation of WR stars showing the processed products of H-burning (via the CNO cycle) and core-He fusion reactions. Massive stars below 25 $M_\odot$ do not undergo the WR-phase as the winds are not strong enough to remove the H-rich envelopes and expose the He-burning products (Ekström et al., 2012). Therefore, based on Georgy et al. (2012); Ekström et al. (2012), a rough evolutionary scheme for non-rotating single O-type MS stars was estimated (Rosslowe, 2016), as mentioned below:

For Mass> 60 M$_\odot$: O (MS) ⇒ WNL ⇒ BSG/LBV ⇒ WNE ⇒ WC
For 40 < Mass < 60 M$_\odot$: O (MS) ⇒ BSG ⇒ WNL ⇒ WNE ⇒ WC
For 25 < Mass < 40 M$_\odot$: O (MS) ⇒ BSG ⇒ RSG ⇒ WNL ⇒ WNE
For Mass < 25 M$_\odot$: O (MS) ⇒ BSG ⇒ RSG

Rotation significantly influence the evolution and characteristics of WR stars. Rotating evolutionary models reduce the initial mass threshold for forming WR stars to 20 $M_\odot$ (Ekström et al., 2012). Rotation facilitates internal mixing, which leads to an earlier onset of the WR phase and a more gradual transition, effectively extending WR lifetimes. For instance, at solar metallicity ($Z = 0.014$), stars over 60 $M_\odot$ with rotation experience WR lifetimes approximately twice as long as non-rotating counterparts, primarily due to an extended WNL phase caused by rotational mixing and enhanced mass loss (Vink & de Koter, 2005). Rotationally induced mixing also enables certain WR stars, with initial masses of 30–60$M_\odot$, to display both hydrogen- and helium-burning products on their surfaces, signifying the WN/WC transition phase. In Fig. 1.3, the positions of the WR stars in the MW are plotted with the evolutionary model tracks for single-rotating O-type stars as a function of initial mass.

Metallicity profoundly impacts WR stars by modulating their mass-loss rates. In high-metallicity environments, stronger winds (see Fig. 1.4) result from increased

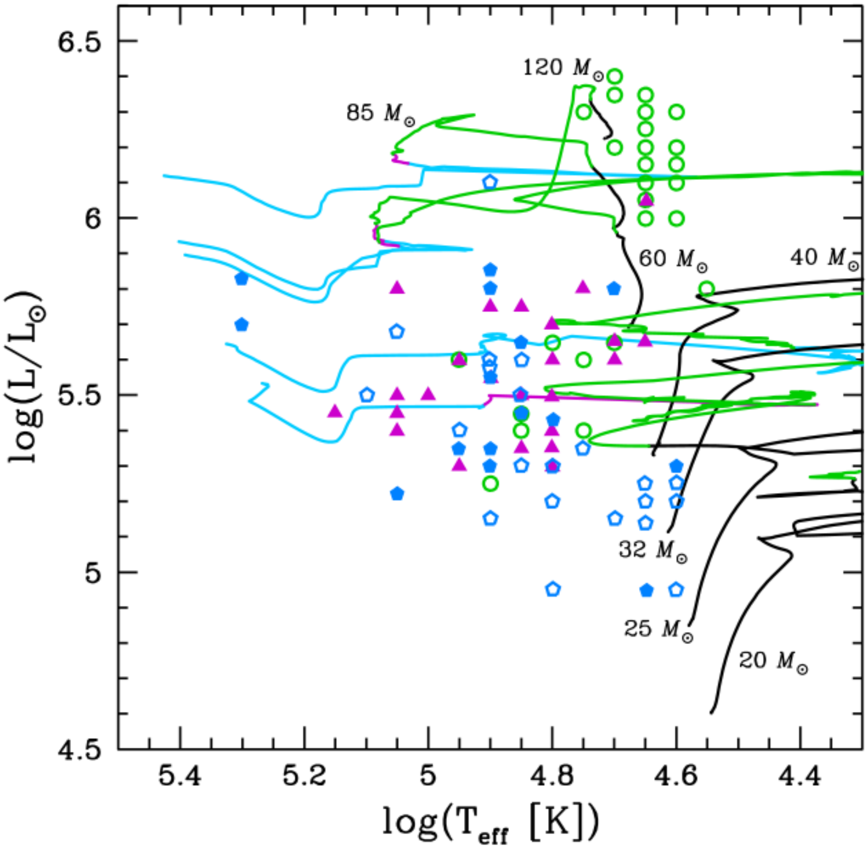

Figure 1.3: HR diagram showing the positions of WR stars in the MW and the tracks (Ekström et al., 2012) of rotating single star evolutionary models. WR phases in the model tracks are marked in different colors: WNL (in *green*), WNE (*purple*), and WC (*blue*). The symbols following the same color convention as the WR phases represent the observed WR subtype population in the MW. Taken from Georgy et al. (2012).

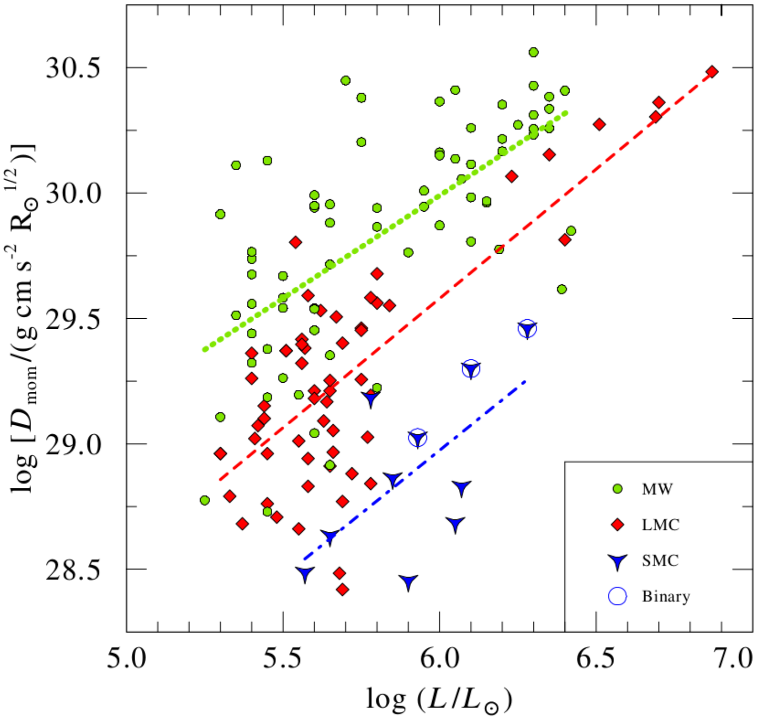

Figure 1.4: Dependance of the wind momentum (D_{mom}, as an alternative measure of the mass-loss rate) on the metallicity of the environment is seen by Hainich et al. (2017).

radiation pressure on highly ionized species, driving substantial mass loss and enabling earlier transitions into WR phases (Vink et al., 2001). Consequently, WR lifetimes are extended as stars shed their outer envelopes more efficiently. For stars with twice solar metallicity, the WR lifetime of a 60 $M_\odot$ O-type main-sequence star with rotation is doubled compared to solar metallicity conditions (see Fig. 1.5). High-metallicity conditions also promote WR formation via single-star evolution, while in low-metallicity environments ($Z < Z_\odot$), weaker winds are not sufficient enough to remove the outer layers (see Fig. 1.4). The WR lifetimes in such environments, such as the Small Magellanic Cloud (SMC) and Large Magellanic Cloud (LMC), are shorter, typically less than a million years (see Fig. 1.5). Metallicity also alters the relative durations of the WN and WC phases (see Fig. 1.6). High metallicities promote WNE-phase formation, extending durations due to increased mass loss, while the WC-phase duration remains relatively stable across heavier progenitors (Meynet & Maeder, 2003). Furthermore, low-metallicity environments favor the formation of WN-type WR stars with weaker winds, resulting in a lower WC-to-WN ratio (Fig. 1.7).

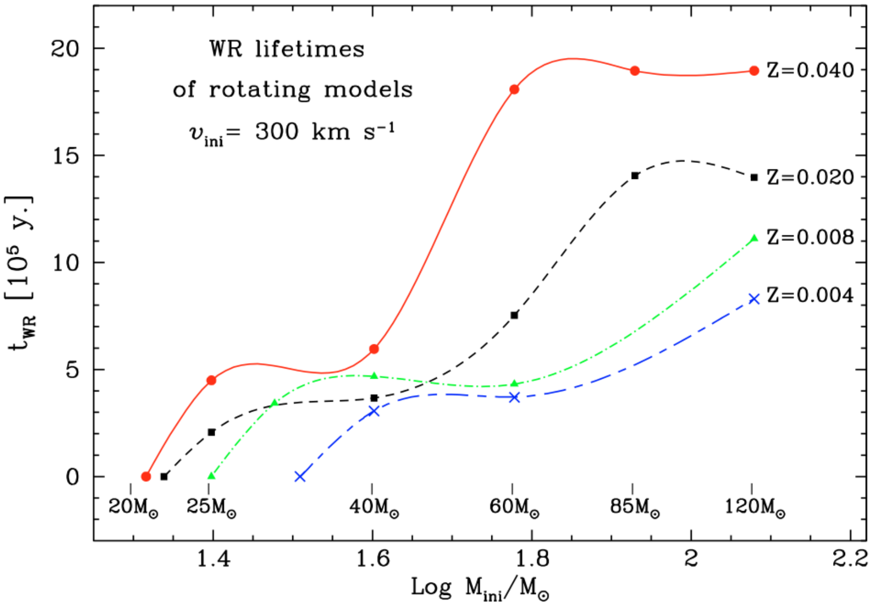

Figure 1.5: Variation of WR lifetimes for various initial masses of rotating O-type MS stars at different metallicities. Taken from Meynet & Maeder (2005).

Binary star system

The evolution of a massive star in a binary system is shaped by several key factors, including the mass ratio, orbital separation, and eccentricity of the orbit. Massive stars in a close binary system evolve by mass exchange from the primary (more massive) to the secondary (less massive companion) as the former in the supergiant phase expands beyond the Roche Lobe, in which material is gravitationally bound to the star. Material starts flowing from the primary to the secondary star via the inner Lagrangian point, beginning mass transfer through the Roche Lobe Over-Flow (RLOF) process (Paczyński, 1967). The higher the mass ratio, the faster the primary evolves than its companion. The distance between the two stars determines their interaction. Based on the primary star's evolution, mass transfer in binary systems can follow either of the three cases (Kippenhahn & Weigert, 1967): Case A occurs during core-hydrogen burning (i.e. MS) in binaries with short orbital periods (a few days), Case B during hydrogen-shell burning in binaries with periods up to around 1000 days, and Case C during helium-burning with orbital periods of several thousand days (Podsiadlowski et al., 1992). Case A initiates when a close binary's primary star reaches its Roche lobe early in the MS, shedding most of its hydrogen-rich envelope onto the secondary. However, cases B and C are more prevalent than Case A due to the wider range of orbital periods that can support them. Also, if the secondary expands such that both stars fill their Roche lobes, a Common Envelope (CE) phase can occur. Additionally, if the primary enters the LBV phase, the likelihood of a CE increases

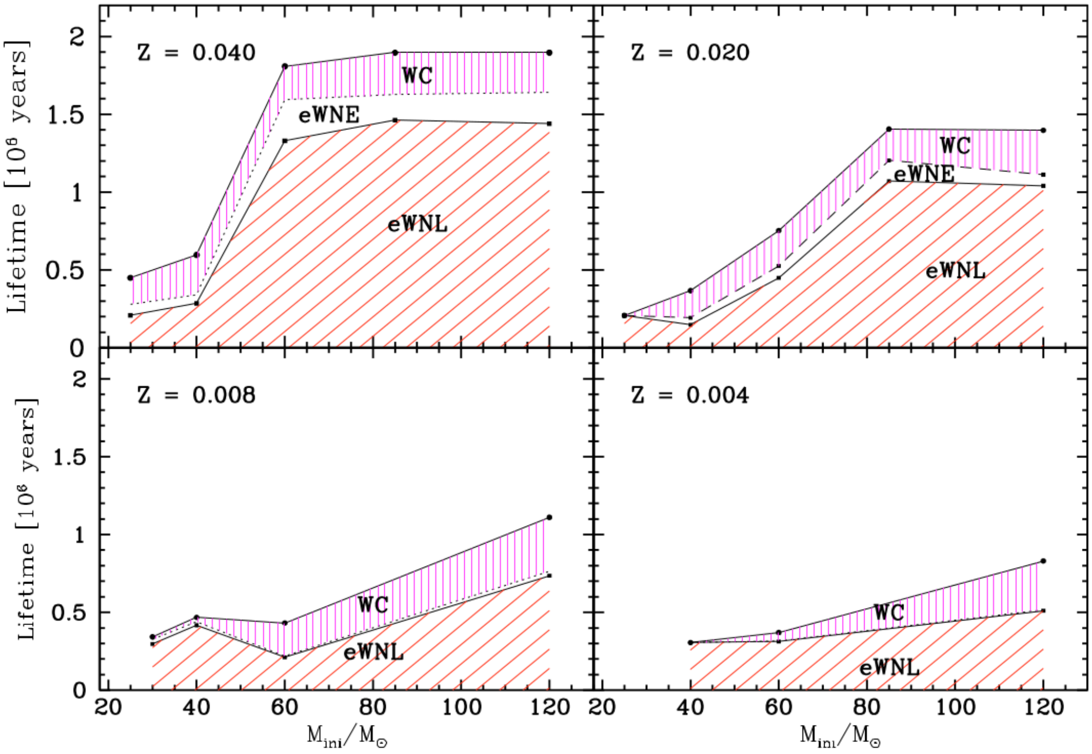

Figure 1.6: Lifetimes of WR-subtypes show variation with the initial masses of O-type MS stars rotating at an initial velocity of 300 kms^{-1} at different metallicity environments. Taken from Meynet & Maeder (2005).

compared to traditional RLOF, accelerating the primary's evolution into a WR star by enhancing envelope stripping (Vanbeveren et al., 1998). The eccentricity of the binary orbit affects mass transfer rates and the interaction between the stars. Circular orbits allow for more stable mass transfer, while eccentric orbits can lead to periodic interactions. This leads to dust formation in WR-late binaries (such as WR 140, WR 25, etc.) with a massive O-type MS as the secondary star (further discussed in Sec. 1.4.1).

The binary evolution models (with flat mass-ratio and orbital separation) predict that the WR lifetime of the primary star depends on the metallicity (see Fig. 1.8). The stars with initial masses above 15 $M_\odot$ can enter the WR phase in a binary system. In Fig. 1.9, the positions of the WR stars in the MW are plotted with the evolutionary model tracks for binary O-type stars as a function of mass and period. The average lifetime of the RSG phase decreases with the increasing metallicity due to RLOF and CE processes. Among the WR subtypes, the stars stay in the WNE phase longer than in the WNL phase at higher metallicity. Also, stars at Z = 0.02 undergo a longer WC phase compared to those at lower metallicity. The binary evolution models predict the metallicity-dependent observed population of WC relative to WN (see Fig. 1.7).

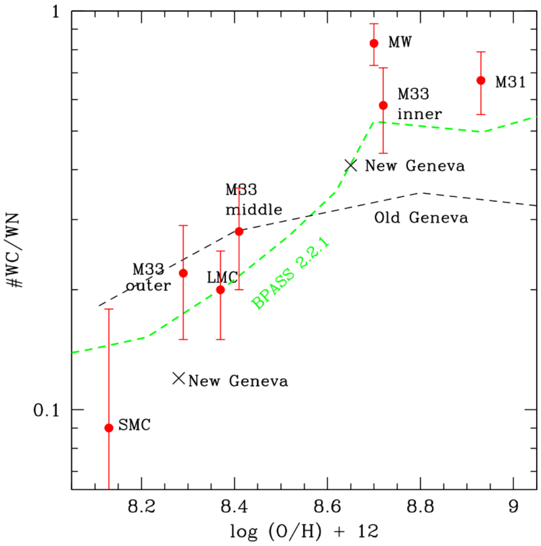

Figure 1.7: WR subtype-population dependance on the metallicity (log (O/H)+12) is shown. Also the evolutionary model predictions by the single star (GENEVA, Meynet & Maeder (2005) and binary star evolutionary (BPASS, Eldridge et al. (2008)) pathways are compared for different metallicities. Taken from Neugent & Massey (2019).

1.3.3 Distribution and Population

WR stars are typically clustered in star-forming regions within spiral arms, as these regions provide the necessary gas density and conditions for high-mass star formation. This clustering reflects the short lifespans of WR stars, which usually evolve and die within a few million years, rarely moving far from their natal regions. The WR stars in any galaxy show distribution similar to that of massive O-type MS.

Milky Way

In the spiral arms (see Fig. 1.10), WR stars are found either in starburst clusters (such as Westurlund 1, NGC 3603) or in OB associations (such as Cygnus OB). A significant population of WR stars are located close to the Galactic Center (GC) as members of massive star clusters (such as Arches, Quintuplet, and GC Cluster).

From the Near-InfraRed (NIR) narrow-band imaging surveys followed by the spectroscopic follow-ups, a large population of WR stars has been discovered across the last two decades (Shara et al., 2009; Shara et al., 2012; Kanarek et al., 2015) especially targeting the dust-obscured regions of the galaxy i.e. from −90° to +60° along the Galactic longitude and 1° above and below the Galactic plane in latitude.

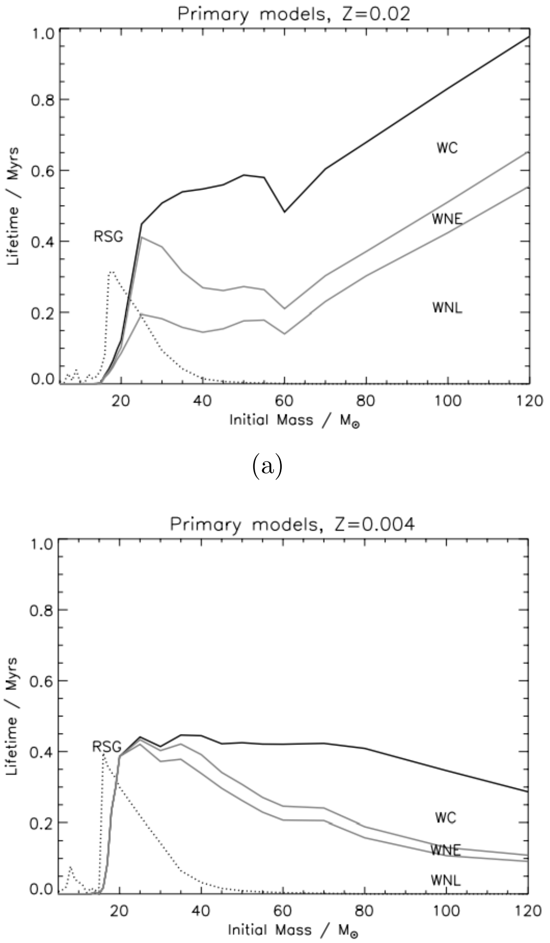

(a)

(b)

Figure 1.8: Comparison among the mean lifetimes of different WR subtypes as a function of the masses of the primary stars for two different metallicities. Taken from Eldridge et al. (2008).

From the Galactic center to the outer spiral arms, the MW exhibits a decreasing metallicity gradient, with its inner regions having higher and the outer parts having lower metallicities. The gradient impacts WR star formation, since higher metallicity facilitates significant mass loss via stellar winds, stripping outer envelopes, and revealing the WR star's inner layers. This metallicity dependence also affects the relative frequency of WR subtypes. WN stars are more commonly found across a range of metallicities however they are mostly prevalent in the outer Galactic regions (Rosslowe & Crowther, 2015). WC/WO stars considered to have descended from WN-type are seen in higher metallicity regions since stronger winds allow stars to shed their outer envelopes enriched with hydrogen and nitrogen, exposing the carbon and oxygen-rich layers. Consequently, WC/WO stars are more concentrated in the inner disk, where metallicities are higher. Rosslowe

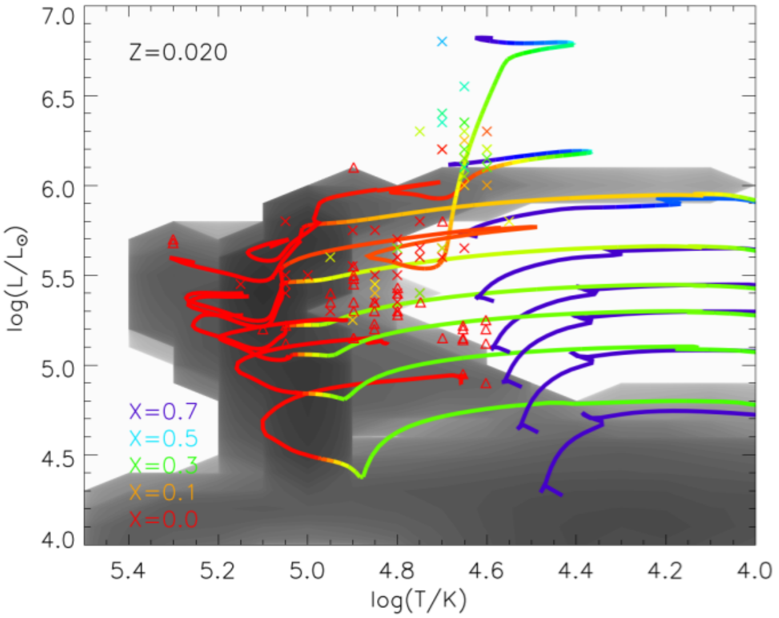

Figure 1.9: Positions of galactic WR stars and the evolutionary tracks (Stanway & Eldridge, 2018) generated for the binary stellar systems from the Binary Population and Spectral Synthesis (BPASS) code are shown on the HR diagram. Observed WN-class are represented by cross, WC by triangles and WO as diamonds. WR-phases are determined based on the value of the surface H-abundance (X_H): WNL-phase in cyan, WNE-phase in green, WC/WO in orange and red. Taken from Eldridge et al. (2017).

& Crowther (2015) found that WNE and WNL stars do not show any significant difference in their distribution at solar and sub-solar metallicity regions while there is a substantial decrease in the population of WC-subtypes where the WCL mostly occupy the inner super-solar regions. The revised relative population of WC and WN-type supports the binary evolutionary and non-rotating single-star models.

In subsequent years, numerous discoveries of WR stars resulted in the compilation of WR catalogs (Campbell, 1884; Fleming & Pickering, 1912; Payne-Gaposchkin, 1930; Roberts, 1962; Smith, 1968; van der Hucht et al., 1981; van der Hucht, 2001). The total recorded population of WR stars in the Milky Way was 227 until narrow-band InfraRed (IR) surveys resulted in additional discoveries in the dust-obscured galactic regions. The most recent WR catalogue by Rosslowe & Crowther (2015) has documented approximately 670 WR stars identified through various IR surveys (Mauerhan et al., 2009; Shara et al., 2012; Rosslowe & Crowther, 2015). WR stars are often found in binary systems with either a massive OB/WR or a compact objects (i.e. Neutron star/Black hole). However, till now only about 40% of the detected WR stars in the MW have been identified as a binary. Long-term multi-wavelength monitoring could enhance the popula-

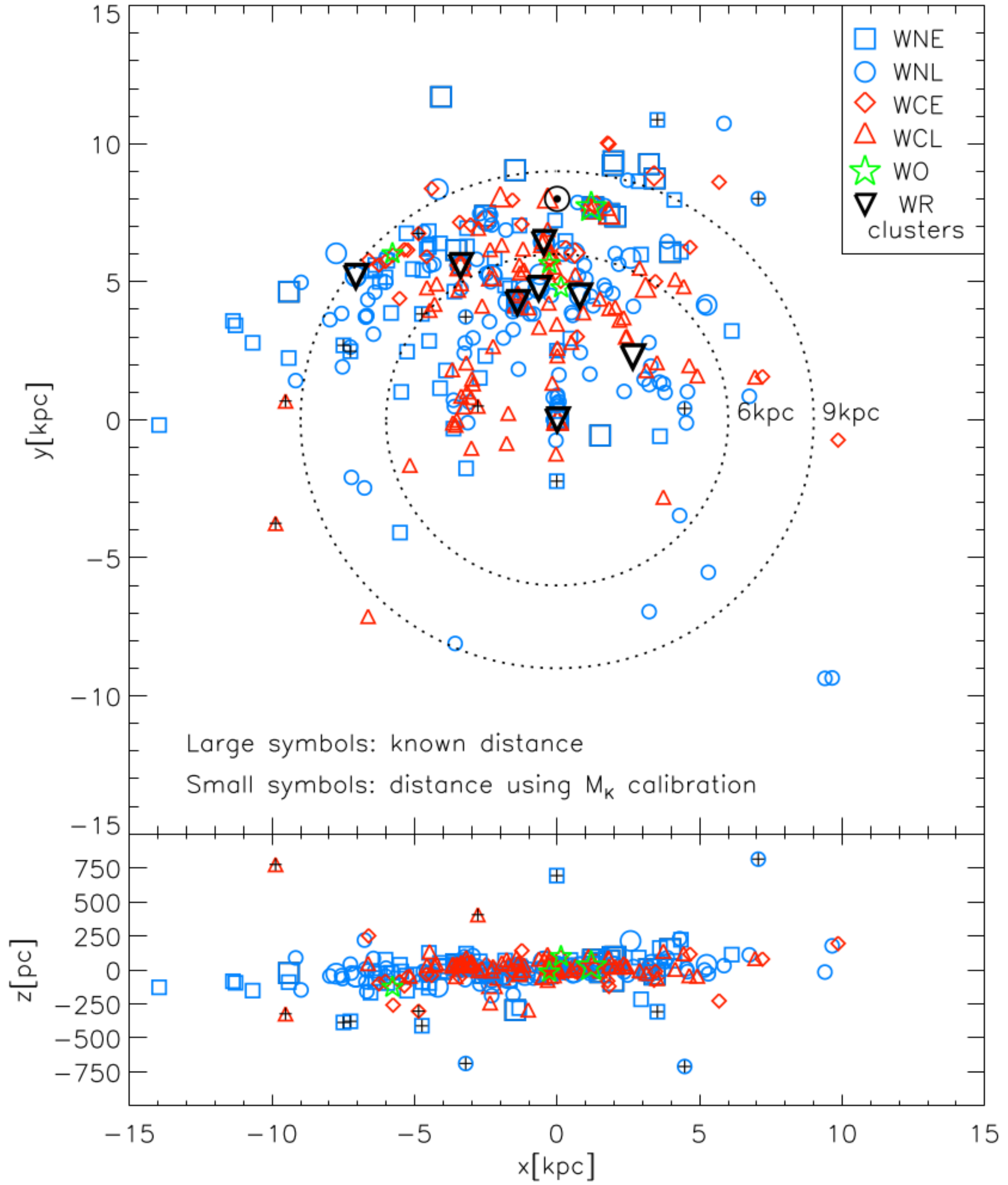

Figure 1.10: Plot showing the positional distribution of known WR stars and the clusters across the plane of the MW (taken from Rosslowe & Crowther (2015)).

tion of WR binaries. Several population synthesis studies have tried to predict the total population of WR stars in the MW. Initially Maeder & Lequeux (1982) estimated about 1200 WR stars based on a surface density model as a function of the radius similar to H II regions. The population model as a function of Galactocentric radius (R_G) derived by Shara et al. (1999) predicted about 2500 WR stars. Later van der Hucht (2001) derived a population of 6500 considering that the WR sample in the local Galactic region (R_G=7-12 kpc) to be complete. Later Shara et al. (2009), updated the earlier model (Shara et al., 1999) to consider the effect of interstellar extinction and predicted approximately 6400 WR stars. The latest model by Rosslowe & Crowther (2015) predicted the Galactic WR population to be close to 2000.

Extra-Galactic sources

- **Magellanic Clouds**: The nearby satellite galaxies of the MW, i.e. Magellanic Clouds are also found to host massive star clusters consisting of WR stars. In the LMC, 154 WR stars (Neugent & Massey, 2019; Breysacher et al., 1999) have been identified that are primarily of the WN-type. These stars are concentrated in central regions, such as dense clusters like R136 in 30 Doradus. The R136 cluster of LMC (see Fig. 1.11 (a)) also hosts unique objects such as WN3/O3 hybrid stars (Massey & Hunter, 1998), which exhibit both WR-like and O-star spectral features. These stars appear to represent a transitional evolutionary phase rather than binaries. The WC/WN ratio in the LMC is approximately 0.2 (Neugent & Massey, 2019), consistent with its intermediate metallicity (Z=0.5$Z_\odot$). Most WC stars in the LMC are early-type (WC4) with lower mass-loss rates (Crowther et al., 2002) than the Galactic WC stars due to the influence of metallicity. A significant fraction of WR stars in the LMC (∼30%) are in binary systems (Foellmi et al., 2003), impacting their evolution. In contrast, the SMC hosts a much smaller WR population, with only 12 known stars (Massey et al., 2003), 11 of which are WN type (see Fig. 1.11(b)). This lower number aligns with the SMC's low metallicity (Z=0.25$Z_\odot$). Among its WR stars, the SMC includes a single WO-type star (Neugent et al., 2012), which is rare and typically associated with higher metallicities, suggesting binary influence. The WC/WN ratio in the SMC is extremely low (0.09), a direct result of reduced stellar wind efficiency in its low-metallicity environment. The binary fraction among WR stars in the SMC is significant (∼40%), with evidence that binary evolution may contribute to the presence of exceptional stars like the WO.

- **Local Group**: Also, other galaxies in the Local group exhibit diverse WR populations shaped by metallicity and binary evolution. M33 hosts 206 WR stars, with the WC/WN ratio increasing from 0.22 in its low-metallicity outskirts to 0.58 in its higher-metallicity center. M31, the most metal-rich galaxy, has 154 WR stars and a WC/WN ratio of 0.67, with most stars in OB associations and a significant fraction in binary systems. Low-metallicity dwarf galaxies like IC 1613 and NGC 6822 have few WR stars,

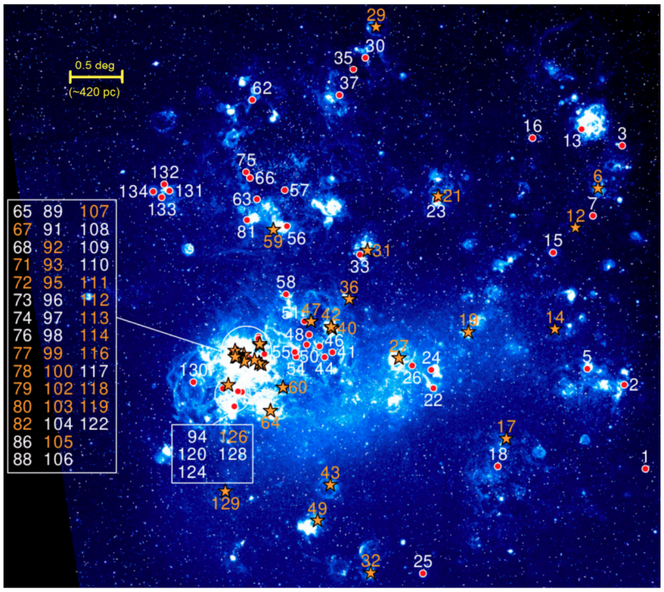

(a) In LMC. Taken from Shenar et al. (2019)

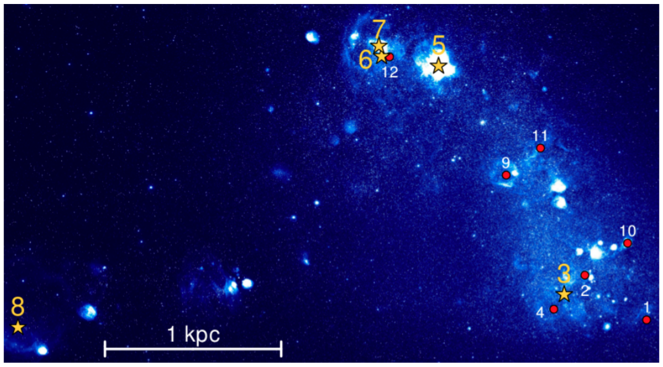

(b) In SMC. Taken from Shenar et al. (2016)

Figure 1.11: WR stars (WN-type) that have been identified in the Magellanic Clouds. The single WR stars are marked as *red* circles while the binary systems in *yellow* stars.

mainly of the WN type, while the starburst galaxy IC 10 stands out with 29 WR stars, predominantly WC types.

- **WR Galaxies**: Galaxies that have WR stars display strong optical emission blends around 4600–4700 Å (the 'blue bump', attributed to N III λ4634, 4640, C IV λ4658, and He II λ4686 from WNL stars) and 5750–5850 Å (the 'red bump' from C IV λ5808 from WCE stars). Such galaxies are also called WR Galaxies (Osterbrock & Cohen, 1982), first identified by Allen et al. (1976). Mrk 178 (shown in Fig. 1.12) is a dwarf metal-poor WR galaxy that is present in the Local Group.

  The WR population in a WR galaxy is influenced by several key factors

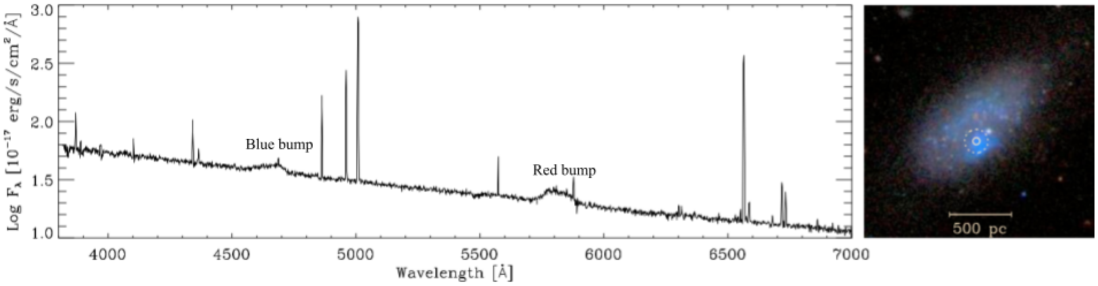

Figure 1.12: Flux calibrated optical spectrum (left) of Mrk 178 (on the right) shows signatures of blue and red bump which are characteristics of a WR galaxy. Taken from Brinchmann et al. (2008).

(Mas-Hesse et al., 2000): a) metallicity impacts the mass-loss rate of massive stars, thereby affecting the WR/O population; b) The slope of the Initial Mass Function (IMF) determines the WR population; c) massive stars in binary systems often evolve into WR stars due to mass stripping; d) prolonged star formation periods dilute the WR phase. A population of WR galaxies of different shapes (and at different redshifts) has been identified from the Integrated Field Spectroscopy (Zhang et al., 2007; Brinchmann et al., 2008; Agienko et al., 2013) using the Sloan Digital Sky Survey. WR content across the galaxies (see, for example, Fig. 1.13, where the distribution of WR stars is shown in a WR galaxy) present in the Local Group (see Neugent & Massey (2019) for review) and beyond (Miralles-Caballero et al., 2016) has been noted utilizing different observational methods: image subtraction, filter interference, and crowded-field photometry. The relative population of WR subtypes (as a function of metallicity) across WR galaxies is discussed in Sec. 1.3.2.

1.3.4 Variability

Classical Wolf Rayet (cWR) stars (WR stars which lack hydrogen and are undergoing He-burning at the core) exhibit spectroscopic, photometric, and polarimetric variability due to the structured and asymmetric nature of the winds. Most of the cWR stars show intrinsic variability, while the binary systems show extrinsic variability. Below, I discuss the characteristics of both of these observational phenomena:

Intrinsic variability

Winds of WR stars are inhomogeneous and structured which is primarily attributed to processes that occur at the base of the winds. These winds are known

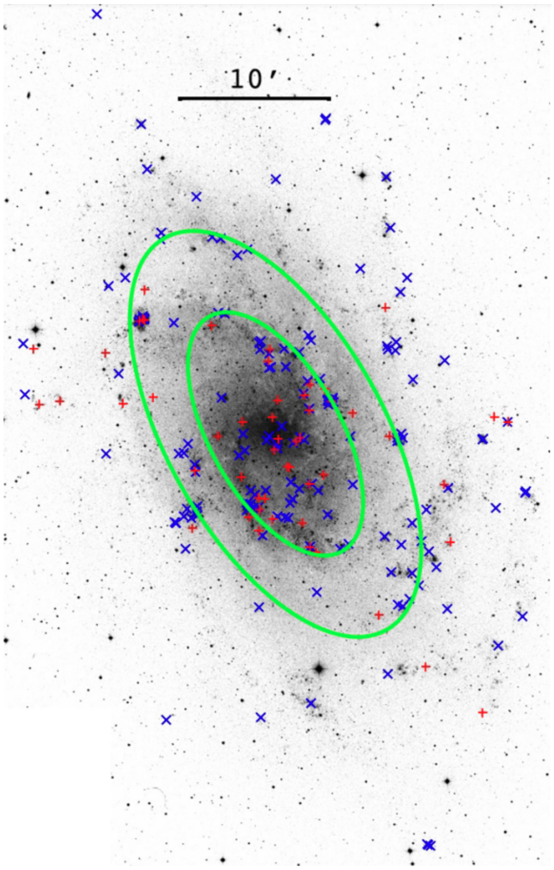

Figure 1.13: WR star distribution in M33 (a WR galaxy): WC stars represented as red plus signs (+) and WN stars as blue crosses (x). The subtype population ratio (WC/WN) decreases from the center to the arms of the galaxy, indicating a reduction in metallicity. Taken from Neugent & Massey (2011).

to exhibit 3 types of intrinsic variabilities:

1. **Stochastic variability**: Observational studies such as St-Louis et al. (2009); Chené & St-Louis (2011); Chené et al. (2020); Lenoir-Craig et al. (2022) have reported stochastic variations in the emission lines and photometric flux of WR stars, attributed to wind inhomogeneities (Moffat et al., 1988) within their radiatively driven winds. The non-periodic radially outward displacement of the line subpeaks from the line center to the scattering wings indicates that the wind inhomogeneities are stochastic (see Fig. 1.14). Small-scale variability (Chené et al., 2020) in the spectral lines ($\sigma < 5\,\%$) is caused by the motion of discrete wind emission elements (Lépine & Moffat, 1999; Lépine et al., 2000) or small, inhomogeneous density structures in stellar winds. Inhomogeneities arising from line-driven instabilities (LDI) (Owocki et al., 1988), result in variable mass-loss rates and influence wind density, thereby affecting spectral and photometric variability (St. -Louis et al., 1987; Drissen et al., 1987). High-resolution spectroscopy is essential for analyzing line-profile variations, characterizing wind-clumping factors, and understanding wind-induced mass-loss mechanisms in WR stars.

2. **Pulsational variability**: Some WR (especially WNL) stars exhibit low-amplitude spectroscopic (Chené et al., 2011), and photometric (Lefèvre et al., 2005; Nazé et al., 2021) periodic (less than a day) variations (see Fig. 1.15) that are considered to result from stellar pulsations. Generally, asteroseismic activities in massive stars are due to the Carnot-heat engine effect caused by the Fe-opacity in the convective stellar core. The unstable modes of pulsations in β Cephei stars (8-30$M_\odot$) are caused by the Fe-opacity located much deeper than the opacity due to partial-ionization of helium (Dziembowski & Pamiatnykh, 1993; Dziembowski et al., 1993). Townsend & MacDonald (2006) proposed that oscillations, though rare in WR stars, are induced by the deep-opacity peak due to Fe M-shell transitions, located at higher temperatures. Alternatively, the pulsations are caused by the strange modes (Glatzel et al., 1993) in the radiative stellar envelopes with opacity peaks that acoustically isolate regions into distinct cavities. Small phase differences between pressure and density changes within these cavities cause resonant instabilities, driving pulsations (Glatzel, 1994). Such pulsations in non-linear space (Glatzel, 2008) often generate shocks leading to inflated layers, consequently increasing the pulsational periods that closely resemble the observed values. Grassitelli et al. (2016) demonstrated that for OB stars: stellar pulsations and wind inhomogeneities arise from perturbations produced at the base of the stellar winds due to instabilities.

3. **Large-scale variability**: Rotational modulation of large-wind structures in some early WR stars (WR 1, WR 6, WR 134) are said to be responsible

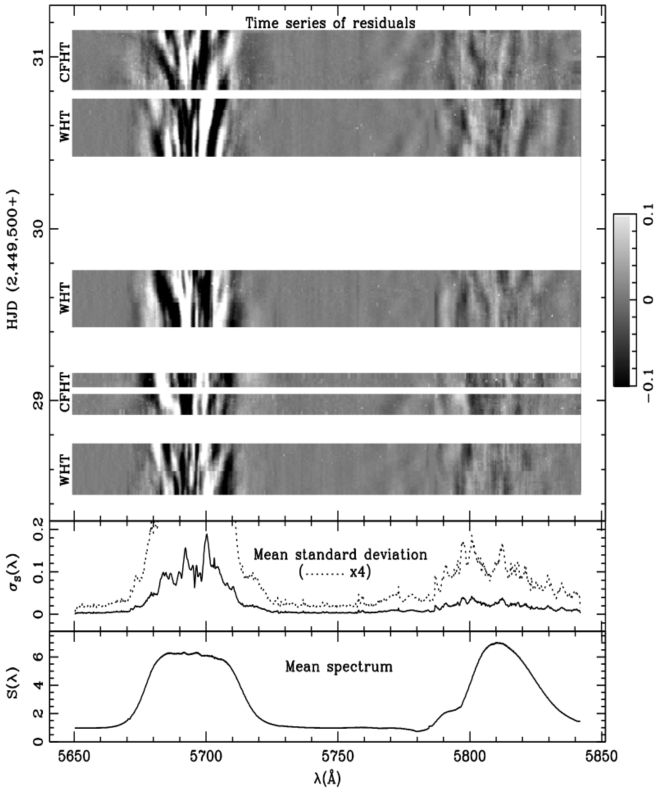

Figure 1.14: Spectroscopic time-series observations of WR 135 show variable subpeaks on C III 5696 and C IV 5802-12. The gray-scale residuals (top panel) reveal the stochastic nature of these emission subpeaks as they move outward over time. The standard deviation of the spectra (middle panel) highlights the variability in the emission lines. Taken from Lépine et al. (2000).

for the observed periodic variability (few days) in their emission lines (Morel et al., 1999b,a). The P-Cygni profiles of O-type supergiants show large-scale wind structures through Discrete Absorption Components (DAC)s, while WR stars show significant wind variability in about 20% of cases (St-Louis et al., 2009; Chené & St-Louis, 2011). Cranmer & Owocki (1996) showed that wind structures with different velocities upon collision form Co-rotating Interaction Region (CIR) which exhibit large-scale variability in O-type supergiants. Later, Dessart & Chesneau (2002) observed that the emission lines of WR stars exhibit CIRs primarily attributed to the spiraling motion (see Fig. 1.16) of large-density structures in their stellar winds. The CIRs identified from the epoch-wise periodic displacements of subpeaks across the primary broad line profile show large-scale variability ($\sigma > 5\,\%$). Spectropolarimetric studies (Robert et al., 1992) reveal periodic changes in the continuum are reminiscent of the CIRs in the winds. Using time-independent phenomenological modeling (Ignace et al., 2015), the

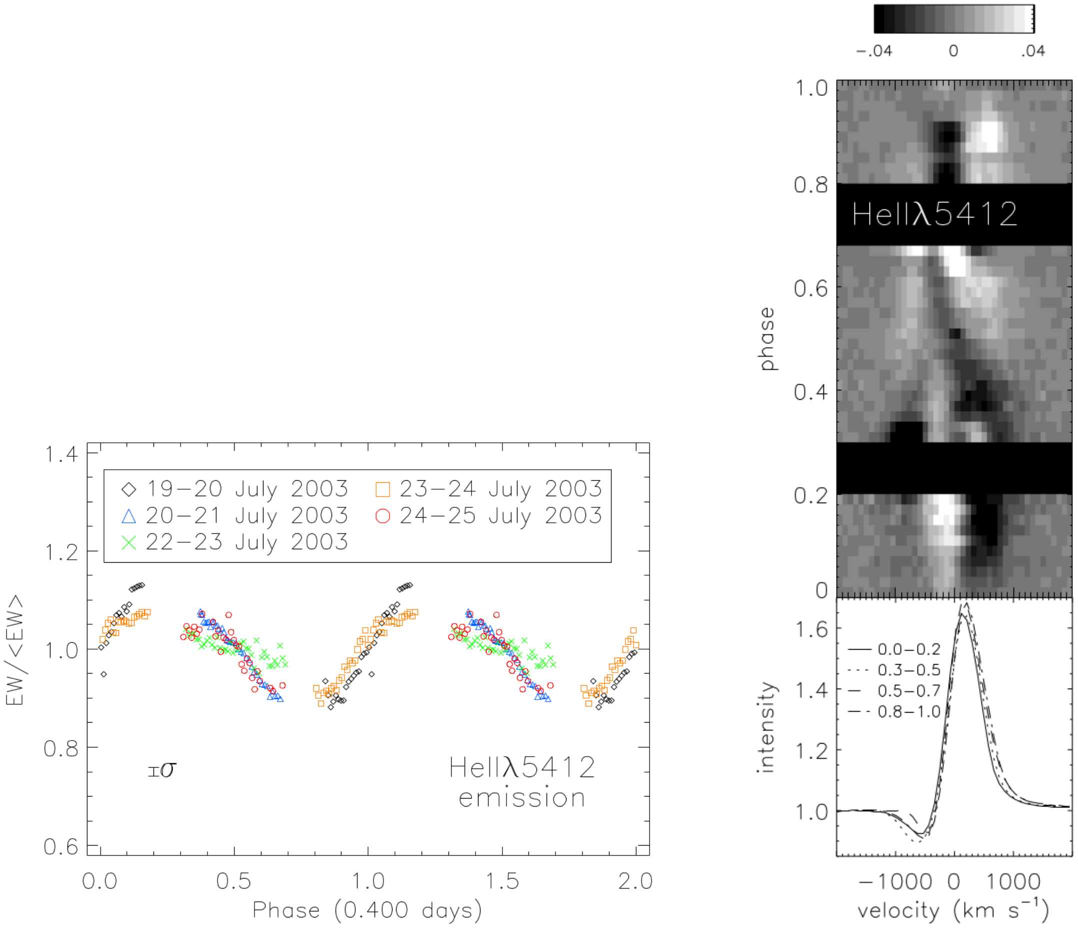

(a) Line strengths folded with the phase.

(b) Phase-folded residuals of the line profile (*top*) and variation of line profiles across different phase intervals (*bottom*).

Figure 1.15: Pulsations (with P=9.8 hour) detected from the spectroscopic monitoring of He II 5412 in WR 123. Taken from Chené et al. (2011).

polarimetric lightcurves can be fitted to determine the location and orientation of CIRs; angle and inclination of the rotation axis; density difference between the CIR and the surrounding winds, etc.

Extrinsic variability

Extrinsic variability in WR stars is mainly caused by the periodic binary interactions. These phenomena provide vital information about WR binaries such as mass ratio, orbital period, inclination angle etc. The extrinsic variability in a

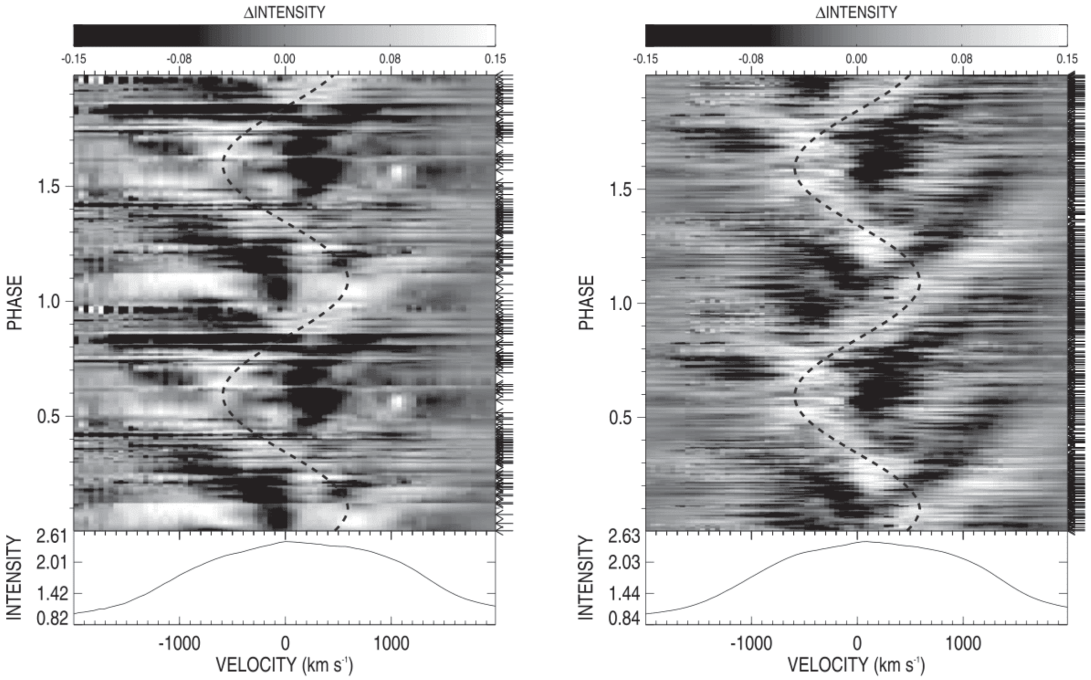

Figure 1.16: Spiral-like pattern is observed in the grey-scale difference images of He II 5412 of WR 134. The large-scale variability due to the CIRs is seen across two different epochs (left and right). Taken from Aldoretta et al. (2016).

WR binary is detected observationally across different wavelengths, as discussed below:

1. Optical observations: WR stars in colliding-wind binaries (CWB) exhibit periodic changes in the radial velocity (RV) of both absorption and emission lines in the optical band (see Fig. 1.17). Certain optical lines produced in the winds of the WR star exhibit variability in their line profiles that correlate with the binary period. Eccentricity, inclination angle, and masses can be estimated by modeling the changes in line profiles and radial velocity variations (see for example, Hill et al. (2018)).

2. IR line profiles: Periodic modulation in the IR spectra arises from profile variability of He I 10830Å (see Fig. 1.18) which forms at a greater radius in the stellar winds of a WR star and overlaps with the wind collision region of the binary system. Certain CWBs exhibit periodic variations in excess IR emission caused by dust formation in the circumstellar environment (discussed further in Sec. 1.4.1).

3. X-ray flux variations: WR CWB often show periodic X-ray variations due to changes in binary separation or circumstellar opacity, influenced by the system's orientation to the observer. Phase-locked X-ray variability has

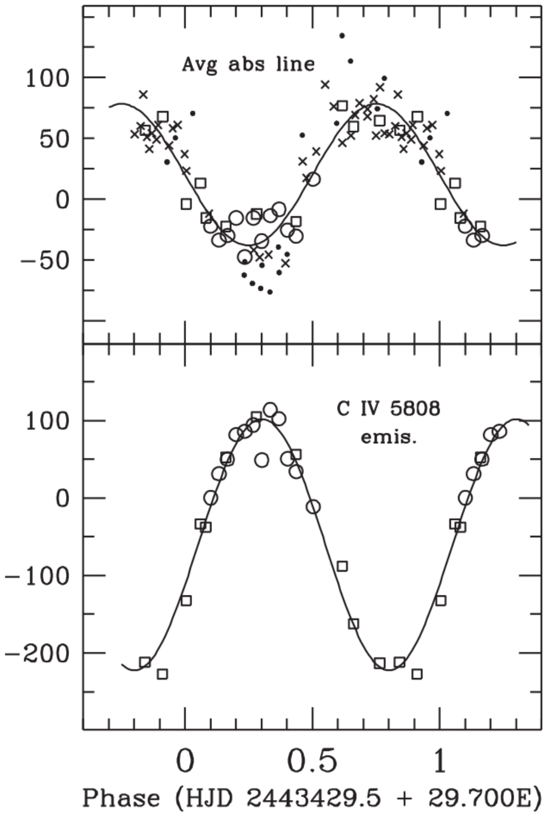

Figure 1.17: Periodic RV variations in the average of all the absorption lines (top) and a C IV emission line of WR 113 were observed by Hill et al. (2018).

been observed (see Fig. 1.19) in several WR stars (eg: WR 25 by Pandey et al. (2014); Arora et al. (2019)), revealing that changes in X-ray flux align with orbital periodicity and wind dynamics.

1.4 Significance of WR stars

In this section, I briefly highlight the important roles played by these objects in our universe.

1.4.1 Chemical Enrichment and Stellar Feedback Mechanisms

WR stars are primary agents of chemical enrichment within galaxies, expelling large quantities of heavy elements such as carbon, nitrogen, and oxygen into the surrounding ISM. This continuous ejection of enriched material plays a critical

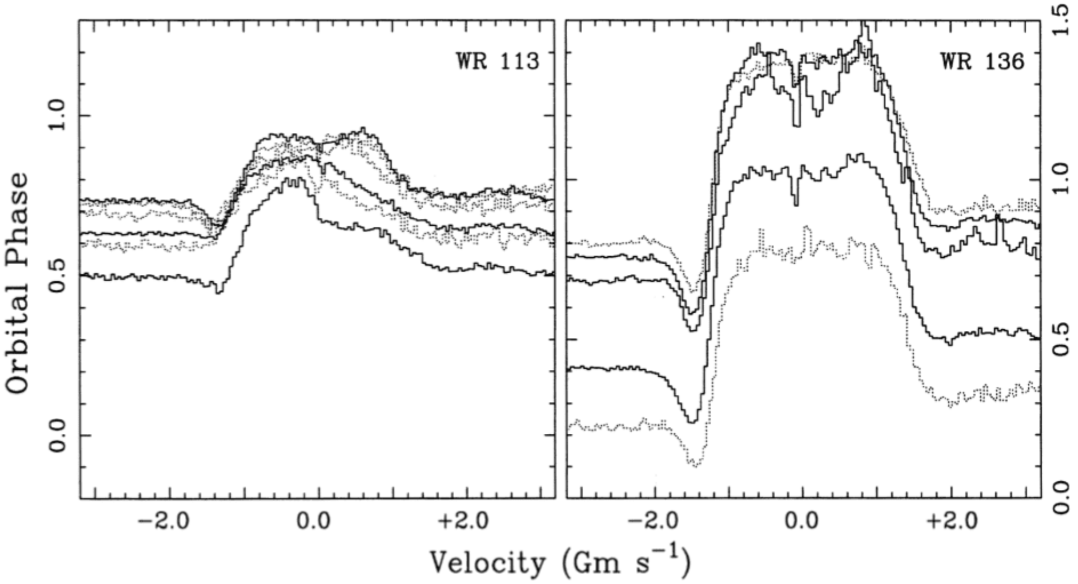

Figure 1.18: Line profile variability of He I 1.083μm is observed in WR binaries. Taken from Stevens & Howarth (1999).

role in the galactic ecosystem, creating an environment enriched with the building blocks necessary for subsequent star formation. The feedback from WR stars, in the form of both mechanical energy and ionizing radiation, influences star-forming regions by compressing surrounding gas clouds, thereby triggering the formation of young massive stars (discussed further in Sec. 1.4.3).

About 30% (van der Hucht, 2001) of Galactic WR stars are found to be surrounded by complex nebular structures (with nebular temperature $\sim 10^4$K) that are said to have been formed from the interaction between the stellar winds and the mass ejecta from the previous evolutionary (LBV or RSG) phases. The scarcity of nebular bubbles around most of the WR stars is said to be either a consequence of the evaporation by hydrodynamical instabilities or due to the presence of a high-mass binary companion. Based upon the several classifications (Chu, 1981; Toalá et al. (2015)) the WR star ring nebulae are found to exist either in the form of Bubble-shaped, Clumpy/disrupted or Mixed nebular morphologies. Those nebulae have been observed to show different morphologies (see Fig. 1.20) in different wavelength bands which makes them fascinating science objects. IR studies of the optically bright regions of the nebulae have resolved their sub-morphological structures and have detected dust made of multiple grain sizes (Rubio et al., 2020). The chemical composition of the nebulae surrounding WR stars reveals insights into the nucleosynthesis processes occurring within these massive stars. WR nebulae generally exhibit enhancements in helium and nitrogen (Stock et al., 2011) and, in some cases, a depletion of oxygen (Esteban

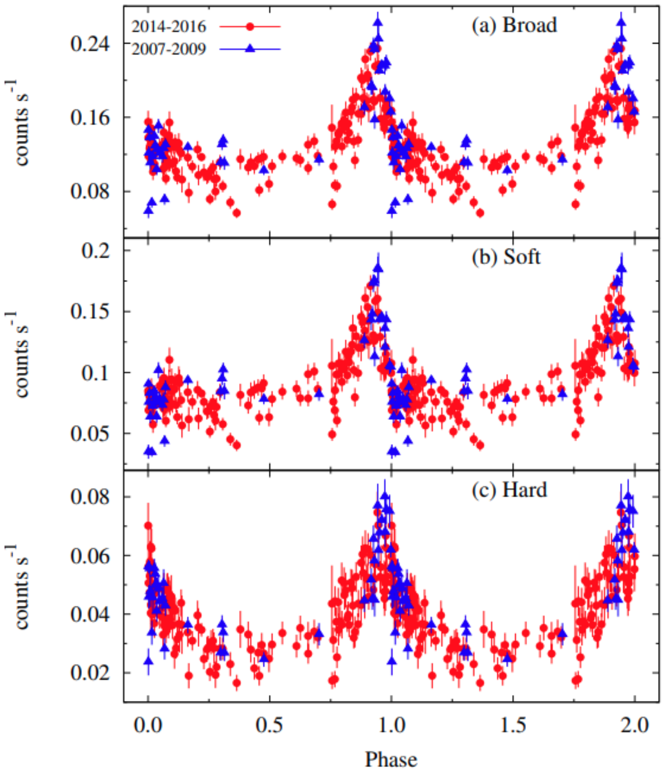

Figure 1.19: Phase-folded light curves of WR 25's X-ray emissions exhibit periodic variability across different SWIFT-XRT bands. Taken from Arora et al. (2019).

et al., 2016). This pattern indicates active C-N-O cycle processes in the WR star progenitors. Nebulae such as NGC 6888 (of WR 136) and G2.4+1.4 exhibit lower-than-expected Ne/O ratios (Esteban et al., 2016), possibly indicating the influence of the NeNa cycle in a high-temperature H-burning zone of the progenitor massive stars.

WR-late (mainly WC7-9) stars are sometimes found to show excess emissions in the IR-bands (Allen et al., 1972; Gehrz & Hackwell, 1974) due to the presence of circum-stellar dust shells. The variation in excess emission in the NIR was initially observed in WR 137 and WR 140 by Hackwell et al. (1976), subsequently interpreted by Williams et al. (1978) and Williams et al. (1985) as a consequence of alterations in the properties of the dust shell. However, the dust formation mechanism under hot and ionizing conditions was poorly understood until Usov (1991) based on analytic interpretation, showed that in WR 140, cold carbon-rich gas from the primary (WC7) flows out with the shock generated from the colliding winds and later condenses as dust shell in a period of 7.9 years. After years of monitoring, Williams et al. (2009) detected dust shells from earlier dust formation episodes which were later resolved (see Fig. 1.21) using the Mid-IR Imager mounted on the James Webb Space Telescope (JWST) by Lau et al. (2022).

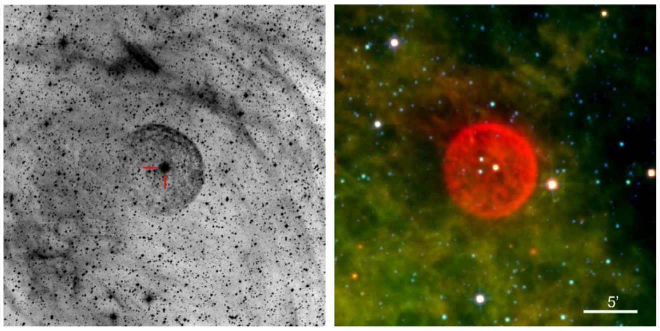

(a) Nebula around WR 16 (WN8h-type).

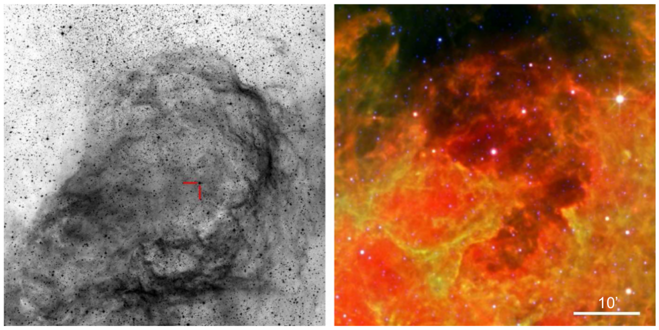

(b) Nebula around WR 23 (WC6-type).

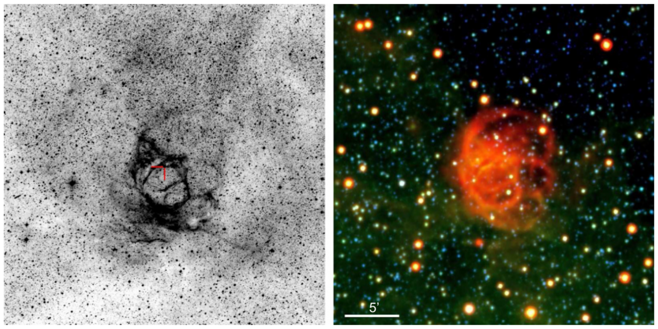

(c) Nebula (G2.4+1.4) around WR 102 (W02-type).

Figure 1.20: Nebular shells formed as a result of the interaction of WR stellar winds and ejecta material from the RSG or LBV phase. The *left* panel indicates the optical while the *right* panel are MIR color-composite images. Taken from Toalá et al. (2015).

Episodic dust producers predominantly exist in orbits characterized by significant eccentricities and frequently exhibit periodic fluctuations of the notable subpeaks within the typically flat-topped He I 1.083 μm emission line at periastron passage (Varricatt et al., 2004). Some WCL stars showed no change in the excess emission (Williams et al., 1987) and are considered to be *persistent* dust producers. Such binaries are said to have fixed separation and maintain circular orbits. In addition, they may occasionally exhibit a spiral stream of dust. For instance,

(a) WR 140 imaged using MIRI instrument

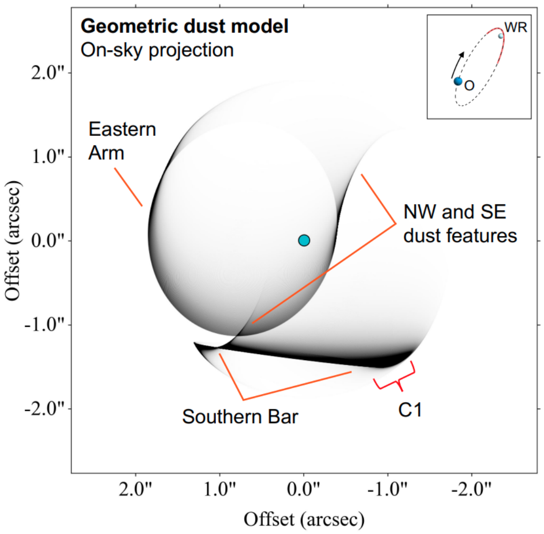

(b) Single-shell of dust. The binary orbit is shown at the *top right corner*.

Figure 1.21: The circumstellar dust shells produced from the episodic dust formation in WR 140 were recently resolved by Lau et al. (2022) using the MIRI instrument mounted at the JWST.

WR 104, which was imaged using the Keck telescope in the NIR at 1.65 μm and 2.27 μm bands (Tuthill et al., 1999), features a pinwheel nebula. In WR 104, dust forms at the collision front between the winds of the WR star and the massive OB companion (see Fig. 1.22). This interaction creates shock fronts that allow dust formation, which is then swept into an Archimedean spiral pattern by the WR star wind, rotating with the companion in a 220-day orbital period. Dust temperature can be measured from the MIR color, such as W1-W2, obtained from the WISE.

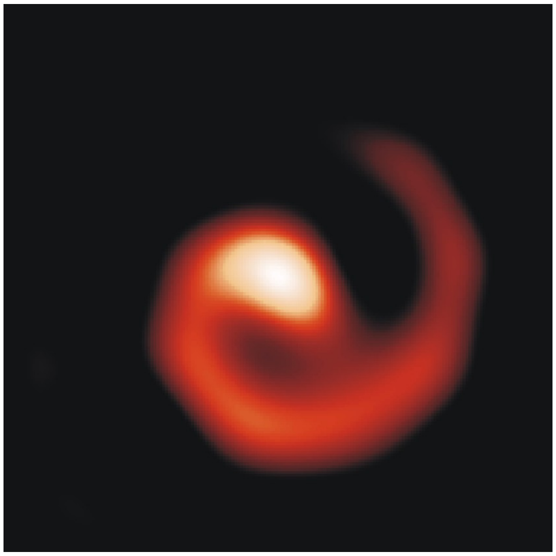

(a) NIR image of WR 104

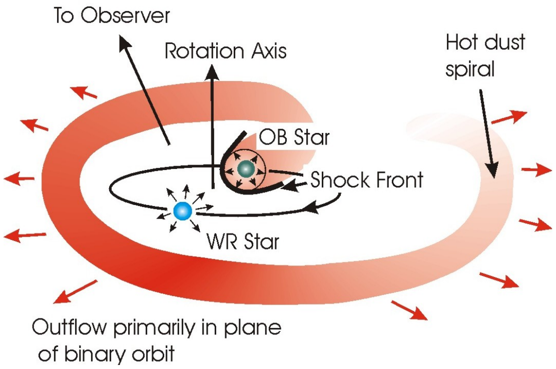

(b) Schematic image of the dust formation mechanism

Figure 1.22: WR 104, being a close-wind binary system, forms dust continuously at the collision front, which is swept away by the fast stellar winds of the WR star. Taken from Tuthill et al. (1999).

1.4.2 Progenitors of Core-Collapse Supernovae

WR stars represent a brief but critical phase in the evolution of massive stars, particularly those exceeding 20 $M_\odot$. The evolution of such massive stars provides insight into the physical processes underlying core-collapse Supernova (SN)e and the formation of compact stellar remnants, such as neutron stars and black holes. cWR stars are potential progenitors (Gaskell et al., 1986) for Type Ibc SNe (lack hydrogen in their spectra), which occur when the stars exhaust their nuclear fuel and undergo gravitational collapse. Illuminating the late stages of massive stellar evolution, these SNe enrich the interstellar medium with heavy elements. As potential sources of both Type Ib/c SNe (Crowther & Hadfield, 2007) and Gamma Ray Burst (GRB), WR stars occupy a central role in high-energy astrophysics, providing observational links to some of the universe's most violent processes.

It remains a mystery whether single WR stars (with M_i>$25M_\odot$) are capable of undergoing Type Ibc SNe (Smartt, 2009; Eldridge et al., 2013). Yoon et al. (2012) found that single cWR stars at the pre-SN phase are optically faint due to the expansion of their He-rich outer envelope. This result was later confirmed by Groh et al. (2013c) based on their single evolutionary models. Groh et al. (2013a) used evolutionary and atmospheric modeling methods and showed that a WR star of WN7-8 type could be the progenitor of the SN Ib iPTF13bvn (see Fig.1.23). From the single star evolutionary models (Ekström et al., 2012; Georgy et al., 2012), Groh et al. (2013b) predicted that most of the SNe Type Ib occur from WNL stars of initial mass lying within 25-30 $M_\odot$ and 32-45 $M_\odot$ for rotating and non-rotating O-type MS progenitors respectively. However, the WO spectral class (WO1-3) was predicted to be the possible pre-SN progenitors for the remaining SNe Ib.

A significant population of WR stars exist in binary systems, interacting closely with a massive companion, and are considered the most likely progenitors of observed bright SNe Ibc events in the Galaxy (Fryer et al., 2007; Eldridge et al., 2013). Such SNe events produce black hole remnants. WR binaries (Trenti et al., 2015) are predicted to be progenitors of long GRB. However, Eldridge et al. (2011) predicted that the observed distribution of long-GRBs can be understood from the perspective of runaway stars before they undergo core collapse.

1.4.3 Influence young star formation

WR stars affect their environment through significant mass loss and UV radiation. Their robust feedback can trigger the formation of the following generation of stars in the galaxy. However, during the earlier phase of their evolution, an ionized gas shell/bubble is formed around the star. These shells expand, reach a critical density, and collapse to form stars (Dewangan et al., 2016). This process creates distributed star formation along the shell's edges, often resulting in clusters. Alternatively, strong UV energy from massive stars can compress the side of the cloud facing the star, creating a high-pressure front that drives material into the clump. This compression may cause the clumps to collapse, forming stars within it (Panwar et al., 2014).

WR stars can have a substantial influence on their surrounding star-forming regions (Baug et al., 2019). Due to their intense stellar winds and high mass-loss rates, WR stars create gas-deficient cavities and drive expanding molecular shells

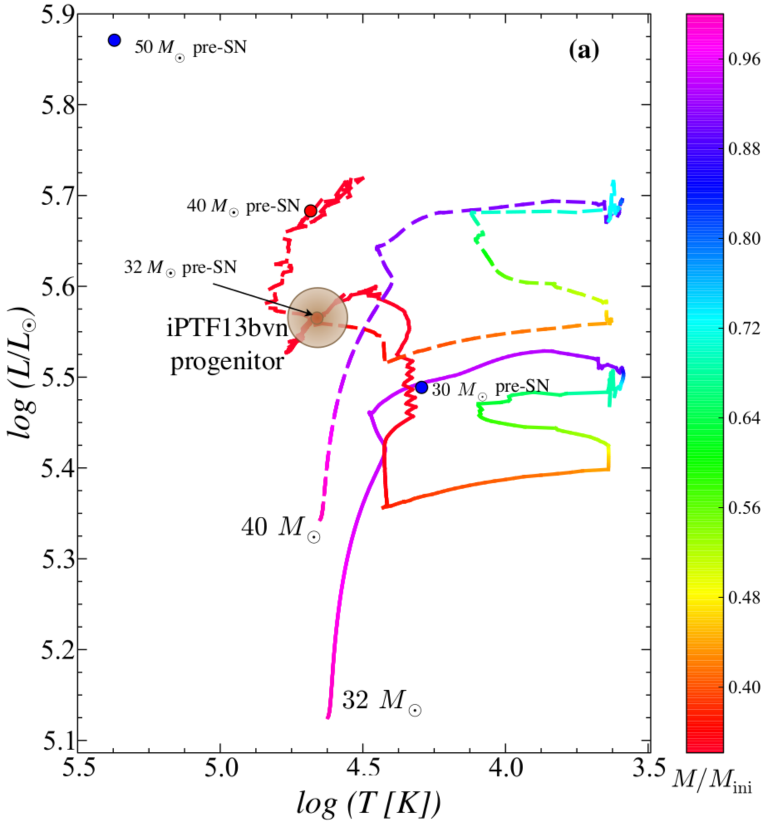

Figure 1.23: Single star evolutionary model tracks for non-rotating stars are plotted on the HR diagram. Also, the position of the SN Ib iPTF13bvn is shown. Taken from Groh et al. (2013a).

in the surrounding interstellar medium (see Fig. 1.24). These expanding shells, primarily formed through the pressure of WR winds, sweep up nearby molecular gas to distances of several parsecs. While the cavities created by WR stars tend to suppress star formation within their centers, active star formation is often observed around the outer shells where gas is compressed. This suggests a dual effect: the winds from WR stars can quench star formation within close proximity but also potentially trigger new star formation at the boundaries of these shells by accumulating and compressing gas.

1.5 Motivations

In recent decades, great strides have been made in the understanding of WR stars, yet many challenges remain. In my thesis work, I have examined some of the less understood phenomena of WR stars, mainly focusing on the WCL type stars. WC stars play a crucial role in contributing carbon and oxygen to the

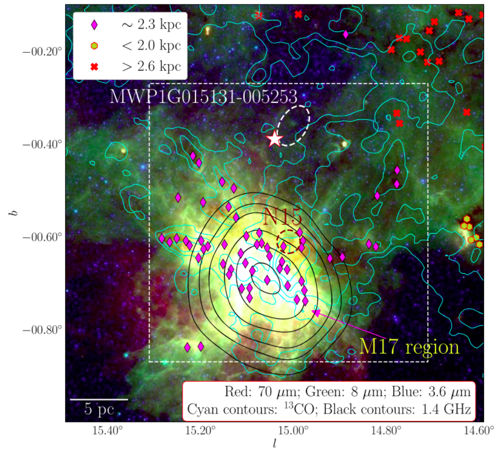

(a) Color composite image showing distribution of dust clumps

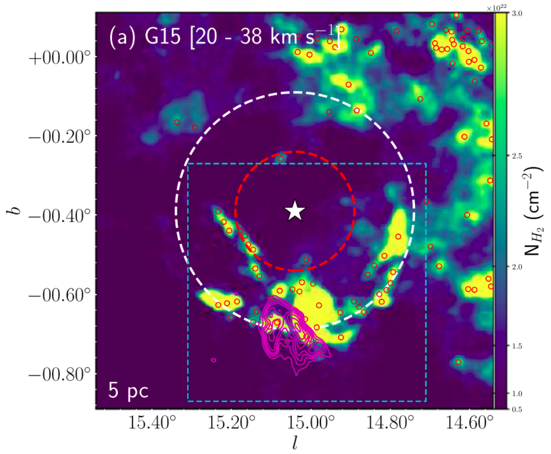

(b) Column density maps made using ^{12}CO and ^{13}CO molecular line data showing gas cavity within concentric circles around the star.

Figure 1.24: G15.010–0.570, a region with M17, a high star-forming region which is strongly influenced by the WR star (2MASS J18192219–1603123), indicated by a white star. Taken from Baug et al. (2019).

surrounding ISM and are widely recognized as potential progenitors of Type Ic SNe (Crowther et al., 2002). Latest surveys in the NIR (Rosslowe & Crowther, 2015; Shara et al., 2012; Mauerhan et al., 2009) have identified more WCL stars in high-extinction Galactic areas. The metallicity has a significant impact on the high mass-loss rates of WC9-type stars, which are primarily present in the inner spiral arms of the Galactic disk. As mentioned in Sec. 1.4.1, WC9-type stars in a binary system often show excess emissions due to the presence of dust in the circumstellar environment. Thus, these objects play a significant role in the chemical and mechanical feedback to the ISM and affect the nearby star-forming regions. The stratified nature of their stellar winds, the impact of mass-loss rates on their evolution, and circum-stellar environments remain unclear and are explored in chapter 3.

The driving mechanism behind the mass outflow in cWR stars remains a major challenge. Also, the cool WR-late stars known for wind velocities slower ($<$ 2000 $\mathrm{km\,s^{-1}}$) than early, show stronger intrinsic variability Chené et al. (2020). Opacity peak due to Fe-M shell transitions (Fe IX-XVI; Sander et al. 2020) in the cWR stars are said to be responsible for the driving of inner winds and can also explain the low temperatures (due to envelope inflation; Gräfener et al. (2012)) observed in WR-late stars. As stated in Sec. 1.3.4, such opacity source may trigger strange mode instabilities (SMI) (Glatzel, 1994, 2008)), leading to wind inhomogeneities and strange mode pulsations (SMP)s. In WR stars, energy transport in radiation-dominated atmospheres occurs mainly through diffusion, causing phase shifts in pressure and density that result in damped and excited strange modes. The frequency of the SMPs depends on the position of the opacity (κ) maxima (Saio, 2009), while the SMIs are not influenced by the κ-mechanism. An alternative solution to explain pulsations and stochastic variability in the line-driven stellar winds of cWR stars was proposed by Owocki et al. (1988). Inhomogeneities within stellar winds arise due to LDI, which are triggered by self-excited radiative acoustic waves at the base of the winds (Abbott, 1980; Sundqvist et al., 2018). In the supersonic regions, LDIs amplify long-period non-radial pulsations that originate in the subsonic winds due to these instabilities. Among WC stars, WCL stars have higher mass-loss rates and mainly exhibit stochastic variability observed over hours (Lenoir-Craig et al., 2022). Therefore, studying the variable nature of WCL stars can provide constraints on the mass-loss rates influencing their later evolutionary stages. Chapter 4 explores the physical mechanisms responsible for the observed intrinsic variability in a WCL star.

As mentioned in Sec. 1.3.3, the population of WR stars in the MW is still incomplete due to observational constraints. Distinguishing WR stars from other stellar objects using optical colors and magnitudes remains challenging due to significant interstellar dust extinction. In contrast, IR colors experience far less obscuration, making them more effective for identifying WR candidates. With advanced instruments like JWST and the upcoming Roman Telescope, we are poised to uncover thousands of these evolved stellar objects within the Local Group of galaxies. The IR selection criteria proposed by Mauerhan et al. (2011) help filter out the non-WR stars, while emissions from free-free transitions and circumstellar dust aid in WR identification. The large volume of IR data makes manual identification a cumbersome and challenging task, making Machine Learning (ML) techniques a promising solution for stellar classification, as demonstrated in recent studies by Morello et al. (2018) and Dorn-Wallenstein et al. (2021). In chapter 5, I utilize some of the ML methods to develop models that can identify WR stars in the MW.

Chapter 2

Methodologies

2.1 Data observation

The thesis is based on astronomical data observed using the 2m-Himalayan Chandra Telescope (HCT) and processed archival data observed from ground-based optical telescopes and space telescopes. Data from other telescopes such as 2.3m-Vainu Bappu Telescope (VBT) and 3.6m-Devasthal Optical Telescope (DOT) were observed in the Optical and NIR bands. I discuss the observations that I carried out during my research in the following subsections.

2.1.1 2m-Himalayan Chandra Telescope

The HCT is part of the Indian Astronomical Observatory (IAO) operated by the Indian Institute of Astrophysics (IIA). The observatory is located at Mt. Saraswati in Hanle, Ladakh (India) at an altitude of 4500 m (approximately 15,000 ft) above sea level, offering ideal conditions for astronomical observations. The site has been recognized as a part of India's Dark Sky reserve by the International Dark Sky Association. The telescope is situated at a longitude of 78°57'51" E and a latitude of 32°46'46" N, making it well-placed for clear and stable atmospheric conditions. The HCT is operated remotely from the Center for Research & Education in Science & Technology (CREST) in Hosakote, Bangalore, Karnataka via a satellite-based network. The telescope is equipped with several advanced instruments, including the Hanle Faint Object Spectrograph and Camera (HFOSC) for optical imaging and spectroscopy, the TIFR InfraRed SPectrograph (TIRSPEC) for NIR observations, and the Hanle Echelle SPectrograph (HESP) for high-resolution spectroscopy in the optical band. With a Field of View (FoV) of 30', the telescope can be used to perform a wide range of astronomical observations, such as studying faint objects, observing NIR-bright celestial bodies, and conducting detailed spectroscopic analyses. The ability to quickly switch between instruments during an observation makes the HCT highly versatile in meeting various scientific demands. Playing a crucial role in advancing astronomical research in India, the HCT provides valuable data for numerous studies in the field of astrophysics. I carried out spectroscopic observations using the instruments mounted at the Cassegrain focus of the telescope. Across, 20 accepted observing proposals, I observed about 40 Galactic WR stars (see Table. 2.1 for the data log of observations) in the optical and NIR wavebands using dedicated spectrographs, discussed in the following subsections.

Figure 2.1: Image showing 2m-Himalayan Chandra telescope. Photo credits: Dorje Angchuk

HFOSC

The HFOSC (see Fig. 2.2) is an optical imager and spectrograph (with a wavelength coverage of 350-900 nm) designed for use at the HCT. Developed in collaboration with the Copenhagen University Observatory, the HFOSC is a focal reducer-type instrument that supports a large field coverage for the detector, which is a 2048×4096 CCD with a total pixel area of 15×15 microns. It provides both low and medium-resolution grism spectroscopy and enables quick switching between imaging and spectroscopic modes. The spectrograph is equipped with 11 grisms, providing resolutions ranging from 150-4500. The available slits for spectroscopy have a length ranging from 10-11” while widths ranging from

Table 2.1: Log of observations from HCT (date-wise)

Source	Date	Configuration	Exposure (sec)
Optical (HFOSC)			
WR 111-9	2020 June 8	Gr7/Gr8	1500
WR 114	...	...	720
WR 115	...	...	600
WR 119	...	...	720
WR 120	...	...	720
WR 150	...	...	900
WR 1	2020 September 10	...	420
WR 2	...	...	300
WR 4	...	...	90
WR 155	...	...	60
WR 156	...	...	600
WR 157	...	...	180
WR 158	...	...	300
WR 159	...	...	180
WR 3	2020 September 11	...	600
WR 5	...	...	180
WR 6	2021 January 25	...	600
WR 7	...	...	30
WR 105	2021 June 28	...	720
WR 106	...	...	720
WR 107	...	...	1200
WR 128	2022 June 25	...	600
WR 131	...	...	900
WR 116	2022 July 23	...	720
WR 128	...	...	600
WR 153ab	...	...	300
WR 135	2023 September 19	...	15/60
WR 154	...	...	300
WR 120	2023 September 20	...	300
WR 156	...	...	240
Optical (HESP)			
WR 135	2023 August 10	star+sky	8frames×2400s
NIR (TIRSPEC)			
WR 7	2021 January 25	K_s	5frames×2pos×100s
WR 114	2021 June 26	YJ & HK_s	5frames×2pos×100s
WR 130	...	...	5frames×2pos×100s
WR 143	...	...	5frames×2pos×100s
WR 150	2021 October 23	HK_s	6frames×2pos×500s
WR 1	2021 October 24	HK_s	5frames×2pos×100s
WR 154	...	YJ & HK_s	5frames×2pos×100s
WR 156	...	YJ & HK_s	5frames×2pos×100s
WR 157	...	HK_s	5frames×2pos×100s
WR 158	...	HK_s	3frames×2pos×100s
WR 111-9	2022 June 25	YJ & HK_s	5frames×2pos×500s
WR 2	2023 January 30	HK_s	6frames×2pos×500s
WR 5	...	...	3frames×2pos×500s
WR 4	2023 January 31	...	6frames×2pos×500s

0.77”-15.41”. The imager is equipped with broad-band (Bessell UBVRI) and narrow-band filters (372.7, 486.1, 500.7, 656.3 and 672.4 nm). The limiting magnitude for the spectrograph is V=18.5 mag. For the spectroscopic observations, I used the long-slit (of dimension 1.92”×11’) and Grisms 7 and 8 to cover the whole optical wavelength range (3800-9000 Å) and acquired data of a total of 30 Galactic WR stars during 2020-2023. The observing strategy is discussed further in Sec. 2.1.4.

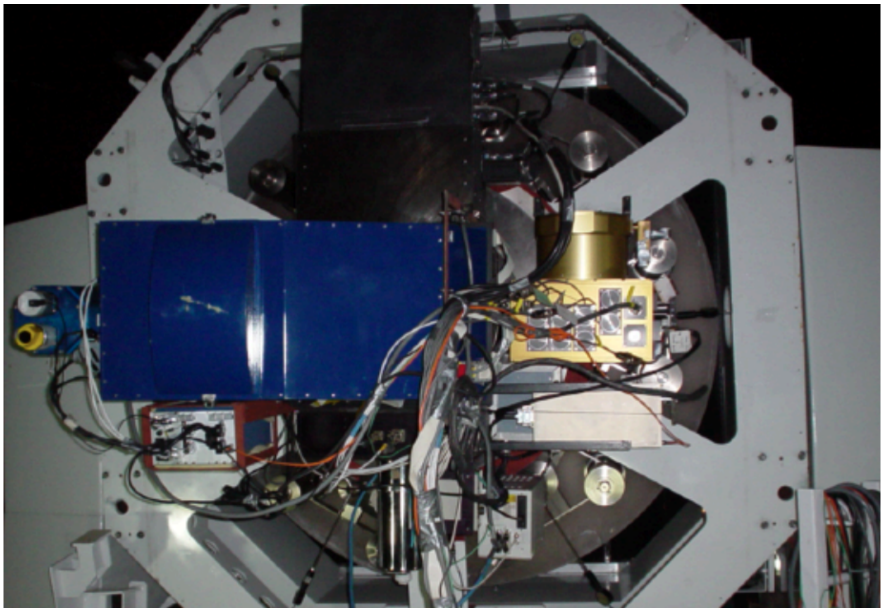

Figure 2.2: Image showing the HFOSC instrument mounted at the HCT. Photo credits: Prof. G C Anupama

TIRSPEC

The TIRSPEC (shown in Fig. 2.3) is designed for the NIR (1-2.5 μm) imaging and spectroscopic observations (limiting magnitude K_s=10 mag). The imager has different broad (J, H, K_s) and narrow band filters (CH$_4$, Fe II, H2, Br γ, K-cont, CO). The available slits for spectroscopy have either a length of 50” (short slit) or 300” (long-slit) while widths ranging from 1.0”-7.92”. The spectroscopic observations were carried out using the same grism (with a resolution of 1200) but either in single-order (with slit length of 300”): Y (1.02-1.20 μm), J (1.21-1.48 μm), H (1.49-1.78 μm), K_s (2.04-2.35 μm); or cross-dispersed modes (with slit length of 50”): YJ (1.02-1.49 μm) and HK_s (1.95-2.45 μm). The images and spectra are recorded using a 1024×1024 (1K×1K) HAWAII-1 PACE-array on 18×18 pixels square area. Based upon the sky conditions; and availability and brightness of the objects, I observed 14 WR stars in the cross-dispersed mode using a short-slit (1.97”×50”) dithered at two positions. The observing strategy is discussed further in Sec. 2.1.4.

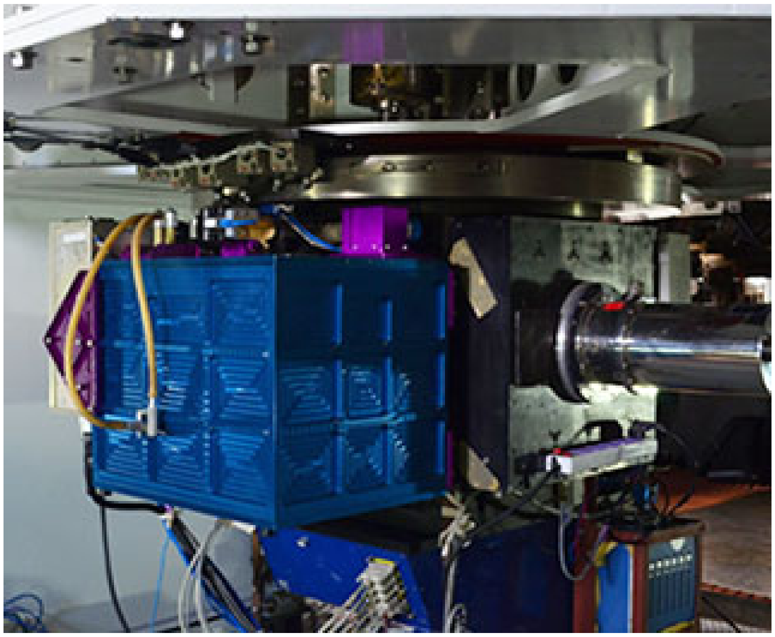

Figure 2.3: Image showing the TIRSPEC instrument mounted on the side port of the HCT. Photo credits: World Scientific.

HESP

HESP is a high-resolution spectrometer (shown in Fig. 2.4) detecting echellegram images of bright (V-mag<11) stellar objects with a 4K×4K E2V detector of 15 pixels square area. An F/3.6 beam of light is passed through a 100 μm fibre image (similar to 0.34 mm slit width) that enters the spectrograph and is dispersed into multiple spectral orders using an R2 echelle grating (with 52.67 lines/mm), along with two cross-dispersing prisms, that allow for continuous wavelength coverage in the optical band (350-1000 nm). The instrument offers two types of spectral resolutions: low (R = 30,000) and high (R = 60,000). The high-resolution mode utilizes an image slicer, which divides the 2.85” fibre image into two 1.2” slices (corresponds to a slit width of 0.14mm), effectively doubling the resolution while the low-resolution mode is achieved without the slicer. Based on the science behind an astronomical observation, the instrument can be used in either of 4 observing modes (using the single or dual fibres): star only, star+sky, star+calib, or calib+calib. In the star-only mode, the single fibre is illuminated with the starlight. The star+sky mode is chosen for the precise measurement of chemical abundances of the star in which case the sky background needs to be subtracted.

The star+calib mode is chosen for the precise measurements of the radial velocity of the star. In the calib+calib mode, both the fibres are illuminated by the lamps. This mode is used either for wavelength calibration or flat-fielding using ThAr and ThNe lamps; or Halogen lamps. respectively. The high resolution spectroscopic time-series data of a sufficiently bright WR star was observed in the star+sky mode. The wavelength calibration data were recorded in the calib+calib mode. The observing strategy is discussed further in Sec. 2.1.4.

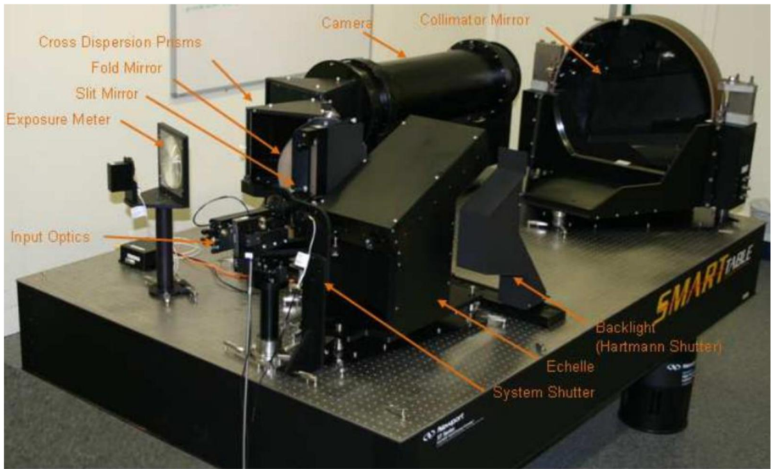

Figure 2.4: Image showing the HESP instrument kept on an optical bench. Different components of the instrument are indicated. Taken from Sriram et al. (2018).

2.1.2 2.3m-Vainu Bappu Telescope

The VBT at the Vainu Bappu Observatory (VBO) in Kavalur, Tamil Nadu, India, is a key optical astronomy instrument managed by IIA. The VBO is located at a latitude of 12° 34’, a longitude of +78° 50’, and an altitude of approximately 750 meters. Completed in 1986 and named after Indian astronomer M.K. Vainu Bappu, the VBT (see Fig. 2.5) is equatorially mounted and features a 2.34-meter Ritchey-Chrétien mirror that minimizes aberrations and provides a flat field of view, ideal for high-precision imaging and spectroscopy. Two foci are used by the telescope: an f/3.5 prime focus with an image scale of 27 arcsec/mm and an f/13 Cassegrain focus with a scale of 6.7 arcsec/mm. For imaging, CCD cameras are used at the prime focus using different filters. In spectroscopy, two instruments are utilized: the Echelle spectrograph (positioned at the Prime focus) and the Optomechanics Research (OMR), located at the Cassegrain focus. With various instruments, the VBT can detect faint and bright objects across the optical band, supporting a wide range of research areas. The spectroscopic data of a handful of WR stars (see Table 2.2) were acquired at both low and high resolution using the instruments mounted on the telescope. Such data will be used for the future studies.

Figure 2.5: An image of VBT located at Kavalur, Tamil Nadu. Photo credits: Prateek Karandikar

OMR spectrograph

The OMR spectrograph (see Fig. 2.6), also housed at the VBT but at the Cassegrain focus, offers a versatile low-resolution spectral alternative. It operates with a 1K×1K CCD featuring pixels with a size of 24×24-micron and supports a range of resolutions through different gratings. These configurations include a 150 grooves/mm grating with a dispersion of ∼10 Å/pixel and a spectral resolution of $R \sim 250$, a 300 grooves/mm grating providing ∼5 Å/pixel with $R \sim 500$, a 600 grooves/mm grating at ∼2.6 Å/pixel for $R \sim 1000$, and a 1200 grooves/mm grating with ∼1.3 Å/pixel, achieving $R \sim 2000$. The OMR spectrograph's slit width is 300 microns, corresponding to approximately 2" on the sky per two-pixel resolution, and it has a 150 mm camera focal length along with a 1000 mm focal length collimator. This setup makes the OMR spectrograph well-suited for low-resolution spectroscopic observations of stellar objects.

Table 2.2: Log of observations from VBT (date-wise)

Source	Date	Configuration	Exposure (sec)
		Instrument: OMR	
WR 11	2021 May 9	Grating: 1200 grooves/mm; λ_c: 5000 Å	15
...	...	Grating: 1200 grooves/mm; λ_c: 6500 Å	5
WR 16	...	Grating: 1200 grooves/mm; λ_c: 5000 Å	1800
...	...	Grating: 1200 grooves/mm; λ_c: 6500 Å	600
		Instrument: Echelle	
WR 6	2024 February 17	Without slicer	6frames×2700
...	2024 February 18	...	3frames×2700
...	2024 February 19	...	3frames×2700
...	2024 February 20	...	3frames×2700

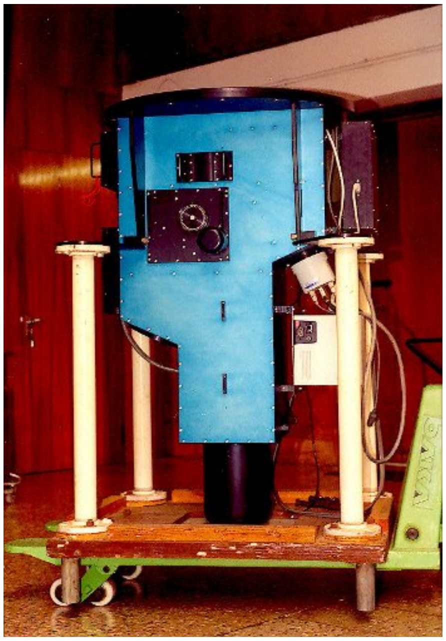

Figure 2.6: OMR spectrograph of VBT. Pic credits: Indian Institute of Astrophysics

Echelle spectrograph

The VBT is equipped with a high-resolution fiber-fed echelle spectrograph at its prime focus, facilitating intricate spectral observations using a 4K×4K CCD detector (with 12×12 microns pixel size). The optical fibre with a 100-micron width covers an area of about 2.7” in the sky, providing high-resolution capabilities for astrophysical studies. The spectrograph offers two main resolutions, achieving a spectral resolution of $R = 27,000$ with a 100-micron slitless width, which is suitable for observing stars up to a limiting magnitude of $V \approx 11$. To achieve a signal-to-noise ratio (S/N) of 60 in clear skies, three 40-minute exposures are required. A higher resolution of $R = 72,000$ is also achievable with a 60-micron width, which has a limiting magnitude of $V \approx 9$ and requires two 40-minute exposures for a similar S/N.

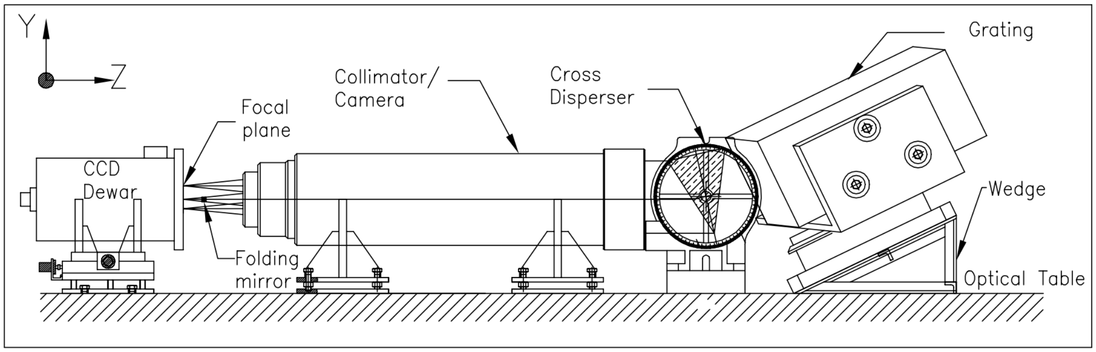

Figure 2.7: Layout of the spectrometer showing the path of optical beam from the fibre to the echelle grating. The dispersed beam is re-focused by the collimator on the CCD. Taken from Rao et al. (2005).

2.1.3 3.6m-Devasthal Optical Telescope

The DOT is an advanced optical telescope located at an altitude of ∼2430 metres in Devasthal (29°21’22”N 79°41’4”E), near Nainital in the state of Uttarakhand, India. The DOT (see Fig. 2.8) is hosted by the Aryabhatta Research Institute of Observational Sciences (ARIES) and is known to be one of the largest optical/IR telescopes in India. This astronomical telescope features a Ritchey-Chretien optical configuration with an f/9 effective focal ratio and *alt-azimuth* mounting, designed to deliver high-quality imaging over a broad operational wavelength range (350 to 5000 nm) with a FoV of 10’ (at the axial ports) and 30’ (on the axial port) achieved using the field corrector. The telescope includes three Cassegrain ports (one axial main port and two side ports), allowing multiple instruments to be mounted for optical and NIR spectroscopy and photometry. The notable instruments are the IMAGER, ADFOSC, TIRCAM2, and TIFR-ARIES Near Infrared Spectrometer and Imager (TANSPEC). I used the TANSPEC instrument for time-series observations of some of the cWR stars (see Table 2.3), and the data collected will be utilized in future work.

Figure 2.8: Night view of the DOT at ARIES, Devasthal. Photo credit: euttaranchal.

Table 2.3: Log of observations from the DOT (date-wise).

Source	Date	Configuration	Exposure (sec)
WR 135	2022 November 15	Cross-dispersed mode; 1”×20’ slit	6 frames × 2 pos × 50 s × 5 sets
WR 136	...	...	6 frames × 2 pos × 50 s × 5 sets
WR 135	2023 May 15	...	6 frames × 2 pos × 50 s × 8 sets
WR 136	...	...	6 frames × 2 pos × 50 s × 3 sets
...	2023 May 16	...	6 frames × 2 pos × 50 s × 7 sets

TANSPEC

The TANSPEC an advanced instrument mounted on the DOT’s main port (see Fig. 2.9), is designed for medium-resolution spectroscopy and imaging across a broad wavelength range from 550 to 2540 nm. Equipped with a 1024 × 1024 HgCdTe (H1RG) detector array, TANSPEC provides imaging capabilities with a pixel scale of 0.25”, covering a $1' \times 1'$ FoV. For spectral observations, it uses a 2048×2048 H2RG array, allowing both cross-dispersed ($R \sim 2750$) and prism modes ($R \sim 100-350$), with slits of 20' length but of varying widths between 0.5 to 4". This setup enables high-resolution spectra (R ∼ 2750) for bright objects and low-resolution spectra for fainter sources. The instrument's optical layout includes an Offner relay to re-image a 60"×60" field onto a set of slits that direct the f/12 beam to the spectrograph.

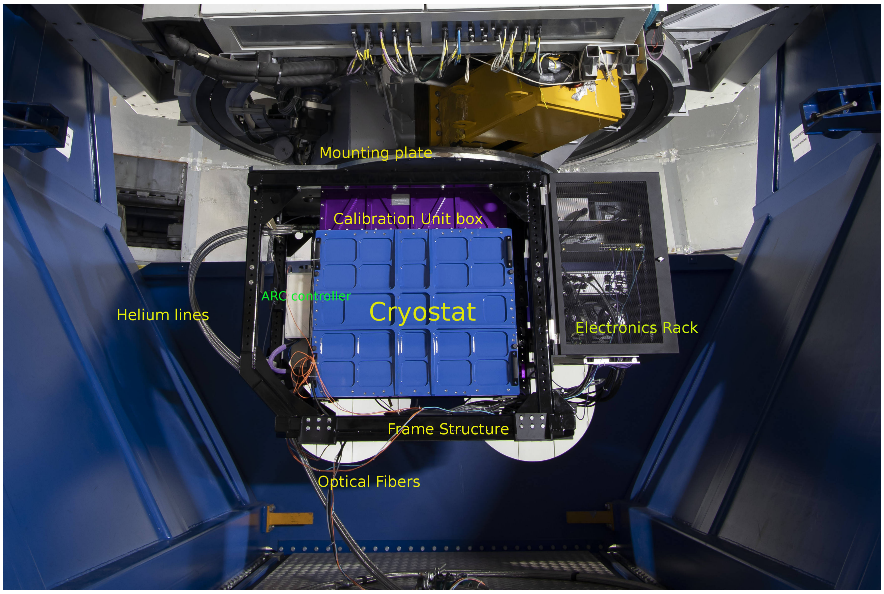

Figure 2.9: Image showing different components associated with the TANSPEC mounted on the Cassegrain focus of the DOT. Taken from Sharma et al. (2022).

Designed for studies from star formation to extragalactic astronomy, TANSPEC provides robust capabilities for high-sensitivity observations, with a detection limit of 17.3 magnitudes in J-band in prism mode and 15.4 magnitudes in cross-dispersed mode for 1-hour exposures under optimal seeing conditions. The spectrograph employs a filter wheel with broad-band (r', i', Y, J, H, K_s) and narrow-band (H_2, Brγ) filters, as well as a calibration unit with Argon and Neon lamps to ensure accurate wavelength and flat-field calibration across its spectral range. Further details are provided in Sharma et al. (2022).

2.1.4 Observing Strategy

Spectroscopic observations of WR stars were carried out in optical and NIR bands. The observational procedures for carrying out observations are discussed in the following subsections.

Optical

In the optical wavebands, I carried out both the long-slit (for low resolution) and slit-less (high resolution) spectroscopy using different instruments that require different observing strategies.

- **Long-slit spectroscopy:** For low-resolution spectroscopy i.e. using HFOSC (at HCT), OMR (at VBT), I followed these steps:
  1. **Slit selection:** An appropriate slit available in the aperture wheel of HFOSC was selected from the User Interface of HFOSC.
  2. **Grism/Grating selection:** After slit selection, a suitable grism (for HFOSC) or grating (for OMR) as per the requirement was chosen from the wheels of the instruments.
  3. **Calibration source selection:** For wavelength calibration, the available lamps were Fe-Ne, Fe-Ar, and HgCd. For flat-fielding, a Halogen lamp was used.
  4. **Spectral imaging area:** Before the frame exposure, the imaging area for the 2D-slit image was selected.
  5. **Slit alignment:** An offset was provided to position the object at the center of the slit.
  6. **Flux standard star:** For flux calibration, a suitably bright spectrophotometric star located within the same nearby airmass range as the science object was observed.
- **Slit-less spectroscopy:** The high-resolution spectroscopy of WR stars using the Echelle spectrographs (on HCT and VBT) were carried out as per the following strategy:
  1. **Science frames:** The star+sky mode was utilized for the science observations. For a bright star (V-mag<9), high S/N ($\sim$20$-$30 per frame) can be achieved from an exposure of 40 minutes depending upon the sky conditions and the spectral type of the star.
  2. **Bias frames:** The voltage bias of the detector was recorded at different instances during the entire observation. The science frames were corrected using the median bias frame.
  3. **Continuum flats:** A sufficient number of continuum flats were observed in the calib+calib mode. The median combined flat was subtracted from the science frames for the flat-fielding.
  4. **Wavelength calibration:** A suitable number of lamp frames were observed in the calib+calib mode for wavelength calibration.

Near-IR

I performed slit-based spectroscopy of WR stars in the NIR bands (using the TIRSPEC and TANSPEC), following the steps outlined below.

1. **Dark current frames**: At least 3 frames of dark current before (the sunset) and after (the sunrise) the observations were recorded that were average combined and subtracted from the science frames.
2. **Continuum flats**: A tungsten lamp was used for recording the continuum flats.
3. **Slit selection**: A short slit was used for observing the WR stars in the cross-dispersed mode.
4. **Dithering of slits:** To avoid any loss or exposure of starlight on a bad pixel, the slit was dithered at two positions along the length of the slit.
5. **Calibration frame:** For wavelength calibration of the 1-dimensional (1D)-spectra, proper Argon lamp frames in case of TIRSPEC and Argon-Neon lamps (to cover all the spectral orders) for the TANSPEC were recorded using the same slit configuration as the science object.
6. **Telluric standard:** A bright rotating spectrophotometric star was observed to remove the telluric OH-lines of the earth's atmosphere and calibrate the apparent flux of the science object.

2.2 Data Extraction

2.2.1 Optical data reduction

Low-resolution

The low-resolution optical spectroscopic data were reduced using the standard pipelines based on the IRAF packages (Tody, 1986). The basic data reduction was done in the following manner:

1. **Data Pre-processing**:
    - **Bias-level correction:** A median bias frame was subtracted from the science frames to remove the voltage bias level and enhance the Signal-to-Noise ratio (S/N) of the frames.

   - **Cosmic ray removal:** The cosmic rays generate photons that are detected along with the signal from the target source. I removed those artifacts when their counts were above a certain threshold value.

2. **1D spectra extraction**: After data was cleaned, the 2-dimensional spectral images were reduced to 1D spectra. For this, the spectral beam is chosen within the aperture widths and two windows are marked on both sides of the aperture to select the regions for sky background. Thereafter, a polynomial function (Spline, Legendre, etc.) of suitable order was fitted (with the least root mean square error) to the pixel data along the dispersion axis of the spectral beam image to extract the 1D spectrum. The science, lamp, and standard star spectra were extracted using this approach.

3. **Wavelength calibration**: In this step, a polynomial was fitted to convert the scale from pixel-to-wavelength of an extracted lamp spectrum which was immediately observed after the science frame using the same observing configuration. Thereafter, the same scaling information was applied to the science spectrum and also to the standard star spectrum.

4. **Flux calibration**: Prior to this, the airmass present during the observation of both science and the spectrophotometric standard star was estimated. Thereafter, the CCD response was computed by comparing the bandpass flux values of atmospheric extinction corrected tabulated spectrum (available in the IRAF database) of the standard star with its observed spectrum. Thereforth, the sensitivity function i.e. CCD response as a function of wavelength and atmospheric extinction was determined. Finally, the estimated sensitivity function was applied to the science frames for flux calibration.

High-resolution

The high-resolution echellegrams from the HESP and Echelle spectrograph (at VBT) instrument were reduced as per the following methods:

1. **Header correction**: The headers of the data files were inspected to remove the inconsistencies (if present).

2. **Data Pre-processing**: During this step, overscan correction was applied to remove the overscan regions; bias subtraction was carried out to eliminate bias signals; and cosmic ray correction was executed to detect and remove cosmic ray artifacts from the spectral images.

3. **Data extraction**: Prior to the extraction, the order traces in the processed files were inspected and adjusted (if necessary). The spectral data were extracted along the traces of each spectral order.

4. **Wavelength calibration**: The lamp frames were calibrated using the lamp list data. Thereafter, the calibrated lamp files were used to wavelength calibrate the science frames.

2.2.2 NIR data reduction

Low-resolution NIR astronomical spectra were extracted using the semi-automated pipelines described in Ninan et al. (2014) (for TIRSPEC) and Ghosh et al. (2023) (for TANSPEC). However, prior to data extraction, I selected only the high-quality science frames (i.e. those with high S/N) with appropriate calibration data. It must be noted that the dark current is treated during the data observation by subtracting the dark frames observed at the beginning and end of the same night. The reduction methods for the NIR spectroscopic data are discussed below:

1. **Data pre-processing**:
   The science frames were pre-processed to eliminate instrumental noise and improve the S/N of the spectral images, for which I followed these steps:
   - Several frames observed at the same dither were median combined to identify the frame with the lowest instrumental noise.
   - Similarly, the tungsten continuum flats were median combined and divided to generate a normalized flat. Thereafter, the normalized flat was subtracted (i.e. flat-fielding) from all the science frames to account for pixel-to-pixel variations in detector sensitivity.
   - Also, the cosmic rays (from other astronomical sources) detected as artifacts in the spectral images were removed.
2. **Sky Background Subtraction**:
   To remove the sky background, flat-corrected and cosmic-ray-cleaned object frames from both dithered positions were subtracted from each other.
3. **Extraction of 1D Spectra and Wavelength Calibration**:
   The 1D object spectra from each spectral order were extracted and wavelength calibrated using line-identified lamp spectra: Argon for TIRSPEC; while both Argon and Neon for TANSPEC data to cover all the orders.
4. **Averaging Spectra from Dithered Pairs**:
   The final spectrum was obtained by averaging the spectra extracted from each dithered pair, improving the overall S/N of the resulting spectrum.

5. **Telluric Line Correction**:
   Telluric correction involved removing atmospheric absorption lines. The hydrogen absorption lines from the standard star were first removed, and then the science spectra were divided by the corrected telluric standard star spectrum to account for atmospheric effects.

6. **Flux Calibration**:
   The blackbody spectrum of the telluric standard spectra was generated and combined with the Two Micron All Sky Survey (2MASS) apparent photometric magnitudes of the science object to flux calibrate the science spectra.

2.3 Frequency detection

The photometric and spectroscopic time-series datasets were analyzed using the Fourier transformation method. The Fourier transform is a fundamental mathematical operation that converts a signal from its time domain to its frequency domain. It expresses the original function as a sum of sinusoidal components characterized by distinct frequencies, amplitudes, and phases. Mathematically, the Fourier transform $F(\omega)$ of a continuous function $f(t)$ is given by:

$$F(\omega) = \int_{-\infty}^{\infty} f(t)e^{-i\omega t}\, dt \tag{2.1}$$

In my research work, I used PERIOD04 (Lenz & Breger, 2005), a software which Fourier transforms the time-series datasets and generates power v/s frequency spectra.

2.4 Spectroscopic modeling

To understand the stellar atmosphere, I performed the quantitative analysis of the spectroscopic data across optical to IR bands using appropriate modeling techniques. For data modeling, I utilized CMFGEN based on Radiative Transfer (RT) for 1D spectroscopic modeling (Hillier & Miller, 1998; Hillier, 2003, 2012). It adheres to both statistical and radiative equilibrium i.e. non-local thermodynamic equilibrium (NLTE) conditions by solving the RT equations for a spherically expanding atmosphere in the comoving frame. To maintain consistency between the radiation field, atomic level populations, and temperature structure, this modeling code uses a linearization technique. Because the level populations and radiation field are explicitly interdependent, a converged model is produced through an iterative process.

The WR stellar winds are driven by the strong radiation pressure from the stellar core. The hydrostatic core radius (R_c) of the stellar atmosphere is challenging to measure accurately due to the increasing optical depth of WR stars, which are characterized by an optically dense atmosphere that is driven by UV photons. In accordance with stellar evolutionary models, the radius of the star (R_*) is defined at a Rosseland optical depth of 20, and its stellar temperature (T_*) is calculated based on the Stefan-Boltzmann's law. Using the gray approximation, the radius and temperature of the photosphere are determined for WR stars at an optical depth of 2/3.

For modeling a WC-type star with different line widths at different radius, a two-component beta velocity (see Eqn. 2.2) law (Hillier, 2003) has been used across various earlier works (Aadland et al., 2022; Sander et al., 2012; Hillier, 1989).

$$v(r) = \frac{v_{phot} + (v_{\infty,2} - v_{phot})\left(1 - \frac{R_*}{r}\right)^{\beta_1}}{1 + (v_{phot}/v_{core} - 1)\exp\left[(R_* - r)/\Delta R\right]} + \frac{(v_{\infty,2} - v_{\infty,1})\left(1 - \frac{R_*}{r}\right)^{\beta_2}}{1 + (v_{phot}/v_{core} - 1)\exp\left[(R_* - r)/\Delta R\right]} \tag{2.2}$$

where, v_{core} is the velocity at the star's core (considering R_c at $\tau_{ross} > 20$); v_{phot} indicates the wind velocity at the photosphere; v_∞ is the wind terminal velocity, which denotes the maximum velocity of the winds; ΔR is the scale height of the photosphere; while the acceleration exponent (β) defines the expansion rate of the winds. The scale height ΔR is selected to ensure velocity continuity between the inner boundary and the supersonic wind regions. Higher excitation lines display slightly narrower profiles, so I selected a small β_1 (e.g., 0.8 or 1.0; Hillier 1991; Sander et al. 2012) for inner winds. For outer winds, a larger β_2 (e.g., 20 or 50; Hillier 2003) is used, where wind velocity stabilizes due to minimal radiative acceleration. The model atmosphere (see Fig. 2.10) can be divided into several zones based on velocity. These zones vary in volume according to optical depths, which are influenced by the mass-loss rate.

The red-shifted wings, a consequence of the Thomson scattering, usually appear on the red edges of the line profiles (Aadland et al., 2022) due to wind velocities exceeding electron thermal velocities. All emission lines are treated using the Sobolev approximation (Sobolev, 1960) following the Castor et al. (1975) wind model, which simplifies wind modeling by assuming ions interact with photons only when Doppler shifts bring them into resonance, focusing radiative transfer on likely absorption regions.

Clumpiness is confirmed in the stellar winds of WR stars by numerous studies (Owocki et al., 1988; Hillier, 1991; Crowther et al., 2006; Williams et al., 2015). In CMFGEN, I incorporated clumping through a velocity-dependent volume filling

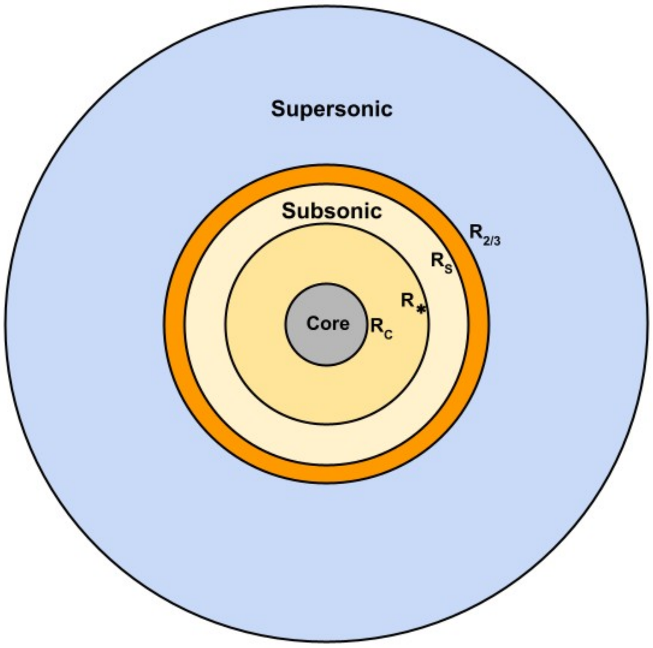

Figure 2.10: Schematic diagram of the model atmosphere showing different velocity zones (not to scale). R_c, R_* R_s, and $R_{2/3}$ indicate the stellar core, stellar radius (at $\tau_{ross} = 20$), sonic point, and photosphere radius, respectively. The colors are used for clarity.

factor (VFF) denoted by f, as described by the following relation:

$$f = f_{\infty} + (1 - f_{\infty})exp\left(\frac{-v(r)}{v_{clump}}\right) \tag{2.3}$$

where v_{clump} regulates the rate at which clumping alters with velocity, and f_{∞} denotes the filling factor at larger radii. I chose clumping parameters to account for variations in clump size at different radii, especially in the outer regions of the wind. CMFGEN models assume the space between clumps is void. Although clumps are small, their impact is observed on electron scattering wings (Hillier, 1991) and emission line subpeaks (Lépine et al., 2000; Lépine & Moffat, 1999; Moffat et al., 1988). However, prior research (Hamann & Koesterke, 1998) has reported that the emission line strengths are unaltered when the rate of mass loss is scaled by $\sqrt{f_{\infty}}$. The acceleration of the wind is also influenced by clumping (Schmutz, 1997), as denser clumps can impede the wind's acceleration, resulting in a decrease in terminal velocity.

In WC stars, emission lines and the continuum arise from multiple mechanisms that CMFGEN addresses simultaneously, including excitation from thermal collisions (e.g., C III λ1909, C IV λ1549); radiative recombinations (e.g., He II λ5411, C IV λ5471); effects of fluorescence on the spectral continuum (such as, C IV $\lambda\lambda$5802–12); and transitions at low temperature (Hillier, 1989) through dielectronic recombinations (such as C III $\lambda\lambda$2297, 4649, 5696, 6741, 9710).

To ensure that the stellar winds are sufficiently driven by radiation, the atomic data containing the line and continuum opacities of a variety of ionization states of several elements is chosen. For the dominant elements, He, C, O, and Fe, which undergo complex atomic transitions in the winds, the super-level approach (Gräfener et al., 2002) is taken into consideration in order to account for the wind blanketing effect. Table. 2.4 specifies the atomic data source for the photoionization cross-sections, energy levels, oscillator strengths, dielectronic recombinations, collision strengths, and autoionization reactions.

2.5 Machine learning methods

ML is a class of the Artificial Intelligence. ML methods utilize certain mathematical algorithms to perform different types of tasks on large datasets.

2.5.1 ML Types

There are 4 types of ML algorithms, as discussed below in brief:

Table 2.4: Source of model atomic data. Taken from Kar et al. (2024b).

Type	Database
Photoionization cross-section	NORAD (Nahar, 1998, 2010) OPACITY Project(Seaton, 1987) Davey et al. (2000) Kurucz (2009, 2010) PJ Storey (2012) Iron Project data (Hummer et al., 1993) Luo & Pradhan (1989)
Energy levels	Kurucz (2009, 2010) NIST(Kramida et al., 2022)
Oscillator strengths	Leibowitz (1972) OPACITY Project (Seaton, 1987) Luo & Pradhan (1989) Kurucz (2009, 2010)
Dielectronic data	Nussbaumer & Storey (1983)
Collision strengths	Cochrane & McWhirter (1983) Mendoza (1983) Zhang et al. (1994) Zhang & Pradhan (1997) Chen & Pradhan (1999) Tayal (2008)
Autoionization data	Safronova et al. (1998)

- **Supervised Learning**: In supervised learning, the model is trained on labeled data, learning the relationship between input and output to make predictions on unseen data. There are two main types of Supervised Learning algorithms:

  1. **Classification**: Data is categorized into predefined classes or labels on which the models are trained. The trained models are applied on the unseen data with same features as training data to predict the possible outcomes.
  2. **Regression**: Continuous outcomes are predicted based on input features to identify their relationship with the data.
  3. **Other types**: Various other supervised learning algorithms are used for regression or classification. K-Nearest Neighbor (KNN) identifies the k nearest training examples and predicts the class or value based on their majority or average. *Linear models* describe the relationship between input features and the output variable using a linear equation. *Naive Bayes* is a probabilistic classifier that employs Bayes' theorem and assumes independence among features. Support Vector Machine

(SVM) constructs a hyperplane to separate n-dimensional space into classes, with the closest points, called support vectors, determining the boundary. *Decision Tree* splits the data into subsets based on feature values to make decisions at each node forming a tree-like structure. *Ensemble* model is a combination of multiple decision trees to improve performance and reduce the risk of overfitting.

- **Unsupervised Learning**: ML algorithm that works with unlabeled data, identifying patterns or structures within it is termed as Unsupervised learning.
    1. **Clustering**: Data points without predefined labels are grouped if they depict similar characteristics to identify the relationships in the data.
    2. **Dimensionality Reduction**: Reduces the number of features while preserving important information.
- **Semi-Supervised Learning**: This approach combines labeled and unlabeled data, enhancing learning efficiency when labeling data is costly or time-consuming. The model leverages both labeled and unlabeled data to identify relationships with enhanced accuracy. It can be trained in two ways: by iteratively labeling unlabeled data or by training two models on different data views that teach each other.
- **Reinforcement Learning**: This involves training an agent to optimize decision-making through rewards and penalties. Models can be defined in two ways: a) the agent learns directly from interactions without modeling the environment, or b) the agent creates and uses a model of the environment to plan future actions.

2.5.2 ML model

Based on the dataset and type of task to be undertaken, one can choose among different types of algorithms. In my thesis (see Chapter 5), I developed a robust classifier model for identifying WR stars in the MW using their intrinsic properties, such as photometric colors. Given the large astronomical datasets with known labels, supervised learning algorithms were the optimal choice for the ML model. In the next subsections, I discuss the algorithms and basic model architecture used for my research work.

Model architecture

The basic architecture of the ML model for classification purposes consists of the following steps (also depicted in Fig. 2.11):

- **Data Acquisition**: The raw data on which the model would be applied is acquired.
- **Pre-Processing**: Selecting high-quality data and eliminating outliers and redundancies before model development is essential for improving prediction accuracy.
- **Feature Engineering**: From the processed data, the model features are extracted. If required, new features are generated to improve model performance.
- **Data splitting**: The dataset, containing extracted features, is divided into two parts: the majority for training the model and the remainder for testing its validity.
- **Model Training**: The ML model is trained on the training dataset with or without labels to determine patterns and relationships among the data.
- **Model Evaluation**: The trained model is applied to the validation datasets and the performance of the model is judged from the wrong predictions.
- **Optimization**: The model parameters are tuned to optimize the model's accuracy.

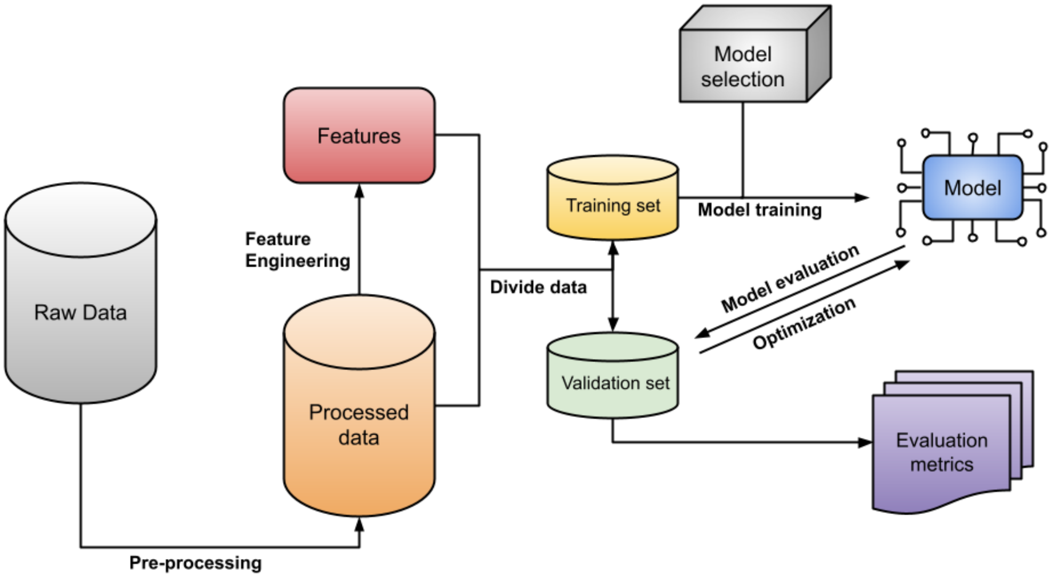

Figure 2.11: Workflow used for developing the classifier models.

Model types

I chose the ensemble-based algorithms as it is known to be highly efficient for classification problems. Ensemble algorithms merge diverse decision tree models to create a more accurate and robust model. A brief overview of the ensemble methods I've utilized in my research is provided below:

- **Bootstrap aggregation**: Also known as bagging (Breiman, 2001), in this method several *decision trees* are trained in parallel (see Fig. 2.12 (a)) using a subset of features on a random subset (using bootstrap sampling) of data. Thereafter, the models are aggregated (averaging or majority voting) to find the final model (for regression or classification respectively) which predicts the most accurate results among them. Random Forest (RF) (Breiman, 2001)) is one of such algorithms which uses this ensemble method.
- **Boosting**: In this technique, several weak models are trained sequentially by increasing the weights of the misclassified instances from the previous model and passing them on to the next model so the prediction errors are minimized (see Fig. 2.12 (b)). The final model is more robust and predicts with better accuracy than all the other weaker models. Boosting methods such as Gradient Boosting (GB) (Friedman, 2001)) work on the same principle except that it optimizes a specified loss function (e.g., mean squared error for regression or log loss for classification) rather than varying the weights of the instances (e.g. AdaBoost).

In addition, I utilized some important data handling algorithms to treat the imbalance in the sizes of different classes of objects present in the training dataset on which the model was trained. Here I used two such methods as mentioned below:

- **Random Oversampling**: This method is used to resample the randomly chosen data from the minority class of the dataset such that there are equal instances of the minority and majority class instances.
- **Stratified K-fold cross-validation**: The datasets are randomly divided into K-number of subsets in a manner such that the proportion of the minority and majority classes remains the same in each of the subsets.

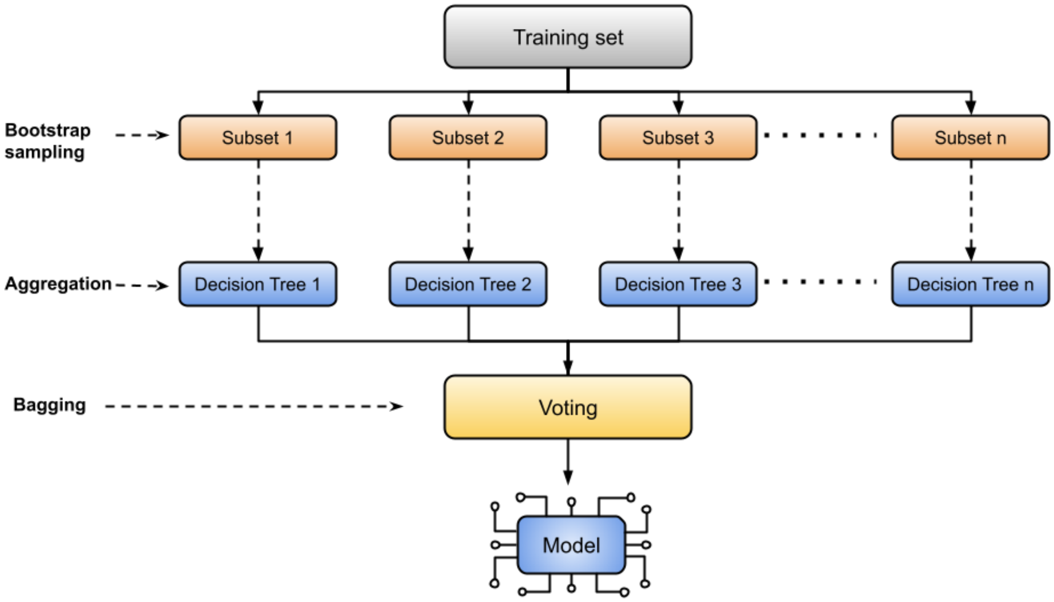

(a) Bootstrap aggregation method: Randomly divided subsets of data are trained on different trees to find the best model.

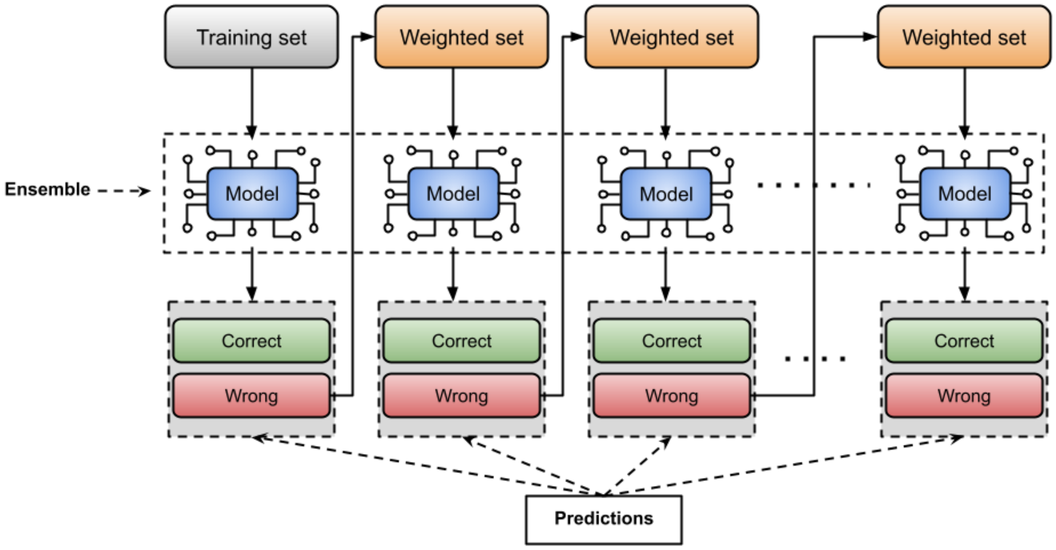

(b) Boosting method: The weights of the wrong predictions are used to improve the model.

Figure 2.12: Schematic diagram of the Ensemble algorithms which I used in my research work.

Chapter 3

Atmospheric characterization of a highly extinguished WC9-type star

In this chapter, I address the analysis of the stellar winds and circumstellar environment of a WC9-type discovered by Kanarek et al. (2015) in the inner Galactic region. This research work was published in Kar et al. (2024b).

3.1 Introduction

WC9-type stars, the coolest among the WCL subtypes, exhibit spectra dominated by C III lines with stronger strengths than the C IV; broader C II lines, and lacking O V lines. As stated by Sander et al. (2019a), these stars have similar luminosities ($10^{4.7-5.5} L_\odot$) to the WCE subtypes. However, they differ in that they have lower stellar temperatures ($4 \times 10^4 - 5 \times 10^4$ K) and lower wind terminal velocities (roughly $1300\,\mathrm{kms}^{-1}$). The evolutionary pathways of single WC9-type stars remain poorly understood, with current hypotheses favoring a binary evolutionary origin. This scenario predicts (Crowther, 2007) typical WC-object masses of 9–16 $M_\odot$.

In CWB systems, the WC9-type stars produce carbon dust due to the compression of wind at the shock interface that creates cold, dense regions conducive to dust formation (Usov, 1991). These dusty WC9 binaries can be either persistent or episodic sources of dust. A study by Williams (2019) revealed that most dusty WC9 systems are persistent, displaying short-term (1–2 days) large amplitude, non-periodic variability in their spectral line profiles. Such variations likely result from non-adiabatic and unstable shock-cone structures formed through wind-wind interactions in the binary system (Desforges et al., 2017).

A search investigation of WR stars using J and K_s and four IR-narrowband filters (He II 2.192 μm, Br-γ 2.169, C IV 2.081, and He I 2.062) by Shara et al. (2009) was conducted within the Galactic region defined by $-1° < b < +1°$ and $-90° < l < +60°$. Subsequently, Kanarek et al. (2015) applied image subtraction techniques to identify potential WR stars in the same region and confirmed their spectral types through spectroscopic follow-up. One such candidate, [KSF2015] 1381-19L, was first identified by them during their observations targeting the same Galactic disc as by Shara et al. (2012, 2009). This object is situated in the inner Galactic region at RA = 18h12m02.42s and Dec = $-18°06'55.28"$, corresponding to Galactic coordinates $l = 12.392°$ and $b = 0.167°$. The star was classified as WC9-type by Kanarek et al. (2015) using the emission-line ratio C IV 2.07–2.084 μm/C III 2.112–2.137 μm. The object has since been cataloged as WR 111-9 in the WR star database, based on GAIA DR2 data (Rosslowe & Crowther, 2015), as reported by Rate & Crowther (2020).

We found that the [KSF2015] 1381-19L is situated in the inner Galactic region ($6 < R_G < 9$ kpc; Rosslowe & Crowther 2015). In this study, we focused on its atmospheric stratification, a key factor influencing the chemo-dynamic evolution of its surroundings. The physical properties of this star were compared with those of other WC9-type stars in the supersolar metallicity region ($R_G < 6$ kpc) of the Galaxy, highlighting notable differences. The analysis also explored potential signatures of circumstellar dust and examined its evolutionary pathway from an O-type MS progenitor utilizing both single-star and binary evolution models.

In addition, we investigated the physical and chemical characteristics of the star's atmosphere and its environment through spectroscopic observations. Details of the optical and IR observations are presented in Sec. 3.2, followed by a description of the data analysis in Sec. 3.3. The spectroscopic modeling is outlined in Sec. 3.3.1, and the star's evolutionary phases are discussed in Sec. 3.5.2. The study concludes with key findings summarized in Sec. 3.6.

3.2 Data observation

We obtained the spectroscopic data of the object in optical (using HFOSC) and NIR (using TIRSPEC) mounted at the HCT (see Sec. 2.1.1). The observation log is shown in Table 3.1.

3.2.1 Spectroscopic observation in optical

We obtained low-resolution optical spectra (R∼1400 and 2200) using the HFOSC instrument (details in Sec. 2.1.1) with Grism-7 (3800–7000 Å, referred to as the

Table 3.1: Observation log for [KSF2015] 1381−19L

Observation Date	UT (h:m:s)	Instrument	$\lambda/\delta\lambda$	λ	Exposure Time
2020 June 8	18:57:33	HFOSC (Grism-7)	1400	3800−7000 Å	1 frame×1500s
...	19:23:58	HFOSC (Grism-8)	2200	5200−9000 Å	1 frame×1500s
2022 June 25	18:30:49	TIRSPEC (HK_s)	1200	1.50−1.84 μm 1.98-2.45 μm	5 frames×500s
...					

blue spectrum) and Grism-8 (5200–9000 Å, referred to as the red spectrum). To calibrate wavelengths, we observed FeAr and FeNe lamp spectra immediately after capturing each object spectrum. On the same night, we observed the spectrophotometric standard star Feige 66 (Massey & Gronwall, 1990) through both Grisms. Table 3.1 provides a summary of the observations.

We used a standard pipeline based on the IRAF software package (Tody, 1993) to process the optical spectra. As part of our reduction workflow, we eliminated cosmic rays and subtracted the master bias frame from every science frame. In IRAF, we employed the *apall* task to extract the 1D spectra from the 2-dimensional (2D) images. The wavelengths were calibrated using the calibration lamps' dispersion-corrected spectra, and the atmospheric extinction and detector sensitivity functions obtained from the standard star data were used to calibrate the flux.

3.2.2 NIR spectra observation

Using the TIRSPEC instrument mounted on the HCT, we obtained medium-resolution ($R \sim 1200$) NIR spectra in the H (1.5–1.84 μm) and K_s (1.98–2.45 μm) bands (Ninan et al., 2014). The cross-dispersed configuration allowed simultaneous coverage of both wavebands. Using an ABBA slit-nodding pattern, we performed slit-spectroscopic observations at two dithered positions.

Each frame was exposed for 500 seconds, resulting in an S/N of approximately 40. We acquired five consecutive frames of the object at each dither position. To ensure accurate calibration, we recorded Argon lamp spectra and Tungsten continuum flats immediately after each dataset. We employed the same slit across all spectral orders to observe the nearby, relatively bright telluric standard star HD 172792 (H-mag = 8.77, spectral type A0V) for telluric correction. Additionally, we captured dark frames before and after the observations on the same night. Table 3.1 summarizes the observation details.

We processed the data using the semi-automated TIRSPEC pipeline (Ninan et al., 2014). To enhance the S/N and eliminate cosmic rays, we median combined the object frames. We corrected these frames by dividing them by normalized median-combined continuum flats for each dither position. To remove the sky background, we subtracted flat- and cosmic-ray-corrected object frames from their counterparts in A-B and B-A formats. We then extracted the 1D spectral data and calibrated the wavelengths using the corresponding Argon lamp spectra.

Finally, we averaged the extracted and wavelength-calibrated spectra from each dithered pair to produce the final spectra. We performed telluric corrections and used the 2MASS photometric magnitudes (Table 4.1) of the H and K_s bands for flux calibration for the target object.

3.2.3 Photometric data

Additionally, the Vizier data catalog [1], an online repository of various astronomical databases, provided us with optical and IR integrated flux density data as well as the apparent photometric magnitudes.

Catalog catalog I/297, which contains the Naval Observatory Merged Astrometric Dataset (Zacharias et al., 2004), provided the optical B- and V-band data used in the analysis. The G-band data was sourced from GAIA DR3 (Gaia Collaboration et al., 2023), which is hosted in catalog I/355/gaiadr3 (Gaia Collaboration, 2022).

The 2MASS database (Skrutskie et al., 2006) is accessible through catalog II/246 (Cutri et al., 2003), from which we obtained the NIR photometric data. Catalog II/328/allwise (Cutri et al., 2021), which contains Wide-field Infrared Survey Explorer (WISE) data (Wright et al., 2010), and catalog II/293/glimpse (Spitzer Science, 2009), which contains Spitzer-IRAC band data from the GLIMPSE-I survey (GLIMPSE Team, 2020) were the sources of MIR data. Table 3.2 lists the integrated flux density values measured in each photometric band, from optical to MIR, along with the corresponding databases.

3.3 Analysis of Data

For every emission line in the spectra, spectral parameters like EW and FWHM were calculated in order to categorize and describe the object's spectroscopic nature. Prior to determining the FWHM and EW, each band's spectral continuum was established. Using the Levenberg-Marquardt (LM) algorithm (Levenberg, 1944; Marquardt, 1963), the traditional polynomial fitting procedure was used to identify the continuum by choosing regions devoid of spectral features. The flux-calibrated spectrum was then divided by the best-fitted continuum. This

---

[1] `https://vizier.cds.unistra.fr/`

Table 3.2: Integrated flux density of [KSF2015] 1381-19L. See Sec. 3.2.3.

Band	Apparent Magnitude (mag)	λ_c (nm)	Flux density (Jy)	Database
V	13.86	554	$2.45e^{-3}$	Zacharias et al. (2004)
G	13.60	673	$1.06e^{-2}$	Gaia Collaboration (2022)
J	9.66	1240	$2.15e^{-1}$	Cutri et al. (2003)
H	8.62	1650	$3.74e^{-1}$	"
K_s	7.80	2160	$5.14e^{-1}$	"
$W1$	7.34	3350	$3.55e^{-1}$	Cutri et al. (2021)
$IRAC-3.6$	7.17	3550	$3.8e^{-1}$	Spitzer Science (2009)
$W2$	6.62	4600	$3.83e^{-1}$	Cutri et al. (2021)
$IRAC-5.8$	6.34	5730	$3.32e^{-1}$	Spitzer Science (2009)
$IRAC-8.0$	6.01	7870	$2.53e^{-1}$	"
$W3$	5.90	11600	$1.26e^{-1}$	Cutri et al. (2021)
$W4$	4.89	22100	$9.2e^{-2}$	"

method was similarly applied to normalize spectra in the NIR bands, where excess emissions from free-free processes or circumstellar dust are often present.

Astronomical Python libraries, such as the *astropy* modules (Astropy Collaboration et al., 2013, 2018, 2022) (e.g., *models, units, io*) and *specutils* modules (e.g., *spectra, fitting, analysis, SpectralRegion, manipulation*), were used to estimate the EW and FWHM of the emission lines. The *extract_region* task of the *manipulation* module was used to extract spectral regions that contained emission lines, and the *fit_lines* task of the *fitting* module was used to fit the line profiles with 1D Gaussian functions. LM chi-square minimization was used to identify the best-fit line profiles, and from the fitted model the EW of each spectral line was calculated.

After selecting the continuum from a featureless spectral region, the normalized mean fluxes for the spectral line ($\overline{F_{\rm line}}$) and continuum ($\overline{F_{\rm cont}}$) were computed. The chosen pseudo-continuum region was used to calculate the spectra's S/N. Errors in the EW measurements were estimated using the method described in Sec. 3.2 of Vollmann & Eversberg (2006).

To correct the measured FWHM values for the spectrograph's broadening effects, the spectral resolution of the corresponding dispersing elements was applied following the procedure outlined in Sec. 3.1 of Zhekov et al. (2014). This correction was performed for both optical and NIR wavebands. In Tables 3.3 and 3.4, the parameter values for every identified emission line are given.

Optical spectra

Due to the target object's faintness (B-mag ∼16), only a few emission lines with low S/N were detected in the bluer region of the spectrum (3800–5000 Å). Within the 4000–5000 Å range, the spectrum revealed the presence of C III λ4651 and He II λ4686 emission lines, as shown in Figure 3.1(a). However, other diagnostic emission lines such as He II λ4339, He I λ4472, C II λ4267, C IV λ4441, C III λ4326, C III λ4517, and O II λ4416 (van der Hucht, 2001) were not detected in this region.

In contrast, the red spectrum (5200–9000 Å) exhibited more prominent emission lines with higher S/N. It was found to have broad and strong emission line features, mainly from lower ionization states of helium and carbon, which are typical of a WC9-type star. The inner layers of the expanding atmosphere produced prominent optical emission lines, such as He II λ5411; C IV $\lambda\lambda$5802–12, λ7063–68; C III λ5696, $\lambda\lambda$6727–6773, λ7487, λ8348, λ8500, λ8664; and O III λ5592. Moreover, emission lines from less ionized atmospheric regions were identified, including C II λ6578, λ7231 and He I λ5876, λ6681 (Hillier, 1989). These lines offer important information about the dynamics and structures of the expanding atmosphere's outer layers. There was a noticeable blend between the adjacent He I λ6768 line and the C III $\lambda\lambda$6727–6773 line.

The technique described in Sec. 3.3 was used to estimate the spectral parameters for each emission line. To conduct the analysis, pseudo-continuum regions were chosen at 4700–4850 Å for the blue spectrum and 5920–6120 Å for the red spectrum, as these regions are devoid of significant spectral features. The blue spectrum's S/N was roughly 20 and the red spectrum's was about 28 based on the S/N calculated from these pseudo-continuum regions.

The spectral parameters and statistical errors related to the EW of each observed emission line in the optical spectra are shown in Table 3.3. We also present the atomic transitions that correspond to the emission lines.

NIR spectrum

In contrast to the optical and UV radiative zones, the NIR spectral region of WR stars contains critical emission lines that are the result of higher-level atomic transitions. These transitions occur at larger stellar radii (Rosslowe, 2016). As a result, the profiles and strengths of these lines offer valuable insights into the impact of clumping on mass-loss rates and the geometry of the outer wind.

From the observed spectra, prominent emission lines were identified, including C IV 1.736 μm, He II 1.572 μm, and He I 1.701 μm in the H-band. In the K_s-band, detected lines include the C IV 2.070–2.084 μm triplet, C III 2.325 μm, He II 2.189 μm,

Table 3.3: The EW and FWHM of the optical emission lines.

λ (Å)	Ion	FWHM (Å)	EW (Å)	Atomic transition
4651	C III	19.70	109± 15	$3p\ ^3P^o_0 - 3s\ ^3S^e_1$
4686	He II	17.99	36± 6	$4 - 3$
5696	C III	33.66	454±22	$3d\ ^1D^e_2 - 3p\ ^1P^o_1$
5802/12	C IV	29.08	124±7	$3p\ ^2P^o_{3/2} - 3s\ ^2S^e_{1/2}$
5876	He I	24.82	78±5	$3d\ ^3D^e - 2p\ ^3P^o$
6578	C II	45.26	192±10	$3p\ ^2P^o_{3/2} - 3s\ ^2S^e_{1/2}$
6681	He I	38.48	43±4	$3d\ ^1D^e - 2p\ ^1P^o$
6727-73	C III	31.08	125±10	$3p\ ^3D^e - 3s\ ^3P^o$
7063/68	C IV	30.32	73±5	$9z\ ^2Z - 7z\ ^2Z$
7231	C II	42.55	267±13	$3d\ ^2D^e_{3/2} - 3p\ ^2P^o_{1/2}$
7487	C III	66.13	32±6	$5d\ ^3D^e - 6f\ ^3F^o$
7727	C IV	38.35	31±4	$11z\ ^2Z - 8d\ ^2D^e$
8197	C III	29.41	56±5	$6h\ ^3H^o - 5g\ ^3G^e$
8348	C III	59.07	125±12	$3d\ ^3F^o_3 - 4d\ ^3D^e_2$
8500	C III	39.49	70±5	$3p\ ^1P^o_1 - 3s\ ^1S^e_0$
8664	C III	37.80	54±5	$6w\ ^2W - 6z\ ^2Z$

He II 2.165 μm, C III+He I 2.112–2.137 μm, and He I 2.059 μm. Spectral characterization was conducted by calculating the EW and FWHM of these emission lines.

With the lack of notable spectral features, pseudo-continuum regions were selected for this analysis for the H-band (1.520–1.543 μm) and the K_s-band (2.212–2.232 μm). The S/N, calculated from these regions, was approximately 35. In the H- and K_s-bands, Table 3.4 summarizes the spectral parameters and their statistical errors for each emission line. In addition, the table includes the measured line strengths of [KSF2015] 1381-19L in the K_s-band, as reported by Kanarek et al. (2015).

3.3.1 Modeling spectroscopic data

Quantitative analysis of the observed optical and NIR spectra was conducted using CMFGEN, as detailed in Sec. 2.4, to investigate the nature of the stellar atmosphere. The fitting of spectral line profiles involved several interdependent physical parameters, including luminosity, temperature, mass-loss rate, and surface chemical composition. The best-fitting spectroscopic model is illustrated in Fig. 3.1.

Both the EWs of emission lines from different ionization states of the same atomic species and the wind ionization structure were found to be affected by the stellar luminosity. The mass-loss rate, in turn, impacted the density-dependent (ρ) recombination lines. Heating of the stellar winds occurred due to photoionization

Table 3.4: The EW and FWHM of the NIR emission lines observed in H and K_s) bands.

NIR band	Wavelength (μm)	Atomic species	FWHM (Å)	EW (Å)	FWHM (Å)	EW (Å)	Transition
H	1.572	He II	41	15±3	-	-	13-7
	1.701	He I	71.74	49±7	-	-	$4d\ ^3D^e - 3p\ ^3P^o$
	1.736	C IV	62.25	48±6	-	-	$9z2Z - 8z2Z$
K_s	2.059	He I	85.36	99±12	63.3	88.10	$2p\ ^1P^o - 2s\ ^1S^e$
	2.078	C IV	169.32	181±14	193.5	170.15	$3d\ ^2D^e_{5/2} - 3p\ ^2P^o_{3/2}$
	2.117	C III	103.09	110±11	224.5	123.28	$8h\ ^3H^o - 7i\ ^3I^e$
	2.165	He II	100.30	44±8	117.9	40.83	$14 - 8$
	2.189	He II	111.20	32±8	160.5	43.35	$10 - 7$
	2.217	He II	-	-	156.4	61.83	$22 - 9$
	2.325	C III	76.38	20±5	-	-	$5p\ ^3P^o - 5s\ ^3Se$

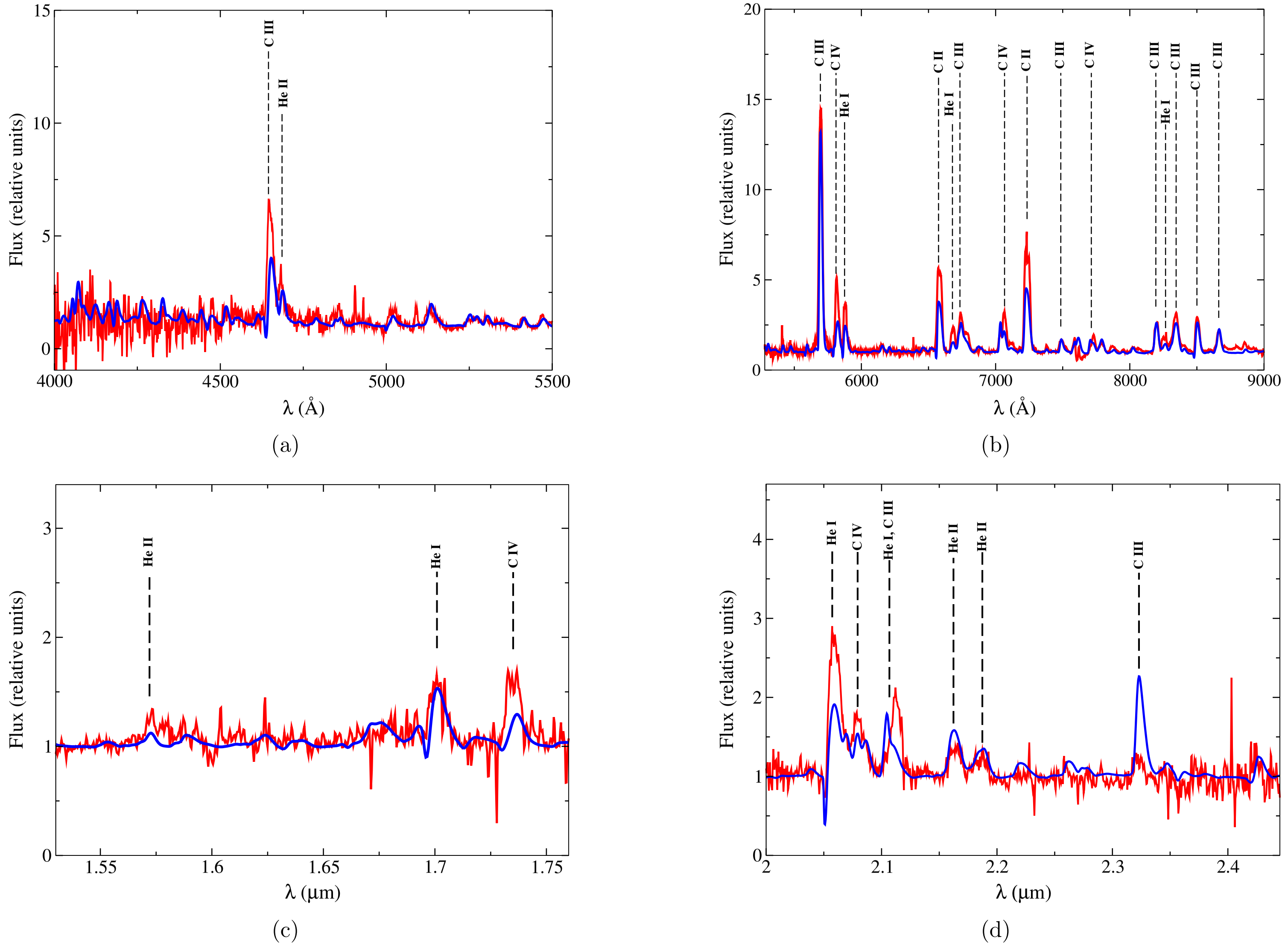

Figure 3.1: Observed (in red) and model generated spectra (in blue): Optical-(a) Gr7, (b) Gr8; NIR-(c) H-band (d) K_s-band are shown.

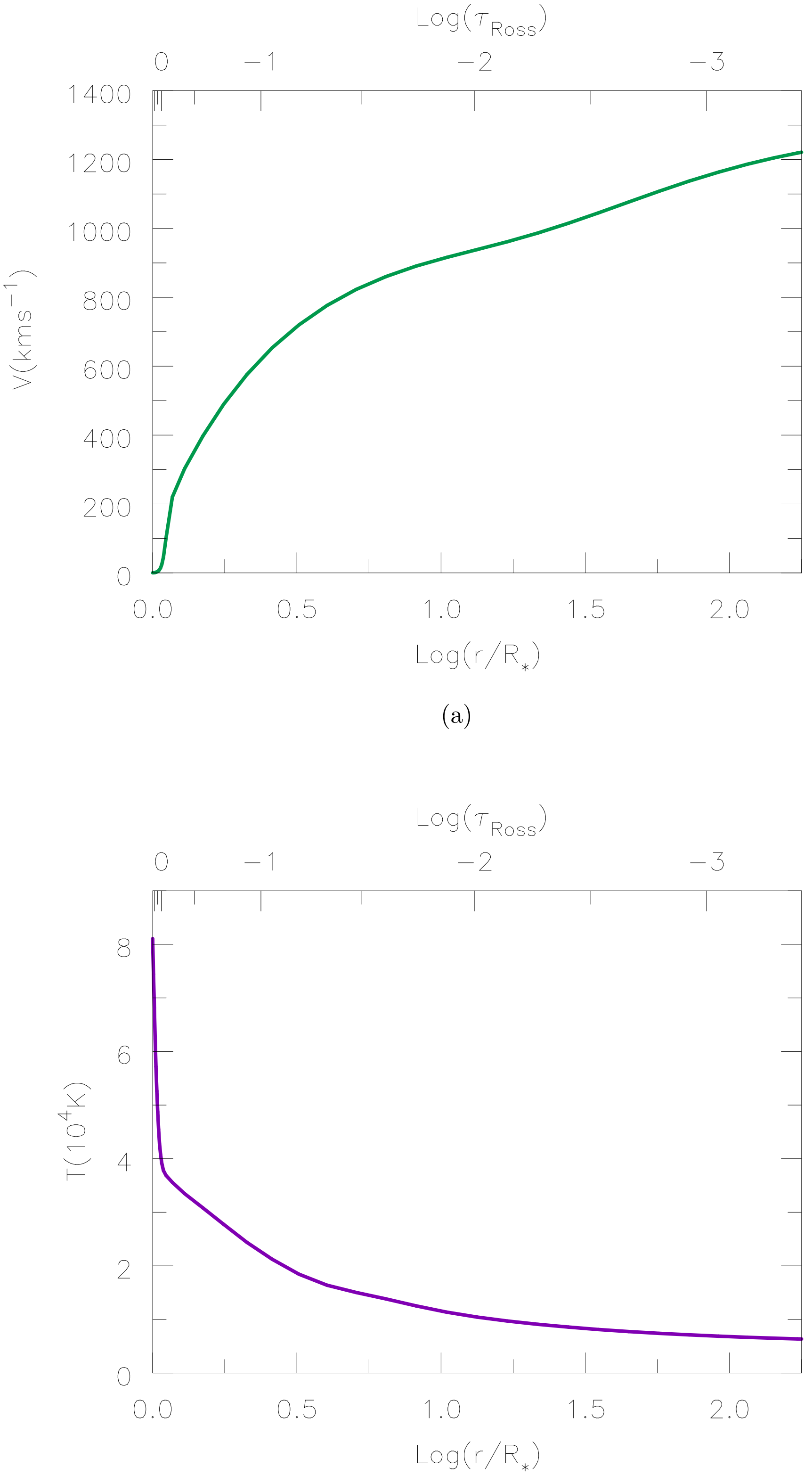

(a)

(b)

Figure 3.2: (a) The velocity of stellar winds and (b) temperature variation of the model atmosphere is shown (for discussion refer Sec. 3.4.1)

.

processes. Figure 3.2(b) illustrates how radiative recombination cooling caused the temperature to drop quickly in the inner wind, while free-free and thermal collisional cooling processes caused the temperature to drop nearly exponentially as electron density decreased in the outer wind (Hillier, 1989). The line widths of lower ionization states revealed information about terminal velocity and wind turbulence, while the line strengths of higher ionization emission lines allowed for insights into stellar temperature.

Table 3.5: Atomic models used for the analyses.

Atomic species	No. of Full levels	No. of Superlevels
He II	30	22
He I	69	45
C IV	64	59
C III	141	81
C II	338	104
O IV	60	41
O III	80	44
O II	102	46
Ne IV	52	17
Ne III	102	31
Ne II	96	22
Si IV	33	22
Si III	45	25
S VI	20	18
S V	31	29
S IV	77	36
S III	41	25
Ar V	50	25
Ar IV	107	31
Ar III	150	25
Ca VI	30	16
Ca V	35	21
Ca IV	40	12
Ca III	50	20
Ca II	60	53
Fe VI	80	10
Fe V	182	19
Fe IV	280	21
Fe III	607	65

All major atomic transitions, including low- and high-temperature dielectronic recombinations from doubly excited autoionized states, were included in the modeling of the spectral lines in WR stars, which are frequently blends of several adjacent lines from different elements (Hillier, 2011). Various atomic datasets were compared to determine the optimal set of atomic levels that reproduced the spectroscopic features most accurately. The atomic model adopted, similar to Rosslowe (2016), included species such as Fe III-VI, Ca II-VI, Ar III-V, S III-VI, Si III-IV, Ne II-IV, O II-IV, C II-IV and He I-II. The optimal model was composed of 3052 full levels and 985 super levels that underwent approximately 45,000 NLTE transitions. Table 3.5 provides the adopted atomic levels for each ionization state.

Helium remained doubly ionized (He^{+2}) until $N_e > 10^{11}\,\mathrm{cm}^{-3}$, as evidenced by the stratified wind structure (Fig. 3.3(a)). Conversely, neutral helium (He^0) increased outward (beyond $100\,R_*$), resulting in stronger IR line strengths. The confined formation zone of C^{+3} ions was the cause of the weakness in C IV transitions (Fig. 3.3(b)). A significant enhancement in C^{+2} population occurred at $N_e \sim 3\times10^{11}\,\mathrm{cm}^{-3}$ due to recombinations from C^{+3}, with C^{+2} dominating in the outer wind ($N_e > 10^{9}\,\mathrm{cm}^{-3}$), producing broad C III emission lines. Similarly, O^{+2} ions were the dominant species within the range of $\tau_{\mathrm{ross}} = 0.1 - 0.01$ as a result of recombinations from O^{+3}. However, at lower optical depths ($\tau_{\mathrm{ross}} > 0.01$), O^{+2} transitioned to O^{+1}.

The overall ionization structure of the atmosphere (Fig. 3.3) revealed equilibrium zones between consecutive ionization states for each element. At these zones, both ions contributed equally to electron opacity. Neon, Silicon, and Iron were the most highly ionized states, and their line opacity was the primary source of the inner wind (Fig. 3.3(d)-(f)). Peaks in higher ionization states and troughs in lower ionization states near the optical photosphere boundary ($\tau_{\mathrm{ross}} = 0.66$) indicated rapid population changes due to UV radiation pressure associated with Fe-opacity.

The model reproduced approximately 90% of the emission line strengths observed in the spectra (Fig. 3.1). Deviations in line strengths were attributed to limited opacity data or the size of the atomic model, consistent with suggestions by Rosslowe (2016); Aadland et al. (2022). The physical and chemical characteristics of the stellar model atmosphere that best fits the data are summarized in Table 3.6.

3.4 Key results

In the following subsections, the important results are summarized.

3.4.1 Physical characteristics

The physical parameters were constrained by comparing models based on the line strength ratios: He I/He II, C III/C IV, and C II/C III. Diagnostic optical emission lines include He II λ5411, C II λ6574, λ7231, C III λ5696, C IV λ5471, $\lambda\lambda$5802-12, while in the NIR emission like He II 2.189 μm, He II 2.165 μm, He I 2.058 μm, C III+He,I 2.112–2.137 μm, and C IV 2.070–2.084 μm, were utilized for parameter

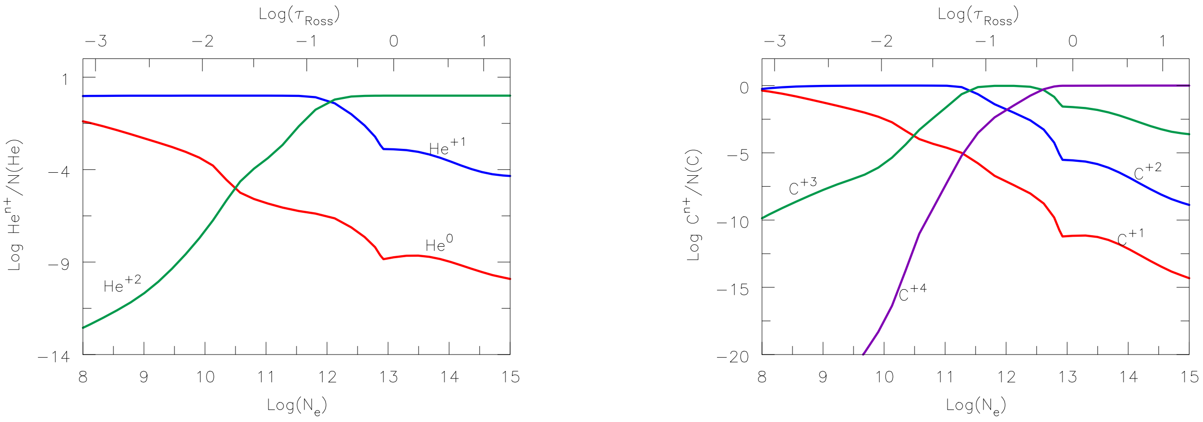

(a) Helium (b) Carbon

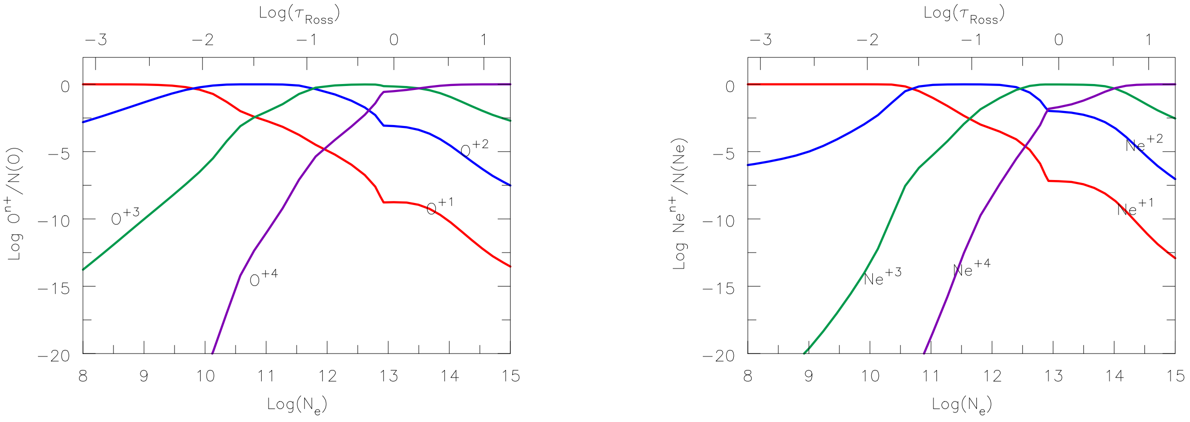

(c) Oxygen (d) Neon

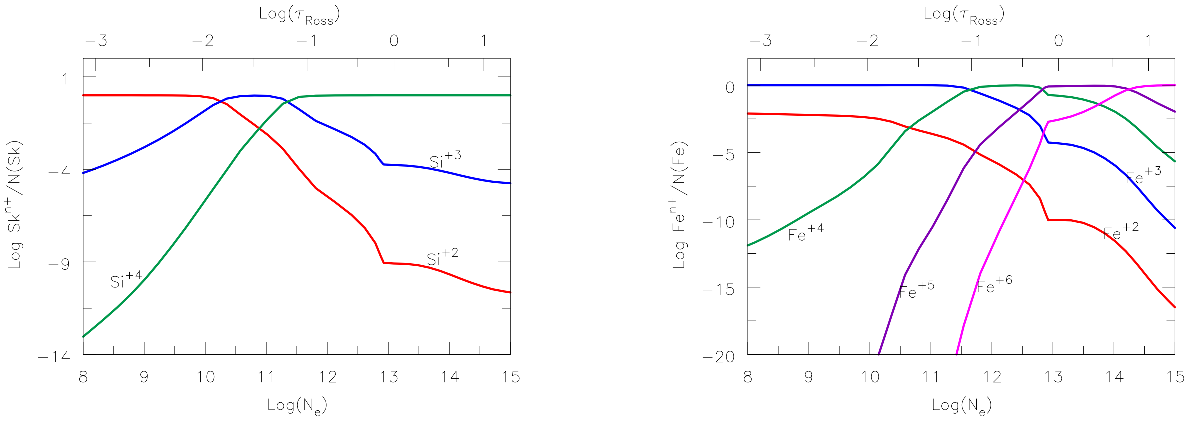

(e) Silicon (f) Iron

Figure 3.3: The stratification of wind ionization within the stellar atmosphere is shown for the selected atomic species, excluding those with the lowest abundances. (Sec.3.3.1).

estimation. The line C III 2.325 μm was excluded due to limitations in the atomic data within the CMFGEN models (Rosslowe, 2016).

The stellar luminosity ($L_* = 10^{5.89}\,L_\odot$) was determined from both the continuum and the relative strengths of key optical emission lines: He I λ5876, λ6574, C IV $\lambda\lambda$5802-12, C III λ5696, and C II λ6574, λ7231. Variations in the line strength ratios of C II λ7231/C III λ5696 were used to calculate the luminosity uncertainties. The upper limit was estimated to be $L_* = 10^{6.05}\,L_\odot$ (+0.16 dex), and the lower limit to be $L_* = 10^{5.75}\,L_\odot$ (-0.14 dex). Using the ratio of C III/C IV (Hillier, 1989), the inner core radius of the atmosphere was calculated using the ionization structure of the stellar wind (see Figure 3.3). Because the C II/C III

Table 3.6: Best fitted model parameters of [KSF2015] 1381-19L.

Parameters	Values
$\log L_*(L_\odot)$	$5.89^{+0.16}_{-0.14}$
T_* (K)	44330
$R_*(R_\odot)$	15.09^{+2}_{-2}
$T_{2/3}$ (K)	40630
$R_{2/3}(R_\odot)$	17.96
$\log \dot{M}(M_\odot \mathrm{yr}^{-1})$	$-4.408^{+0.042}_{-0.046}$
f	0.1
$\log \dot{M}/\sqrt{f}(M_\odot/yr)$	-3.908
$v_{core}(\mathrm{kms}^{-1})$	0.4
$v_{phot}(\mathrm{kms}^{-1})$	100
$v_{dop}(\mathrm{kms}^{-1})$	50
$v_{\infty,1}(\mathrm{kms}^{-1})$	1000
$v_{\infty,2}(\mathrm{kms}^{-1})$	1300
β_1	1
β_2	50
η	2.981
M ($M_\odot$)	24

Chemical elements	Fractional abundance	Relative abundance
Hydrogen	0.00	0.00
Helium	0.542	1.00
Carbon	$0.406^{+0.111}_{-0.379}$	$0.25^{+0.15}_{-0.24}$
Nitrogen	0.00	0.00
Oxygen	0.043	0.02
Neon	$6.02e^{-3}$	$2.2e^{-3}$
Silicon	$8.62e^{-4}$	$2.26e^{-4}$
Sulphur	$3.82e^{-4}$	$8.75e^{-5}$
Argon	$1.04e^{-4}$	$1.92e^{-5}$
Calcium	$6.15e^{-5}$	$1.12e^{-5}$
Iron	$1.66e^{-3}$	$2.18e^{-4}$

line ratio is more sensitive to temperature changes, it was used to infer the outer photospheric radius (Williams et al., 2015). Based on the estimated stellar radii (provided in Table 3.6), the optical photosphere was found to be close to the stellar core ($R_{\tau=2/3}/R_* \simeq 1.2$). The line ratios C II λ7231/C III λ5696 and He I 2.059/He II 2.189 were employed to evaluate the uncertainties in the radius, which demonstrated a high degree of sensitivity to variation in the stellar radius.

Due to their impact on wind density and ionization structure, the temperature ($T_* = 44330\,\mathrm{K}$) and mass-loss rate ($\dot{M} = 10^{-4.408}\,M_\odot\,\mathrm{yr}^{-1}$) were measured simultaneously (Rosslowe, 2016). The relative line strengths of C III λ5696 and C II λ6578 were used to estimate the errors in the mass-loss rate.

The fitting of electron scattering wings of lower ionization species was used to determine the clumping onset velocity ($v_{clump} = 100\,\mathrm{kms}^{-1}$) and the clumping factor ($f_\infty = 0.1$). These parameters affected the density and mass distribution within the wind. Following Crowther et al. (2006), a reduced mass-loss rate ($\dot{M}/\sqrt{f} = 10^{-3.908}\,M_\odot\,\mathrm{yr}^{-1}$) was derived.

Line profiles of lower and higher ionization ions were fitted using a two-component velocity law. In order to estimate the microturbulent velocity ($v_{dop} = 50\,\mathrm{kms}^{-1}$), wind terminal velocities ($v_{\infty,1} = 1000\,\mathrm{kms}^{-1}$, $v_{\infty,2} = 1300\,\mathrm{kms}^{-1}$), and acceleration parameter (β), the line widths of ions emitting in both optical and NIR bands (e.g., C III, C II, He II, He II, He I) were fitted. The velocity profile (Figure 3.2(a)) indicated a high acceleration in the inner layers, with velocities flattening beyond $100\,R_*$.

The stellar mass was not directly estimated through the modeling due to the deep location of the hydrostatic core within the optically thick region. Instead, the mass ($24\,M_\odot$) was inferred from the mass-luminosity relation for WC-type stars as proposed by Sander et al. (2012) and based on Langer (1989).

3.4.2 Surface composition

By fitting the set of emission lines in the observed spectrum, the chemical composition of the star was estimated. Since He II λ5411 and C IV λ5471 are generally weak in late-type WC stars, deriving the surface carbon abundance accurately using these diagnostic lines proved challenging. However, the carbon abundance was approximated by comparing model flux values with prominent emission lines, including C III λ5696, 6727–73, 8198, 8348, 8500, and 8664. Uncertainty limits for the relative carbon abundance were determined using the C III λ5696/He I λ5876 line ratio. When the model and observed lines were equal in strength or reversed, the lower limit was set; when the model line ratio differed from the observed data, the upper limit was set (see Fig. 3.4).

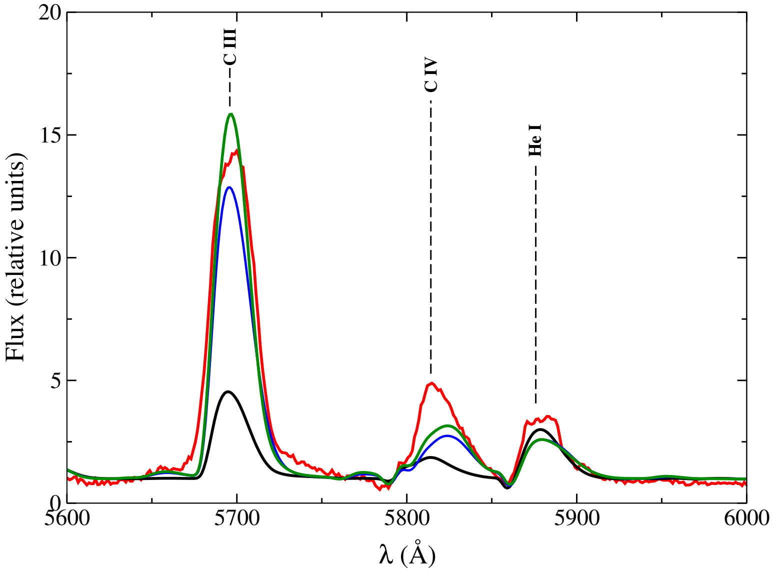

Figure 3.4: Models with different relative chemical abundances are fitted to the diagnostic emission lines (C III λ5696 / He I λ5876) to determine the composition range. The observed spectra with the lower and upper limits of the abundances are shown in red, black and green respectively. While the best-fitted model is plotted in blue. Refer Table 3.6 for details.

The determination of oxygen abundance was more complex due to the absence of strong emission lines. Owing to blending with adjacent carbon lines, only a few oxygen emission lines, such as O II λ4415–4417 and O III λ3754–3759, 5592, were available in the optical spectrum. The former two lines were undetected due to poor S/N in the 4000–5000 Å spectral region (see 3.3). Consequently, the oxygen abundance was adopted from Sander et al. (2012).

Neon abundances were derived from a study conducted by Crowther et al. (2006) on WC9-type stars. Abundances from previous studies (Ignace et al., 2007; Crowther et al., 2006; Smith & Houck, 2005; Hillier & Miller, 1999) were utilized for heavier elements, such as silicon, sulfur, argon, calcium, and iron. In Table 3.6, the mass fractions and relative chemical abundances of the atomic elements are given.

3.4.3 Nature of the SED

The CMFGEN model spectrum was scaled and the updated distance to the source of 4.33 kpc, as established by Rate & Crowther (2020) GAIA DR2 (Bailer-Jones et al., 2018; Gaia Collaboration et al., 2018), was used to estimate the extinction parameters. This was done using the Python package *dust_extinction*, which implemented the average extinction law G23 (Gordon et al., 2023). The NIR-

MIR data is incorporated into this law by G21 (Gordon et al., 2021) and optical de-reddening is incorporated by FM19 (Fitzpatrick et al., 2019). To achieve a match between the de-reddened observed spectrum and the model spectrum, the color excess parameter E_{B-V} was adjusted for a variety of R_V values within the range of 2.3–5.6, which is indicative of the high extinction in the Galactic region where the object is situated. A good match was obtained with $E_{B-V} = 2.5$ at $R_V = 3.55$.

The extinction law CCM89 (Cardelli et al., 1989) was used in the optical-NIR region to test for deviations in extinction along the line of sight (for $R_V = 2$–6). In the MIR, the CT06 (Chiar & Tielens, 2006) extinction law for the local ISM was used to account for silicate absorption features at 9.7 and 18 μm. The selection of extinction laws did not result in any substantial differences in the derived interstellar extinction. Using the derived extinction magnitude (A_V), the absolute visual-band magnitude (M_V) was determined (Table 3.7).

A slight discrepancy between the flux values of the observed spectra and the photometric bands in the optical-NIR region was observed during the simultaneous fitting of the observed spectra and photometric flux data (Figure 3.5). This discrepancy is likely due to the low S/N in the region.

The archival photometric dataset (integrated flux density) across different wavebands and the observed NIR spectral dataset were de-reddened and compared with the model Spectral Energy Distribution (SED) using the derived extinction law and the estimated E_{B-V} (Figure 3.5). The extinction (A_λ) and absolute magnitudes (M_λ) across NIR bands were estimated using the relations from Stead & Hoare (2009) and Rieke & Lebofsky (1985) for stars located outside the Galactic center. High interstellar extinction was observed in the optical bands ($A_V = 8.87$), consistent with the object's location in a Galactic region with dense interstellar dust. However, lower extinction values were found in the NIR bands ($A_{K_s} = 0.98$, $A_H = 1.68$, $A_J = 3.04$). The corresponding absolute magnitudes in the NIR were $M_{K_s} = -6.36$, $M_H = -6.23$, and $M_J = -6.55$ (Table 3.7).

A suitable fit was achieved (see Figure 3.5) between the observed and model data in all wavebands, with a root mean square flux difference of $\sim$0.1. In the K_s and H bands, free-free emission was the consequence of the extreme mass loss. Although, no excess emission indicative of circumstellar dust was detected in the IR bands. This absence of dust signatures was attributed to the object's high luminosity, which caused its evaporation.

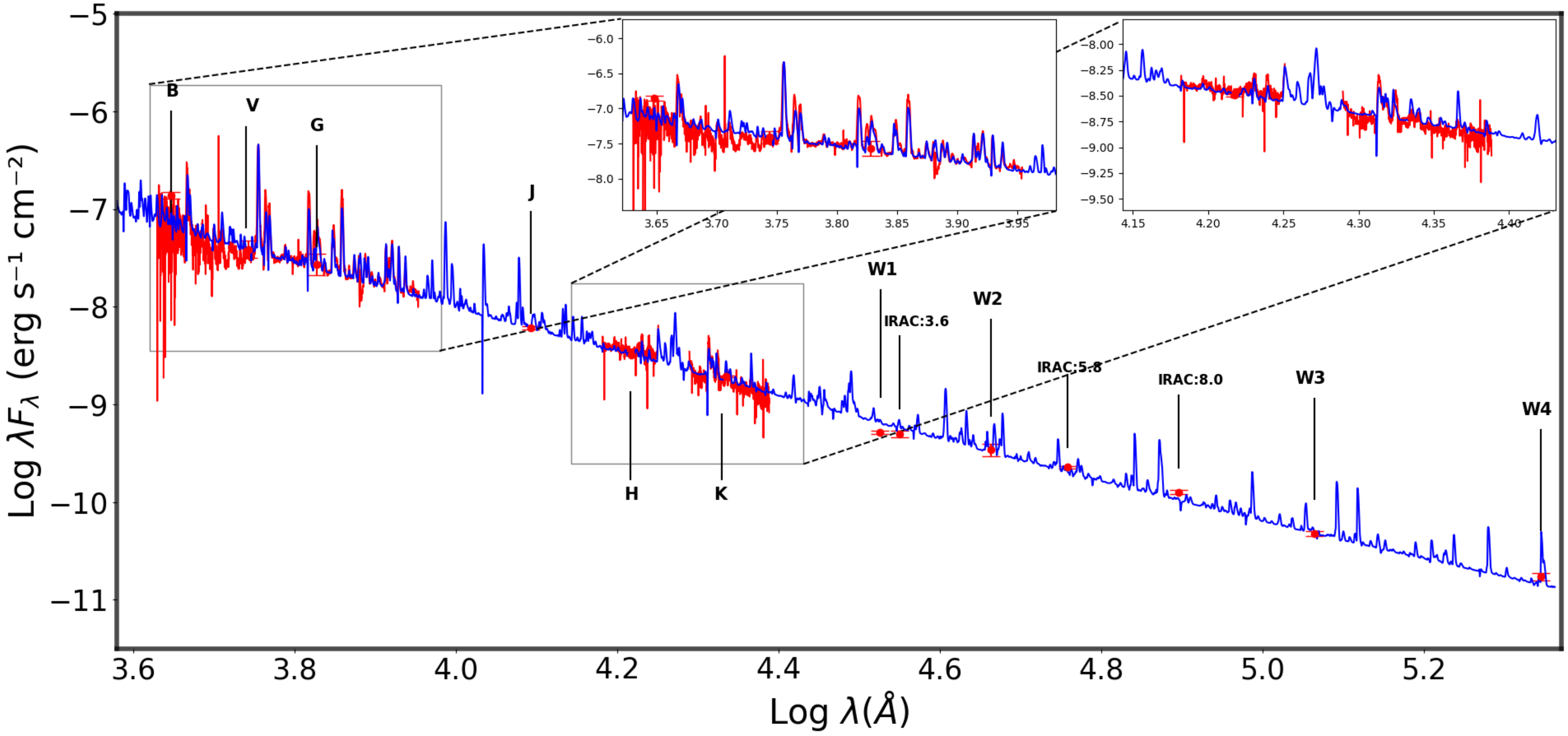

Figure 3.5: The scaled model SED (in blue) was used to fit the observed optical/NIR spectra (in red) and de-reddened photometric SED (with error bars) over the range of $10^{3.60}$–$10^{5.35}$ Å(4000–221000 Å). Photometric bands are referenced using conventional symbols.

Table 3.7: Photometric attributes of [KSF2015] 1381-19L are presented. See Sec. 3.4.3 for details.

Band	Apparent magnitude	Absolute magnitude	Extinction magnitude	Extinction relation
V	13.86	-8.18	8.87	$A_V = R_V * E_{B-V}$
J	9.66	-6.55	3.04	$A_J = 3.1 * A_{K_s}$
H	8.62	-6.23	1.68	$A_H = 1.71 * A_{K_s}$
K_s	0.98	-6.36	7.79	$A_{K_s} = 0.11 * A_V$

3.5 Discussion

3.5.1 Spectroscopic comparison

Key differences in the K_s band spectrum were identified upon comparison with the earlier study (Kanarek et al., 2015). The observed spectrum did not contain a line feature assigned to He II at 2.217 μm, which was previously reported by Kanarek et al. (2015). The observation, however, revealed a prominent feature of C III at 2.325 μm, which was previously found in WCL stars by Rosslowe (2016).

The FWHM values for all emission lines were found to remain nearly constant, indicating no significant variation in the wind structure. Furthermore, no evidence of circumstellar dust was detected, as discussed in Sec. 3.4.3, where the absence of excess IR emission in the stellar continuum was noted. The object's normalized optical spectrum was compared to that of WR 119 in order to highlight differences from WC9-dusty type stars. As described in Sec. 3.2.1, the latter was reduced using the same techniques and observed on the same night under similar configurations. According to this comparison (see Fig. 3.6), the line widths and strengths of C III λ5696 and C IV $\lambda\lambda$5802-12 were similar, but there were some significant differences. These differences suggested an extended line formation region and higher ionization in the object's winds. However, the strength ratio between these emission lines was found to be consistent. Additionally, the line width of C II λ7231 appeared unchanged, implying similar wind terminal velocities.

Because the C III λ6737/He I λ6683 line ratio was the same for both, it was determined that the object was as chemically evolved as WR 119. Table 3.8 presents a comparison of estimated stellar parameters with those of other Galactic WC9-d type stars (e.g., WR 59, 69, 80, 103, 117, 119, 121), mainly based on the findings of Sander et al. (2019a), which used updated distances. The object had a slightly higher luminosity than WR 59, a star that is thought to be a binary (Sander et al., 2019a). The object's temperature (44,330 K) was similar to the average for WC9-type stars, which is 45,000 K. According to the model parameters (Table 3.6), the photosphere ($T_{2/3}$) and the stellar core (T_* at $\tau \sim 20$) had temperatures

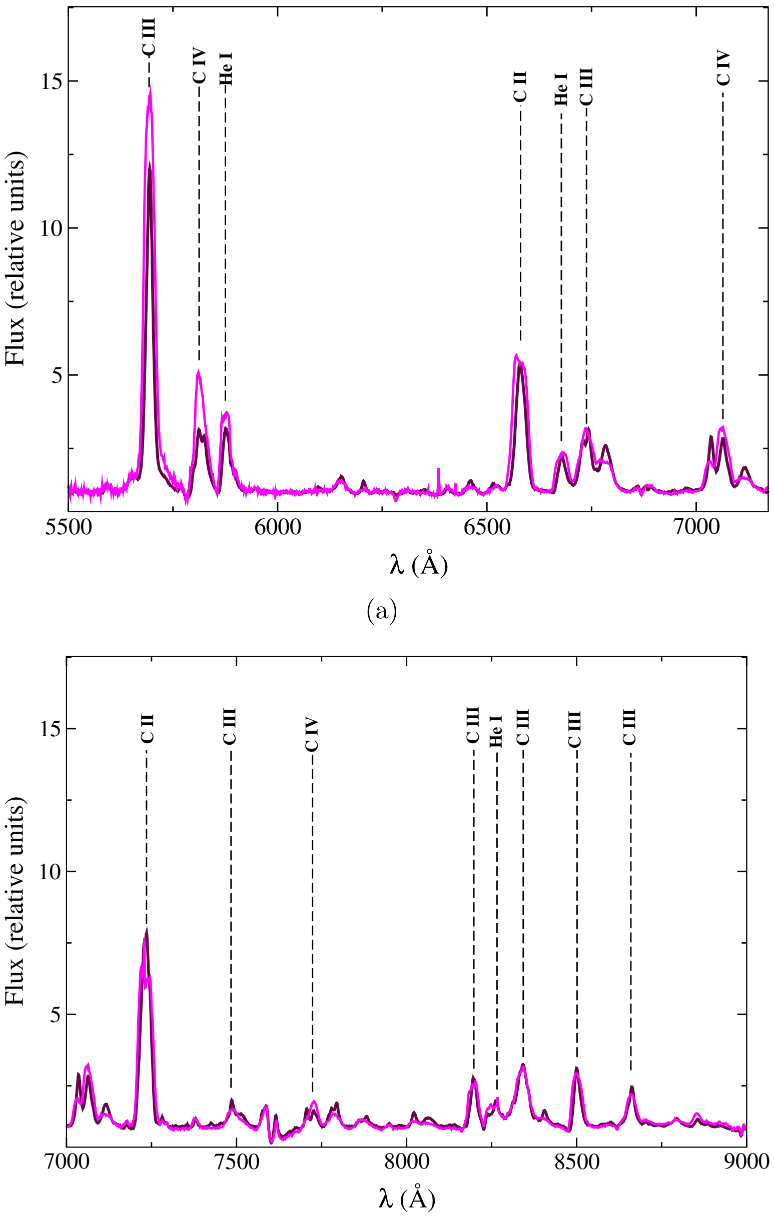

(a)

(b)

Figure 3.6: Optical spectral lines of [KSF2015] 1381-19L (in magenta) are compared to that of WR 119 (in maroon) across the optical band are shown (for details, see Sec. 3.5.1).

that differed by about 3700 K. Because of the high metallicity of the Galactic region, which propels strong stellar winds through iron opacity in the inner atmospheric layers, WC9-type stars have been found to have extreme mass-loss rates (Gräfener & Hamann, 2005). As demonstrated by spectroscopic comparisons (see Fig. 3.6), the wind terminal velocity ($v_\infty = 1300\,\mathrm{km s^{-1}}$) was marginally higher than that of the majority of objects in Table 3.8, closely matching WR 59 and WR 119.

We compared the relative elemental abundances with those of the well-studied WC9d-type star WR 103, as reported by Williams et al. (2015). The relative carbon abundance differed by approximately 0.03, which was within the model uncertainties (Table 3.6). The derived parameters were consistent with those obtained from the PoWR spectroscopic model grid (Sander et al., 2019a), where $\mathrm{X_{He}} = 0.55$ and $\mathrm{X_C} = 0.4$ were reported[1]. These chemical abundances showed that WCL stars, like [KSF2015] 1381-19L, has an atmosphere that is as chemically evolved as that of Milky Way WCE-type stars (Crowther et al., 2006; Sander et al., 2012). Furthermore, in Sec. 3.5.2, the possible formation channels of isolated Galactic WC9-type stars are investigated.

3.5.2 Evolutionary channels

Models from Geneva[2], MESA[3] for single stars, and BPASS [4] for binary systems have been utilized to derive the evolutionary channels that can reproduce evolved phases of massive MS stars, like WR stars, LBVs, and RSGs. The Geneva (single-star) models are derived as a function of metallicity with different mass-loss prescriptions for various stages of stellar evolution. BPASS binary models simulate the evolution of a primary massive star within a close binary system, incorporating matter and momentum exchange via RLOF (Eldridge et al., 2008) and accounting for metallicity-dependent stellar wind mass loss.

The object was determined to be in the solar metallicity region ($Z = 0.014$, Asplund et al. 2009) of the Galactic disk, approximately 7 kpc from the galaxy's center, as indicated by the metallicity gradient of the Galactic plane as illustrated in Rosslowe & Crowther (2015). BPASS models were chosen for the binary evolution scenario based on a fiducial IMF with a slope of 1.35, an upper mass limit of $300\,M_\odot$, a range of mass ratios (0.1–0.9), and initial binary periods ranging from 2 to 100 days. WR stars are efficiently produced by these short-period binaries (Rosslowe, 2016). We obtained binary stellar tracks at solar metallicity

---

[1] https://www.astro.physik.uni-potsdam.de/~wrh/PoWR/powrgrid1.php

[2] https://www.unige.ch/sciences/astro/evolution/fr/recherche/geneva-grids-stellar-evolution-models/

[3] https://github.com/MESAHub/mesa

[4] https://bpass.auckland.ac.nz/9.html

Table 3.8: Physical and chemical parameters of [KSF2015] 1381-19L is tabulated with that of other Galactic WC9d-type stars for comparison.

Object	$\log L_*(L_\odot)$	T_* (K)	$R_*(R_\odot)$	$v_\infty(\mathrm{kms}^{-1})$	f	$\log \dot{M}(M_\odot/\mathrm{yr})$	C/He	Reference
WR 59	5.76	40000	15.89	1300	0.1	-4.48	0.24	Sander et al. (2019a)
WR 69	5.33	40000	9.77	1090	0.1	-4.87	0.24	...
WR 80	5.24	45000	6.89	1600	...	-4.79	...	...
WR 103	4.90	48000	3.2	1140	...	-4.50	0.20	Crowther et al. (2006)
...	5.00	40000	4.1	975	...	-4.50	0.22	Williams et al. (2015)
...	5.50	45000	9.31	1190	...	-4.56	0.24	Sander et al. (2019a)
WR 117	5.36	56000	5.12	2000	...	-4.44	...	...
WR 119	4.70	45000	3.70	1300	...	-5.13	...	...
WR 121	5.16	45000	6.35	1100	...	-4.85	...	...
[KSF2015] 1381-19L	5.89	44330	15.09	1300	...	-4.41	0.25	This study

($Z = 0.014$) from the BPASS v2.2 model release (Stanway & Eldridge, 2018), and arranged and analyzed the data using the *hoki* package (Stevance et al., 2020). BPASS binary models that progressed to the WC phase were identified using the criteria established by Eldridge et al. (2008), which are similar to those applied in the Geneva single-star models (Georgy et al., 2012). When the stellar temperature surpasses $10^{4.45}$ K and the hydrogen mass fraction (X_H) falls below 0.4, the primary star with a $M_i > 15\,M_\odot$ transforms into a WR star (WN-type) (Eldridge et al., 2017). The star remains in the WN phase until the X_H falls below 10^{-3}, while the WC phase begins when the combined mass fraction of carbon and oxygen surpasses 0.03 ($X_C + X_O \geqslant 0.03$). From our analysis, we found that 5452 models entered the WR phase and transitioned to the WC phase, but only 1475 of these matched the physical parameter space (luminosity and temperature) of the observed object. From these, 558 models were selected with binary periods of 2–100 days, as such configurations are likely to involve RLOF and potentially lead to CE formation (Rosslowe, 2016) which was necessary to achieve the observed properties. The initial masses of the primary stars in these models ranged from 50 to 300 $M_\odot$. The binary stellar tracks are shown in Fig. 3.7. The model tracks successfully replicated the temperature ($T_* = 44330$ K, Table 3.6) and luminosity ($\log L_* = 5.89$), yet failed to meet the WC-condition. This finding is consistent with the extended lifetime of the WN phase in interacting binaries, which is attributed to prolonged envelope stripping through RLOF, in contrast to the shorter duration of the WC phase (Eldridge et al., 2008). Consequently, no binary models were identified that could simultaneously replicate the object's physical and chemical properties. Additionally, we checked the binary stellar tracks with twice the solar metallicity ($Z = 0.04$) however, none of these models matched the temperature of the object during the WC phase (see Fig. 3.7(b)). (Eldridge et al., 2017) attributed this discrepancy to the absence of an envelope inflation mechanism across BPASS models at all considered metallicities.

The evolutionary scenario for single stars was examined utilizing the GENEVA models (Ekström et al., 2012). The grid of published stellar models (Yusof et al., 2022) was examined to identify potential evolutionary tracks leading to the formation of WR 111-9 and to estimate the mass of the progenitor. Based on their initial mass, O-type MS stars undergo specific evolutionary stages that are characterized by substantial mass loss and rotational mixing, ultimately leading to core-collapse SNe. It was determined that massive O-type stars with initial masses exceeding 25 $M_\odot$ transitioned into the WR phase (Georgy et al., 2012; Ekström et al., 2012) when their effective temperature (T_{eff}) surpassed 10^4 K and the hydrogen mass fraction (X_H) dropped below 0.3. These stars remained classified as WN-type until X_H declined to less than 0.05. The transition to the WC phase occurred when the carbon mass fraction (X_C) exceeded that of nitrogen (X_N). To model this process, stellar evolutionary tracks were generated from the

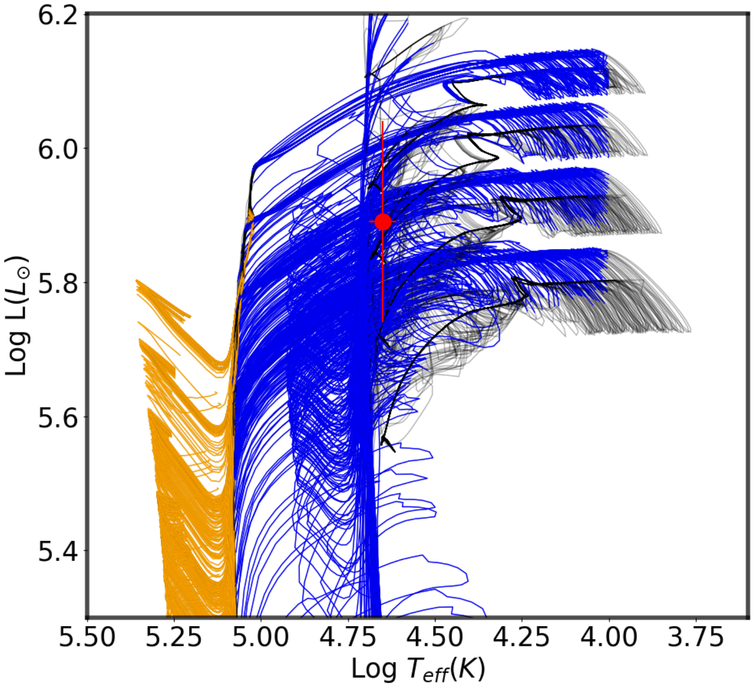

(a) Tracks for Z=0.014.

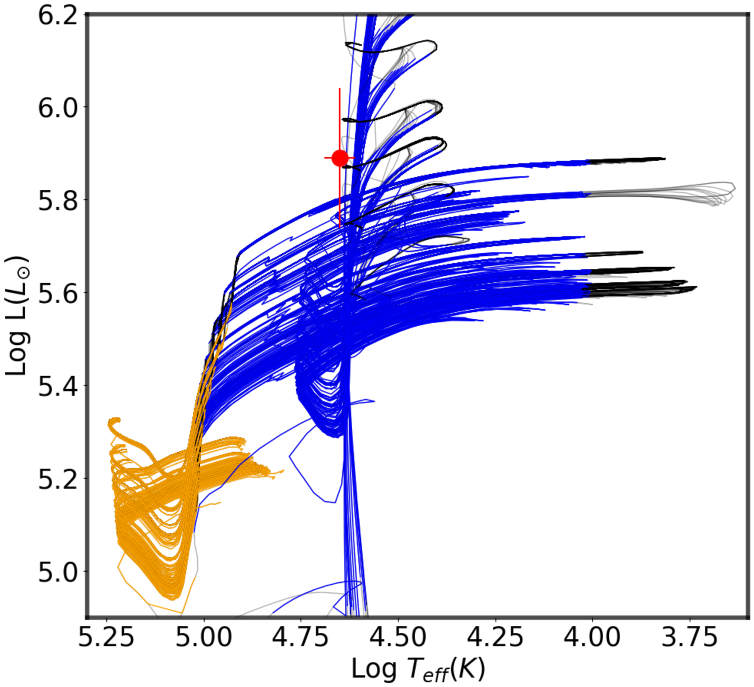

(b) Tracks for Z=0.04.

Figure 3.7: Model tracks of primary evolution in close binaries (P_{ini}=2-100d) at solar and twice-solar metallicities are shown. The object's position is marked by a red dot in the HR diagram. Distinct stellar evolutionary phases are indicated by different colors: black for the non-WR phase, blue for the WN phase, and orange for the WC phase, all within the life cycle of a massive O-type star.

SYCLIST[1] database. Tracks for solar metallicity were interpolated for a range of masses (40, 60, 85, and 120 $M_\odot$). In order to investigate the physical properties and surface chemical composition of the WC-type evolutionary phase, it was necessary to analyze both non-rotating and rotating single-star evolutionary tracks ($v_{\rm rot,ini} = 300\,{\rm kms}^{-1}$, as per Meynet & Maeder (2003)). The position of the object on the HR diagram was plotted alongside a comprehensive set of evolutionary tracks for masses ranging from 50–100 $M_\odot$ (see Fig. 3.8). A non-rotating MS O-type star with an initial mass of 90 $M_\odot$ and a rotating progenitor star with an initial mass of 67 $M_\odot$ were able to replicate the observed characteristics of [KSF2015] 1381-19L. These closely matching evolutionary tracks are compared to the stellar atmospheric model and are discussed in the following subsections.

Physical parameters

The initial WC phase of the object is characterized by core helium burning, as indicated by the model parameters that correspond to the evolutionary tracks of both rotating (67 $M_\odot$) and non-rotating (90 $M_\odot$) stars (also listed in Table 3.9). The mass of the WR phase is estimated to be approximately 24 $M_\odot$, from both rotating and non-rotating evolutionary models, and was found to be similar and consistent with the value estimated from the mass-luminosity relationship (see Sec. 3.4.1).

The mass-loss rate was determined during the WR phase by adhering to the prescription of Vink et al. (2001), which was empirically linked to metallicity. The estimated rates were determined to be higher ($\dot{M} = 10^{-4.32}\,M_\odot{\rm yr}^{-1}$ for the rotating 67 $M_\odot$ model and $\dot{M} = 10^{-4.297}\,M_\odot{\rm yr}^{-1}$ for the non-rotating 90 $M_\odot$ model) than the predictions from spectroscopic models ($\dot{M} = 10^{-4.408}\,M_\odot{\rm yr}^{-1}$). This disparity was ascribed to the evolutionary models' lack of wind-clumping effects.

Chemical abundances

As shown in Table 3.9, the evolutionary models for a rotating star with an initial mass of 67 $M_\odot$ and a non-rotating star with 90 $M_\odot$ produced different surface mass fractions. When the elemental abundances from these evolutionary models were compared with those from the spectroscopic model (Table 3.6), small differences were identified in the most abundant species, such as helium (X_{He}) and carbon (X_C). These differences, however, remained within the uncertainty limits of the models.

---

[1] https://www.unige.ch/sciences/astro/evolution/fr/base-de-donnees/syclist/

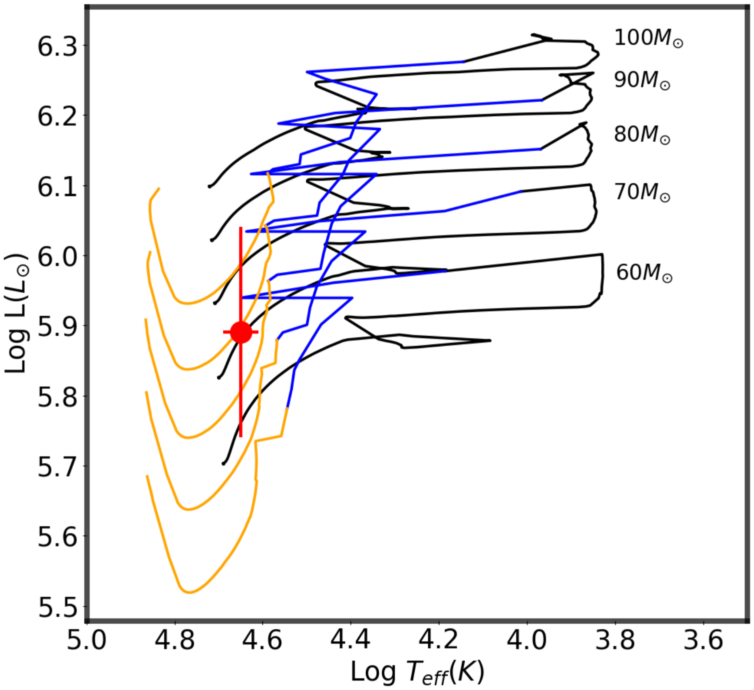

(a) For non-rotating (v_{ini}=0) progenitors.

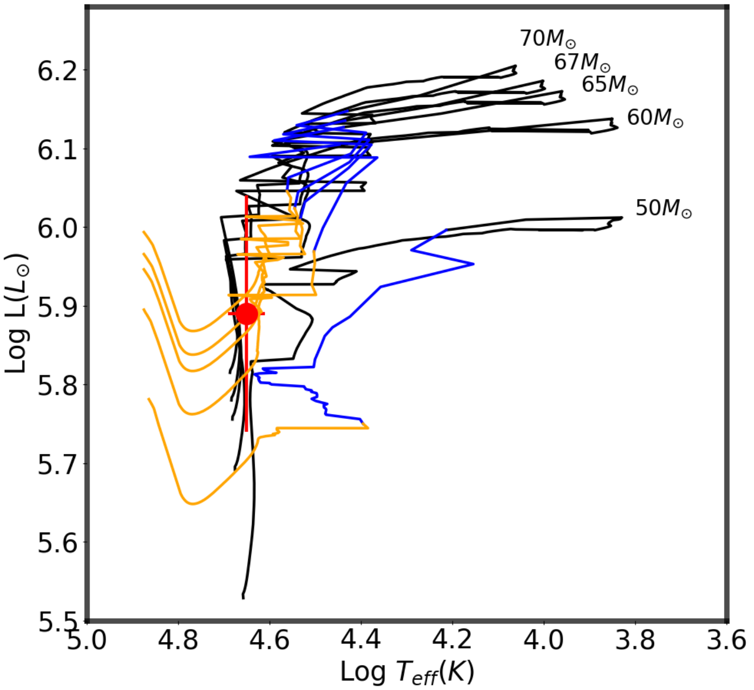

(b) For rotating (v_{ini}=300 kms^{-1}) progenitors.

Figure 3.8: Evolution model tracks of O-type MS stars at solar metallicity (Z=0.014). The red dot shows [KSF2015] 1381-19L in the HR diagram, with black for non-WR, blue for WN, and orange for WC phases in massive O-type stars.

The oxygen abundance (X_O) predicted by the evolutionary models was found to be higher than that obtained from the spectroscopic model. Similarly, the neon abundance (X_{Ne}) was higher by 6×10^{-3} in the evolutionary models. These differences were ascribed to variations in the physical conditions, including the empirically determined mass-loss rates, and nuclear reaction rates used in the evolutionary models. However, these small discrepancies were deemed to be within the uncertainties of the spectroscopic analysis.

Table 3.9: Parameters for single star evolution of non-rotating and rotating progenitors.

Parameter	Non-Rotating (M=90 $M_\odot$)	Rotating (M=67 $M_\odot$)
$\log L_*$ ($L_\odot$)	5.90	5.89
T_* (K)	44258	44360
$\log \dot{M}(M_\odot/yr)$	-4.297	-4.320
M ($M_\odot$)	24.63	24.00
X_H	0	0
X_{He}	0.483	0.544
X_C	0.416	0.377
X_O	0.083	0.061
X_{Ne}	0.012	0.012

3.6 Summary and Conclusion

The optical and IR characteristics of [KSF2015] 1381-19L, a WC9-type star situated in the disk of the MW and highly obscured by the dense ISM in the Galactic plane, were analyzed. The atmospheric characteristics were examined utilizing the CMFGEN code to simulate the observed spectra, and the physical and chemical attributes were extracted from the optimal fitting model. The mass-loss rate and luminosity significantly influenced the emission line strengths, whereas the stellar radius remained unchanged. Compared to other Galactic WC9-type stars, we found the object to be the most luminous isolated WC9-type star, and the metallicity of the surrounding Galactic region resulted in its extreme mass loss rate. A comparison with the spectroscopic properties of WR 119 revealed notable similarities, indicating a chemically evolved atmosphere characterized by a high mass-loss rate that is conducive to dust formation in the circumstellar environment. We measured the interstellar extinction and discovered that it was greater in the optical band than in the NIR band. In the NIR, the absolute photometric magnitudes that were calculated were strikingly similar to those of WC9d-type stars. The circumstellar dust was not the cause of the excess emissions in the IR bands; rather, they were attributed to free-free processes. However, the potential for dust formation could not be entirely ruled out without multi-epoch monitoring of the object in IR bands. Our analysis suggested that it was improbable that the object had evolved within a close binary system. Rather, the object most likely came from a rotating ($M = 67\,M_{\odot}$) or non-rotating ($M = 90\,M_{\odot}$) O-type MS star, according to results from the Geneva single-star evolutionary models at a solar metallicity (Z=0.014). It was concluded that the object is burning helium at the core and is in the initial WC phase. Variations in elemental abundances were found to be caused by differences in nuclear reaction rates and rotational mixing, highlighting the significance of including rotational velocity in spectroscopic modeling.

Chapter 4

Investigating the wind-driving mechanism of WR 135: insights into a pulsating WC8 Star

In this chapter, the research work published in Kar et al. (2024c) is examined.

4.1 Introduction

There have been only a handful of WCL stars that have been observed to exhibit both stochastic and pulsational variability simultaneously. The C IV $\lambda\lambda$5802-12 and C III λ5696 emission lines were intensively monitored by Lépine et al. (2000), which revealed the presence of small-scale structures within the stellar winds of WR 135, a single WC8-type star. Later research (Lenoir-Craig et al., 2022; Chené et al., 2020) found that clumpy winds were responsible for the distinctive small-scale stochastic phenomena observed in WR 135 (Owocki et al., 1988). WR 135 was further classified as a pulsating WR star in a photometric survey (Nazé et al., 2021). As a result, WR 135 was observed to exhibit both pulsational and stochastic variability, which were probably the result of SMPs and SMI-induced wind clumping, respectively.

In order to ascertain how both phenomena could occur simultaneously, the driving mechanisms of the stellar winds of WR 135 were examined in this work. The analysis of the varying strengths of unblended emission lines within a short-cadence spectroscopic time-series dataset was conducted to investigate pulsational variability, as detailed in Sec. 4.3. In an additional effort to identify higher-order harmonics, photometric time-series data were examined. In Sec. 4.4.2, the impact of velocity gradients and clumping factors on line formation in the optically thin regions of the supersonic winds is assessed. The wind-driving source is explored in Sec. 4.4.3, and the physical conditions supporting the pulsation harmonics are discussed in Sec. 4.5. The conclusions of this work are presented in Sec. 4.6.

4.2 Observational data

4.2.1 Photometric data

This investigation employed optical photometric data (600−1000 nm) observed by the Transiting Exoplanet Survey Satellite (TESS). Having a FoV of 96° × 24°, TESS is a cutting-edge space telescope that is specifically designed to detect exoplanets and asteroseismic phenomena (Ricker et al., 2014). The telescope records Full Frame Images (FFI)s that encompass the entire FoV at longer cadences (30 minutes during the TESS Prime Mission and 10 minutes during the first Extended Mission), while focused data is captured for pre-selected targets at a cadence of 2 minutes. TESS observes a particular portion of the sky (known as a Sector) for approximately 27 consecutive days during each orbit. The intrinsic variability of massive stars, including WR stars, is optimally monitored by TESS due to its precise detection capabilities, which span timescales from hours to days.

In Sectors 41, 54, and 55, the photometric time series data of WR 135 (at 10-minute cadence) were obtained from TESS observations for this analysis. The lightcurves were extracted from the 10-minute FFIs using the MIT Quick Look Pipeline (Huang et al., 2020; Kunimoto et al., 2021), as described by Kunimoto et al. (2022). An optimal aperture was employed during the extraction process, and the lightcurves were subsequently post-processed using the Presearch Data Conditioning algorithm (Smith et al., 2012; Stumpe et al., 2012) to eliminate outliers and reduce trends caused by instrumental noise. The mean flux values of the resultant light curves were used to normalize them. These flux-normalized lightcurves were obtained from the Mikulski Archive for Space Telescope (MAST) as High-Level Science Products (HLSP). The *Lightkurve* package (Lightkurve Collaboration et al., 2018) was used to retrieve and analyze the data for this study. The processed lightcurve data utilized in this work are presented in Fig. 4.1.

Additionally, the publicly available Vizier[1] data catalog was used to obtain optical and IR photometric data (integrated flux density). The photometric data from the optical to MIR bands and the associated catalogs are shown in Table 4.1. The V-band and B-band flux data were obtained from the datasets published by Lasker et al. (2008) and Esa (1997), respectively. The GAIA DR2 data release

---

[1] `https://vizier.cds.unistra.fr/`

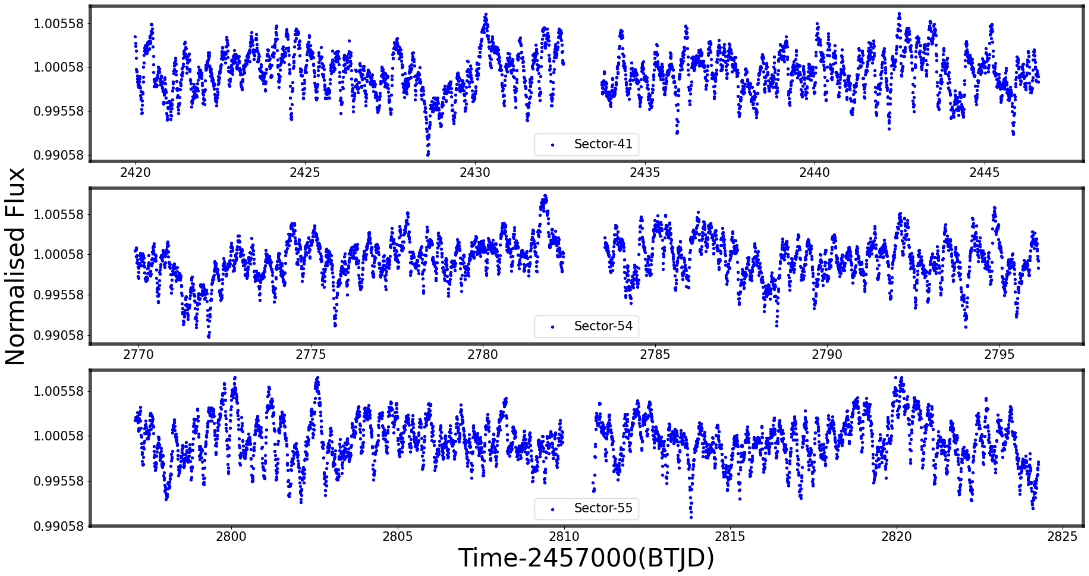

Figure 4.1: The normalized lightcurves of WR 135 with a 10-minute cadence were derived from the FFIs observed in Sectors 41, 54, and 55.

(Gaia Collaboration et al., 2018) provided the G-band optical data. We used data from the 2MASS data release (Skrutskie et al., 2006) for the NIR bands. The SASS (Spitzer Atlas of Stellar Spectra) data release (Ardila et al., 2010a) and the WISE data release (Cutri et al., 2012) were used to extract MIR photometric data.

4.2.2 Spectroscopic data

High-resolution

From the Canadian Astronomy Data Centre[1] (CADC), high-resolution optical spectroscopic time-series data (S/N$\sim$ 300 − 400 pixel^{-1}) for WR 135 were obtained. These spectropolarimetric observations were carried out (by de la Chevrotière et al. 2014) using the fiber-fed ESPaDOnS[2] instrument installed on the 3.6m Canadian French Hawaii Telescope (CFHT). The spectrograph provided full optical coverage (3500−10000 Å) across 40 spectral orders in a single exposure, enabling the simultaneous monitoring of several spectroscopic features spread across a broad wavelength range. The Libre-ESpRIT (Donati et al., 1997) software integrated with Upena was used to reduce and wavelength-calibrate the Echelle spectroscopic data, as detailed by de la Chevrotière et al. (2014). The spectral

---

[1] https://www.cadc-ccda.hia-iha.nrc-cnrc.gc.ca/en/

[2] http://www.cfht.hawaii.edu/Instruments/Spectroscopy/Espadons/

Table 4.1: Photometric flux density across optical-IR bands of WR 135.

Band	Integrated flux density ($\mathrm{erg\,s^{-1}\,cm^{-2}\,\AA^{-1}}$)	λ_c (nm)	Database
B	$3.01e^{-12}$	444	Lasker et al. (2007)
V	$2.03e^{-12}$	554	Esa (1997)
G	$1.79e^{-12}$	623	Gaia Collaboration (2018)
J	$3.94e^{-13}$	1240	Cutri et al. (2003)
H	$1.65e^{-13}$	1650	...
K_s	$9.35e^{-14}$	2160	...
W1	$2.26e^{-14}$	3350	Cutri & et al. (2012)
W2	$9.45e^{-15}$	4600	...
IRAC-8.0	$1.63e^{-15}$	7870	Ardila et al. (2010b)
W3	$4.8e^{-16}$	11600	Cutri & et al. (2012)
W4	$7.74e^{-17}$	22100	...

continuum was fitted with a polynomial from regions with few or no prominent spectral features. The fitted continuum was then used to normalize the spectra used in the study. The observation log is presented in Table 4.2. The emission lines that were found to be the least blended with neighboring features were He I λ5876, C IV λ5802-12, and C III λ5696. Figure 4.2 illustrates the profiles of the initial two emission lines.

To conduct this analysis, the *astropy*[1] package was employed to extract the spectral regions that contained emission lines (Astropy Collaboration et al., 2013, 2018, 2022). The *fit_lines* task from the *fitting* module was used to fit individual line profiles using a one-dimensional Gaussian function after the *extract_region* task was applied. The LM chi-square minimization (Levenberg, 1944; Marquardt, 1963) was used to identify the best-fitting profiles. The fitted models were used to determine the EW of the spectral lines, and the associated uncertainties were estimated using the methodology described by Vollmann & Eversberg (2006). The ratio of flux associated with the emission line to the adjacent continuum and its inverse dependence on the S/N of the same continuum region were used to determine the estimated EW error. This was achieved by determining the normalized mean flux of the continuum ($\overline{F_{cont}}$) and the line ($\overline{F_{line}}$) from featureless areas close to the emission lines. We calculated the S/N of the spectra using the same pseudocontinuum regions.

---

[1] https://www.astropy.org/

Table 4.2: Details of spectroscopic observations for WR 135

Epoch (JD 240000+)	Date	Telescope: Instrument	$\lambda/\Delta\lambda$	λ (Å)	Exposure
54645.96573- 54646.05832	2008 June 28	CFHT: ESPaDOnS	68000	3000-10000	12 frames×600 s
60207.29852	2023 September 19	HCT: HFOSC/Gr7	1400	3800−7000	1 frame×15 s
60207.30182	...	HCT: HFOSC/Gr8	2200	5000−9000	1 frame×60 s

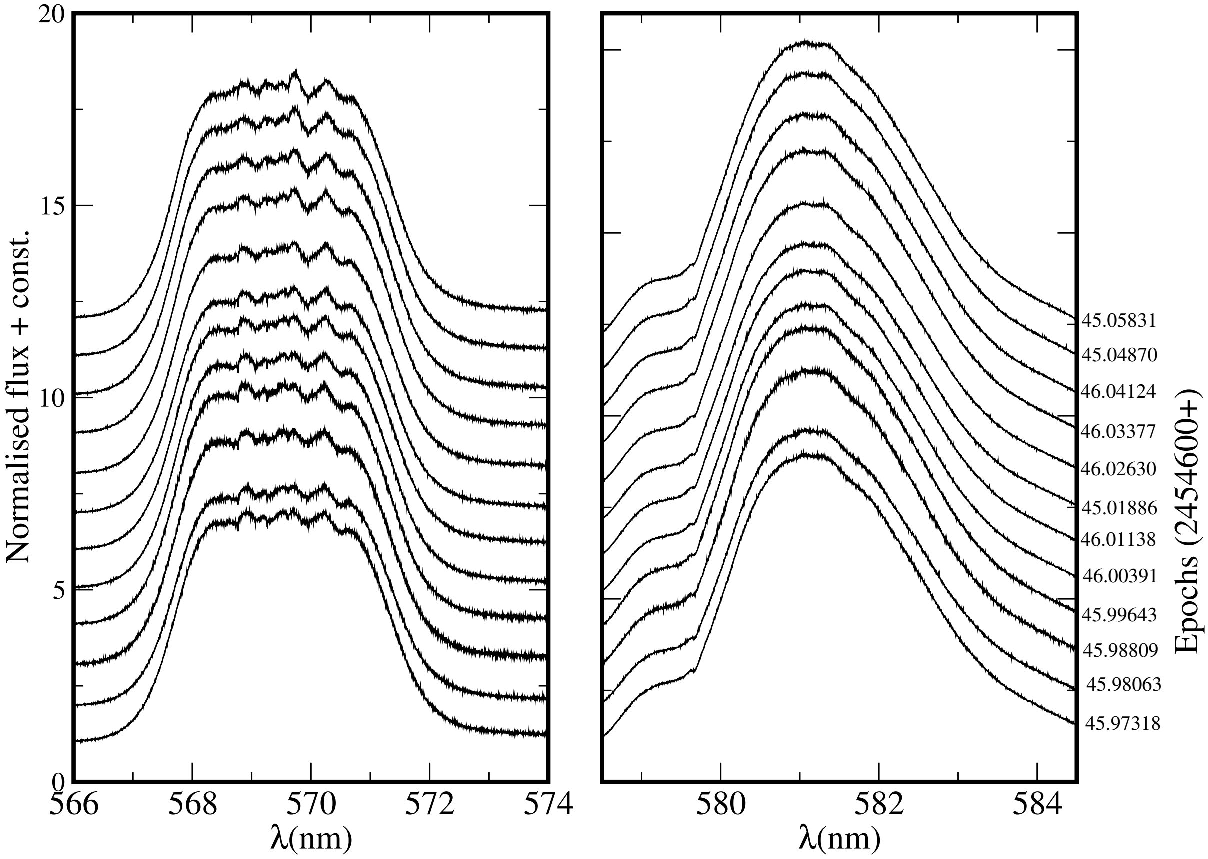

Figure 4.2: The emission line profiles of C III $\lambda5696$ (left panel) and C IV $\lambda\lambda5802$-12 (right panel) observed from the CFHT (see Table 4.2).

Low-resolution

The HFOSC, mounted on the HCT was used to obtain low-resolution (R∼1400−2200) spectra (S/N∼40) of WR 135. To cover the optical band, Grism-7 (3800−7000 Å) and Grism-8 (5200−9000 Å) were utilized. Wavelength calibration was performed using Argon and Neon lamp spectra, which were recorded immediately after each science spectrum. Flux calibration was achieved by observing Feige 110 (Massey & Gronwall, 1990), a spectrophotometric standard star, using both Grisms 8 and 7 on the same night. A 2k×4k CCD was used to record every observation. In Table 4.2, the observation log is presented.

Using IRAF (Tody, 1993), the two-dimensional spectral images were processed. This included steps like cosmic ray removal, master bias subtraction, and wavelength and flux calibration of the 1D spectra that were taken from the 2D images. A detailed description of the reduction techniques is provided in Sec. 2.2.1.

4.3 Analysis

Frequency detection

The variable nature of the source was analyzed using Fourier transformation (see Sec. 2.3) of the TESS lightcurves (refer to Fig. 4.3) from Sectors 55, 54, and 41 along with the EW time series (see Fig. 4.4) of the emission lines C IV 5802-12 and C III 5696. The analysis was conducted using the PERIOD04 software (Lenz & Breger, 2005). The lightcurves were fitted with co-sinusoids in an iterative manner, as described in Li et al. (2018), to extract frequencies with a S/N≥3, which enable the detection of low-amplitude higher-order harmonics. The optimal uncertainties for the identified frequencies were estimated by simultaneously applying a non-linear least-squares fit, as described in Toalá et al. (2022).

The derived frequencies were further validated by applying Generalized Lomb-Scargle Periodograms (GLSP)[1] introduced by Zechmeister & Kürster (2009) to each lightcurve. Measurement errors and a constant term are incorporated into the GLSP method when fitting trigonometric functions. Using the normalization scheme proposed by Zechmeister & Kürster (2009), an error-weighted LSP was implemented.

---

[1] https://pyastronomy.readthedocs.io/en/latest/pyTimingDoc/pyPeriodDoc/gls.html

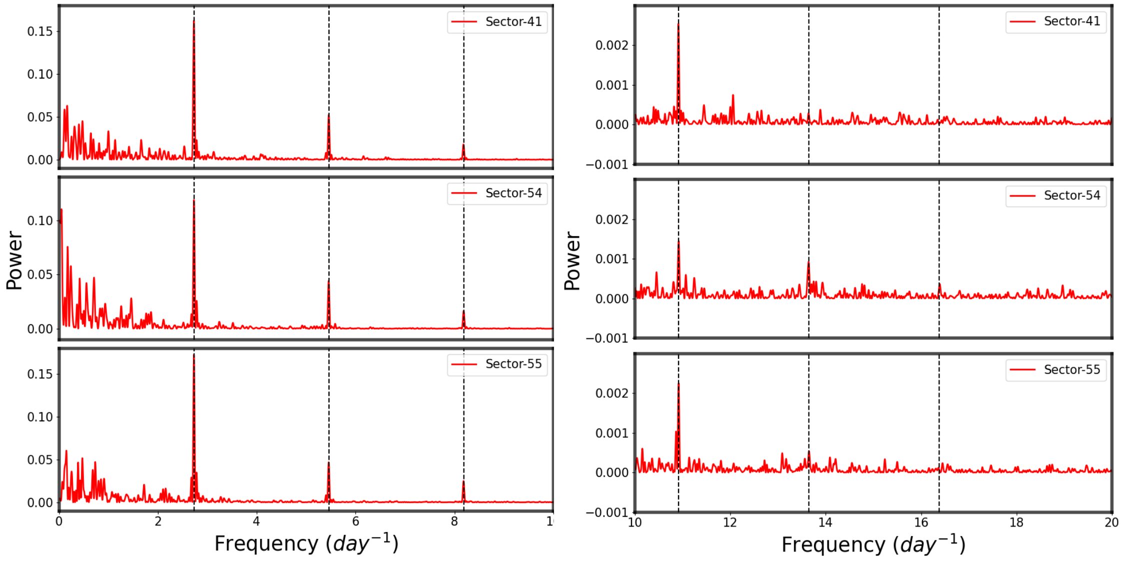

(a) Harmonics from $1^{st} - 3^{rd}$ order (b) Harmonics from $4^{th} - 6^{th}$ order

Figure 4.3: The LSP generated the power spectra of WR 135 using the photometric lightcurves from TESS Sectors 41, 54, and 55.

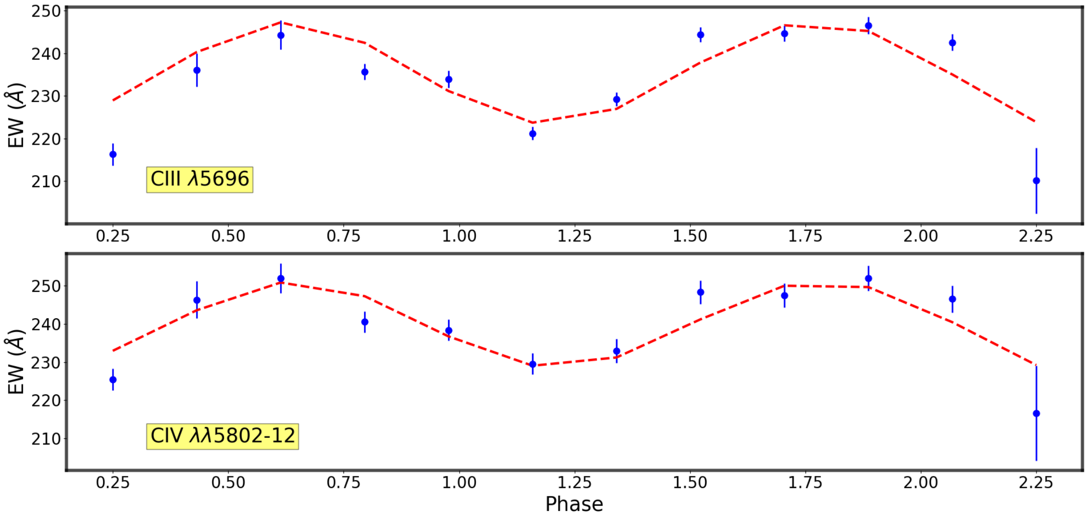

Figure 4.4: The time series data of EW of emission lines are fitted with dual phase sinusoids with $\nu = 21 \pm 1$ day^{-1}.

Modeling spectra

The object's physical and chemical properties were analyzed using the 1D radiative transfer code CMFGEN, as outlined in Sec. 2.4. The model parameters were estimated following the procedure mentioned in Sec. 2.4, including radius, wind velocity, VFF, atomic data, and super-levels. Distinct atomic transitions were modeled to generate the emission lines in WC-type stars. The continuum fluorescence is thought to be the primary cause of the C IV $\lambda\lambda$5802-12 transition, whereas the dielectronic recombination process is associated with the C III λ5696 line.

The atmosphere was hypothesized to be devoid of both hydrogen and nitrogen, with a He-burning stellar core surrounded by accelerating stellar winds (see Fig. 2.10). Atomic opacity data as photoionization cross-sections, collision and oscillator strengths, and dielectronic recombination rates were employed to investigate the ionization states of abundant elements, as described in Sec. 2.4. Among them were Fe III-IX, Ca II-VI, Ar III-V, S III-VI, Si III-IV, Ne II-IV, O II-IV, C II-IV, and He I-II. This large dataset was used to study the mechanisms behind the radiative acceleration of stellar winds.

4.4 Results

4.4.1 Search for variability

The Fourier transform analysis of the photometric lightcurves (see Fig. 4.1) revealed several harmonics of the fundamental frequency (2.729 day^{-1}) (see Table 4.3). We observed a slight discrepancy between the first and second harmonics, which were previously reported by Nazé et al. (2021), and those reported in Lenoir-Craig et al. (2022). In all three sectors, the fourth harmonic (corresponding to a period of about 2.198 hours) had a S/N greater than 4, and the frequencies 2.729 day^{-1}, 5.456 day^{-1}, and 8.183 day^{-1} had a S/N greater than 7. The sixth (P∼1.465 hours) and fifth (P∼1.758 hours) harmonics were also detected (S/N>3) only in Sector-54, albeit weaker, perhaps because of detector sensitivity.

A semi-Lorentzian model was fitted to the lightcurves in previous studies (Nazé et al., 2021; Lenoir-Craig et al., 2022) to determine the red and white noise levels of the data, so these were not recalculated by us. For 10-minute cadence data, the mean amplitude of the frequency-dependent red noise was nearly identical to that of 30-minute cadence data, while the characteristic frequency remained constant (Lenoir-Craig et al., 2022). This conclusion is substantiated by the finding that the mean red-noise amplitude for the 10- and 30-minute cadence data

Table 4.3: The frequencies (with S/N≥3) found in various time series observations.

Dataset	1st (d^{-1})	2nd (d^{-1})	3rd (d^{-1})	4th (d^{-1})	5th (d^{-1})	6th (d^{-1})	7th (d^{-1})	8th (d^{-1})
Photometric								
Sector-41	2.729±0.001	5.457±0.001	8.183±0.002	10.912±0.006	-	-	-	-
Sector-54	2.730±0.001	5.456±0.001	8.186±0.002	10.915±0.008	13.642±0.009	16.386±0.015	-	-
Sector-55	2.730±0.001	5.456±0.001	8.185±0.001	10.915±0.005	13.65±0.012	-	-	-
Spectroscopic								
$\mathrm{EW}_{\mathrm{C\,III}\lambda5696}$	-	-	-	-	-	-	-	21±1
$\mathrm{EW}_{\mathrm{C\,IV}\lambda\lambda5802-12}$	-	-	-	-	-	-	-	21±1

was within 1-σ of the red noise from the 2-minute cadence data. The previously detected red noise ($1.512\,\mathrm{day}^{-1}$) was attributed to stochastic variability. We found that the wave propagation velocity exceeded the dynamical outflow velocity, as indicated by the fundamental pulsation frequency being nearly double the stochastic variability frequency.

The EW of the emission lines (C III λ5696 and C IV $\lambda\lambda$5802-12) time-series (Fig. 4.4) showed sinusoidal variability at a frequency of about $22\,\mathrm{day}^{-1}$, which was the eighth harmonic of the fundamental frequency ($2.729\,\mathrm{day}^{-1}$) of the stellar pulsation.

Apart from the harmonics of the fundamental pulsation, epoch-dependent frequencies were not detected in WR 135, unlike those found in WR 7 by Toalá et al. (2022) which was attributed to the large-scale intrinsic variability due to the CIRs (see 1.3.4). The frequencies found in WR 135 were not associated with CIRs, as they persisted consistently across all three epochs, as indicated by the absence of such epoch-dependent features.

4.4.2 Spectroscopic modeling

The physical and chemical parameters (Table 4.4) were varied to generate atmospheric models for the observed SED using CMFGEN. The emission lines and continuum of the SED were reliably reproduced by spectroscopic models across optical to IR wavelengths. Models were modified to account for the spectrograph resolution to match the observed data. The upper and lower bounds for physical parameters (such as luminosity, radius, and mass-loss rate) and chemical parameters (such as carbon/helium abundance) were determined using the relative line strengths (C IV/He I and C IV/C III) of diagnostic emission lines found in WCL stars.

The derived model was able to replicate the line strengths of the majority of observed emission lines, including the targeted C IV $\lambda\lambda$ 5802-12 and C III λ5696, as illustrated in Fig. 4.5(a). Comparing estimated model parameters (Table 4.4) showed that the luminosity and core radius were higher, but the temperature and carbon abundance were in line with those reported by Sander et al. (2019b) for WR 135. Previous investigations of WC8-type stars (Sander et al., 2012) were considered to derive the chemical composition of less-abundant elements. The stellar mass, which is approximately $21\,M_{\odot}$, was determined using the mass-luminosity relationship for helium-burning chemically homogeneous WC-type stars (Gräfener et al., 2011).

The observed SED was de-reddened (Fig. 4.5(b)) and fitted using the average interstellar extinction law G23 (Gordon et al., 2009; Fitzpatrick et al., 2019; Gordon et al., 2021; Decleir et al., 2022; Gordon et al., 2023). This was done

Table 4.4: The stellar parameters of the best model atmosphere.

Stellar parameters	Values	
$\log L_*(L_\odot)$	$5.72^{+0.15}_{-0.15}$	
T_* (K)	60740	
$R_*(R_\odot)$	$6.56^{+0.5}_{-0.5}$	
$T_{2/3}$ (K)	53400	
$R_{2/3}(R_\odot)$	8.49	
$\log \dot{M}(M_\odot \mathrm{yr}^{-1})$	$-4.66^{+0.035}_{-0.032}$	
f	0.29	
$\log \dot{M}/\sqrt{f}(M_\odot \mathrm{yr}^{-1})$	-4.167	
$v_{core}(\mathrm{kms}^{-1})$	0.4	
$v_{phot}(\mathrm{kms}^{-1})$	100	
$v_{dop}(\mathrm{kms}^{-1})$	50	
$v_{\infty,1}(\mathrm{kms}^{-1})$	1000	
$v_{\infty,2}(\mathrm{kms}^{-1})$	1400	
β_1	1	
β_2	50	
η	2.623	
$M(M_\odot)$	20.89	
Chemical elements	Fractional abundance	Relative abundance
Hydrogen	0.00	0.00
Helium	0.542	1.00
Carbon	$0.406^{+0.111}_{-0.374}$	$0.25^{+0.15}_{-0.24}$
Nitrogen	0.00	0.00
Oxygen	0.043	0.02
Neon	$6.02e^{-3}$	$2.2e^{-3}$
Silicon	$8.62e^{-4}$	$2.26e^{-4}$
Sulphur	$3.82e^{-4}$	$8.75e^{-5}$
Argon	$1.04e^{-4}$	$1.92e^{-5}$
Calcium	$6.15e^{-5}$	$1.12e^{-5}$
Iron	$1.66e^{-3}$	$2.18e^{-4}$
E_{B-V}	0.5	
A_V	1.55	

using the *dust_extinction* module in *Astropy*. The GAIA DR2 distance (Rate & Crowther, 2020) estimate of 2.36 kpc was used to scale the model SED. The velocity law and clumping factor had a substantial impact on the fit of emission lines from various species, as evidenced by the physical parameter analysis. In subsequent subsections, the role of wind acceleration and clump size in the stellar atmosphere is further investigated.

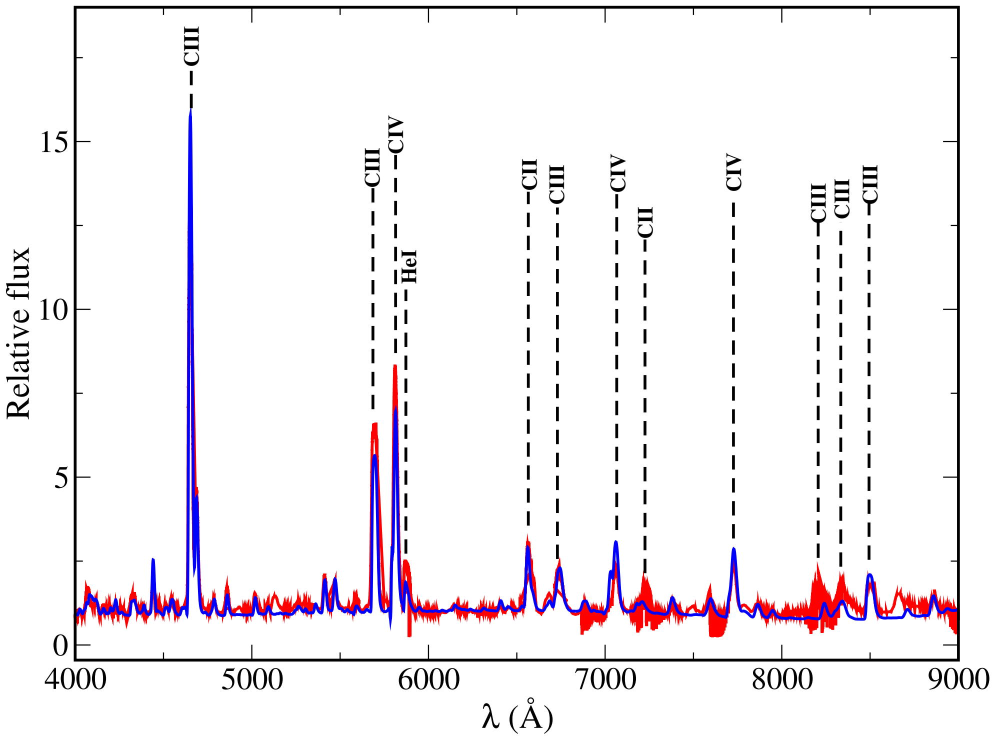

(a) Normalised data

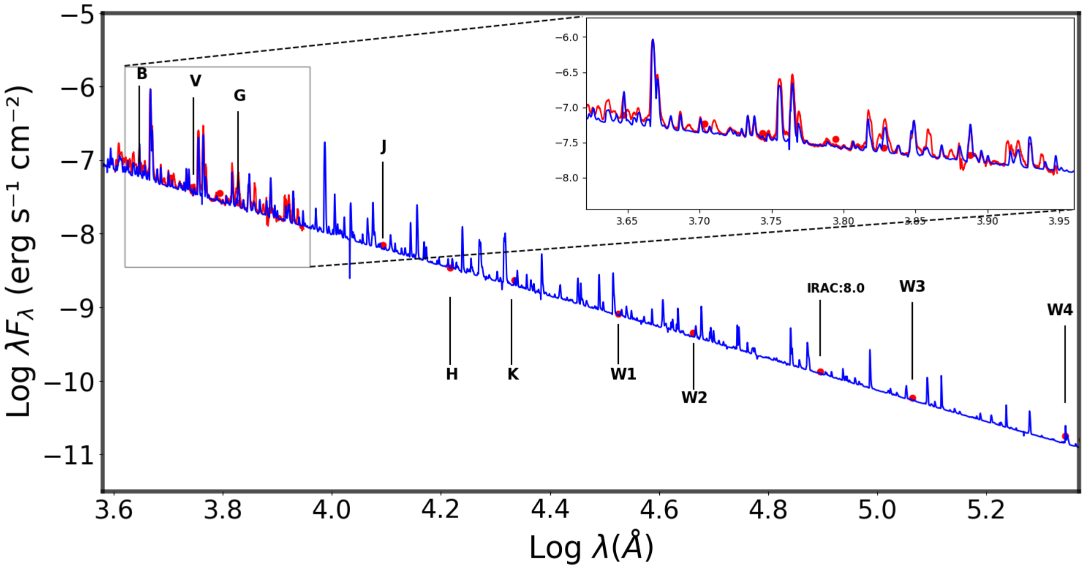

(b) Distance scaled model SED fitted with dereddened observed SED across 4000-22000 Å

Figure 4.5: Fitting of the spectroscopic model with the observed data.

Influence of wind acceleration

Our investigation focused on the influence of the velocity gradient on the mass-loss rate and the emission line strengths. It was examined how acceleration affected the outer, optically thin supersonic winds. Only the outer-wind acceleration exponent (β_2) was changed, while all other parameters remained unchanged, to produce matching spectroscopic models (Fig. 4.6). The line strength of C IV $\lambda\lambda$ 5802-12 was found to be almost unaffected by changes in the outer acceleration exponent, whereas C III λ5696 showed notable fluctuation. The results showed that a large fraction of C III ions experienced changes in the outer winds.

It was notable that C III λ5696 exhibited diminished line strengths for β_2 values of 10 and 50, while the strength increased for β_2 values ranging from 20 to 40. This implied that to replicate both emission lines simultaneously, small-scale inhomogeneities were required to exist within the overlapping line formation region. Such inhomogeneities could only be accounted for by the presence of numerous small clumps in the winds.

Clumping in the winds

VFF, which scales as ρ^2/f_{VFF}, and density (ρ) were compared with recombination line strengths. To assess its impact on the emission lines, the VFF—which is defined as the inverse of the clumping factor ($D_{cl} = 1/f_{VFF}$)—was changed from 0.1 to 0.3 (Fig. 4.7). The slope of the SED was influenced by larger clumps ($f_{VFF} = 0.1 - 0.2$), while the line strengths were primarily influenced by smaller clumps.

According to Fig. 4.7, the modeled and observed strengths of C III λ5696 and C IV $\lambda\lambda$ 5802-12 matched most closely at $f_{VFF} = 0.27 - 0.3$, whereas He I λ5876 aligned closely at $f_{VFF} = 0.2$. The C III λ5696 transition was also found to be more vulnerable to fractional changes in clump size than C IV $\lambda\lambda$ 5802-12. The line strengths were significantly changed by even small changes in clump size, indicating that the optically thin regions of the stellar winds contain clumps of different sizes. These clumps are most likely the result of velocity perturbations that are caused by instabilities at the base of the wind.

4.4.3 Driving mechanisms

We looked at the physical processes responsible for driving the stellar winds and the pulsations observed in the spectroscopic and photometric time-series observations. It was found that the primary factors affecting the radiative envelopes of such an expanding stellar atmosphere were radiation pressure and opacity. In the subsequent subsections, the respective roles are investigated.

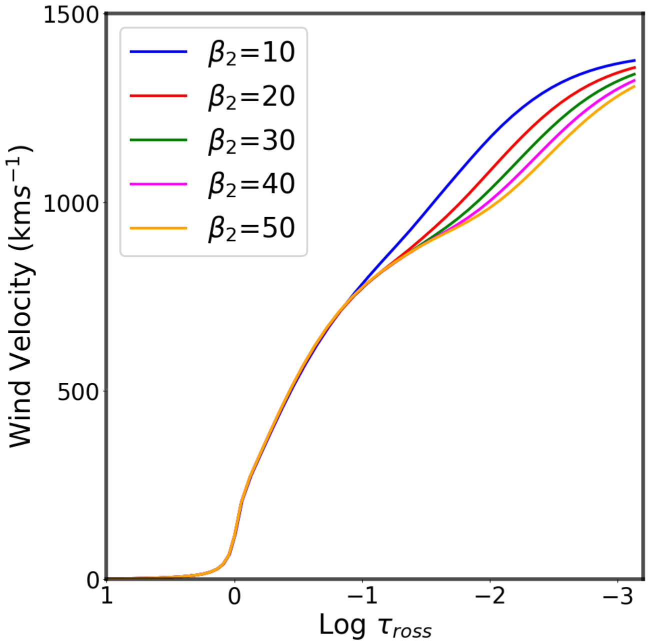

(a) Velocity profiles corresponding to different β_2 values.

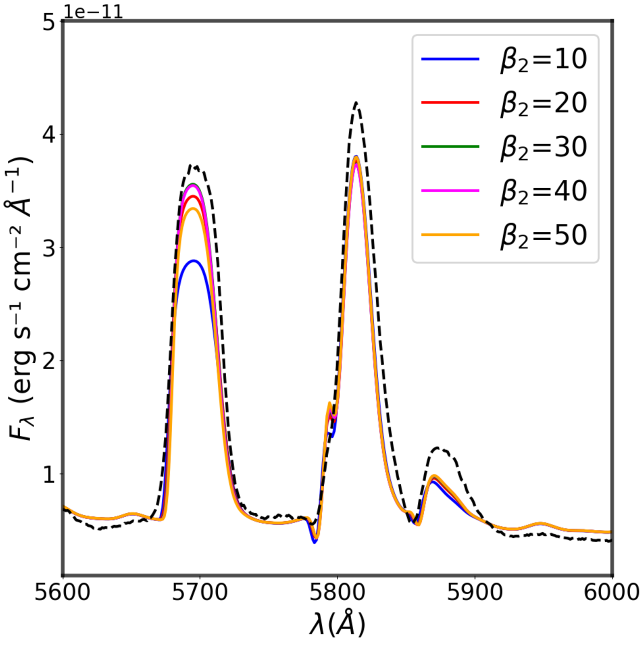

(b) Corresponding changes in the emission line strengths. The black-dashed curve indicate the observed emission lines of the spectrum.

Figure 4.6: Impact of the acceleration exponent (β_2) on the diagnostic emission lines that are not blended (for $f_{VFF} = 0.29$). The line strengths are influenced by the outer wind (τ_{ross} >0.1) density, which is influenced by the β_2-exponent.

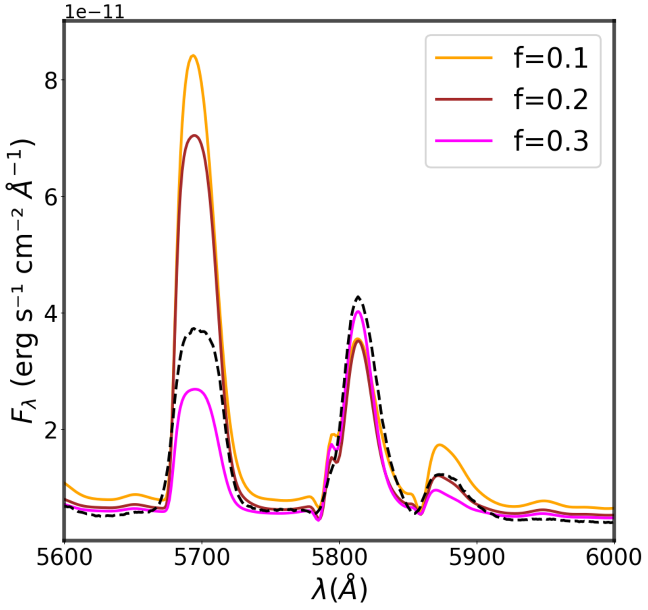

(a) Clump size variation (coarse)

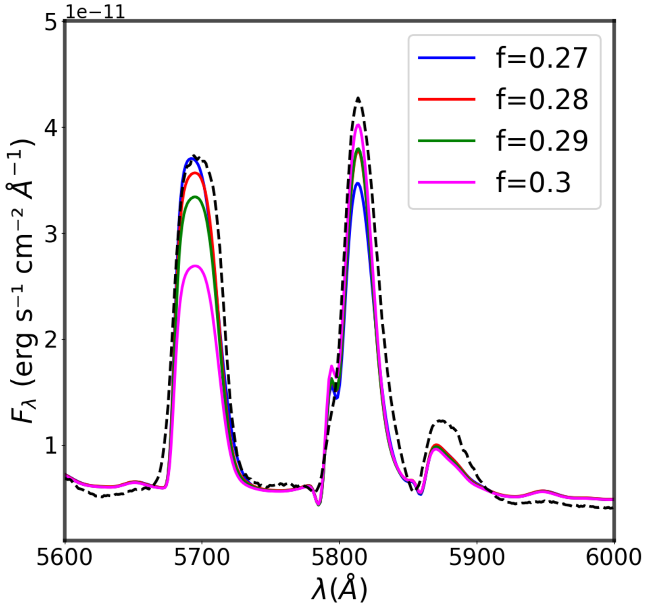

(b) Clump size variation (fine)

Figure 4.7: The unblended diagnostic emission lines are affected by VFF for a fixed outer-wind acceleration exponent ($\beta_2 = 50$). A black-dashed curve represents the observed spectrum. Also, the models that are computed for varying VFF values are labeled.

Role of Pressure

A steady decline in the $P_{\mathrm{gas}}/P_{\mathrm{rad}}$ curve was noted in Fig. 4.8 (a) as radiation pressure (P_{rad}) took over in the stellar atmosphere outside of the stellar surface (R_*). The slope of the curve became less steeper as the wind reached supersonic velocities above the photosphere ($\tau_{\mathrm{ross}} \leq 1$). The gas maintained its dominant isothermal sound speed ($\sim$25 km s^{-1}) until it reached the sonic point, R_s (at $\tau_{\mathrm{ross}} \sim 1.7$). Beyond R_s, the stellar winds were more strongly influenced by radiation pressure (see Fig. 4.8 (a)).

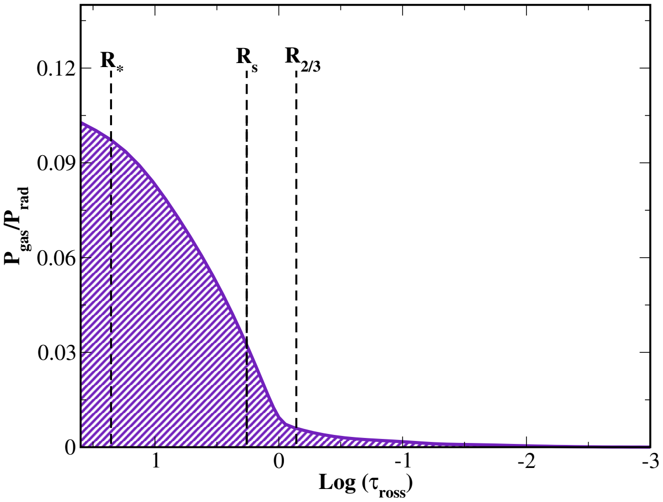

(a) Overall

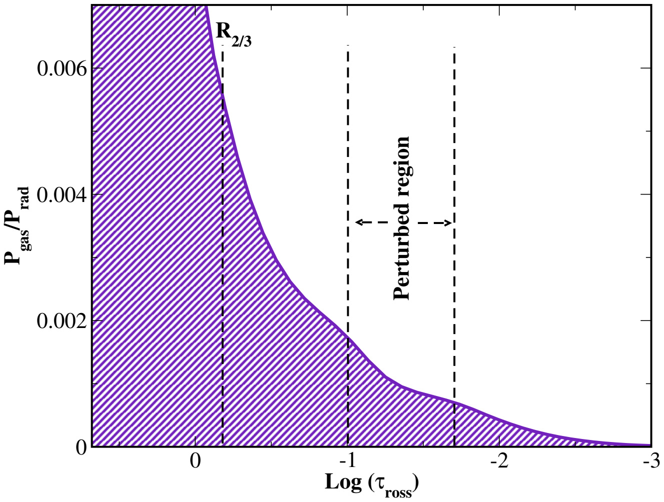

(b) Ouer winds

Figure 4.8: Stratification of the gas pressure (P_{gas}) relative to the radiation pressure (P_{rad}) in the model atmosphere of WR 135. The P_{gas} becomes almost negligible in the supersonic regime as the P_{rad} increases.

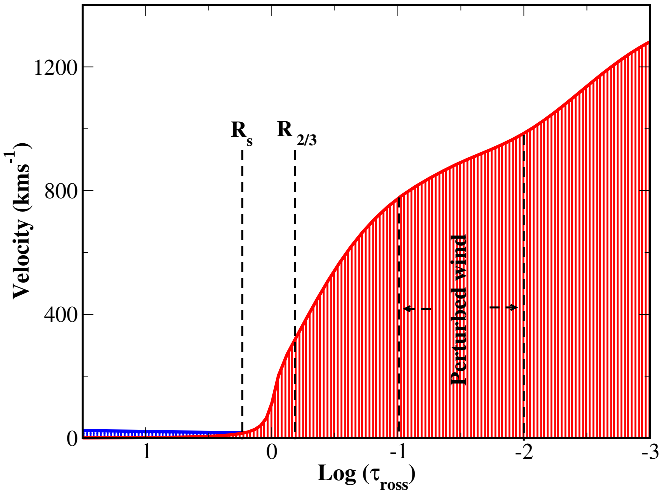

(a) Overall atmosphere

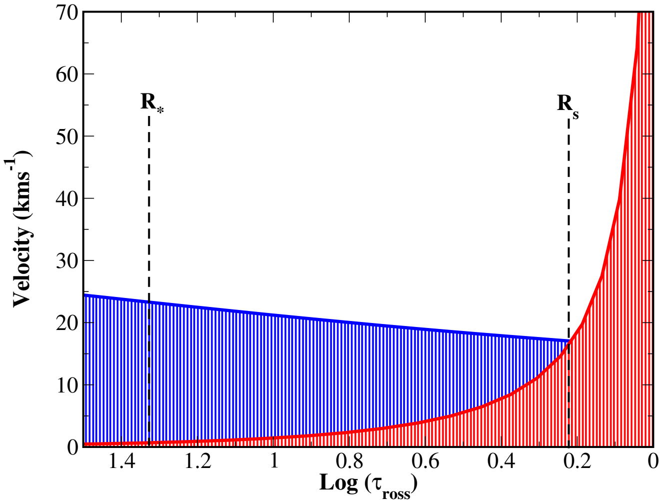

(b) Inner layers

Figure 4.9: The model atmosphere of WR 135 exhibits velocity stratification, which is characterized by isothermal sound speed (in *blue*) and wind velocity (in *red*). Beyond the sonic point (R_s), the mass outflow adheres to the wind velocity profile.

The $P_{\rm gas}/P_{\rm rad}$ curve (Fig. 4.8 (b)) revealed a change in slope (designated as the perturbed region) in the radiation pressure within the same optical depths ($\tau_{\rm ross} = 0.1 - 0.01$) as the velocity. This characteristic was ascribed to the two-component velocity law, which reflected the hydrodynamic wind's properties as reported by Sander et al. (2020) for WR 111 (a WC5-type star).

Role of opacities

Line opacities influence the origin of emission lines, which are generated in distinct stellar wind regions. On the other hand, the continuum opacity is determined by a variety of transitions (free-free, bound-free, and Thomson-scattering processes) that transpire throughout the volume of the stellar winds and are not influenced by wavelength.

The stellar model revealed that the mean-Rosseland and mean-flux opacities (Fig. 4.10) exhibit analogous behavior up to the sonic point. Analysis (Fig. 4.11 (d)) revealed that Fe VII-IX bound-bound transitions were the driving force behind the inner sub-sonic winds. The stellar surface ($\tau_{\rm ross} \sim 20$) and sub-photospheric layers were both near the Eddington limit, as evidenced by the results (Fig. 4.12). The Fe-opacity peak was found to be deeply embedded in the convective layer beneath the stellar surface (R_c), which caused the outer radiative envelopes to inflate (Gräfener & Vink, 2013) and the stellar radius to increase. As a result, the sonic point (R_s) was located in a region with lower optical depth. The majority of optically thin transitions occurred at a particular optical depth ($\tau_{\rm ross} \sim 0.1 - 0.01$), which was identified as the cold opacity bump (COB), where both mean-Rosseland and mean-flux opacities changed abruptly. In comparison to the mean-flux opacity, the electron-scattering (Thomson) opacity had a negligible effect on the wind-driving mechanism.

The formation zones of the emission lines in the stellar winds are marked by the respective line emissivities. According to emissivity analysis (Fig. 4.13), it was found that C IV $\lambda\lambda$ 5802-12 peaks at $\tau_{\rm ross} \sim 0.1$ indicating that it originates at an optical depth deeper than the sonic point (R_s), whereas C III λ5696 exhibited peak emissivity at approximately $\tau_{\rm ross} \sim 0.03$, indicating that the associated upper-level UV transitions, C IV λ193 and C III λ312, possess significant opacities within the same range ($\tau_{ross} \sim$ 0.1-0.01).

The opacities of He II and C IV were identified as the primary factors driving the optically thin wind ($\tau_{\rm ross} \sim 0.1 - 0.01$). This conclusion was supported by enhanced excitation of C^{+3} and He^{+1} ions, as shown by their relative population density (Fig. 4.11 (a) and (b)) within the same region. As a result, the He II and C IV transitions contributed more to the mean-flux opacity in those regions of the supersonic winds than did the O III-IV and Fe III-VI opacities. There was a discernible shift in the decreasing slope of the $P_{\rm gas}/P_{\rm rad}$ curve at the same optical

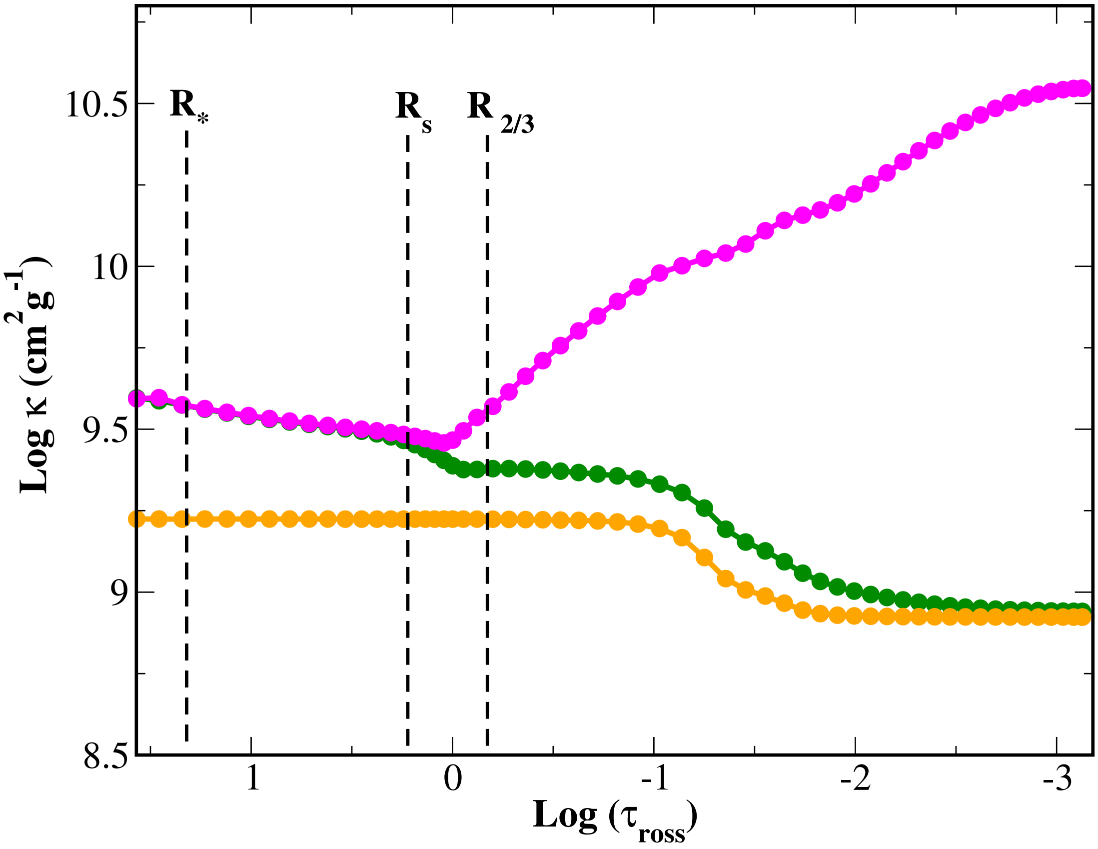

Figure 4.10: Comparison of the electron-scattering (or Thomson in *orange*), mean-flux (in *magenta*), and mean-Rosseland (in *green*) opacities contributed by various atomic species in the stratified winds of the model atmosphere (in Fig. 4.11).

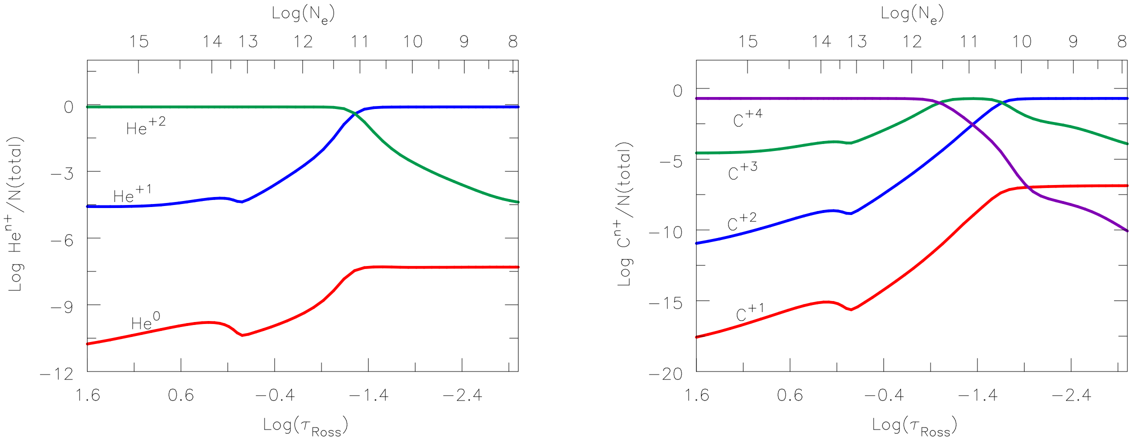

(a) Helium (b) Carbon

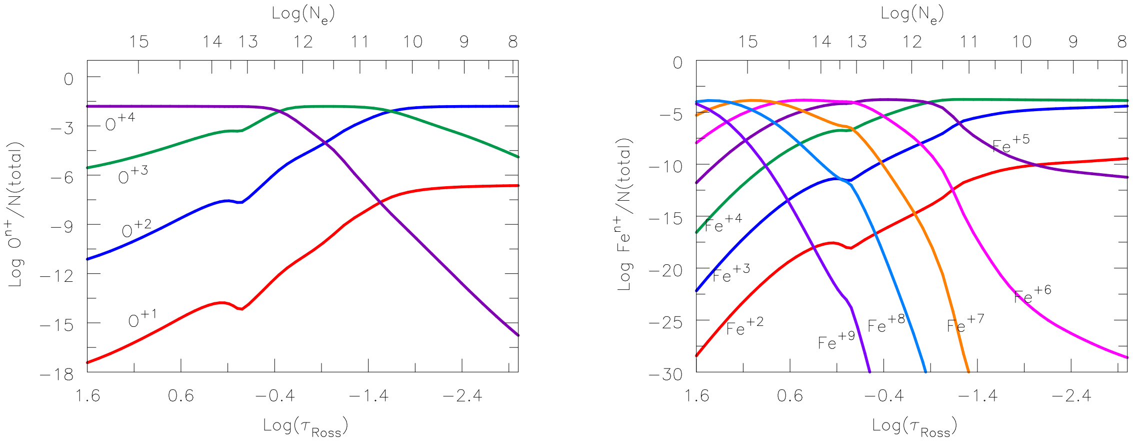

(c) Oxygen (d) Iron

Figure 4.11: Relative ionic distribution of the predominant atomic species influencing the opacities (in Fig. 4.10) that affect various layers of the model atmosphere.

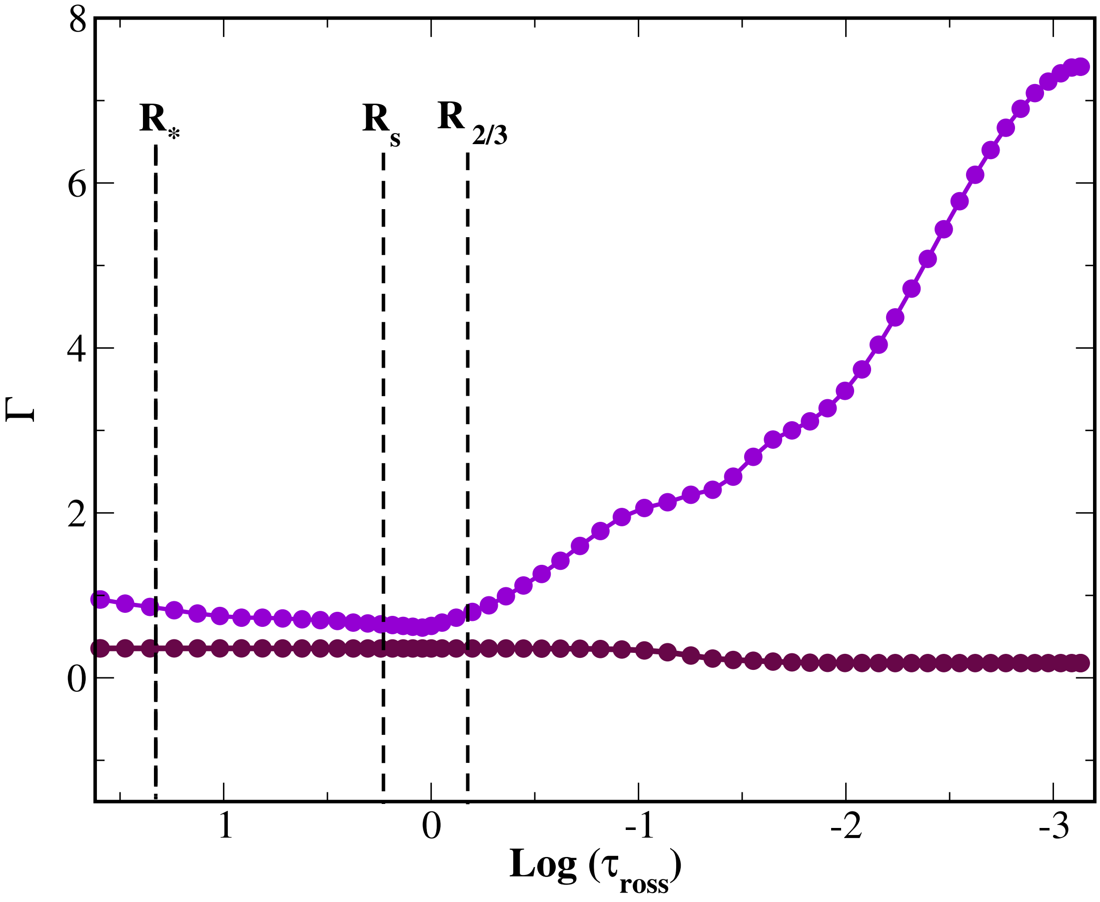

Figure 4.12: Atmospheric stratification of the Thomson scattering acceleration (Γ_{elec}, in *maroon*) and radiative acceleration (Γ_{rad}, in *violet*) with respect to the gravitational acceleration are displayed.

depths (Fig. 4.8(b)). It was discovered that the wind in these atmospheric layers is driven by the C IV and He II UV transitions, which result in increased opacity and enhanced radiation pressure.

4.5 Discussion

From our analysis, WR 135 was found to oscillate predominantly with its fundamental frequency (Sec. 4.4.1). Considering the frequency to be associated with a rotating star with $R_* = 6.5\,R_\odot$ and $M = 21\,M_\odot$, the corresponding rotational velocity was found to be near the star's breakup velocity (640 kms^{-1}). The hypothesis that the star is part of a binary system with a compact object (10 $M_\odot$) at a separation of $8.54\,R_\odot$ affecting the observed period was dismissed, as this distance is too close to the photosphere. In light of this, the variability was de-

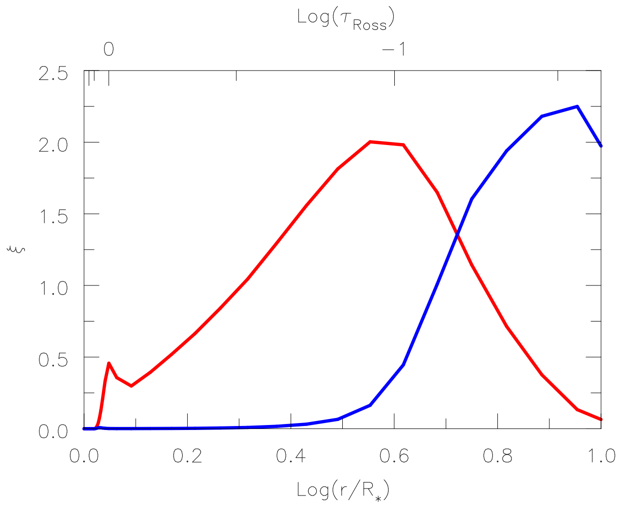

(a) Inner region

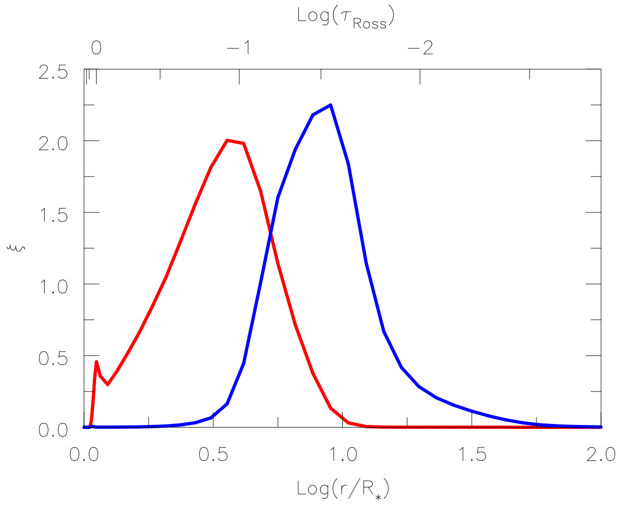

(b) Overall region

Figure 4.13: The line formation region in the model atmosphere is depicted by the emissivity plots for C IV $\lambda\lambda$5802-12 (in *red*) and C III λ5696 (in *blue*).

termined to be unrelated to either stellar rotation or a binary companion. The fundamental pulsation frequency was accompanied by multiple harmonics in all observed epochs (TESS Sectors 41, 54, and 55). Optical photometric light curves detected harmonics up to the sixth order, while the variability of optically thin emission lines sampled at regular intervals revealed higher-order harmonics (up to the eighth order).

With zero phase difference, the line strengths of C IV $\lambda\lambda$ 5802-12 and C III λ5696 displayed the same variability period (Sec. 4.4.1), demonstrating coherent temporal behavior brought on by regular variations in line opacities. As seen in Fig. 4.13 (a), emission line formation was concentrated in the inner layers of the stellar atmosphere, which made them susceptible to higher-order harmonics. The optically thin supersonic winds' (Fig. 4.9) line formation region was dominated by smaller clumps ($f_{VFF} = 0.27 - 0.3$) that were found to be involved in these transitions (Sec. 4.4.2). It was discovered that the outer winds were further influenced by the COB (Fig. 4.10) at the same optical depth. The clump sizes increased as the radius increased ($f_{VFF} = 0.2$), which impacted the properties of optically thin winds. Due to less flux scattering, smaller clumps made it easier to identify high-order frequencies with small amplitudes in the line strength variations of C IV and C III. Larger clumps were responsible for overall flux (line and continuum opacity) and bound-bound transitions (He I λ5876). Consequently, it was established that clumps of varying sizes were present at distinct optical depths, influencing opacities and pulsing at harmonics of the fundamental frequency (2.73 day^{-1}), with all clump types contributing to the stochastic variability in WR 135.

Pulsations in WR stars, like WR 123, have been ascribed to either strange modes induced by SMIs (Dorfi et al., 2006) or gravity modes from the κ-mechanism (Townsend & MacDonald, 2006). Pulsations from the κ-mechanism, associated with an opacity peak caused by Fe L-shell transitions at $T = 10^{6.25}$ K, matched observed periods but presented problems with respect to the assumed stellar radius. Strange pulsation modes, on the other hand, required high hydrogen abundance and showed shorter periods (e.g., $X = 0.35$ for WR 123). Nevertheless, Glatzel (2008) proposed that non-linear shock-induced inflations from SMIs might prolong strange-mode periods in He-Zero Age Main Sequence (ZAMS) stars that are depleted of hydrogen and resemble cWR stars.

We discovered that radiative envelope inflation (Gräfener & Vink, 2013) was the result of intense Fe-opacity (Fe VII-IX transitions) beneath the stellar surface (Sander et al., 2020), which subsequently produced SMIs. Those SMIs initiated the strange-mode acoustic waves (Glatzel, 2008), which resulted in the observed pulsations in WR 135. The radiative inflation was concluded from the derived stellar radius (R_* at $\tau_{\rm ross} = 20$) which is slightly larger than the hydrostatic core radius ($R_c = 6.49\,R_\odot$; Fig. 4.10). Also, we noted that in the non-linear regime, the same SMIs lead to the density inhomogeneities (clumps) in the stellar winds. Inflation of the radiative envelope, leading to density inversion, was noted by Gräfener et al. (2012), in a static He-ZAMS star without wind-driven mass loss. However, the hydrodynamic CMFGEN models, which mainly analyze the optically thin atmospheres that are not affected by the dense optically-thick hydrostatic layers. Therefore, the CMFGEN models were unable to fully capture density stratification between R_c and R_*.

On the other hand, pulsations may have been the consequence of self-excited waves near the wind base that were induced by velocity perturbations. Sound waves generated in the subsonic wind region can be amplified in supersonic winds through LDIs, as described by Owocki et al. (1988). The radiation pressure beyond the sonic point converted these waves into inward radiative-acoustic modes that were moving at a rate that was faster than the characteristic outflows (Abbott, 1980). Upon reaching the optically thin supersonic region ($\tau_{\text{ross}} = 0.1 - 0.01$, such amplified sound waves are detected through spectroscopic and photometric observations.

In pure He-ZAMS stars with $M > 14\,M_{\odot}$, radial SMPs were shown to be damped Grassitelli et al. (2016) and their amplitude decreased with increasing mass (Glatzel, 2008). WR 135 ($M \sim 21\,M_{\odot}$; $C/\text{He} = 0.25$) chemically resembled a He-ZAMS star, where radial strange-mode pulsations would exhibit small amplitudes. Nevertheless, neither Nazé et al. (2021) nor we (see Fig. 4.3) observed such reduced amplitudes connected to the pulsations. As an alternative, it was thought that WR 135 exhibits non-radial pulsations. In addition, the fundamental period (8.8 hours) of WR 135 was found to be nearly identical to the 9.8-hour period observed in WR 123 (WN8-type) by Lefèvre et al. (2005) and Chené et al. (2011), with minor variations attributed to their respective MS progenitors.

4.6 Conclusion

This study examined the mechanisms that drive the stellar winds in WR 135, a pulsating WCL star. The LSP analysis of photometric and spectroscopic temporal datasets revealed higher-order harmonics of the pulsation up to the 8th order. In order to investigate the physical conditions in the stellar atmosphere, spectroscopic models that best fit the observed data were built using CMFGEN. It was found that the stellar winds were dominated by radiation pressure, which maintained a hydrodynamic outflow.

It was found that inner subsonic winds lay near the Eddington limit and the opacity from Fe VII-IX transitions was found to be sufficient to drive them. On the other hand, the He II and C IV opacities affected the outer supersonic winds. The same Fe-opacity was proposed as a possible driver for SMPs, which generate different pulsation harmonics, and SMIs, which create wind inhomogeneities (clumps).

It was found that a large fraction of the stellar winds were made up of the gas that produced the unblended optical emission lines (such as C IV and C III). This suggested that both transitions involved clumps of similar size (Lépine et al., 2000). The size of the clumps inside the stellar winds was found to have a significant impact on the detected harmonics. C IV and C III recombination transitions involved smaller clumps that oscillated at higher-order harmonics. These clumps grew larger and dominated the outer winds as the radial distance increased in the less-accelerated areas of the winds. These larger clumps were mainly responsible for the overall variability of the winds and neutral He I transitions.

Chapter 5

ML based identification of galactic WR stars

In this chapter, I discuss the application of ML techniques for robust classification of the Galactic WR stars. This work is published as Kar et al. (2024a).

5.1 Introduction

In order to differentiate between WR candidates and non-WR objects, selection criteria that are based on narrow-band IR colors and magnitudes, as developed by Mauerhan et al. (2011); Hadfield et al. (2007), have been effective. Excess color in the IR, resulting from circumstellar dust emission or free-free transitions facilitates the detection of WR candidates from the photometric two-color diagrams. Manual classification efforts have become increasingly impractical due to the increasing availability of extensive IR survey data in recent decades (e.g., 2MASS, IRTF, WISE, Herschel). ML techniques are recognized as effective tools for processing large datasets, offering a robust and adaptable framework for stellar classification. Earlier studies have shown the application of ML for classifying different types of stars. Morello et al. (2018) used KNN which is a distance-based algorithm, while SVM was used by Dorn-Wallenstein et al. (2021). However, those works utilized small datasets with several constraints leading to the limited scope of application. Also, Yoshino et al. (2023) showed that for stellar classification tasks, ensemble-based algorithms like eXtreme Gradient Boosting (XGB) and RF consistently outperformed simpler models like *Decision Trees*, KNN, and SVM.

In this work, we employed XGB methods to construct a highly efficient stellar classifier optimized for identifying WR stars using a handful of IR colors and astronomical positions. The classifier was designed to process large datasets containing a diverse range of bright-IR stellar objects. Sec. 5.3 describes the approach used to create the classification models, and Sec. 5.4 presents the findings, along with a comparison with other ensemble approaches like RF. Furthermore, Sec. 5.4.2 addresses the utilization of ML models to differentiate between WR subtypes (WC and WN) and non-WR stars. In Sec. 5.4.3, I have provided a list of novel WR star candidates, including their chemical subtypes, predicted by both the models from an unlabeled and previously unseen Galactic stellar dataset. Sec. 5.5 discusses how well these models perform in comparison to more conventional color-selection techniques. Sec. 5.6 provides a summary of the study's findings.

5.2 Observed data

The apparent photometric magnitudes of the stellar objects in the NIR and MIR were obtained from the InfraRed Science Archive (IRSA), hosting the 2MASS and the WISE. The photometric observations from 2MASS covered three broad bands: J, H, and K_s with wavelengths centered at 1.25 μm, 1.65 μm and 2.16 μm respectively. The WISE data comprised observations in four broad bands: 3.4 μm (W1), 4.5 μm (W2), 12 μm (W3), and 22 μm (W4). We selected sources with object-type flags from the SIMBAD database and used the Vizier catalogs from the WISE and 2MASS surveys: II/328/allwise (Cutri et al., 2021) and II/246/out (Cutri et al., 2003) respectively to cross-match them within a 5-arcsec radius. To alleviate problems arising from the high concentration of sources near the Galactic Center, redundant sources were additionally removed through cross-matching within a 1" radius. In addition to the WR stars, the dataset contained other stellar objects. These included Asymptotic Giant Branch (AGB) stars (that also included OH/IR and Mira subtypes), MS stars, Be stars, Ae stars, R Coronae Borealis stars (RCrB) stars, RV Tauri Variables (RVTauV), S-type stars, High Mass X-ray Binaries (HMXB), Eclipsing Binaries (EB), Emission line stars (Emline) stars, Carbon stars (C) stars, Yellow SuperGiants (YSG), Planetary Nebula (PN), RR Lyrae variables, Long Period Variables (LPV), Symbiotic stars, High Proper Motion stars (High PM) stars, Beta Cepheid Variables (bCepV), Red Giant Branch stars (RGB) stars, Orion Variables (OrionV), Hot Sub-dwarfs, Young Stellar Objects (YSO), Horizontal Branch stars (HB) stars, Variables, Pulsars, BSG, post-Asymptotic Giant Branch stars (pA), Classical Cepheids (Ce), and RSG.

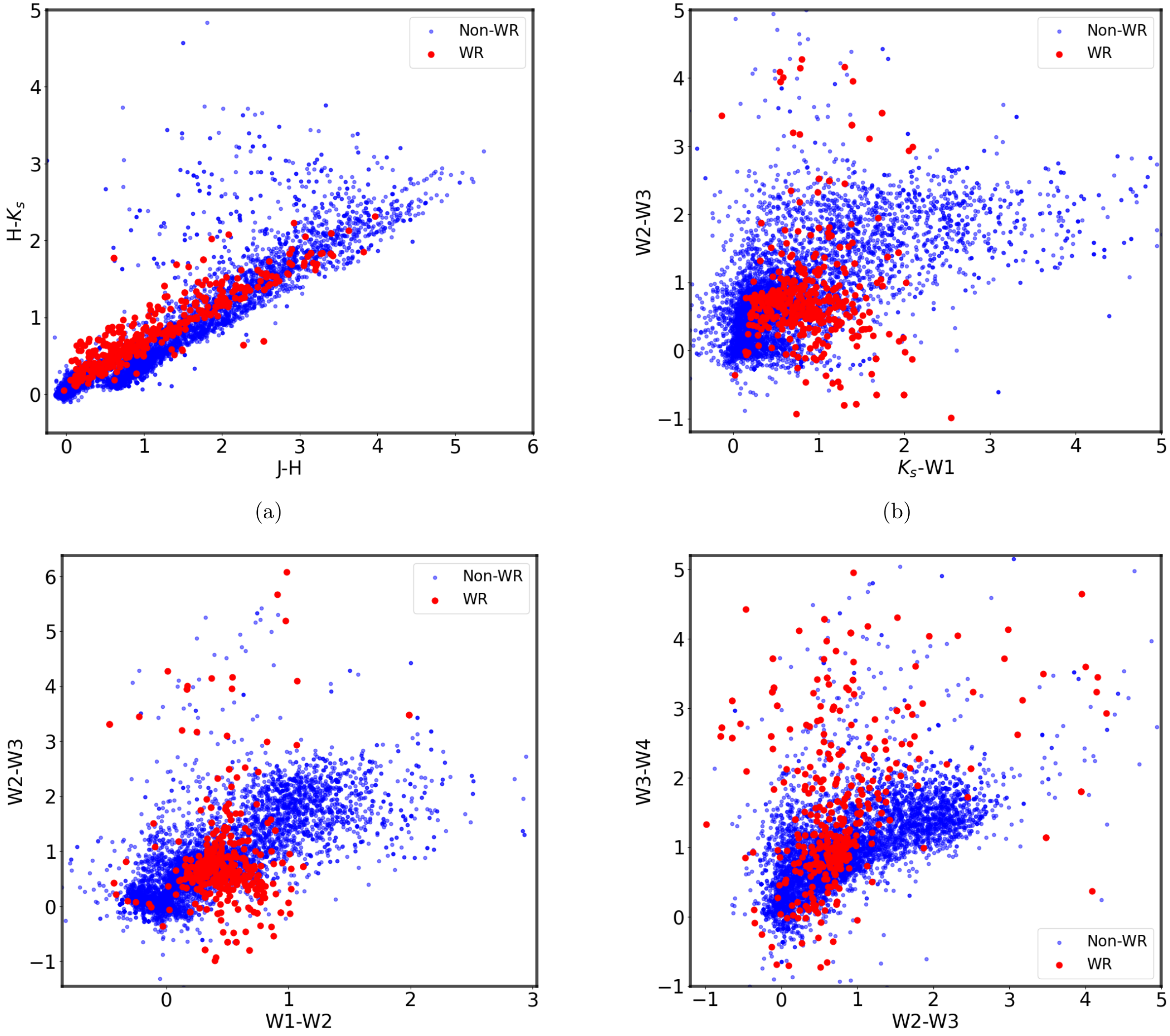

(a) (b) (c) (d)

Figure 5.1: IR color-color diagrams that highlight the unique characteristics of WR candidates (in *red*) in the MW in comparison to non-WR candidates (in *blue*). The non-WR sources encompass a variety of objects stated in Sec. 5.2.

5.3 Methodologies

The methodology described in the subsequent subsections (Sec. 5.3.1-5.3.5) was implemented in this investigation. Sorting the data and choosing the model features were part of the pre-processing of the dataset before the ML model was defined.

5.3.1 Data and Feature Sorting

In order to rule out objects that are part of the Magellanic clouds, we selected stellar sources with declinations greater than -63°.5. We selected a total of 10,242 Galactic stellar objects with apparent magnitudes available in the WISE ($W1$, $W2$, $W3$, $W4$) and 2MASS (J, H, K_s) bands. Additional filtering was implemented in accordance with the quality of the 2MASS photometric data, resulting in the selection of only objects classified as A, B, or C. These flags indicate varying degrees of data quality, with A indicating a high S/N and D marking the poor data quality, as outlined in Skrutskie et al. (2006). Furthermore, the selection process took into account the completeness and sensitivity limits of each photometric band, as indicated by Morello et al. (2018).

To identify regions with a high concentration of WR stars in the dataset, the color space was manually inspected following Mauerhan et al. (2011). After this inspection, the following criteria were used for selection: $J \in [5, 17]$, $H \in [5, 15]$, $K_s \in [2, 14]$, $W1 \in [3, 15]$, $W2 \in [3, 15]$, $W3 \in [0, 10]$, and $W4 \in [0, 9]$. As shown by Mauerhan et al. (2011), these constraints enhanced sampling efficiency and raised the probability of WR star identification.

The two-color diagrams of the final sorted dataset (henceforth referred as Dataset-1) with 6,555 stellar objects are presented in Fig. 5.1 while Fig. 5.2 shows the census of the objects considered in the dataset. While WR stars made up about 7% of the total population, the majority of the stars in the dataset were Be-type and AGB stars. The category “Others” was applied to objects with fewer than 40 occurrences (refer to Table 5.1). Objects such as pAs, PNe, and YSOs were excluded as a result of the employed color-selection criteria. However, the model's performance was not impacted by the exclusion of these sources, as long as the same color cuts were implemented on the datasets used for training and testing.

Discrete values were assigned to a label column: 1 for WR stars and 0 for non-WR objects, as documented in the SIMBAD database. The non-WR sources (6,122 objects) irrespective of their spectral type were treated as a single, majority class, while the WR stars (433 objects) represented the minority class. This binary classification approach introduced a substantial class imbalance, simplifying model implementation in comparison to a previous classification study (Morello et al.,

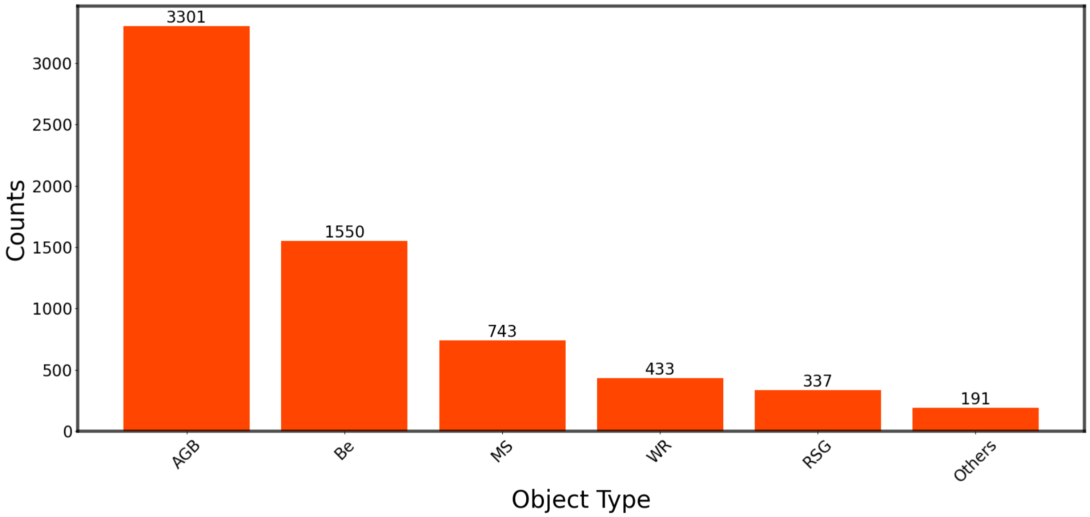

Figure 5.2: Distribution of stellar candidates in Dataset-1, grouped by object type.

2018) that evaluated each stellar group as a distinct class of object. Class imbalance arises when the minority class is inadequate in population, resulting in models that exhibit bias towards the majority class and demonstrate suboptimal performance on the minority class. To address the class imbalance, the *RandomOversampler* module from the *imbalanced-learn* library[1] was used. Random oversampling involves duplicating randomly selected instances from the minority class to balance the dataset. This methodology enabled the classifier to acquire knowledge from a distribution that was more representative and made predictions that were more accurate for the minority class. Although under-sampling the majority class was an alternative, it was avoided due to the risk of underfitting.

In the second phase of this study, an alternative dataset (Dataset-2) was utilized, incorporating an extra column that classified the WR chemical subtypes into distinct categories. We assigned a label of 0 to the non-WR objects, 1 to the WC subtypes, and 2 to the WN subtypes. WO-type sources were excluded from the dataset because their limited number holds the potential to introduce a significant imbalance that could affect accuracy. Cross-matching of the database with SIMBAD was performed to identify WR candidates with established spectral types, confirming their presence within the identical IR color space as the entities in Dataset-1. The population distribution of various spectral types in Dataset 2, which includes 6,510 candidates, is depicted in Fig. 5.3. To address the class imbalance in Dataset-2, we used the random oversampling technique to resample the minority classes (WN and WC).

We divided both the balanced datasets (Dataset-1 and Dataset-2) randomly into respective training and testing subsets. Of the samples, 80% were chosen for the

---

[1] `https://imbalanced-learn.org/stable/index.html`

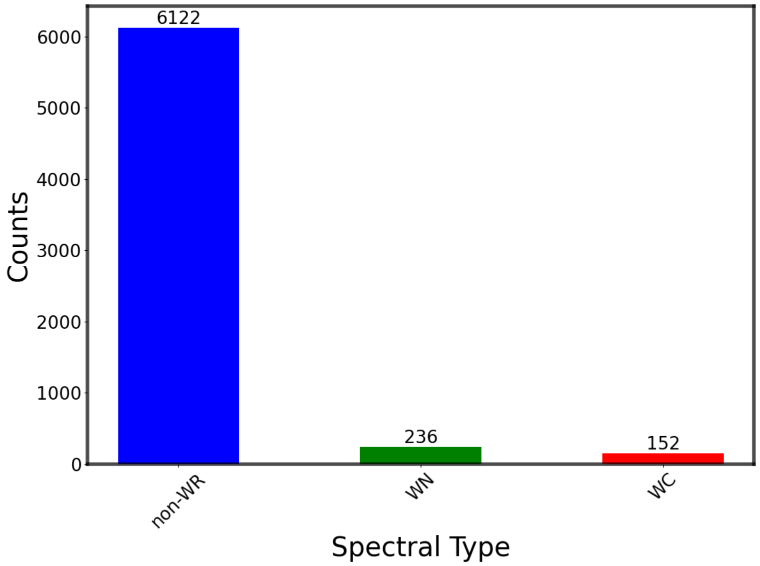

Figure 5.3: Population distribution of WR subtype against non-WR stellar candidates in Dataset-2.

Table 5.1: Stellar sources with populations below 40, grouped under "Others" (refer to Sec. 5.3.1).

Object Type	Population
LPV	33
HMXB	36
C	31
Ae	13
S	25
RGB	8
bCepV	13
Star	8
BSG	5
Emline	4
HB	2
PNe	3
OrionV	2
RVTauV	2
Ce	2
Pulsar	1
Symbiotic	1
Variable	1
Total	191

training (Trd-1 and Trd-2), and the remaining 20% for the testing (Tsd-1 and Tsd-2).

Positional characteristics (Right Ascension and Declination) and IR colors ($J-H$, $H-K_s$, $J-K_s$, $W1-W2$, $W2-W3$, $W3-W4$, and K_s-W1) were chosen as the model features. Magnitudes were excluded from consideration due to the lack of proper extinction estimates and distance values for the entire data sample. Although IR colors are susceptible to distance-dependent extinction effects, these effects are less severe than their influence on optical colors or magnitudes. Positional coordinates (RA and DEC) have been effective as model features to identify Cataclysmic Variable (CV)s within the MW and nearby galaxies, in conjunction with other observational attributes (Mistry et al., 2022)). In many cases, stars of a particular class are concentrated in specific regions of a galaxy, which facilitates their identification regardless of the galaxy in which they are situated. As a result, it was anticipated that the detection of WR stars, particularly those within the MW, would be improved by the utilization of positional attributes as model features. The dataset consisted of a substantial number of sources that were dispersed throughout the observable disc of the MW, with no discernible bias toward the galactic plane (refer to Fig. 5.4). As a result, the model was optimized for the identification and classification of WRs within the MW. However, its applicability beyond the MW is not recommended.

5.3.2 ML algorithms

This study used two supervised ML algorithms (see Sec. 2.5 for an overview): RF[1] and *Gradient Boosting* (GB) (Friedman, 2001), both of which were implemented using the *Scikit-learn* library (Pedregosa et al., 2011). These models were trained using labeled datasets, enabling predictions and classifications over extensive datasets. Through the provision of labeled examples, supervised learning enabled the models to recognize patterns and generate precise predictions for data that had not been previously observed.

The ensemble-based classification models are generally defined using the following parameters:

- *n_estimators*: Specifies the number of base learners (in this case *decision trees*) to be used in the ensemble.
- *max_features*: Defines the maximum number of features each base learner can use, controlling feature randomness and reducing overfitting.

---

[1] `https://scikit-learn.org/stable/modules/ensemble.html`

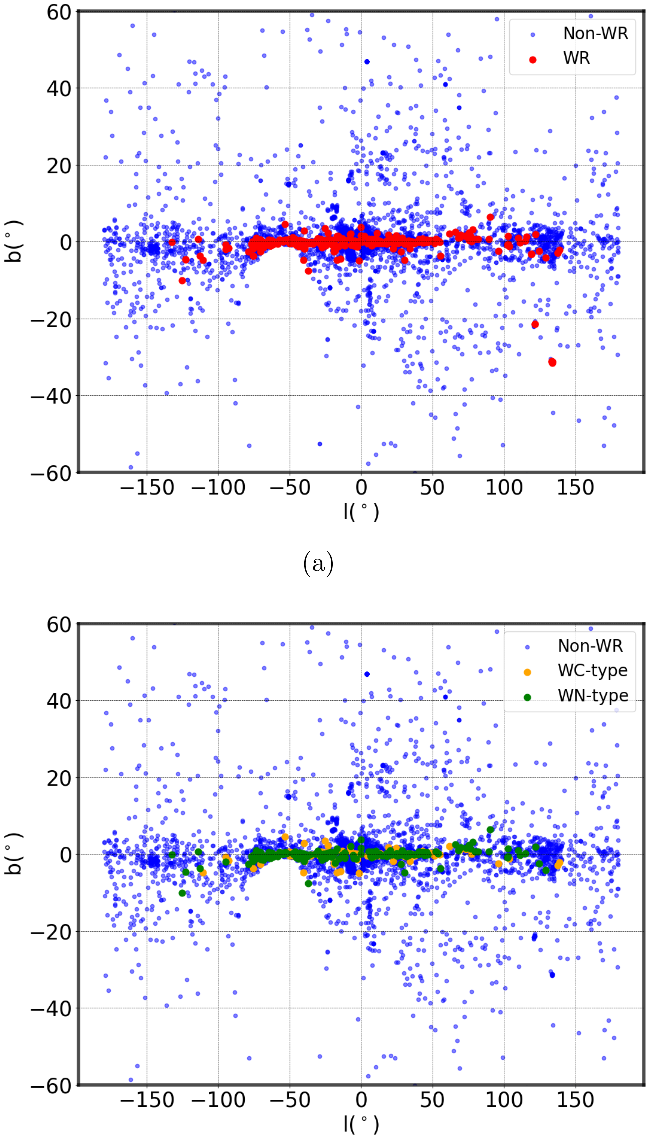

(a)

(b)

Figure 5.4: Distribution of stellar sources based on their positions: (a) Dataset-1 (*blue*: non-WR candidates, *red*: WR candidates) and (b) Dataset-2 (*blue*: non-WR candidates, *orange*: WC-type, *green*: WN-type objects).

- *max_depth*: Sets the maximum depth of each base learner, balancing model complexity and risk of overfitting.
- *subsample*: Determines the fraction of the training data randomly sampled for each base learner, helping to prevent overfitting and improving generalization.

XGB Classifier

We made use of the XGB[1] (Chen & Guestrin, 2016) library, which is an improved version of the GB classification algorithm (see Sec. 2.5.2). This approach employs a boosting strategy in which multiple weak learners are combined to form a robust predictive model. Based on feature values, a base learner iteratively splits the feature space into smaller regions. The model's predictions are contained in each *leaf node*, each *branch* indicates the decision's outcome, and each *internal node* represents a decision criterion. The outputs from the ensemble of weak learners are aggregated to compute the *training loss* function, which is subsequently used as input for the next learner in the sequence. Sequentially, learners were built with the goal of minimizing the cumulative loss of the ensemble while using *regularization* to reduce overfitting. The XGB implementation was designed to outperform traditional GB by allowing parallel construction of base learners, thereby improving computational efficiency when handling large datasets.

In addition to the standard parameters (see Sec. 5.3.2), the XGB classifier model also relied on other parameters, such as:

- *learning_rate*: Controls the step size for updating feature weights in subsequent learners, balancing convergence speed and model performance.
- *min_child_weight*: Specifies the minimum sum of instance weights required in a leaf node, acting as a regularization parameter to prevent overfitting.
- *min_split_loss*: Sets the minimum loss reduction required for a leaf node to split, ensuring splits only occur when they provide meaningful improvements.

Recent research, including Gomes et al. (2023) and Chao et al. (2019), has illustrated the efficacy of XGB algorithms in a variety of applications. These applications include regression tasks for predicting rotation periods and classification tasks for distinguishing between stars and galaxies.

---

[1] `https://github.com/dmlc/xgboost`

Random Forest Classifier

To serve as a benchmark, an RF classifier model was created, which was trained by an ensemble of trees using numerous random subsets of the features. In order to foster diversity among the trees, each tree in the forest was trained on a randomly selected subset of both the data and features. The *entropy* function was employed to determine the selection of features. Bootstrap aggregation (see Sec. 2.5.2) was applied to estimate the final model prediction from the ensemble of trees, helping to reduce overfitting. Due to this bootstrapping process, it was determined that RF models outperformed a single *decision tree* model. Similar to other ensemble algorithms, the RF depends on the basic model parameters (as discussed in Sec. 5.3.2). Compared to a sequential GB classifier, it was noted that RF classifiers with built-in parallelization were less susceptible to overfitting. To effectively assess the performance of the XGB model, the RF model was employed as a benchmark.

5.3.3 Evaluation of models

For the evaluation of the classifier models, we applied them to an unknown dataset to generate model predictions. These predictions were tabulated as confusion matrices. The performance of the models was further assessed using different metrics: Recall (R), Precision (P), f1-score (f1), and Accuracy (A):

$$R = \frac{TP}{TP + FN} \tag{5.1}$$

$$P = \frac{TP}{TP + FP} \tag{5.2}$$

$$f_1 = 2 * \left(\frac{1}{\frac{1}{P} + \frac{1}{R}} \right) = \frac{2TP}{2TP + FP + FN} \tag{5.3}$$

$$A = \frac{TP + TN}{TP + FP + TN + FN} \tag{5.4}$$

where FN, FP, TN, and TP denote False Negative, False Positive, True Negative, True Positive respectively. Recall measures the model's ability to correctly identify positive class instances, reflecting the proportion of true positives out of all actual positives. Precision, on the other hand, indicates the proportion of correctly predicted positive instances relative to all predicted positives, with higher values signifying fewer false positives. The f1-score, the harmonic mean of precision and recall, provides a balanced assessment of the model's effectiveness in predicting the positive class. Finally, accuracy (Eqn. 5.4) represents the overall proportion of correctly classified instances (both positive and negative) out of all instances evaluated by the model. WR sources were classified as the positive class in this investigation, while non-WR objects were classified as the negative class.

5.3.4 Significance of features

The significant features utilized in this study were identified based on the values of each performance metric (evaluated using Eqns. 5.1, 5.2, and 5.3). First, classifier models were created for every feature, and the feature with the highest f1-score (Eqn. 5.3) was determined. The Recursive Feature Elimination with Cross-Validation (RFECV)[1] method was employed to determine the best features significant for the classifier's f1-score. To avert data leakage, a pipeline was established that utilized the *RFE* function on the oversampled five-randomized subsets of the training dataset employing the *StratifiedKfold* technique (refer to Sec. 2.5.2), and the mean f1-score was computed. The best set of features was predicted by the classifier model using the cross-validation scores produced for each of the k-fold subsets. In cross-validation (explained in Sec. 2.5.2), the dataset is repeatedly divided into a predetermined number of subsets (in this case, k-fold), the model is trained on any combination of k-1 subsets, and it is tested on any k^{th} subset. Rather than relying on a single train-test split, this method reduces overfitting by verifying that the model performed consistently well across various data segments.

5.3.5 Tuning model hyper-parameters

Our classifier, utilizing the significant features, was trained and cross-validated on randomly oversampled subsets (employing the *StratifiedKfold* method) of the training dataset. We conducted a Bayesian optimization and optimized the f1-score using *optuna* (Akiba et al., 2019). From a grid of model parameters that produce the highest f1-score, the optimal set of hyper-parameters was determined. As a final step, an additional classifier model was established by utilizing the identified set of model hyperparameters and the significant features. The final classifier was trained on the entire oversampled TrD. We subjected the TsD to this model in the subsequent step and predicted the labels.

---

[1] `https://scikit-learn.org/stable/modules/generated/sklearn.feature_selection.RFECV.html`

Table 5.2: Final model parameters for the Object classifiers.

Model	Parameters	Values
RF	*max_depth*	None
	n_estimator	130
	max_features	sqrt
	min_samples_leaf	2
	min_samples_split	5
XGB	*max_depth*	3
	n_estimator	147
	min_child_weight	2
	learning_rate	0.66
	subsample	0.587

5.4 Results

5.4.1 Classification of WR stars

The optimal number of features for the classifier model was determined using the RFECV method (as discussed in Sec. 5.3.4). The RFECV curves for our set of model features are illustrated in Fig. 5.5.

It is evident that the mean f1-score for each of the stratified 5-fold randomized subsets of Dataset-1 increased as additional features were sequentially added. The model achieved its maximum predictive capability employing only these eight features, as evidenced by the fact that the mean f1-score reaches a saturation point beyond W3-W4. Consequently, the highest f1-scores were achieved by models that were constructed according to these features and are arranged in the same order (as illustrated in Fig. 5.5). These features were employed to create an additional XGB and RF classifier. These classifiers were trained over five randomly oversampled subsets of TrD-1 to determine the optimal set of hyperparameters (refer to Table 5.2) through the Bayesian Optimization method (see Sec. 5.3.5). The initial *decision tree* with model features and classification conditions of the final XGB model is shown in Figure 5.6. Based on the features' importance in object classification, the *decision tree* automatically chose and modified the feature order during training. Furthermore, the model functioned on the concept that if a feature value met the selection criteria ('yes'), it was forwarded to the subsequent internal node; if it did not (in this case, only 'no' was considered), it was sent to another pertinent internal node.

In order to evaluate the classifiers' performance, the Precision-Recall (PR) curve was derived (refer to Fig. 5.7). The RF classifier detected fewer FPs than the XGB

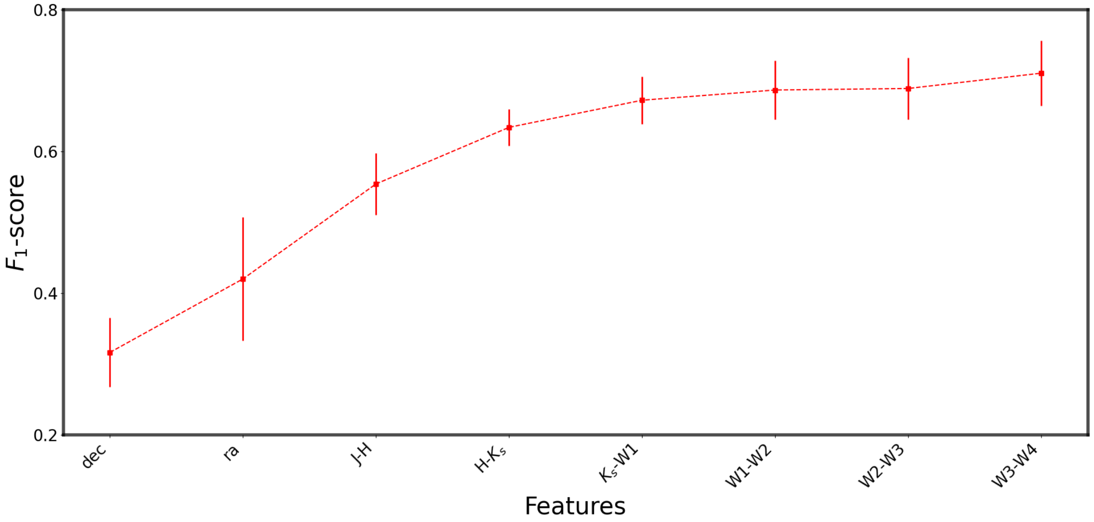

(a) RF model

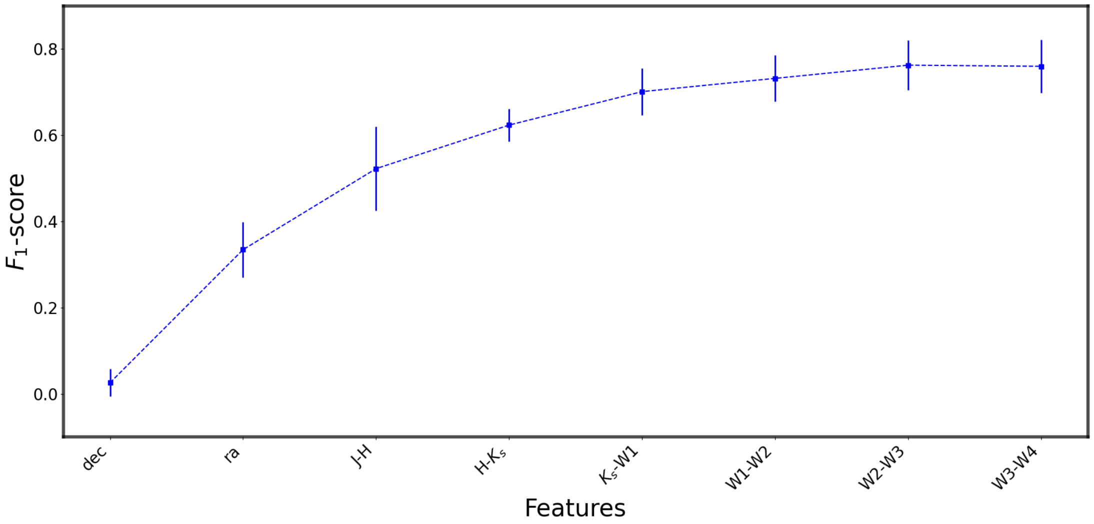

(b) XGB model

Figure 5.5: Plot showing the f1-metric scores of the models, evaluated with successive combinations of features (from left to right), demonstrate improved prediction efficiency, ultimately peaking with the inclusion of these 8 significant features.

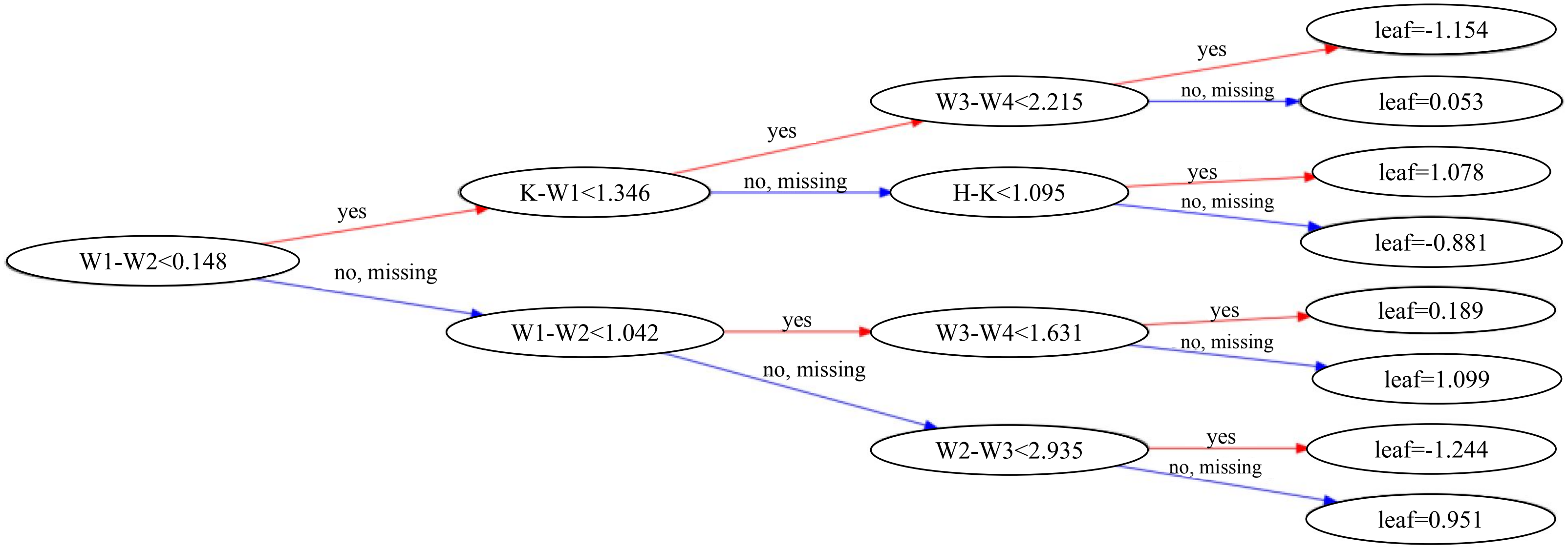

Figure 5.6: The initial *decision tree* (learner) of the XGB classifier. *Internal nodes* represent features that branch based on specific criteria, while *leaf nodes* contain the final predictions.

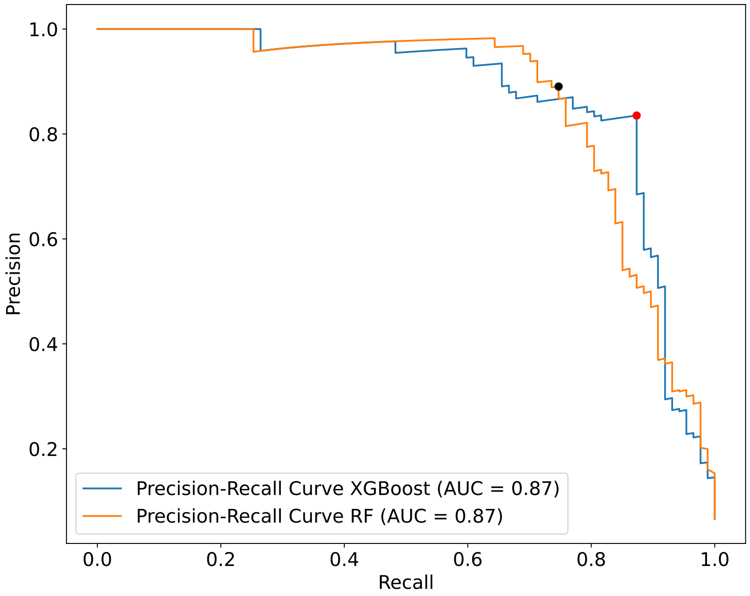

Figure 5.7: Precision-Recall curves for the optimized object classification models show identical AUCs, but XGB achieves higher recall with fewer WR star misclassifications compared to RF, at the cost of precision. The black and red points mark the maximum F1 scores for RF and XGB, respectively, with XGB outperforming RF.

classifier, as evidenced by its high precision. It was determined that the XGB classifier's Area Under the Curve (AUC) and that of the RF classifier were identical. The XGB exhibits superior performance over the RF model, as evidenced by the maximum f1-scores (denoted in the plot). The confusion matrices (see Fig. 5.8) were also employed to demonstrate the classifiers' performance. These matrices offer a comprehensive analysis of the model's predictions by contrasting the actual and predicted classes. The correctly predicted instances are represented by the diagonal elements, while the misclassifications are indicated by the remaining elements. The XGB classifier (Fig. 5.8(b)) was found to be more accurate in predicting the minority class than the RF classifier (Fig. 5.8(a)). These performances are further compared in Sec. 5.5.

Table 5.3: Evaluation metrics of object classifier models applied to TsD-1.

Metric	XGB model	RF model
Recall	86	71
Precision	83	92
f1	84	80
Accuracy	98	98

Upon application to the test dataset (TsD-1), the color-color predictions of TPs by the final classifiers were generated (see Figures 5.9 and 5.10). Our datasets are dominated by AGB and Be-type stars, which are known to have IR colors that are comparable to those of WR stars. The NIR color space of classical Be-type stars, which exhibit free-free emissions from the ionized circumstellar disks, is similar to that of WR stars. The models (see Fig. 5.9(a) and 5.10(a)) detected these stars as FPs, with the majority of them clustered in the color spaces (Lee et al., 2011). Strong free-free emissions and/or circumstellar dust cause WR stars to have color excess, and their SED typically peaks around the W2-band (Lau et al., 2023), which corresponds to the emission features of AGB stars with dust emissions (Suh, 2020). WR stars in the W2-W3 color space exhibit poor detection statistics as a consequence of this overlap (refer to Fig. 5.9(b) and 5.10(b)). However, the dust emission from AGB stars is significantly less pronounced at longer MIR bands than that from WR stars, which makes WR stars better recognizable in the W3-W4 color space (see Fig. 5.9(d) and 5.10(d)). The WR and AGB stars' circumstellar envelopes provide an explanation for this phenomenon. The circumstellar envelopes of WR stars are more extensive due to their larger radii and higher mass loss rates compared to AGB stars. These envelopes emit intensely, resulting in significant excesses across multiple color bands. Also, due to their dusty circumstellar envelopes, AGB stars exhibit comparable excesses. Due to the shorter outer envelopes of AGB stars, this effect is not present in the W3-W4 band.

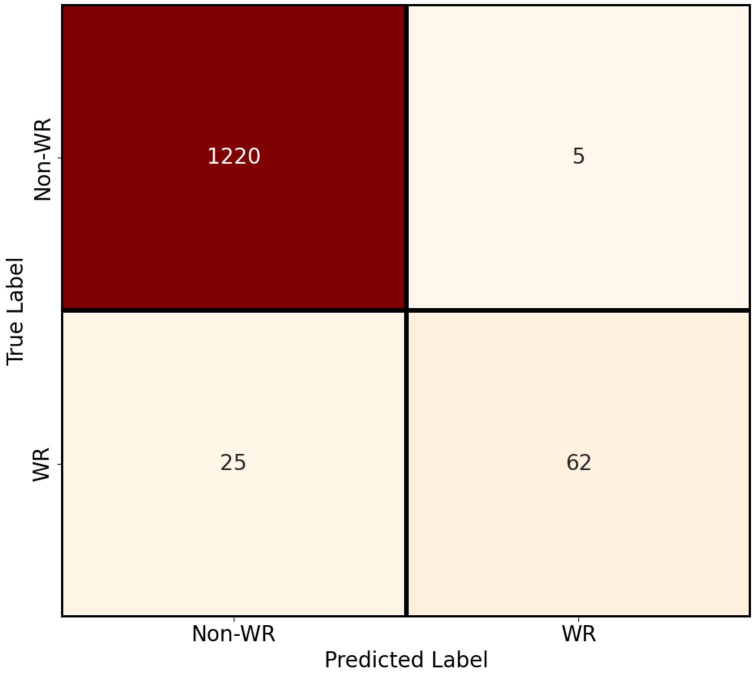

(a) RF model

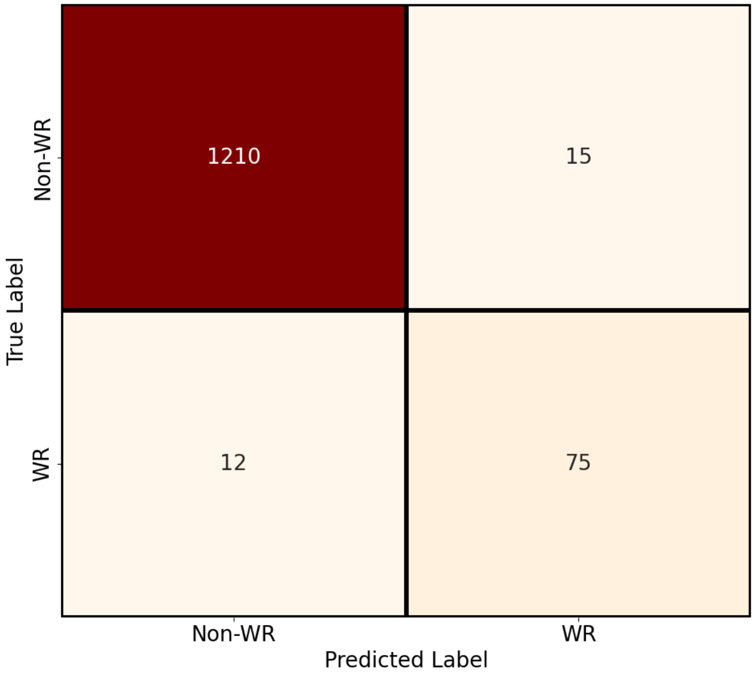

(b) XGB model

Figure 5.8: Confusion matrices for the classifiers applied to TsD-1. The true labels (y-axis) represent the actual class, while the model predictions are shown on the x-axis (see Sec. 5.4.1 for more details).

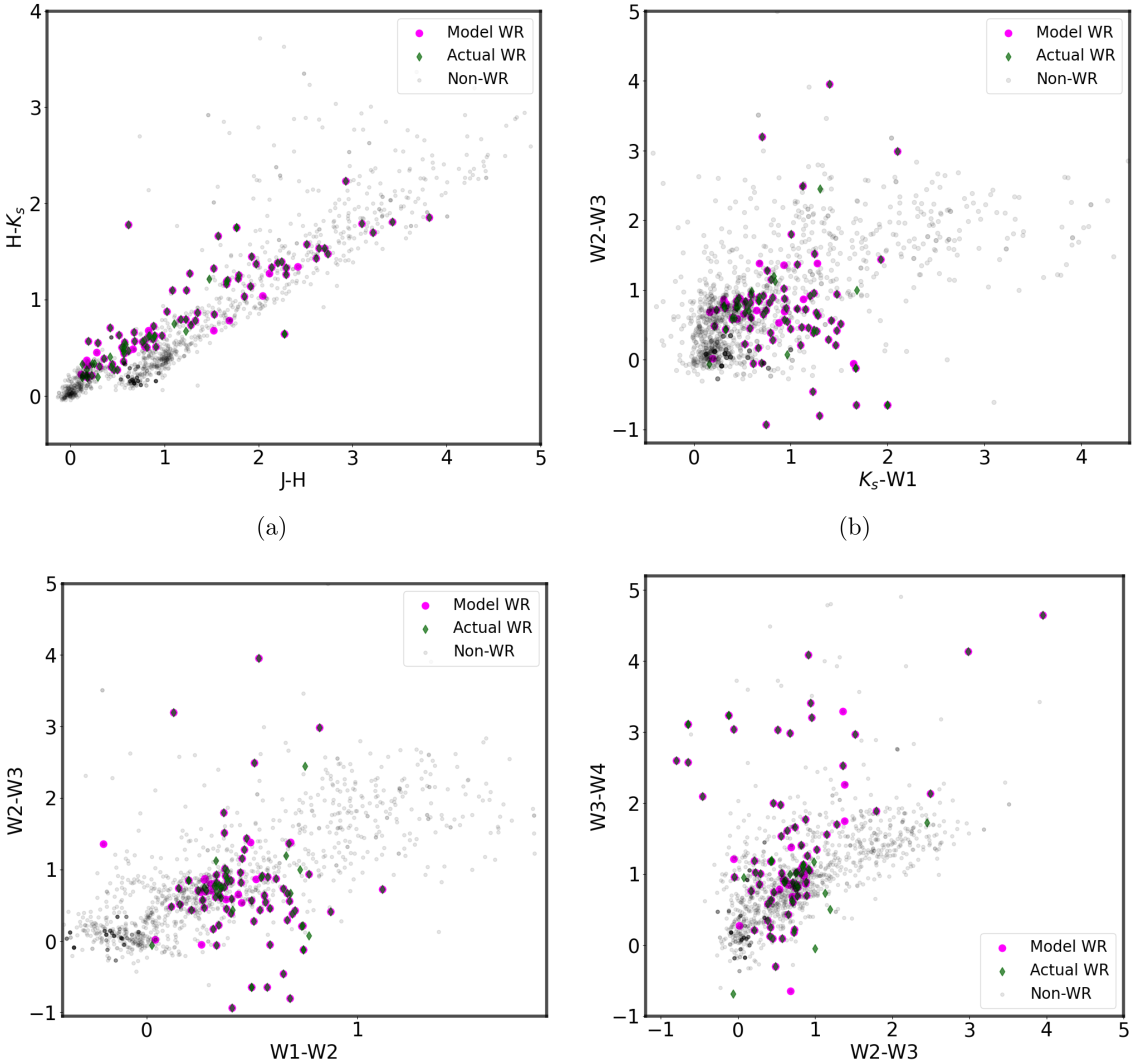

(a)

(b)

(c)

(d)

Figure 5.9: Model predictions from the best XGB classifier on TsD-1. *Grey* circles represent non-WR candidates (mainly Be and AGB sources), while *green* diamonds and *magenta* circles correspond to actual and model WR candidates, respectively. Overlapping symbols (green diamonds and magenta circles) indicate true positives (TPs).

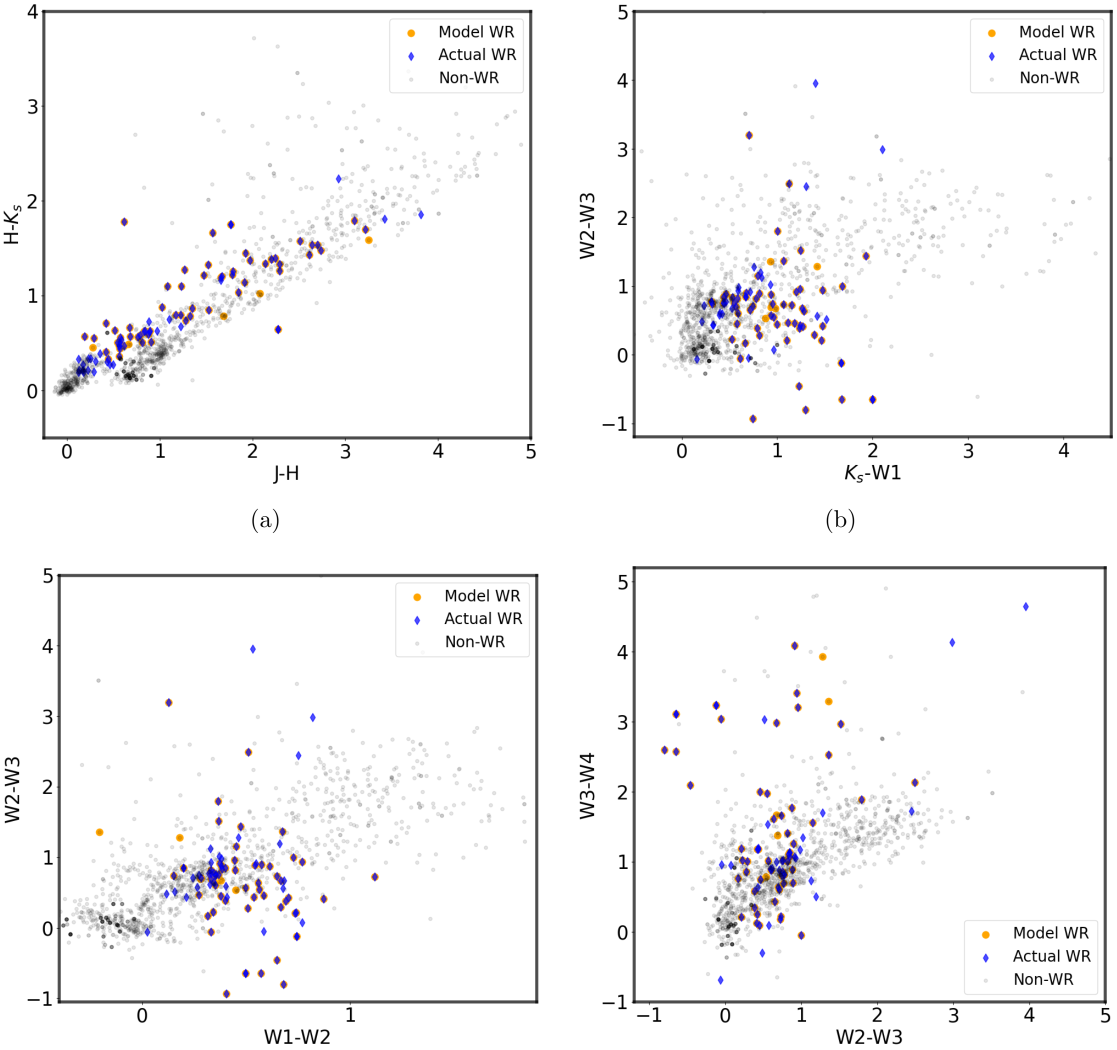

(a)

(b)

(c)

(d)

Figure 5.10: The best RF classifier is fitted on TsD-1, and predictions are analyzed from the 2-color diagrams. *Grey* circles represent non-WR candidates (same as in Fig. 5.9), while *blue* diamonds and *orange* circles denote actual and model-predicted WR candidates, respectively. Overlapping blue diamonds and orange circles indicate true positives (TPs).

Table 5.4: The parameters for the final subtype classifier model.

Model	Parameters	Values
XGB	*max_depth*	3
	n_estimator	131
	min_child_weight	3
	learning_rate	0.305
	subsample	0.529

5.4.2 Classification of WR sub-types

It was determined from the previous section that the XGB model is an extremely effective classifier. Accordingly, a multi-class XGB classifier model was created to distinguish between non-WR objects and the WR subtypes (WN and WC types). To find the key features that the model needed to get the best f1-score, the same feature selection strategy utilizing the RFECV method (as described in 5.3.4) was used. The macro f1-score, which is the average of f1-scores for various classes, was utilized because this involved more than two classes. The Bayesian optimization technique was employed to determine the optimal parameters by training and cross-validating the model on five randomized subsets of Dataset-2, each of which contained known spectral types. The macro f1-score was prioritized during this process. The oversampled training dataset (TrD-2) was used to fit the final classifier, and the model's predictions were evaluated on TsD-2.

A confusion matrix representing the model's prediction on the TsD-2 is displayed (see Fig. 5.11). The WN and WC subtypes were identified with a recall of 60% and 71%, respectively, according to Table 5.5. The model's capacity to correctly differentiate between WR subtypes was demonstrated by a lower number of misclassifications between WC and WN as well as an overall high detection accuracy (roughly 97%). Non-WR sources (as FPs) were more frequently misclassified as WN-type stars than WC-type stars. The majority of these non-WR sources were classical Be-type stars (Lee et al., 2011), which contaminated the WN-type stars' color space. WC-type stars were distinguished from the dominant classes (i.e., Be and AGB) of non-WR sources by their color excess, which was caused by strong carbon emission lines and occasionally by circumstellar dust in the K_s-band (Mauerhan et al., 2011).

5.4.3 Identification of novel WR stars

The models were subsequently applied to a diverse and extensive dataset which included stars with unknown object types. For this, SIMBAD was used to retrieve 18,750 stellar objects, with no information on their object types, that were limited

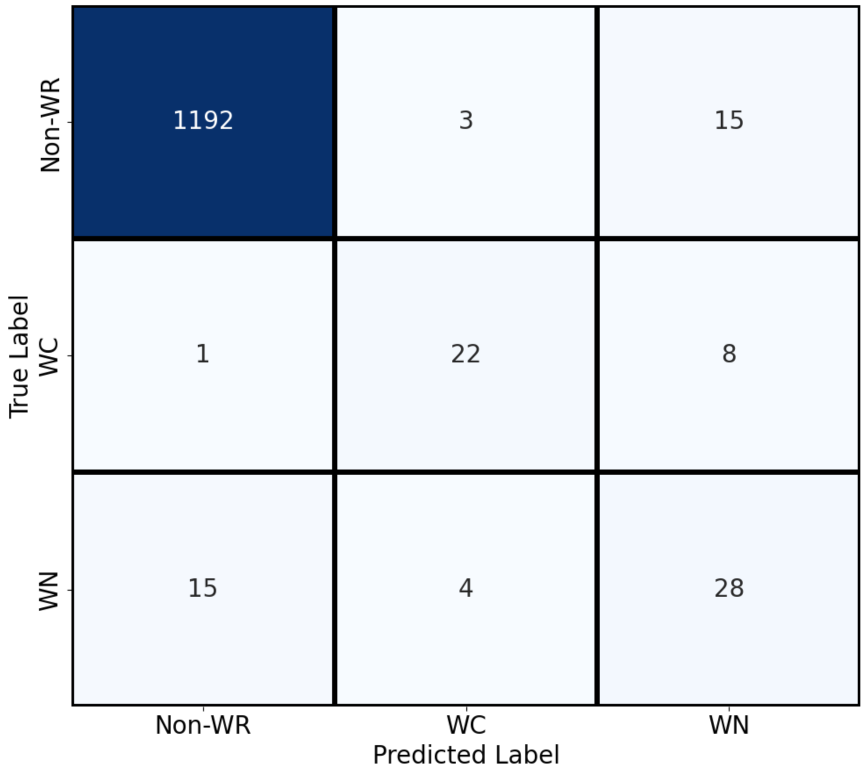

Figure 5.11: Confusion matrix based on the predictions of the WR-subtype model (see Sec. 5.4.2).

Table 5.5: Evaluation metrics of subtype classifier model upon application to TsD-2.

Metric	WN-class	WC-class
Recall	60	71
Precision	55	76
f1	57	73

to Galactic sources using the same positional criteria as described in Sec. 5.3.1. As stated in Sec. 5.3.1, the data was sorted according to the same criteria, namely, objects that were present in the same color space and had available photometric magnitudes. The XGB object type classifier model was then applied to the reduced dataset, which consisted of 6,457 objects. The model identified 58 WR stars (see Table 5.6) among the list of objects. In an additional effort to identify the subtypes, the subtype classifier was implemented on the same dataset. The model found the subtypes of 10 of the 58 WR star candidates that the object classifier found among the predicted list of objects (see Table 5.6).

WR star candidates were cross-matched with Gaia DR3 to determine their parallaxes (Gaia Collaboration et al., 2016, 2023). All objects were found to be within 2 kpc from the sun, except two that had missing parallax information. This is demonstrated in Fig. 5.12, where the WR candidates are superimposed on a 2D X-Y plot from Reid et al. (2019), which shows all the arms of the Galaxy. It was noted that the majority of the detected sources are situated on the Local arm, with a small number of them on the Perseus arm. This is anticipated, as the Local arm is recognized as a massive star-forming region, and it is probable that WR stars will be discovered in these regions (Rosslowe & Crowther, 2015). Given the spatial distributions of the WR candidates, it was expected that a majority of them were actual WR stars. Nevertheless, there is a possibility that FPs may be present in the detected list of WR candidates, as the dataset may contain objects that are different from the training data (e.g., sources with high extinction or weaker sources). This is why it is recommended that a spectroscopic follow-up be conducted on these objects in order to verify the findings. In addition, the dataset may contain a variety of other types of bright astronomical objects that were not taken into account during the model development process, such as OB-type stars and Compact H II regions. This could potentially impact the detection of WR stars.

Table 5.6: Catalogue with the identified WR stars (see Sec. 5.4.3).

Source (2MASS)	Sub-type	RA (hh:mm:ss)	Dec (dd:mm:ss)	J (mag)	H (mag)	K_s (mag)	W1 (mag)	W2 (mag)	W3 (mag)	W4 (mag)	Parallax (mas)
J00463205+6357057	WC	00:46:32	+63:57:05	9.711	9.442	8.411	8.937	9.059	9.036	8.365	4.167±0.022
J04571572-4300560	-	04:57:15.7	-43:00:55.9	10.417	10.735	9.938	9.632	9.643	9.635	8.754	4.934±0.012
J07311370-6230525	-	07:31:13.7	-62:30:52.9	8.033	7.546	7.425	7.285	7.368	7.326	7.227	14.586±0.148
J08221385-6219238	-	08:22:13.9	-62:19:24.0	8.318	7.681	7.515	7.341	7.466	7.372	7.342	0.492±0.015
J08353225-6240293	-	08:35:32.3	-62:40:29.2	9.582	9.215	9.183	9.117	9.148	9.092	8.951	3.488±0.01
J08493645-4132202	WN	08:49:36	-41:32:20	14.465	13.540	13.054	12.390	12.092	9.482	6.409	1.206±0.076
J09093134-5841530	-	09:09:31.3	-58:41:53.0	9.471	9.142	9.084	9.018	9.053	9.002	9.012	6.982±0.015
J10312466-6258152	-	10:31:24.7	-62:58:15.2	10.302	9.738	9.603	9.337	9.356	9.095	7.968	0.592±0.01
J10422925-6211335	-	10:42:29.3	-62:11:33.6	7.627	7.124	6.96	6.741	6.881	6.871	6.598	1.79±0.012
J10435862-6111132	-	10:43:58.6	-61:11:13.4	8.246	7.664	7.546	7.405	7.546	7.297	6.653	1.504±0.023
J10443325-5925084	WN	10:44:33	-59:25:08	12.171	11.777	11.247	10.361	10.055	6.878	2.462	0.435±0.018
J11484789-5806317	-	11:48:47.8	-58:06:31.7	8.512	7.991	7.797	7.723	7.836	7.751	7.75	1.533±0.012
J11531040-6236005	-	11:53:10.4	-62:36:00.5	9.066	8.518	8.385	8.239	8.332	8.335	8.723	0.588±0.011
J12035319-6118524	-	12:03:53.2	-61:18:52.4	8.908	8.402	8.254	8.144	8.226	8.152	8.327	0.704±0.011
J12074283-3449340	-	12:07:42.8	-34:49:34.1	10.308	9.709	9.172	9.008	8.913	8.87	8.372	14.255±0.018
J12233075-6100487	-	12:23:30.7	-61:00:48.5	10.382	9.726	9.485	9.311	9.2	9.127	9.076	8.82±0.023
J12452811-5810127	-	12:45:28.1	-58:10:12.7	9.561	8.958	8.831	8.724	8.802	8.719	8.707	0.879±0.02
J12503209-4943088	-	12:50:32.1	-49:43:09.0	7.745	7.119	6.514	5.393	5.415	5.44	5.369	1.381±0.017
J12585686-5823047	-	12:58:56.8	-58:23:05.6	9.611	9.004	8.834	8.72	8.794	8.756	9.366	1.262±0.031
J13001733-4836115	-	13:00:17.3	-48:36:11.5	6.662	7.489	6.161	4.477	4.277	4.498	4.452	5.62±0.019
J13141592-6143025	-	13:14:15.9	-61:43:02.7	8.329	7.785	7.53	7.042	7.193	7.2	7.088	0.971±0.424
J13263488-5835171	-	13:26:34.9	-58:35:17.1	7.994	7.38	7.195	7.11	7.224	7.133	7.092	1.014±0.013
J13431412-6233017	-	13:43:14.1	-62:33:01.4	6.838	6.103	5.785	5.327	5.198	5.07	5.46	0.456±0.024
J13443908-6054305	-	13:44:39.1	-60:54:30.6	8.764	8.174	8.043	7.958	8.064	8.056	8.98	0.907±0.012
J13493585-5825391	-	13:49:35.9	-58:25:39.1	8.004	7.393	7.221	7.058	7.168	7.108	7.106	0.667±0.015
J13493808-6116287	-	13:49:38.1	-61:16:28.8	9	8.458	8.276	8.113	8.175	8.169	8.959	0.71±0.016
J14450877-6142533	-	14:45:08.8	-61:42:53.4	8.763	8.3	8.241	7.979	8.083	8.144	8.179	10.025±0.032
J14452909-6250395	-	14:45:29.1	-62:50:39.5	7.605	7.132	7.002	6.83	6.922	6.878	6.68	3.409±0.013

Table 5.6: (Continued)

Source (2MASS)	Sub-type	RA (hh:mm:ss)	Dec (dd:mm:ss)	J (mag)	H (mag)	K_s (mag)	W1 (mag)	W2 (mag)	W3 (mag)	W4 (mag)	Parallax (mas)
J15192260-6247247	-	15:19:22.5	-62:47:24.0	7.06	6.556	6.404	5.914	6.274	6.317	6.292	-
J15255056-6126078	-	15:25:50.6	-61:26:08.0	8.069	7.531	7.343	7.188	7.297	7.232	7.112	0.993±0.013
J15314250-5158294	WC	15:31:42	-51:58:29	6.768	7.778	5.617	4.641	4.518	4.631	4.537	1.133±0.059
J15540238-5729050	-	15:54:02.4	-57:29:05.0	7.337	6.649	6.48	6.24	6.365	6.352	6.316	0.965±0.016
J15570966-3204338	-	15:57:09.7	-32:04:33.9	10.549	9.895	9.54	9.261	9.1	9.012	8.174	6.838±0.03
J16162732-5433377	WC	16:16:27	-54:33:37	12.239	11.875	10.635	9.443	9.624	9.387	8.386	1.459±0.02
J16310651-6038454	-	16:31:06.6	-60:38:45.4	8.965	8.418	8.236	8.197	8.293	8.233	8.139	0.963±0.02
J16402333-3955298	-	16:40:23.3	-39:55:29.9	9.818	9.265	9.037	9.013	9.083	9.012	8.813	0.765±0.017
J16512814-6125556	-	16:51:28.1	-61:25:55.8	8.528	7.914	7.791	7.69	7.798	7.693	7.69	0.875±0.015
J17065818-6231038	-	17:06:58.2	-62:31:04.0	8.076	7.556	7.415	7.325	7.423	7.335	7.287	1.53±0.016
J17171583-6016237	-	17:17:15.8	-60:16:23.9	7.557	7.146	6.994	6.823	6.899	6.893	6.89	1.991±0.015
J17251056-5104336	-	17:25:10.6	-51:04:34.2	8.041	7.431	7.23	7.006	7.223	7.134	7.035	1.381±0.086
J17253134-6039193	-	17:25:31.4	-60:39:19.4	5.903	5.062	4.672	4.614	4.305	4.04	3.592	0.601±0.028
J17265830-4408112	-	17:26:58.3	-44:08:11.1	8.029	7.432	7.265	7.161	7.268	7.196	7.262	1.604±0.016
J17292720-4018463	-	17:29:27.4	-40:18:46.9	8.645	8.148	7.852	7.775	7.891	7.871	7.878	2.555±0.021
J17375437-4139504	-	17:37:54.4	-41:39:50.5	8.423	7.804	7.596	7.459	7.615	7.572	7.842	1.266±0.016
J17552065-4109587	-	17:55:20.6	-41:09:58.5	7.97	7.322	7.1	6.909	7.102	7.035	7.055	0.829±0.019
J18201030-1613461	WC	18:20:10	-16:13:46	12.217	11.089	10.155	8.895	8.197	8.323	0.754	-
J18584007+1216021	-	18:58:40.1	+12:16:02.1	7.763	7.17	6.96	6.777	6.947	6.864	6.799	1.93±0.015
J19155721+0213379	WN	19:15:57	+02:13:37	7.979	7.452	7.220	7.114	7.207	7.157	7.116	1.893±0.02
J19170502+2712270	-	19:17:05.0	+27:12:27.0	8.937	8.3	8.118	7.081	6.917	7.412	7.44	0.588±0.023
J19245284+2126294	-	19:24:52.8	+21:26:29.7	7.957	7.347	7.215	6.983	7.116	7.029	6.969	1.775±0.013
J19315235+1502382	-	19:31:52.4	+15:02:38.5	8.013	7.412	7.265	7.164	7.26	7.212	7.23	1.853±0.015
J19445443+5625109	-	19:44:54.2	+56:25:10.6	10.361	10.235	10.101	9.861	9.888	9.892	9.083	1.279±0.11
J19473686+0856269	-	19:47:36.8	08:56:27.0	10.133	9.539	9.239	9.053	9.075	9.015	8.915	10.329±0.176
J19475176+2414284	WN	19:47:51	+24:14:28	12.753	11.767	11.290	10.651	10.249	7.090	5.076	0.592±0.041
J19492779+2743394	WN	19:49:27	+27:43:39	9.814	9.207	8.821	8.076	7.961	7.111	6.251	0.947±0.369
J19531620+1149588	-	19:53:16.2	11:49:58.8	8.067	7.787	7.391	6.787	7.004	6.96	6.914	0.545±0.014
J19531620+1149588	WN	19:53:16	+11:49:58	8.067	7.787	7.391	6.787	7.004	6.960	6.914	14.448±0.011

5.5 Discussion

Here, we discuss the striking differences between our classification findings with those of Mauerhan et al. (2011). We observed that our models were capable of identifying WR stars across the broad IR color space with greater accuracy than selecting WR stars from the so-called 'sweet-spot' in the color-color diagrams, as illustrated in Fig. 5.9 and Fig. 5.10. Furthermore, compared to the 50% detection rate attained by Mauerhan et al. (2011) using color-based manual identification criteria, our models detected WR stars with significantly higher accuracy (see Table 5.3). Furthermore, our models (XGB and RF) performed better in accurately predicting WR star labels than the previous KNN (Morello et al., 2018) and SVM (Dorn-Wallenstein et al., 2021) models. This showed that when it comes to classifying stellar candidates from a large, unbalanced, and diverse dataset, models based on ensemble outperform instance-based ML models.

It was found that WR stars can be identified across various metallicity regions of the MW using both of our object classifier models (see Sec. 5.4.1) (Rosslowe & Crowther, 2015). According to the f1-score, we discovered that the XGB model performs better than the RF model in detecting WR stars (see Table 5.3). Compared to the RF classifier, the XGB classifier detected fewer FNs, which accounts for its high recall. The RF classifier detected fewer FPs than the XGB classifier, as evidenced by its high precision. In the clustered regions of the IR color spaces, the XGB classifier (see Fig. 5.9) was found to be more effective in identifying WR sources than the RF model (see Fig. 5.10).

The major contaminants for WR sources in the NIR color space are Be-type objects, as predicted by both classifiers (Table 5.7). This finding was also reported by Faherty et al. (2014). In the MIR, the primary contaminants are O-rich AGB stars. One of the objects in the FP list is an HMXB system of WR stars, which can be regarded as a TP.

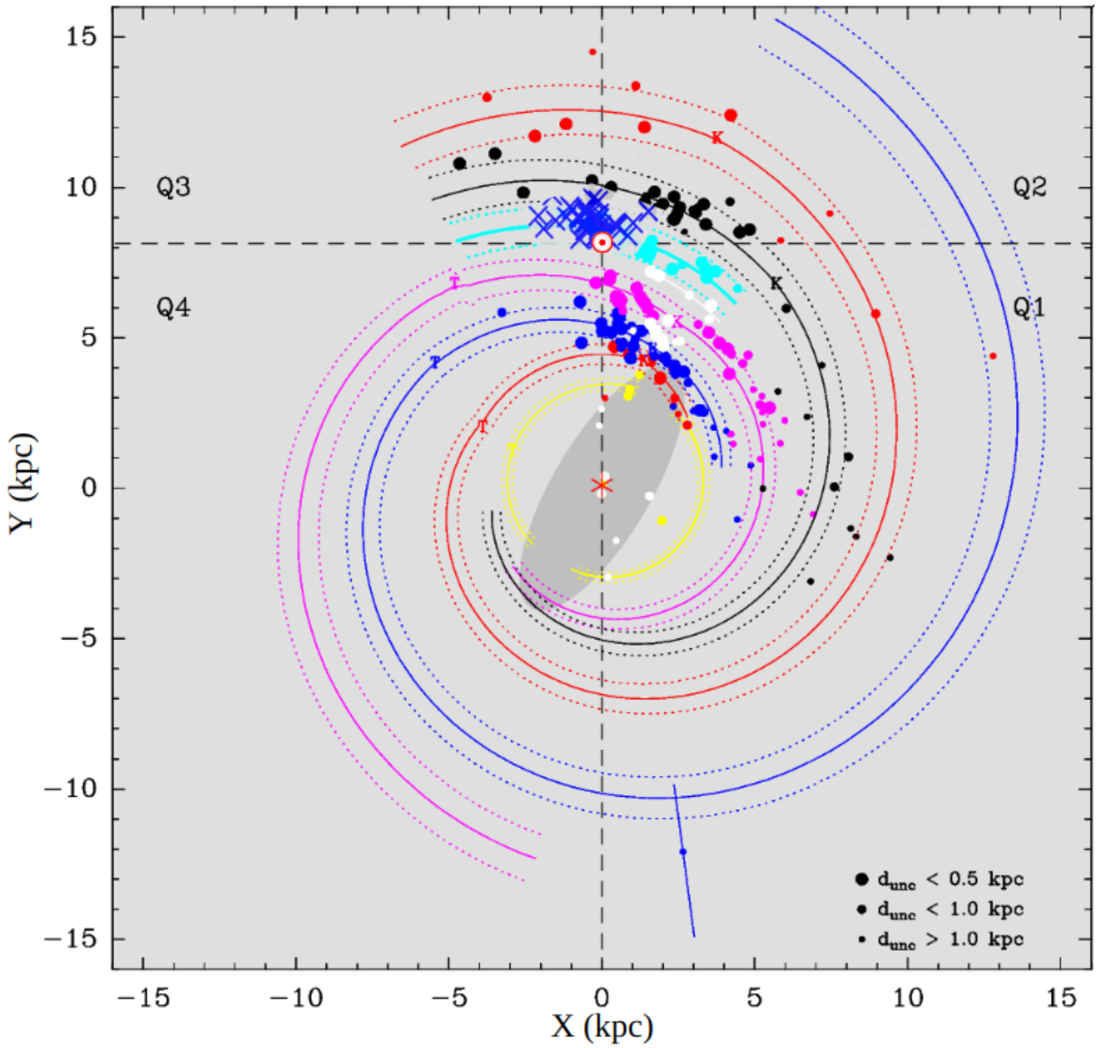

Figure 5.12: Galactic distribution of potential WR star candidates (marked as *blue* crosses) predicted by the XGB object-type classifier (see Sec. 5.4.3). The dataset is overlaid on the Galactic plane, highlighting massive star formation regions across various arms of the MW (for details, see Reid et al. (2019)).

Table 5.7: The object classifier identified FPs on TsD-1.

Source (2MASS)	Object type	RA (deg)	Dec (deg)	Spectral type	H-K_s	J-H	W1-W2	K_s-W1	W2-W3	W3-W4
				XGB model						
J18233443-1439473	AGB	275.8935	-14.6631	M6III	0.783	1.686	-0.206	0.930	1.361	3.289
J10410408-5834130	Be	160.2670	-58.5703	Oe	0.334	0.154	0.274	0.305	0.857	0.979
J11440030-6107364	HMXB	176.0013	-61.1268	B0.5Ve	0.486	0.665	0.282	0.932	0.690	1.381
J15132778-6021388	RSG	228.3658	-60.3608	M0Iab-Ib	0.678	0.828	0.040	0.195	0.018	0.278
J17070515-3545323	Be	256.7715	-35.7590	B1:IIInne	0.450	0.279	0.450	0.875	0.533	0.788
J18390419-4803184	AGB	279.7675	-48.0551	M7	0.506	0.807	0.435	0.516	0.655	0.846
J20322578+4057279	HMXB	308.1074	40.9578	WR+WR(WN4/5-6/7)	1.271	2.117	0.682	1.275	1.380	2.264
J10294719-5636465	Be	157.4466	-56.6129	B0Ve	0.372	0.173	0.276	0.474	0.875	0.868
J10441961-5916590	Be	161.0817	-59.2831	O9.7:V:(n)e	0.321	0.181	0.377	0.444	0.586	0.924
J18400705-0525346	RSG	280.0294	-5.4263	M4Ib	0.681	1.520	0.493	0.677	1.382	1.751
J17210447-3502401	AGB	260.2686	-35.0445	O-rich	1.041	2.043	0.259	1.650	-0.054	1.215
J10302384-6004404	Be	157.5994	-60.0779	B5	0.227	0.115	0.257	0.164	0.681	-0.648
J16075617-1859492	Mira	241.9841	-18.9970	-	0.518	0.787	0.309	0.648	0.705	0.684
J16064773-5225033	AGB	241.6989	-52.4176	O-rich	1.341	2.416	0.519	1.128	0.865	1.046
J15401711-5803497	Be	235.0713	-58.0638	O/Be	0.319	0.166	0.304	0.330	0.802	1.056
				RF model						
J18233443-1439473	AGB	275.8935	-14.6631	M6III	0.783	1.686	-0.206	0.930	1.361	3.289
J11440030-6107364	HMXB	176.0013	-61.1268	B0.5Ve	0.486	0.665	0.282	0.932	0.690	1.381
J17070515-3545323	Be	256.7715	-35.7590	B1:IIInne	0.450	0.279	0.450	0.875	0.533	0.788
J18452531-0323011	RSG	281.3555	-3.3837	M3Ia	1.024	2.078	0.380	0.982	0.672	1.672
J17453819-2917201	AGB	266.4091	-29.2889	-	1.587	3.251	0.180	1.419	1.283	3.932

We discovered that the subtype XGB classifier model accurately classified both WC- and WN-type objects from non-WR sources (see Sec. 5.4.2). It was inferred that the model could differentiate between WR subtypes without necessitating spectroscopic follow-ups or narrow-band IR colors. The majority of the TPs identified by the classifier were of the WCL among the WC-type stars (shown in Table 5.8). This suggested that the model could detect the distinctive color-space of these objects, which are mostly located in galaxies that are rich in metals (Crowther, 2007), like the MW. WN stars (Faherty et al., 2014), which were mainly early-type, were the contaminants for WC-type stars, whereas the opposite was not seen (see Table A.1 in Appendix A).

Additionally, it was observed (as indicated by Table 5.8) that the TPs associated with WN-type stars ranged from WNE to WNL. However, the list was primarily dominated by WNL objects, which as a result of free-free emissions exhibited an excess of color in the W3-W4 space. The model also identified WNh-type objects, which were categorized as non-classical WR stars. Nevertheless, we observed that the model misclassified WNL and WCL stars due to their analogous color patterns (refer to Fig. 5.11). This was additionally verified by the detected FPs that corresponded to WN-type objects (refer to Table A.1 in Appendix A). This is likely the result of excess emissions from free-free transitions and occasionally circumstellar dust that was formed in earlier evolutionary stages (Crowther, 2003).

Table 5.8: The subtype classifier identified TPs on TsD-2.

Source (2MASS)	Sub-type	RA (deg)	Dec (deg)	H-K_s	J-H	W1-W2	K_s-W1	W2-W3	W3-W4
				WC-type					
J14565519-5550585	WC6.5	224.23	-55.8496	0.702	0.467	0.349	0.587	0.424	0.754
J14043667-6129165	WC8	211.1528	-61.4879	1.71	2.871	0.81	1.24	0.369	2.744
J17072379-3919498	WC9	256.8492	-39.3305	0.865	1.37	0.476	0.753	0.63	1.412
J12300386-6250171	WC7	187.5161	-62.8381	0.962	1.11	0.449	0.551	1.064	1.765
J17113590-3911075	WC8	257.8996	-39.1854	1.271	1.266	1.12	1.155	0.722	0.183
J13520184-6226487	WCE	208.0077	-62.4469	1.418	2.175	0.543	0.895	0.751	2.342
J14203074-6048221	WC9	215.1281	-60.8061	1.249	1.987	0.648	1.119	0.794	1.33
J20115352+3611505	WC8+OB:	302.973	36.1974	0.45	0.119	0.457	0.254	0.623	0.801
J18334763-0923077	WC8	278.4485	-9.3855	1.163	1.657	0.584	0.699	-0.051	0.963
J16352331-4809180	WC8	248.8472	-48.155	1.336	2.137	0.537	0.999	0.438	1.178
J19122407+0957290	WC	288.1003	9.9581	1.191	1.657	0.585	1.181	0.46	2.003
J18120241-1806554	WC8+O8/9III/V	1.665	-18.1154	0.791	0.733	0.682	1.062	-0.052	0.277
J18454987-0259560	WC8	281.4578	-2.9989	1.777	0.614	0.572	1.676	-0.647	2.575
J10103191-6038423	WC5	152.633	-60.6451	0.569	0.19	0.331	0.312	0.769	0.689
J17571686-2523135	WC7:	269.3203	-25.3871	1.255	2.168	0.501	0.568	1.421	1.392
J21500557+5042247	WC5	327.5232	50.7069	0.711	0.41	0.375	0.238	0.754	0.726
J13541345-6150018	WC5-6	208.5561	-61.8339	1.202	1.537	0.441	0.896	0.032	1.938
J19202932+1412061	WC-06-d?	290.1222	14.2017	1.352	2.358	0.667	1.126	0.723	1.324
J16123747-4637368	WC9	243.1561	-46.6269	1.325	1.525	0.873	1.265	0.411	0.123
J18361633-0705169	WC9	279.068	-7.088	2.051	3.071	1.011	2.094	-0.128	-0.433
J17112850-3913168	WC8	257.8688	-39.2214	1.221	1.782	0.445	1.239	0.958	3.209
				WN-type					
J12121681-6246145	WN4-6	183.0701	-62.7707	0.839	1.348	0.443	0.840	-0.112	2.415
J16482762-4609227	WN5	252.1151	-46.1563	0.839	2.290	0.558	1.281	0.638	1.611
J14465358-5919382	WN7-8h	221.7233	-59.3273	0.784	1.326	0.400	0.793	0.387	0.344

Table 5.8: (Continued)

Source (2MASS)	Sub-type	RA (deg)	Dec (deg)	H-K_s	J-H	W1-W2	K_s-W1	W2-W3	W3-W4
J18250024-1033236	WN7b	276.2510	-10.5566	0.625	0.974	0.372	0.927	1.017	1.344
J11023296-5926209	WN5-s	165.6373	-59.4391	0.506	0.492	0.442	0.718	0.889	1.042
J12115407-6317037	WN9	182.9753	-63.2844	0.514	1.388	-0.107	0.441	1.509	2.215
J10443211-5750238	WN5	161.1338	-57.8400	0.597	0.566	0.437	0.653	0.843	0.867
J17184971-3357413	WN8/WC9	259.7072	-33.9615	0.512	0.469	0.358	0.493	0.699	0.622
J18255309-1328324	WN6o	276.4712	-13.4757	0.559	0.796	0.357	0.777	0.817	0.961
J17190052-3848513	WN8h	259.7522	-38.8143	0.385	0.422	0.271	0.574	0.313	0.319
J16441069-4524246	WN7	251.0446	-45.4069	0.711	1.060	0.505	0.752	0.917	2.762
J18492733-0104207	WN7h	282.3639	-1.0724	0.595	0.875	0.314	0.661	0.165	0.761
J11130361-6214183	WN4b	168.2651	-62.2384	0.621	0.828	0.452	0.795	1.152	1.557
J11555211-6245022	WN6	178.9671	-62.7506	0.625	0.886	0.420	0.799	0.760	0.405
J10534463-5930428	WN4+O8V	163.4360	-59.5119	0.274	0.210	0.278	0.332	0.797	0.978
J12143309-6258509	WN6	183.6379	-62.9808	0.766	1.280	0.530	1.393	0.686	3.022
J16345746-4704129	WN6	248.7394	-47.0703	1.244	2.043	0.621	1.046	0.517	1.023
J17142539-3809499	WN6	258.6058	-38.1639	0.846	1.526	0.374	1.196	0.913	4.092
J16434036-4557576	WN6	250.9182	-45.9660	0.567	0.857	0.456	0.580	0.600	1.109
J16470761-4549222	WN6h	251.7817	-45.8228	0.691	2.540	1.987	1.741	3.482	1.144
J16285324-4833356	WN5b	247.2219	-48.5599	1.036	1.851	0.366	1.003	1.796	1.887
J18305320-1019370	WN6	277.7217	-10.3270	0.479	0.768	0.222	0.686	0.528	1.323
J15231661-5744198	WN6+O5.5/6	230.8192	-57.7388	0.403	0.568	0.260	0.588	0.610	0.842
J18410086-0426145	WN7	280.2536	-4.4374	0.399	0.493	0.302	0.484	0.674	0.792
J10255650-5748435	WN5ha/O3+O3Vz((f*))	156.4854	-57.8121	0.367	0.608	0.158	0.461	0.863	1.740
J19172235+1213133	WN9	289.3431	12.2204	1.364	2.545	0.564	0.968	0.932	1.061
J18420827-0351029	WN8-9h	280.5345	-3.8508	0.993	1.585	0.631	0.791	0.885	3.267
J18311653-1009250	WN8	277.8189	-10.1569	0.655	0.806	0.172	0.812	0.656	1.505

5.6 Conclusion

In this investigation, we employed ML to classify WR stars from a vast dataset of 6,555 stellar objects, which encompassed a variety of types, including AGB stars and MS stars. Based on the IR colors and positional coordinates, we created a robust and incredibly effective XGB classifier model. RA, Dec, J-H, H-K_s, K_s-W1, W1-W2, W2-W3, and W3-W4 are the only eight features that the models use to achieve their highest classification efficiency. These attributes were determined to be the most signficant in the identification of the WR stars. The models also outperformed the fundamental color-color approach in the detection of WR stars. A comparison between the XGB classifier and an RF model revealed that the former is more precise in its classification of WR stars. According to the models, the hot Be-type stars are the primary contaminants for WR stars, with O-rich AGB sources following thereafter.

Additionally, we used the XGB algorithm to create a novel WR-subtype classifier that shows remarkable accuracy in differentiating between WN and WC subtypes. The model exhibited superior performance in classifying WC-type stars compared to WN-type stars, due to the overlapping color characteristics of the latter with those of Be-type stars, which serve as the primary contaminants. The ML model is particularly well-suited for the detection of WR stars in the MW due to its ability to effortlessly identify WR-Late type stars. Based on the model's predictions, the WC class is significantly contaminated by WNE objects, whereas the WN class is impacted by WCL objects. Furthermore, the model is capable of recognizing non-classical WNh-type stars.

In addition, we implemented the object classifier model on an unlabeled dataset that included 6457 stellar sources and identified 58 novel WR candidates. We identified the chemical subtypes of 10 of these detected sources by employing the WR-subtype classifier. The identified WR candidates are predominantly situated in the solar neighborhood and within the MW's local spiral arm, which contains regions of significant massive star formation.

Chapter 6

Thesis Conclusion

In this thesis, I have addressed some of the less-understood physical phenomena that occur in WR stars of WCL class. These stars are known for their low effective temperatures, high mass-loss rates, often show excess emissions in the IR bands due to circumstellar dust, and exhibit stronger stochastic variability in comparison to other WR sub-classes. WCL stars are mainly found in metal-rich galaxies such as the MW. In my thesis work, I have analyzed some of the Galactic WCL stars which have been either less studied or show some unique observational nature.

For this work, I have observed a handful of WR stars (discussed in Chapter 2) using different state-of-the-art instruments suitable for low and high-resolution spectroscopy across optical and NIR wavebands. High-quality data were acquired using proper observation strategies. Data were extracted using appropriate reduction tools such as IRAF, python-based pipelines, etc. The spectroscopic data were analyzed using CMFGEN which is a NLTE-based atmospheric modeling code. Also, a part of the research was the application of ensemble-based ML techniques to detect WR populations in the MW.

In chapter 3, I discussed the investigation of the stellar atmosphere of a less studied WC9-type star ([KSF2015 1381-19L or WR 111-9) located in a highly obscured Galactic region. For this, I employed the CMFGEN to understand the physical and chemical nature of the stratified winds of the object. The star was found to be the most luminous WC9-type detected ever in the MW. The NIR absolute magnitude of the object resembled that of WC9d-type stars, however, we did not detect any excess emission in the IR bands that could arise from circumstellar dust. Evolutionary models suggested the object originated from a single rotating ($67\,M_\odot$) or non-rotating ($90\,M_\odot$) O-type MS star rather in a binary system.

In general, WR-late stars show stronger intrinsic variability than WR early-type stars due to the stochastic nature of the inhomogeneities. Some WR-late types especially of WN-class show pulsational variability such as WR 123 (WN8), WR 66 (WN8h), etc. However, only a few WCL (WR 135, a WC8-type) stars exhibit both stochastic and pulsational variability simultaneously. In Chapter 4, I reported the detection of high-frequency pulsations in WR 135 from the periodogram analysis of short-cadence (10-minute) optical photometric (from TESS) and spectroscopic (from CFHT) time series data. The best-fitted spectroscopic models to the observed SED were derived using CMFGEN. It was found that the radiation pressure dominates the stratified stellar winds which maintain a hydrodynamic outflow. The strong Fe VII-IX opacity drives the inner sub-sonic winds that are close to the Eddington limit, while He II and C IV opacities drive outer supersonic winds. The Fe-opacity triggers SMI causing both wind inhomogeneities (clumps) which drive the stochastic variability; and pulsational variability observed from the C IV $\lambda\lambda$5802-12 and C III λ5696 emission lines. The clump size correlates with the harmonic frequencies: smaller clumps affect higher-order harmonics, while larger clumps dominate outer winds and He I transitions, impacting global wind variability.

In Chapter 5, I showed the novel application of Supervised Ensemble Learning methods such as XGB and RF in the classification of Galactic WR stars mainly based on NIR and MIR colors and positional coordinates. By utilizing python-based ML libraries such as *Scikit-learn* (for feature selection and model development), *Imbalanced-learn* (for treating unbalanced datasets), and *Optuna* (Bayesian approach for model optimization), I achieved a high WR star identification accuracy (of 86%) against a wide variety of stellar objects such as AGB, Be, MS, RSG, HMXB, LPV, etc. Furthermore, using the XGB algorithm, I developed a novel WR subtype classifier model that accurately distinguishes between WN and WC subtypes against non-WR sources with a reliable accuracy of over 60%. The models predicted that the major contaminants for WR stars are the hot Be-type stars followed by the O-rich AGB sources. The XGB-based classifier models were applied to a randomly selected dataset of 6457 objects, identifying 58 new WR star candidates, including 10 distinct WR star subtypes. The detected WR stars are mainly present in the solar neighborhood (within 2 kpc) and within the MW's Local Spiral Arm that hosts massive star formation regions. Our findings closely align with the observed distribution of WR stars. These models will aid in identifying WR stars in the ongoing and upcoming IR photometric surveys conducted by the Roman telescope in the MW.

Chapter 7

Future works

7.1 Evolutionary modeling of pulsating WR stars

As noted by Nazé et al. (2021), only a few late-type WR stars exhibit pulsations in optical photometric and spectroscopic observations. As the emission lines and continuum are formed in the optically thin stellar winds, it is challenging to investigate the optically thick stellar interiors from where these pulsations originate in WR stars. The physical mechanisms that are responsible for such variability are debatable and need to be investigated.

In this proposed work, I plan to develop evolutionary models that are consistent with the observed aspects of WR-late stars that are also known for exhibiting pulsational variability. Using suitable stellar evolution modeling codes such as MESA, I will generate He-ZAMS models that show similar physical properties as the WR-late stars. Using the derived models, I plan to investigate the unstable modes of oscillations that correspond to observed pulsations in such WR stars. This will help us to develop a better idea about the source of pulsations and understand the nature of stellar atmospheres of such WR stars.

7.2 Astrochemical identification of dusty WR stars

Evolved stellar sources such as AGB, Red Giant (RG), RSG, YSO, etc. often exhibit broad-band emissions in the MIR due to the presence of polycyclic aromatic hydrocarbons (PAH) in their circumstellar environments. PAHs are also detected in the hostile environments of massive stars that produce strong UV radiation.

Marchenko & Moffat (2017) found that WR stars in CWB show PAH emissions at 6.5, 8.0, 8.8 μm and in some cases $\lambda > 10\,\mu$m.

In this project, I plan to develop ML models that are capable of detecting PAHs present in the circumstellar environments of dusty WR stars. For this, I plan to train the models on an extensive dataset acquired from the SPITZER, JWST, etc. databases comprising spectroscopic data of the evolved objects including WR stars that show PAH emissions in the MIR spectra. The trained model will be applied to an unknown dataset comprising MIR spectra of evolved objects to detect new stellar candidates that can host PAHs in their dusty environments. This will benefit our knowledge of the different physical conditions that support the formation of PAHs.

Appendix A

WR-subtype model misclassification

In this Appendix, the limitations of the chemical-subtype WR classifier model are tabulated. These results are further discussed in Sec. 5.5.

Table A.1: FPs detected by the subtype classifier model.

Source (2MASS)	Object Type	RA (deg)	Dec (deg)	Spectral Type	H-K_s	J-H	W1-W2	K_s-W1	W3-W4	W2-W3
				WC-type						
J17063419-3924373	Mira	256.6424	-39.4104	O-rich	1.297	2.119	0.666	1.136	0.925	0.706
J19131919+0955289	WR	288.3299	9.9246	WN6	1.396	2.327	0.646	1.204	0.731	0.373
J14162737-6117562	WR	214.1140	-61.2989	WN5b	1.383	2.206	0.649	1.068	0.221	0.732
J18392341-0602158	RSG	279.847	-6.0377	M0I	1.344	2.511	0.276	1.393	2.139	0.869
J15352652-5604123	WR	233.860	-56.0700	WN7	0.929	1.455	0.403	0.999	0.495	0.704
J15013011-5916120	WR	225.3755	-59.2700	WN4b	1.182	2.014	0.559	1.104	0.537	0.061
J12433281-6306118	Be	190.8867	-63.1033	Be	1.060	-1.328	0.424	2.328	2.010	1.219
				WN-type						
J18332830-1024087	Be	278.3679	-10.4024	B0Ve	0.451	0.419	0.316	0.52	1.839	0.847
J16065065-5231556	Mira	241.7110	-52.5321	O-rich	1.13	2.054	0.525	1.304	0.862	0.622
J11061858-6114138	WR	166.5774	-61.2372	WC7+OB	0.537	0.769	0.243	0.887	0.833	0.623
J17070515-3545323	Be	256.7715	-35.7590	B1:IIInne	0.45	0.279	0.45	0.875	0.788	0.533
J20054514+3554030	Be	301.4381	35.9008	B1:III/Ve	0.306	0.206	0.411	0.538	0.866	0.802
J11061873-6114184	WR	166.5781	-61.2385	WC7	0.537	0.769	0.243	0.887	0.833	0.623
J18352720-0704541	AGB	278.8634	-7.0817	O-rich	1.328	2.707	0.503	0.959	5.149	3.056
J18392955-0544222	RSG	279.8732	-5.7395	K7Ib	0.528	1.325	-0.292	0.583	5.325	0.223
J18411070-0451270	WR	280.2946	-4.8575	WC9	0.725	0.88	0.464	0.758	1.699	1.277
J21250244+4427063	Be	321.2602	44.4518	B1.5V:nnep	0.263	0.226	0.365	0.474	0.827	0.68
J18332777-1035243	HMXB	278.3657	-10.5901	B0.5Ve	0.344	0.511	0.367	0.31	1.082	0.767
J17450900-3150158	WR	266.2875	-31.8377	WC8	0.893	0.844	0.258	0.981	1.074	0.498
J17002524-4219003	HMXB	255.1052	-42.3168	B2e	0.364	0.352	0.199	0.713	1.556	0.74
J18400705-0525346	RSG	280.0294	-5.4263	M4Ib	0.681	1.52	0.493	0.677	1.751	1.382
J16401711-4620098	WR	250.0713	-46.3361	WC7	1.854	3.818	0.533	1.398	4.649	3.955
J13101207-6239065	WR	197.5503	-62.6518	WC5	0.776	0.964	0.481	0.607	3.607	1.766
J16002643-5211099	WR	240.1101	-52.1861	WC7	0.906	1.331	0.508	0.812	1.073	0.605
J17452082-2913424	AGB	266.3368	-29.2285	-	2.133	2.944	0.649	1.923	3.658	0.56
J17532843-2446277	Be	268.3685	-24.7744	B3/5ne	0.406	0.321	0.321	0.681	0.999	0.713

Table A.1: (Continued)

Source (2MASS)	Object Type	RA (deg)	Dec (deg)	Spectral Type	H-K_s	J-H	W1-W2	K_s-W1	W3-W4	W2-W3
J18452531-0323011	RSG	281.3555	-3.3837	M3Ia	1.024	2.078	0.38	0.982	1.672	0.672
J16350555-4717135	WR	248.7732	-47.2871	WC9d?	1.156	1.985	0.579	1.128	1.172	0.603
J10412265-6046325	Be	160.3444	-60.7757	B2	0.346	0.356	0.39	0.579	0.941	1.028
J22195144+5808535	Be	334.9643	58.1482	B0Ve	0.371	0.362	0.319	0.454	0.864	0.857

Acronyms

1D 1-dimensional.

2D 2-dimensional.

2MASS Two Micron All Sky Survey.

AGB Asymptotic Giant Branch.

ARIES Aryabhatta Research Institute of Observational Sciences.

bCepV Beta Cepheid Variables.

BSG Blue SuperGiant.

C Carbon stars.

CE Common Envelope.

Ce Classical Cepheids.

CFHT 3.6m Canadian French Hawaii Telescope.

CIR Co-rotating Interaction Region.

COB cold opacity bump.

CV Cataclysmic Variable.

CWB colliding-wind binaries.

cWR Classical Wolf Rayet.

DAC Discrete Absorption Components.

DOT 3.6m-Devasthal Optical Telescope.

EB Eclipsing Binaries.

Emline Emission line stars.

EW Equivalent Width.

FFI Full Frame Images.

FoV Field of View.

FWHM Full Width Half Maxima.

GB Gradient Boosting.

GRB Gamma Ray Burst.

HB Horizontal Branch stars.

HCT 2m-Himalayan Chandra Telescope.

HESP Hanle Echelle SPectrograph.

HFOSC Hanle Faint Object Spectrograph and Camera.

High PM High Proper Motion stars.

HLSP High-Level Science Products.

HMXB High Mass X-ray Binaries.

HR Hertzsprung-Russel.

IIA Indian Institute of Astrophysics.

IMF Initial Mass Function.

IR InfraRed.

IRSA InfraRed Science Archive.

ISM Inter Stellar Medium.

JWST James Webb Space Telescope.

KNN K-Nearest Neighbor.

LBV Luminous Blue Variable.

LDI line-driven instabilities.

LM Levenberg-Marquardt.

LMC Large Magellanic Cloud.

LPV Long Period Variables.

LSP Lomb-Scargle Periodogram.

MAST Mikulski Archive for Space Telescope.

MIR Mid-InfraRed.

ML Machine Learning.

MS Main Sequence.

MW Milky Way.

NIR Near-InfraRed.

NLTE non-local thermodynamic equilibrium.

OMR Optomechanics Research.

OrionV Orion Variables.

pA post-Asymptotic Giant Branch stars.

PAH polycyclic aromatic hydrocarbons.

PN Planetary Nebula.

RCrB R Coronae Borealis stars.

RF Random Forest.

RFECV Recursive Feature Elimination with Cross-Validation.

RG Red Giant.

RGB Red Giant Branch stars.

RLOF Roche Lobe Over-Flow.

RSG Red SuperGiant.

RT Radiative Transfer.

RV radial velocity.

RVTauV RV Tauri Variables.

S/N Signal-to-Noise ratio.
SED Spectral Energy Distribution.
SMC Small Magellanic Cloud.
SMI strange mode instabilities.
SMP strange mode pulsations.
SN Supernova.
SVM Support Vector Machine.

TANSPEC TIFR-ARIES Near Infrared Spectrometer and Imager.
TESS Transiting Exoplanet Survey Satellite.
TIRSPEC TIFR InfraRed SPectrograph.

UV UltraViolet.

VBO Vainu Bappu Observatory.
VBT 2.3m-Vainu Bappu Telescope.
VFF volume filling factor.

WCE Early WC-type.
WCL Late WC-type.
WISE Wide-field Infrared Survey Explorer.
WNE Early WN-type.
WNL Late WN-type.
WR Wolf Rayet.

XGB eXtreme Gradient Boosting.

YSG Yellow SuperGiants.
YSO Young Stellar Objects.

ZAMS Zero Age Main Sequence.

Bibliography

Aadland, E., Massey, P., Hillier, D. J., & Morrell, N. 2022, ApJ, 924, 44, doi: 10.3847/1538-4357/ac3426

Abbott, D. C. 1980, ApJ, 242, 1183, doi: 10.1086/158550

Agienko, K. B., Guseva, N. G., & Izotov, Y. I. 2013, Kinematics and Physics of Celestial Bodies, 29, 131, doi: 10.3103/S0884591313030021

Akiba, T., Sano, S., Yanase, T., Ohta, T., & Koyama, M. 2019, in Proceedings of the 25th ACM SIGKDD international conference on knowledge discovery & data mining, 2623–2631

Aldoretta, E. J., St-Louis, N., Richardson, N. D., et al. 2016, MNRAS, 460, 3407, doi: 10.1093/mnras/stw1188

Allen, D. A., Swings, J. P., & Harvey, P. M. 1972, A&A, 20, 333

Allen, D. A., Wright, A. E., & Goss, W. M. 1976, MNRAS, 177, 91, doi: 10.1093/mnras/177.1.91

Ardila, D. R., Van Dyk, S. D., Makowiecki, W., et al. 2010a, ApJS, 191, 301, doi: 10.1088/0067-0049/191/2/301

Ardila, D. R., van Dyk, S. D., Makowiecki, W., et al. 2010b, VizieR Online Data Catalog: Spitzer Atlas of Stellar Spectra (SASS) (Ardila+, 2010), VizieR On-line Data Catalog: J/ApJS/191/301. Originally published in: 2010ApJS..191..301A, doi: 10.26093/cds/vizier.21910301

Arora, B., Pandey, J. C., & De Becker, M. 2019, Monthly Notices of the Royal Astronomical Society, 487, 2624, doi: 10.1093/mnras/stz1447

Asplund, M., Grevesse, N., Sauval, A. J., & Scott, P. 2009, ARA&A, 47, 481, doi: 10.1146/annurev.astro.46.060407.145222

Astropy Collaboration, Robitaille, T. P., Tollerud, E. J., et al. 2013, A&A, 558, A33, doi: 10.1051/0004-6361/201322068

Astropy Collaboration, Price-Whelan, A. M., Sipőcz, B. M., et al. 2018, AJ, 156, 123, doi: 10.3847/1538-3881/aabc4f

Astropy Collaboration, Price-Whelan, A. M., Lim, P. L., et al. 2022, ApJ, 935, 167, doi: 10.3847/1538-4357/ac7c74

Bailer-Jones, C. A. L., Rybizki, J., Fouesneau, M., Mantelet, G., & Andrae, R. 2018, AJ, 156, 58, doi: 10.3847/1538-3881/aacb21

Baug, T., de Grijs, R., Dewangan, L. K., et al. 2019, The Astrophysical Journal, 885, 68, doi: 10.3847/1538-4357/ab46be

Breiman, L. 2001, Machine Learning, 45, 5, doi: 10.1023/A:1010933404324

Breysacher, J., Azzopardi, M., & Testor, G. 1999, A&AS, 137, 117, doi: 10.1051/aas:1999240

Brinchmann, J., Kunth, D., & Durret, F. 2008, A&A, 485, 657, doi: 10.1051/0004-6361:200809783

Campbell, W. 1884, Astronomy & Astrophysics

Cardelli, J. A., Clayton, G. C., & Mathis, J. S. 1989, ApJ, 345, 245, doi: 10.1086/167900

Castor, J. I., Abbott, D. C., & Klein, R. I. 1975, ApJ, 195, 157, doi: 10.1086/153315

Chao, L., Wen-hui, Z., & Ji-ming, L. 2019, Chinese Astronomy and Astrophysics, 43, 539, doi: https://doi.org/10.1016/j.chinastron.2019.11.005

Chen, G. X., & Pradhan, A. K. 1999, A&AS, 136, 395, doi: 10.1051/aas:1999464

Chen, T., & Guestrin, C. 2016, arXiv e-prints, arXiv:1603.02754, doi: 10.48550/arXiv.1603.02754

Chené, A. N., & St-Louis, N. 2011, ApJ, 736, 140, doi: 10.1088/0004-637X/736/2/140

Chené, A.-N., St-Louis, N., Moffat, A. F. J., & Gayley, K. G. 2020, ApJ, 903, 113, doi: 10.3847/1538-4357/abba24

Chené, A. N., Foellmi, C., Marchenko, S. V., et al. 2011, A&A, 530, A151, doi: 10.1051/0004-6361/201116567

Chiar, J. E., & Tielens, A. G. G. M. 2006, The Astrophysical Journal, 637, 774, doi: 10.1086/498406

Cochrane, D. M., & McWhirter, R. W. P. 1983, PhyS, 28, 25, doi: 10.1088/0031-8949/28/1/005

Conti, P. 1976

Conti, P. S., Massey, P., & Vreux, J.-M. 1990, ApJ, 354, 359, doi: 10.1086/168694

Cranmer, S. R., & Owocki, S. P. 1996, ApJ, 462, 469, doi: 10.1086/177166

Crowther, P. A. 2003, Ap&SS, 285, 677, doi: 10.1023/A:1026157126395

—. 2007, ARA&A, 45, 177, doi: 10.1146/annurev.astro.45.051806.110615

Crowther, P. A., De Marco, O., & Barlow, M. J. 1998, Monthly Notices of the Royal Astronomical Society, 296, 367, doi: 10.1046/j.1365-8711.1998.01360.x

Crowther, P. A., Dessart, L., Hillier, D. J., Abbott, J. B., & Fullerton, A. W. 2002, A&A, 392, 653, doi: 10.1051/0004-6361:20020941

Crowther, P. A., & Hadfield, L. J. 2007, The Messenger, 129, 53

Crowther, P. A., Morris, P. W., & Smith, J. D. 2006, ApJ, 636, 1033, doi: 10.1086/498051

Crowther, P. A., Smith, L. J., & Hillier, D. J. 1995, A&A, 302, 457

Cutri, R., Skrutskie, M., Van Dyk, S., et al. 2003, 2MASS All-Sky Catalog of Point Sources, Version 17-Apr-2020 (last modified), Centre de Donnees astronomique de Strasbourg (CDS)

Cutri, R. M., & et al. 2012, VizieR Online Data Catalog: WISE All-Sky Data Release (Cutri+ 2012), VizieR On-line Data Catalog: II/311. Originally published in: 2012wise.rept....1C

Cutri, R. M., Wright, E. L., Conrow, T., et al. 2012, Explanatory Supplement to the WISE All-Sky Data Release Products, Explanatory Supplement to the WISE All-Sky Data Release Products

—. 2021, VizieR Online Data Catalog, II/328

Davey, A. R., Storey, P. J., & Kisielius, R. 2000, A&AS, 142, 85, doi: 10.1051/aas:2000139

de la Chevrotière, A., St-Louis, N., Moffat, A. F. J., & MiMeS Collaboration. 2014, ApJ, 781, 73, doi: 10.1088/0004-637X/781/2/73

Decleir, M., Gordon, K. D., Andrews, J. E., et al. 2022, ApJ, 930, 15, doi: 10.3847/1538-4357/ac5dbe

Desforges, S., St-Louis, N., Chené, A. N., de la Chevrotière, A., & Hénault-Brunet, V. 2017, MNRAS, 465, 1227, doi: 10.1093/mnras/stw2769

Dessart, L., & Chesneau, O. 2002, A&A, 395, 209, doi: 10.1051/0004-6361:20021110

Dewangan, L. K., Baug, T., Ojha, D. K., et al. 2016, The Astrophysical Journal, 826, 27, doi: 10.3847/0004-637X/826/1/27

Donati, J. F., Semel, M., Carter, B. D., Rees, D. E., & Collier Cameron, A. 1997, MNRAS, 291, 658, doi: 10.1093/mnras/291.4.658

Dorfi, E. A., Gautschy, A., & Saio, H. 2006, A&A, 453, L35, doi: 10.1051/0004-6361:200600027

Dorn-Wallenstein, T. Z., Davenport, J. R. A., Huppenkothen, D., & Levesque, E. M. 2021, ApJ, 913, 32, doi: 10.3847/1538-4357/abf1f2

Drissen, L., St. -Louis, N., Moffat, A. F. J., & Bastien, P. 1987, ApJ, 322, 888, doi: 10.1086/165783

Dziembowski, W. A., Moskalik, P., & Pamyatnykh, A. A. 1993, MNRAS, 265, 588, doi: 10.1093/mnras/265.3.588

Dziembowski, W. A., & Pamiatnykh, A. A. 1993, MNRAS, 262, 204, doi: 10.1093/mnras/262.1.204

Ekström, S., Georgy, C., Eggenberger, P., et al. 2012, A&A, 537, A146, doi: 10.1051/0004-6361/201117751

Eldridge, J. J., Fraser, M., Smartt, S. J., Maund, J. R., & Crockett, R. M. 2013, Monthly Notices of the Royal Astronomical Society, 436, 774, doi: 10.1093/mnras/stt1612

Eldridge, J. J., Izzard, R. G., & Tout, C. A. 2008, MNRAS, 384, 1109, doi: 10.1111/j.1365-2966.2007.12738.x

Eldridge, J. J., Langer, N., & Tout, C. A. 2011, Monthly Notices of the Royal Astronomical Society, 414, 3501, doi: 10.1111/j.1365-2966.2011.18650.x

Eldridge, J. J., Stanway, E. R., Xiao, L., et al. 2017, PASA, 34, e058, doi: 10.1017/pasa.2017.51

Esa, . 1997, VizieR Online Data Catalog: The Hipparcos and Tycho Catalogues (ESA 1997), VizieR On-line Data Catalog: I/239. Originally published in: 1997HIP...C......0E

Esteban, C., Mesa-Delgado, A., Morisset, C., & García-Rojas, J. 2016, MNRAS, 460, 4038, doi: 10.1093/mnras/stw1243

Faherty, J. K., Shara, M. M., Zurek, D., Kanarek, G., & Moffat, A. F. J. 2014, The Astronomical Journal, 147, 115, doi: 10.1088/0004-6256/147/5/115

Fitzpatrick, E. L., Massa, D., Gordon, K. D., Bohlin, R., & Clayton, G. C. 2019, ApJ, 886, 108, doi: 10.3847/1538-4357/ab4c3a

Fleming, W. P. S., & Pickering, E. C. 1912, Annals of Harvard College Observatory, 56, 165

Foellmi, C., Moffat, A. F. J., & Guerrero, M. A. 2003, Monthly Notices of the Royal Astronomical Society, 338, 1025, doi: 10.1046/j.1365-8711.2003.06161.x

Friedman, J. H. 2001, The Annals of Statistics, 29, 1189 , doi: 10.1214/aos/1013203451

Fryer, C. L., Mazzali, P. A., Prochaska, J., et al. 2007, Publications of the Astronomical Society of the Pacific, 119, 1211, doi: 10.1086/523768

Gaia Collaboration. 2018, VizieR Online Data Catalog: Gaia DR2 (Gaia Collaboration, 2018), VizieR On-line Data Catalog: I/345. Originally published in: 2018A&A...616A...1G; doi:10.5270/esa-ycs, doi: 10.26093/cds/vizier.1345

—. 2022, VizieR Online Data Catalog, I/355

Gaia Collaboration, Prusti, T., de Bruijne, J. H. J., et al. 2016, A&A, 595, A1, doi: 10.1051/0004-6361/201629272

Gaia Collaboration, Brown, A. G. A., Vallenari, A., et al. 2018, A&A, 616, A1, doi: 10.1051/0004-6361/201833051

Gaia Collaboration, Vallenari, A., Brown, A. G. A., et al. 2023, A&A, 674, A1, doi: 10.1051/0004-6361/202243940

Gaskell, C. M., Cappellaro, E., Dinerstein, H. L., et al. 1986, ApJL, 306, L77, doi: 10.1086/184709

Gehrz, R. D., & Hackwell, J. A. 1974, ApJ, 194, 619, doi: 10.1086/153281

Georgy, C., Ekström, S., Meynet, G., et al. 2012, A&A, 542, A29, doi: 10.1051/0004-6361/201118340

Ghosh, S., Ninan, J. P., Ojha, D. K., & Sharma, S. 2023, Journal of Astrophysics and Astronomy, 44, 30, doi: 10.1007/s12036-023-09926-y

Glatzel, W. 1994, MNRAS, 271, 66, doi: 10.1093/mnras/271.1.66

Glatzel, W. 2008, in Astronomical Society of the Pacific Conference Series, Vol. 391, Hydrogen-Deficient Stars, ed. A. Werner & T. Rauch, 307

Glatzel, W., Kiriakidis, M., & Fricke, K. J. 1993, Monthly Notices of the Royal Astronomical Society, 262, L7, doi: 10.1093/mnras/262.1.L7

GLIMPSE Team. 2020, Galactic Legacy Infrared Midplane Survey Extraordinaire, IPAC, doi: 10.26131/IRSA405

Gomes, N. R. C., Del Sordo, F., & Torgo, L. 2023, arXiv e-prints, arXiv:2305.02407, doi: 10.48550/arXiv.2305.02407

Gordon, K. D., Cartledge, S., & Clayton, G. C. 2009, ApJ, 705, 1320, doi: 10.1088/0004-637X/705/2/1320

Gordon, K. D., Clayton, G. C., Decleir, M., et al. 2023, ApJ, 950, 86, doi: 10.3847/1538-4357/accb59

Gordon, K. D., Misselt, K. A., Bouwman, J., et al. 2021, ApJ, 916, 33, doi: 10.3847/1538-4357/ac00b7

Gräfener, G., & Hamann, W. R. 2005, A&A, 432, 633, doi: 10.1051/0004-6361:20041732

Gräfener, G., Koesterke, L., & Hamann, W. R. 2002, A&A, 387, 244, doi: 10.1051/0004-6361:20020269

Gräfener, G., Owocki, S. P., & Vink, J. S. 2012, A&A, 538, A40, doi: 10.1051/0004-6361/201117497

Gräfener, G., & Vink, J. S. 2013, A&A, 560, A6, doi: 10.1051/0004-6361/201321914

Gräfener, G., Vink, J. S., de Koter, A., & Langer, N. 2011, A&A, 535, A56, doi: 10.1051/0004-6361/201116701

Grassitelli, L., Chené, A. N., Sanyal, D., et al. 2016, A&A, 590, A12, doi: 10.1051/0004-6361/201527873

Groh, J. H., Georgy, C., & Ekström, S. 2013a, A&A, 558, L1, doi: 10.1051/0004-6361/201322369

Groh, J. H., Meynet, G., & Ekström, S. 2013b, A&A, 550, L7, doi: 10.1051/0004-6361/201220741

Groh, J. H., Meynet, G., Georgy, C., & Ekström, S. 2013c, A&A, 558, A131, doi: 10.1051/0004-6361/201321906

Hackwell, J. A., Gehrz, R. D., Smith, J. R., & Strecker, D. W. 1976, ApJ, 210, 137, doi: 10.1086/154811

Hadfield, L. J., van Dyk, S. D., Morris, P. W., et al. 2007, MNRAS, 376, 248, doi: 10.1111/j.1365-2966.2007.11424.x

Hainich, R., Shenar, T., Sander, A., Hamann, W. R., & Todt, H. 2017, in IAU Symposium, Vol. 329, The Lives and Death-Throes of Massive Stars, ed. J. J. Eldridge, J. C. Bray, L. A. S. McClelland, & L. Xiao, 171–175, doi: 10.1017/S1743921317002794

Hamann, W. R., & Koesterke, L. 1998, A&A, 335, 1003

Hill, G. M., Moffat, A. F. J., & St-Louis, N. 2018, MNRAS, 474, 2987, doi: 10.1093/mnras/stx2943

Hillier, D. J. 1989, ApJ, 347, 392

—. 1991, A&A, 247, 455

Hillier, D. J. 2003, in A Massive Star Odyssey: From Main Sequence to Supernova, ed. K. van der Hucht, A. Herrero, & C. Esteban, Vol. 212, 70

—. 2011, Ap&SS, 336, 87, doi: 10.1007/s10509-010-0590-9

Hillier, D. J. 2012, in From Interacting Binaries to Exoplanets: Essential Modeling Tools, ed. M. T. Richards & I. Hubeny, Vol. 282, 229–234

Hillier, D. J., & Miller, D. 1999, The Astrophysical Journal, 519, 354

Hillier, D. J., & Miller, D. L. 1998, ApJ, 496, 407

Hiltner, W. A., & Schild, R. E. 1966, ApJ, 143, 770, doi: 10.1086/148556

Huang, C. X., Vanderburg, A., Pál, A., et al. 2020, Research Notes of the American Astronomical Society, 4, 204, doi: 10.3847/2515-5172/abca2e

Hummer, D. G., Berrington, K. A., Eissner, W., et al. 1993, A&A, 279, 298

Ignace, R., Cassinelli, J. P., Tracy, G., Churchwell, E., & Lamers, H. J. G. L. M. 2007, The Astrophysical Journal, 669, 600, doi: 10.1086/521718

Ignace, R., St-Louis, N., & Proulx-Giraldeau, F. 2015, A&A, 575, A129, doi: 10.1051/0004-6361/201424806

Kanarek, G., Shara, M., Faherty, J., Zurek, D., & Moffat, A. 2015, MNRAS, 452, 2858, doi: 10.1093/mnras/stv1342

Kar, S., Bhattacharya, R., Das, R., Pihlström, Y., & Lewis, M. O. 2024a, The Astrophysical Journal, 977, 170, doi: 10.3847/1538-4357/ad8dda

Kar, S., Das, R., & Baug, T. 2024b, The Astrophysical Journal, 968, 60, doi: 10.3847/1538-4357/ad4131

Kar, S., Das, R., Mathew, B., Baug, T., & Mandal, A. 2024c, The Astronomical Journal, 168, 199, doi: 10.3847/1538-3881/ad77d0

Kippenhahn, R., & Weigert, A. 1967, ZA, 65, 251

Kramida, A. E., Ralchenko, Y., Reader, J., & NIST ASD Team. 2022, NIST Atomic Spectra Database (version 5.10) [online]. https://physics.nist.gov/asd

Kunimoto, M., Tey, E., Fong, W., et al. 2022, Research Notes of the American Astronomical Society, 6, 236, doi: 10.3847/2515-5172/aca158

Kunimoto, M., Huang, C., Tey, E., et al. 2021, Research Notes of the AAS, 5, 234, doi: 10.3847/2515-5172/ac2ef0

Kurucz, R. L. 2009, in American Institute of Physics Conference Series, Vol. 1171, Recent Directions in Astrophysical Quantitative Spectroscopy and Radiation Hydrodynamics, ed. I. Hubeny, J. M. Stone, K. MacGregor, & K. Werner, 43–51, doi: 10.1063/1.3250087

Kurucz, R. L. 2010, berkeley. http://kurucz.harvard.edu/

Langer, N. 1989, A&A, 210, 93

Lasker, B., Lattanzi, M. G., McLean, B. J., & et al. 2007, VizieR Online Data Catalog: The Guide Star Catalog, Version 2.3.2 (GSC2.3) (STScI, 2006), VizieR On-line Data Catalog: I/305. Originally published in: 2008AJ....136..735L

Lasker, B. M., Lattanzi, M. G., McLean, B. J., et al. 2008, AJ, 136, 735, doi: 10.1088/0004-6256/136/2/735

Lau, R. M., Hankins, M. J., Han, Y., et al. 2022, Nature Astronomy, 6, 1308, doi: 10.1038/s41550-022-01812-x

Lau, R. M., Wang, J., Hankins, M. J., et al. 2023, ApJ, 951, 89, doi: 10.3847/1538-4357/acd4c5

Lee, C.-D., Chen, W.-P., & Kinoshita, D. 2011, in Active OB Stars: Structure, Evolution, Mass Loss, and Critical Limits, ed. C. Neiner, G. Wade, G. Meynet, & G. Peters, Vol. 272, 404–405, doi: 10.1017/S1743921311010933

Lefèvre, L., Marchenko, S. V., Moffat, A. F. J., et al. 2005, ApJL, 634, L109, doi: 10.1086/498393

Leibowitz, E. M. 1972, Journal of Quantitative Spectroscopy and Radiative Transfer, 12, 299, doi: https://doi.org/10.1016/0022-4073(72)90048-9

Lenoir-Craig, G., St-Louis, N., Moffat, A. F. J., et al. 2022, ApJ, 925, 79, doi: 10.3847/1538-4357/ac397d

Lenz, P., & Breger, M. 2005, Communications in Asteroseismology, 146, 53, doi: 10.1553/cia146s53

Lépine, S., & Moffat, A. F. J. 1999, ApJ, 514, 909

Lépine, S., Moffat, A. F. J., St-Louis, N., et al. 2000, AJ, 120, 3201

Levenberg, K. 1944, Quarterly of Applied Mathematics, 2, 164. https://api.semanticscholar.org/CorpusID:124308544

Li, G., Bedding, T. R., Murphy, S. J., et al. 2018, Monthly Notices of the Royal Astronomical Society, 482, 1757, doi: 10.1093/mnras/sty2743

Lightkurve Collaboration, Cardoso, J. V. d. M., Hedges, C., et al. 2018, Lightkurve: Kepler and TESS time series analysis in Python, Astrophysics Source Code Library. http://ascl.net/1812.013

Luo, D., & Pradhan, A. K. 1989, Journal of Physics B Atomic Molecular Physics, 22, 3377, doi: 10.1088/0953-4075/22/21/005

Maeder, A., & Lequeux, J. 1982, Astronomy and Astrophysics, vol. 114, no. 2, Oct. 1982, p. 409-413., 114, 409

Marchenko, S. V., & Moffat, A. F. J. 2017, Monthly Notices of the Royal Astronomical Society, 468, 2416, doi: 10.1093/mnras/stx563

Marquardt, D. W. 1963, Journal of the Society for Industrial and Applied Mathematics, 11, 431

Mas-Hesse, J. M., Kunth, D., & Cerviño, M. 2000, NewAR, 44, 229, doi: 10.1016/S1387-6473(00)00052-X

Massey, P., & Gronwall, C. 1990, ApJ, 358, 344

Massey, P., & Hunter, D. A. 1998, The Astrophysical Journal, 493, 180, doi: 10.1086/305126

Massey, P., Olsen, K. A. G., & Parker, J. W. 2003, Publications of the Astronomical Society of the Pacific, 115, 1265, doi: 10.1086/379024

Mauerhan, J. C., Van Dyk, S. D., & Morris, P. W. 2009, PASP, 121, 591, doi: 10.1086/603544

—. 2011, AJ, 142, 40, doi: 10.1088/0004-6256/142/2/40

Mendoza, C. 1983, in Planetary Nebulae, ed. L. H. Aller, Vol. 103, 143–172

Meynet, G., & Maeder, A. 2003, A&A, 404, 975, doi: 10.1051/0004-6361:20030512

—. 2005, A&A, 429, 581, doi: 10.1051/0004-6361:20047106

Miralles-Caballero, D., Díaz, A. I., López-Sánchez, Á. R., et al. 2016, A&A, 592, A105, doi: 10.1051/0004-6361/201527179

Mistry, D., Copperwheat, C. M., Darnley, M. J., & Olier, I. 2022, Monthly Notices of the Royal Astronomical Society, 517, 3362, doi: 10.1093/mnras/stac2760

Moffat, A. F. J., Drissen, L., Lamontagne, R., & Robert, C. 1988, ApJ, 334, 1038

Morel, T., Georgiev, L. N., Grosdidier, Y., et al. 1999a, A&A, 349, 457, doi: 10.48550/arXiv.astro-ph/9907356

Morel, T., Marchenko, S. V., Eenens, P. R. J., et al. 1999b, ApJ, 518, 428, doi: 10.1086/307250

Morello, G., Morris, P. W., Van Dyk, S. D., Marston, A. P., & Mauerhan, J. C. 2018, MNRAS, 473, 2565, doi: 10.1093/mnras/stx2474

Nahar, S. N. 1998, Phys. Rev. A, 58, 3766, doi: 10.1103/PhysRevA.58.3766

—. 2010, Phys. Rev. A, 58, 3766, doi: 10.1103/PhysRevA.58.3766

Nazé, Y., Rauw, G., & Gosset, E. 2021, MNRAS, 502, 5038, doi: 10.1093/mnras/stab133

Neugent, K., & Massey, P. 2019, Galaxies, 7, 74, doi: 10.3390/galaxies7030074

Neugent, K. F., & Massey, P. 2011, The Astrophysical Journal, 733, 123, doi: 10.1088/0004-637X/733/2/123

Neugent, K. F., Massey, P., & Morrell, N. 2012, The Astronomical Journal, 144, 162, doi: 10.1088/0004-6256/144/6/162

Ninan, J. P., Ojha, D. K., Ghosh, S. K., et al. 2014, Journal of Astronomical Instrumentation, 3, 1450006, doi: 10.1142/S2251171714500068

Nussbaumer, H., & Storey, P. J. 1983, A&A, 126, 75

Osterbrock, D. E., & Cohen, R. D. 1982, ApJ, 261, 64, doi: 10.1086/160318

Owocki, S. P., Castor, J. I., & Rybicki, G. B. 1988, ApJ, 335, 914

Paczyński, B. 1967, AcA, 17, 355

Pandey, J. C., Pandey, S. B., & Karmakar, S. 2014, The Astrophysical Journal, 788, 84, doi: 10.1088/0004-637X/788/1/84

Panwar, N., Chen, W. P., Pandey, A. K., et al. 2014, Monthly Notices of the Royal Astronomical Society, 443, 1614, doi: 10.1093/mnras/stu1244

Payne-Gaposchkin, C. 1930, in Harvard Observatory Monographs, Vol. 3, 1

Pedregosa, F., Varoquaux, G., Gramfort, A., et al. 2011, Journal of Machine Learning Research, 12, 2825

Podsiadlowski, P., Joss, P. C., & Hsu, J. J. L. 1992, ApJ, 391, 246, doi: 10.1086/171341

Rao, N. K., Sriram, S., Jayakumar, K., & Gabriel, F. 2005, Journal of Astrophysics and Astronomy, 26, 331, doi: 10.1007/BF02702341

Rate, G., & Crowther, P. A. 2020, Monthly Notices of the Royal Astronomical Society, 493, 1512, doi: 10.1093/mnras/stz3614

Reid, M., Menten, K., Brunthaler, A., et al. 2019, The Astrophysical Journal, 885, 131

Ricker, G. R., Winn, J. N., Vanderspek, R., et al. 2014, Journal of Astronomical Telescopes, Instruments, and Systems, 1, 014003, doi: 10.1117/1.JATIS.1.1.014003

Rieke, G. H., & Lebofsky, M. J. 1985, ApJ, 288, 618, doi: 10.1086/162827

Robert, C., Moffat, A. F. J., Drissen, L., et al. 1992, ApJ, 397, 277, doi: 10.1086/171786

Roberts, M. S. 1962, AJ, 67, 79, doi: 10.1086/108603

Rosslowe, C. 2016, PhD thesis, University of Sheffield, UK

Rosslowe, C. K., & Crowther, P. A. 2015, MNRAS, 447, 2322, doi: 10.1093/mnras/stu2525

Rubio, G., Toalá, J. A., Jiménez-Hernández, P., et al. 2020, MNRAS, 499, 415, doi: 10.1093/mnras/staa2837

Safronova, U. I., Shlyaptseva, A. S., Cornille, M., & Dubau, J. 1998, PhyS, 57, 395, doi: 10.1088/0031-8949/57/3/010

Saio, H. 2009, Communications in Asteroseismology, 158, 245

Sander, A., Hamann, W. R., & Todt, H. 2012, A&A, 540, A144, doi: 10.1051/0004-6361/201117830

Sander, A. A. C., Hamann, W. R., Todt, H., et al. 2019a, A&A, 621, A92, doi: 10.1051/0004-6361/201833712

—. 2019b, A&A, 621, A92, doi: 10.1051/0004-6361/201833712

Sander, A. A. C., Vink, J. S., & Hamann, W. R. 2020, MNRAS, 491, 4406, doi: 10.1093/mnras/stz3064

Schmutz, W. 1997, A&A, 321, 268

Seaton, M. J. 1987, Journal of Physics B: Atomic and Molecular Physics, 20, 6363, doi: 10.1088/0022-3700/20/23/026

Shara, M. M., Faherty, J. K., Zurek, D., et al. 2012, The Astronomical Journal, 143, 149, doi: 10.1088/0004-6256/143/6/149

Shara, M. M., Faherty, J. K., Zurek, D., et al. 2012, AJ, 143, 149, doi: 10.1088/0004-6256/143/6/149

Shara, M. M., Moffat, A. F. J., Smith, L. F., et al. 1999, AJ, 118, 390

Shara, M. M., Moffat, A. F. J., Gerke, J., et al. 2009, AJ, 138, 402, doi: 10.1088/0004-6256/138/2/402

Sharma, S., Ojha, D. K., Ghosh, A., et al. 2022, Publications of the Astronomical Society of the Pacific, 134, 085002, doi: 10.1088/1538-3873/ac81eb

Shenar, T., Hainich, R., Todt, H., et al. 2016, A&A, 591, A22, doi: 10.1051/0004-6361/201527916

Shenar, T., Sablowski, D. P., Hainich, R., et al. 2019, A&A, 627, A151, doi: 10.1051/0004-6361/201935684

Skrutskie, M. F., Cutri, R. M., Stiening, R., et al. 2006, AJ, 131, 1163

Smartt, S. J. 2009, ARA&A, 47, 63, doi: 10.1146/annurev-astro-082708-101737

Smith, J. C., Stumpe, M. C., Cleve, J. E. V., et al. 2012, Publications of the Astronomical Society of the Pacific, 124, 1000, doi: 10.1086/667697

Smith, J.-D. T., & Houck, J. R. 2005, The Astrophysical Journal, 622, 1044, doi: 10.1086/427979

Smith, L. F. 1968, MNRAS, 138, 109, doi: 10.1093/mnras/138.1.109

Smith, L. F., Michael M., S., & Moffat, A. F. J. 1996, Monthly Notices of the Royal Astronomical Society, 281, 163, doi: 10.1093/mnras/281.1.163

Sobolev, V. V. 1960, Moving Envelopes of Stars, doi: 10.4159/harvard.9780674864658

Spitzer Science, C. 2009, VizieR Online Data Catalog, II/293

Sriram, S., Kumar, A., Surya, A., et al. 2018, in Society of Photo-Optical Instrumentation Engineers (SPIE) Conference Series, Vol. 10702, Ground-based and Airborne Instrumentation for Astronomy VII, ed. C. J. Evans, L. Simard, & H. Takami, 107026K, doi: 10.1117/12.2313165

St. -Louis, N., Drissen, L., Moffat, A. F. J., Bastien, P., & Tapia, S. 1987, ApJ, 322, 870, doi: 10.1086/165782

St-Louis, N., Chené, A. N., Schnurr, O., & Nicol, M. H. 2009, ApJ, 698, 1951, doi: 10.1088/0004-637X/698/2/1951

Stanway, E. R., & Eldridge, J. J. 2018, MNRAS, 479, 75, doi: 10.1093/mnras/sty1353

Stead, J. J., & Hoare, M. G. 2009, MNRAS, 400, 731, doi: 10.1111/j.1365-2966.2009.15530.x

Stevance, H., Eldridge, J., & Stanway, E. 2020, The Journal of Open Source Software, 5, 1987, doi: 10.21105/joss.01987

Stevens, I. R., & Howarth, I. D. 1999, Monthly Notices of the Royal Astronomical Society, 302, 549, doi: 10.1046/j.1365-8711.1999.02151.x

Stock, D. J., Barlow, M. J., & Wesson, R. 2011, MNRAS, 418, 2532, doi: 10.1111/j.1365-2966.2011.19643.x

Stumpe, M. C., Smith, J. C., Cleve, J. E. V., et al. 2012, Publications of the Astronomical Society of the Pacific, 124, 985, doi: 10.1086/667698

Suh, K.-W. 2020, The Astrophysical Journal, 891, 43

Sundqvist, J. O., Owocki, S. P., & Puls, J. 2018, A&A, 611, A17, doi: 10.1051/0004-6361/201731718

Tayal, S. S. 2008, A&A, 486, 629, doi: 10.1051/0004-6361:200810055

Toalá, J. A., Guerrero, M. A., Ramos-Larios, G., & Guzmán, V. 2015, A&A, 578, A66, doi: 10.1051/0004-6361/201525706

Toalá, J. A., Bowman, D. M., Van Reeth, T., et al. 2022, MNRAS, 514, 2269, doi: 10.1093/mnras/stac1455

Tody, D. 1986, in Society of Photo-Optical Instrumentation Engineers (SPIE) Conference Series, Vol. 627, Instrumentation in astronomy VI, ed. D. L. Crawford, 733

Tody, D. 1993, in Astronomical Society of the Pacific Conference Series, Vol. 52, Astronomical Data Analysis Software and Systems II, ed. R. J. Hanisch, R. J. V. Brissenden, & J. Barnes, 173

Townsend, R. H. D., & MacDonald, J. 2006, MNRAS, 368, L57, doi: 10.1111/j.1745-3933.2006.00157.x

Trenti, M., Perna, R., & Jimenez, R. 2015, The Astrophysical Journal, 802, 103, doi: 10.1088/0004-637X/802/2/103

Tuthill, P. G., Monnier, J. D., & Danchi, W. C. 1999, Nature, 398, 487, doi: 10.1038/19033

Usov, V. V. 1991, MNRAS, 252, 49, doi: 10.1093/mnras/252.1.49

van der Hucht, K. A. 2001, NewAR, 45, 135

van der Hucht, K. A., Conti, P. S., Lundstrom, I., & Stenholm, B. 1981, SSRv, 28, 227, doi: 10.1007/BF00173260

Vanbeveren, D., De Loore, C., & Van Rensbergen, W. 1998, A&A Rv, 9, 63, doi: 10.1007/s001590050015

Varricatt, W. P., Williams, P. M., & Ashok, N. M. 2004, MNRAS, 351, 1307, doi: 10.1111/j.1365-2966.2004.07867.x

Vink, J. S., & de Koter, A. 2005, A&A, 442, 587, doi: 10.1051/0004-6361:20052862

Vink, J. S., de Koter, A., & Lamers, H. J. G. L. M. 2001, A&A, 369, 574, doi: 10.1051/0004-6361:20010127

Vollmann, K., & Eversberg, T. 2006, Astronomische Nachrichten, 327, 862, doi: 10.1002/asna.200610645

Williams, P. M. 2019, MNRAS, 488, 1282, doi: 10.1093/mnras/stz1784

Williams, P. M., Beattie, D. H., Lee, T. J., Stewart, J. M., & Antonopoulou, E. 1978, Monthly Notices of the Royal Astronomical Society, 185, 467, doi: 10.1093/mnras/185.3.467

Williams, P. M., Crowther, P. A., & van der Hucht, K. A. 2015, MNRAS, 449, 1834

Williams, P. M., Longmore, A. J., van der Hucht, K. A., et al. 1985, Monthly Notices of the Royal Astronomical Society, 215, 23P, doi: 10.1093/mnras/215.1.23P

Williams, P. M., van der Hucht, K. A., & The, P. S. 1987, A&A, 182, 91

Williams, P. M., Marchenko, S. V., Marston, A. P., et al. 2009, MNRAS, 395, 1749, doi: 10.1111/j.1365-2966.2009.14664.x

Wolf, C. J. E., & Rayet, G. 1867, Academie des Sciences Paris Comptes Rendus, 65, 292

Wright, E. L., Eisenhardt, P. R. M., Mainzer, A. K., et al. 2010, AJ, 140, 1868, doi: 10.1088/0004-6256/140/6/1868

Yoon, S. C., Gräfener, G., Vink, J. S., Kozyreva, A., & Izzard, R. G. 2012, A&A, 544, L11, doi: 10.1051/0004-6361/201219790

Yoshino, E., Juarto, B., & Kurniadi, F. I. 2023, 2023 International Seminar on Application for Technology of Information and Communication (iSemantic), 187. https://api.semanticscholar.org/CorpusID:264789656

Yusof, N., Hirschi, R., Eggenberger, P., et al. 2022, MNRAS, 511, 2814, doi: 10.1093/mnras/stac230

Zacharias, N., Monet, D. G., Levine, S. E., et al. 2004, in American Astronomical Society Meeting Abstracts, Vol. 205, American Astronomical Society Meeting Abstracts, 48.15

Zechmeister, M., & Kürster, M. 2009, A&A, 496, 577, doi: 10.1051/0004-6361:200811296

Zhang, H. L., Graziani, M., & Pradhan, A. K. 1994, A&A, 283, 319

Zhang, H. L., & Pradhan, A. K. 1997, A&AS, 126, 373

Zhang, W., Kong, X., Li, C., Zhou, H.-Y., & Cheng, F.-Z. 2007, ApJ, 655, 851, doi: 10.1086/510231

Zhekov, S. A., Tomov, T., Gawronski, M. P., et al. 2014, MNRAS, 445, 1663, doi: 10.1093/mnras/stu1880